STUDIES AND APPLICATION OF

QUANTUM INTERFERENCE DETECTORS

by

ALISTAIR ANGUS FIFE

B.Sc., Aberdeen University, Scotland, 1964
M.Sc., University of Alberta, Edmonton, 1966

A DISSERTATION SUBMITTED IN PARTIAL

FULFILLMENT OF THE REQUIREMENTS FOR THE DEGREE OF

DOCTOR OF PHILOSOPHY

in the Department

of

PHYSICS

SIMON FRASER UNIVERSITY
September 1971

APPROVAL

Name : Alistair Angus Fife

Degree : Doctor of Philosophy

Title of Thesis : Studies and Application of Quantum Interference Detectors

Examining Committee:

Chairman: K.E. Rieckhoff

S. Gygax
Senior Supervisor

R.R. Haering

J.C. Irwin

E.J. Wells

J.G. Adler
External Examiner
Associate Professor
University of Alberta
Edmonton, Alberta

Date Approved: September 16, 1971

ABSTRACT

Two similar types of superconducting quantum interference detectors (SQUID) have been successfully developed and their properties studied. The SQUIDS utilise flux quantisation and the Josephson effects in a ring (or rings) containing a weak link section. The rings may be either purely superconducting (M-SQUID) or partially resistive (R-SQUID). The M-SQUIDS are useful as extremely sensitive magnetometers for measuring dc and ac flux. Versions of the M-SQUID which use point-contact weak links have been found to be rather sensitive to vibrations and their properties tend to degrade over a period of months. This has led to the development of reasonably stable, rugged devices employing weak links of $NbSe_2$, a superconducting layer structure.

The R-SQUIDS reported here employ Nb-Nb point contacts, and have been used as the superconducting input for a sensitive superheterodyne receiver for frequencies in the range 10^{10} to 10^{11} Hz. Several of these devices were constructed and tested in the frequency ranges (26.5 - 40) GHz and (67 - 73) GHz. The device response is complicated by the effects on the AC Josephson current of distributed circuit elements and a range of complex behaviour is presented which is only partially understood.

The logic behind developing the latter detector has been to search for stimulated emission of energy gap radiation from superconducting tunnel junctions. The R-SQUID was to be used for frequency and linewidth measurements of the expected energy gap radiation. Broad band sensitivity was provided by a helium cooled Silicon bolometer. Despite extensive studies using a large variety of tunnel junction parameters, the search has turned out to be completely negative in contrast to the measurements of other authors. A thorough analysis of the earlier theory and experiments has led to the conclusion that a stimulated emission process in superconductors is rather unlikely, and earlier experiments have to be interpreted differently.

TABLE OF CONTENTS

LIST OF TABLES

LIST OF FIGURES

LIST OF SYMBOLS

A	Einstein A-coefficient for spontaneous transition
$\bar{A}$	Magnetic vector potential
A'	Weak link cross-section
A''	Squid - rf coil coupling parameter
B	Einstein B-coefficient for stimulated transition
C	Capacitance
C'	Bolometer heat capacity
D	Diffusion constant for quasiparticles
ε	Josephson coupling energy
E	Emf
$\bar{E}$	Electric field
G	Weak link conductance
H_1	Hamiltonian of a Josephson junction
H_2	Hamiltonian of a pendulum
H_c^T	Superconducting critical field at temperature
I	DC current
I'	Moment of inertia
I_c^T	Silsbee critical current for a wire at temperature T
J	Current density
J_n	Bessel function of order n
K	Torsion bar force constant
K_1	Mutual inductance coupling strength
K'	Thermal conductance of bolometer to bath
L	SQUID loop inductance
L'	$(1 + \gamma)L$ $\quad \gamma$ = dimensionless parameter

L_T	Tank circuit inductance
M	Mutual inductance
N	Integer
N_1	Number of condensed pairs within $h\delta\nu$ of energy gap
N_2	Half number of quasiparticles within $h\delta\nu$ of gap edge
N(O)	Normal metal density of states at Fermi energy
Q	Q-value of resonant circuit
R	Resistance
R_o	Bolometer resistance coefficient
R_N	Normal state weak link resistance
R_1	Amplitude of time dependent part of bolometer resistance
S	Cylinder area
S'	Responsivity of bolometer
T	Temperature
T_c	Superconducting critical temperature
T_1	Amplitude of time dependent part of bolometer temperature
T_B	Bolometer temperature
T_o	Bolometer bath temperature
V	Voltage
V_o	DC voltage across weak link
$\overline{V_N^2}$	Mean square noise voltage
W_o	Bolometer absorbed power
Y	Temperature dependence of stimulated gain to pair-breaking loss in superconducting maser

$2a$	Wire diameter
c	Velocity of light in vacuum
d	Weak link barrier thickness Ta tunnel junction tip diameter
e	Electronic charge
f_1	Frequency of applied signal
f'	Pendulum damping constant
f_J	Josephson frequency
f_c	SQUID geometric resonance frequency
f_{BE}	Bose-Einstein distribution function
f_{FD}	Fermi-Dirac distribution function
g	Stimulated gain in maser; acceleration due to gravity
i	SQUID loop current
i_c	Weak link critical current
i_{cn}	Fourier component of weak link critical current
j_c	Critical current necessary to destroy superconductivity
j_T	Maser threshold current
j	Current density
k	Complex part of refractive index
k_i	Maser system losses
k_B	Boltzmann's constant
ℓ	Length
ℓ_F	Mean free path
m	Electron mass
m^*	Effective electron mass

n	Integer
$\hat{n}$	Complex refractive index
n'	Electron concentration
$n_s(t)$	Density of condensed pairs in a superconductor at temperature t
p	Integer
$\bar{p}$	Canonical momentum
$\bar{q}$	Wave vector
t	Time; reduced temperature (T/T_c)
t'	Weak link thickness
$u(\nu)$	Energy density per unit frequency of radiation field
v	Pair velocity
v_F	Fermi velocity
v_1	Voltage induced by external flux Φ_x.
Z	Quantum efficiency
α	Weak link parameter = $2\pi i_c/G\omega_o\Phi_o$
α'	R-SQUID loop parameter = $(1 + (V_o/i_cR)^2)^{-\frac{1}{2}}$
α''	Total photon absorption coefficient in superconductor
α_o	Pair breaking absorption constant
β	Pendulum or SQUID parameter = $\frac{2\pi Li_c}{\Phi_o} = \frac{mgl}{K}$
γ	Weak link parameter = $(mt'/2e^2A'L)$
γ'	Specific heat coefficient $(C_v = \gamma^1T + AT^3)$
2Δ	Energy gap = $\hbar\omega_g$
$\hat{\epsilon}$	Complex dielectric constant = $\epsilon_1 + i\epsilon_2$
$\hat{\sigma}$	Complex conductivity = $\sigma_1 + i\sigma_2$

$\hat{n}$	Complex refractive index = $q + ik$
σ_N	Normal state conductivity
τ'	Scattering time = ℓ_F/v_F
τ_c	Time required for quantum phase to fluctuate by one radian
τ^*	Bolometer time constant
τ	Weak link transition time
θ	Phase difference
θ_x	Phase angle equivalent to external flux Φ_x; pendulum angular displacement
Θ_o	Value of Θ at $t = 0$, $\bar{A} = 0$
ρ	Electron pair density
Φ_{rf}	Amplitude of rf flux
Φ	Total flux
Φ_x	External flux
Φ_o	Flux quantum
ω_1	Angular frequency of applied signal
ω_J	Josephson angular frequency
ω_c	Lower limit sweep frequency for R-SQUID ($= 2\pi/\tau_c$)
ω_c'	High frequency cut-off for SQUID
ω_L	Inductive low frequency cut-off for SQUID
ω_o	Weak link time constant = GC^{-1}
λ	Free space wavelength
λ_g	Waveguide wavelength
λ_o	London penetration depth
λ_c	Waveguide cut-off wavelength
ξ'	Reduced time parameter ($= \omega_o t$)

ξ_o	Pippard coherence distance
ξ	Coherence distance ($\ell_F \not\approx \infty$)
ζ	Ratio of phonon: photon decay = τ_p/τ_R
δE	Superconducting spontaneous radiative linewidth in eV
$\delta\nu$	Superconducting spontaneous radiative linewidth in Hz
$\delta\omega$	Josephson linewidth due to quantum phase fluctuations
δ'	Temperature coefficient of bolometer resistance ($= \frac{1}{R}\frac{dR}{dT}$)
μ_o	$4\pi \times 10^{-7}$ Henry/meter
χ	Bolometer resistence parameter
ν	Frequency
ϕ	Phase of Ginsburg Landau wavefunction
$\hbar$	Planck's constant
Γ	Torque
Ξ	Normalized lineshape function $\int \Xi d\nu = 1$
Ψ	Ginsburg Landau wavefunction

ACKNOWLEDGMENTS

Many people have contributed to the research presented in this thesis. First and foremost, it is a pleasure to thank my supervisor, Dr. Suso Gygax, for initially suggesting this area of study, and for the extensive support and many ideas necessary to complete the investigation. He has contributed long patient hours in the laboratory, and also in the successful analysis of the results.

The SQUID project received a flying start from Dr. J.E. Zimmerman of the U.S. National Bureau of Standards. I wish to thank him for his generosity in freely supplying a great deal of technical information on SQUIDS. My grateful thanks also to Dr. A. Arrott for inviting Dr. Zimmerman to this department and also for a useful exchange of ideas on the SQUID project.

I greatly appreciate the active interest taken in this work by the members of my supervisory committee, Drs. R.R. Haering and J.C. Irwin. Their expertise in the laser field was especially helpful.

I have benefited considerably from the collaboration with Drs. R.F. Frindt, and F. Consadori whose Italian spirit brightened many a dull moment. I thank them for supplying the $NbSe_2$ crystals used to make the weak links, and also for the large part they played in the device design. The ideas of Dr. B. Heinrich were also very useful in this area.

I thank Dr. J.F. Cochran for bringing the superconducting maser to my attention and for his enthusiastic interest. My thanks also to Dr. W. Gregory for supplying some of his Ta tips for study.

I wish to thank the following for advice and assistance: Drs. B. Clayman, L.H. Palmer, A. Griffin, D. Dunn, V. Kambersky and graduate students T. Templeton and P. de Trey.

I have enjoyed excellent technical assistance from: M. Billany, J. Oxton, W. Gloor, S. Chinniah, J. Mercier and M. Dowding. The electronic expertise of P. Garnett was also invaluable. The machine shop under the guidance of F. Wick contributed solidly to the overall success.

I owe a special debt of gratitude to Miss Jean Piovesan for helping to meet the deadlines and for her excellent typing. I greatly appreciate the additional assistance of Mrs. E. Britt, Miss M. Linquist and Mrs. Ann Davy.

Finally, I wish to thank the National Research Council of Canada for a Scholarship during the period 1966-1969, and this Department of Physics for support during the subsequent period.

CHAPTER 1

INTRODUCTION

1.1 Historical Perspective

The modern view of a superconductor as a system in a highly correlated condensed state was originally suggested by London[1] and forms a central theme of the Bardeen - Cooper - Schrieffer (BCS) theory of superconductivity[2]. The quantisation of flux in units of the flux quantum $\frac{h}{2e}$ (where h is Planck's constant and e the electronic charge) presents dramatic confirmation of the existence of this condensed state. Another striking example is the tunnel junction consisting of two superconductors which are weakly coupled together through a thin insulating barrier. This system was first studied theoretically by Josephson[3,4] who predicted a number of remarkable effects which have been subsequently verified by experiment. Josephson demonstrated that for sufficiently thin insulating barriers ($\simeq$10Å thick), a supercurrent flow is possible: i.e. a lossless tunneling current is carried through the barrier with no applied voltage appearing across the junction until a critical current i_c is exceeded. The magnitude of i_c is magnetic field sensitive. Once i_c has been exceeded a voltage V develops across the junction which gives rise to an oscillating supercurrent whose frequency is proportional to V. This frequency is extremely high even for small voltages (483.6 MHz/μV).

Anderson[5] has coined the phrase "weak superconductivity" to describe this tunneling effect since the Josephson junction has some properties akin to those of a superconductor with greatly reduced critical current density.

The aforementioned "DC and AC Josephson effects" have formed the basis of an extensive research effort which has enhanced the understanding of the superconducting state. Experiments on a wide variety of junctions in many laboratories have shown the Josephson tunnel junction to be a device of considerable intricacy which can display subtle non-linear behaviour expecially when interacting with external circuit elements. As will be discussed in Chapter II, a wide variety of structures has been found to display some aspect of the Josephson effects - either ideal or non-ideal behaviour - and a more general term "weak link" is used to encompass all structures. The device potential of the Josephson effects was quickly realised and there have been many applications, often resulting in devices which have performance capabilities greatly exceeding those previously available.

This thesis is primarily concerned with the development and application of two similar types of superconducting devices (SQUIDS) which utilise flux quantisation and the Josephson effects in a ring containing a weak link section. The ring may be either purely superconducting (M-SQUID) or

partially resistive (R-SQUID), the mode of use depending on the precise application. M-SQUIDS are sensitive to both dc and ac external flux and have found application as magnetometers and voltmeters of unparalleled sensitivity. R-SQUIDS on the other hand are insensitive to dc or low frequency audio flux but can function as highly sensitive tunable spectrometers of high Q-value ($> 10^4$).

The purely superconducting ring containing a Josephson junction or junctions was first proposed by Mercereau and co-workers[6] of the Ford Scientific Laboratories to demonstrate quantum interference effects in superconductors on a truly macroscopic scale. The subsequent analysis by Zimmerman and Silver[7], of quantised magnetic flux transitions in a superconducting ring containing a single weak link, laid the groundwork for subsequent developments of flux sensors of extraordinary sensitivity.

The critical feature of all weak link detectors is the weak link itself. A great deal of current effort is involved with construction of weak links which are stable reproducible structures, rugged enough to withstand the stresses involved in thermal cycling between room and liquid helium temperatures. The early Zimmerman devices[7] used point contact weak links formed by carefully adjusting a pair of Niobium screws to make microscopic contact. These devices are now commercially

available(*) and are stable over long periods (> 1 year)[8], provided that the structures are shielded from excessive vibrations and atmospheric corrosion. The experiences with the Zimmerman structure in this laboratory were somewhat less promising, and an alternative form of weak link was developed by Consadori et al[9] making use of the properties of Niobium Diselenide ($NbSe_2$), a superconducting layer structure. The $NbSe_2$ weak links have been found to be stable and reproducible over long periods of time, and are also almost completely insensitive to vibrations. An outline of this development is contained in Chapter III of this thesis.

The $NbSe_2$ weak links have at present been used only in M-SQUID structures. A number of attempts to construct an R-SQUID using these weak links have been singularly unsuccessful. The precise reason for the failure of this approach is somewhat obscure at present. Accordingly all data on the R-SQUIDS were obtained using point contact devices.

Initially the main reason for developing the R-SQUID as a spectrometer was to study the spectral output from the superconducting tunnel junction injection maser proposed by Gregory et al[10]. The R-SQUID is an ideal instrument for studying such a spectral output since it is compact, highly sensitive with Q-values > 10^4, and is tunable over a wide range of wavelengths in the microwave regime. A true test of

*Superconducting Helium Electronics Manufacturing Corp., 3422 Tripp Court, Suite B, San Diego, California 92121.

whether or not a stimulated emission process for photons is taking place in the tunnel junction would be to observe the onset of line-narrowing of the spontaneous emission[11]. The experiments of Gregory et al[10,12,13] involved the use of a broad band detector (a bolometer) and little information about the spectral output from the tunnel junction was obtained.

The Gregory experiment was repeated in the present study using essentially the same tunnel junction system where a specially formed Tantalum tip was adjusted to make contact with the anodised surface of an Aluminium plate. A bolometer was used for broad band detection purposes and the R-SQUID provided narrow-band sensitivity. Despite an extensive search for this radiation using a wide variety of tunnel junction parameters, the results have been completely negative. No narrow band radiation associated with the superconductivity of Tantalum has been observed. This negative result spurred a re-examination of the theory of the maser and a more detailed analysis, making use of some plausible assumptions about the behaviour of superconductors at energy gap frequencies, has revealed that a stimulated emission process for photons is rather unlikely. Thus an alternative explanation of the radiation observed by Gregory et al will have to be found.

1.2 Summary of Thesis Content

In this section a brief summary of the contents of each chapter will be provided.

Chapter II

An outline of the essential features of the Josephson effects is necessary to understand the behaviour of the weak link devices. A survey of weak links which display Josephson effects is given, as well as a comparison with existing theory. A model is presented of the SQUID structures which describes the interaction of a pure Josephson junction with distributed circuit elements. Harmonic generation is discussed as well as mixing effects with external radiation.

Chapter III

This chapter discusses the M-SQUIDS which use either Nb-Nb point contacts or $NbSe_2$ weak links. The description is primarily concerned with the construction and properties of the $NbSe_2$ SQUIDS since the point-contact devices were essentially copies of those described by Zimmerman et al[8].

Chapter IV

Details of the construction and various ways of adjusting point-contact R-SQUIDS are presented here, together with an

extensive study of the device behaviour for frequencies in the microwave regimes (26.5 - 40) GHz and (67 - 73) GHz. This behaviour is discussed in terms of the models presented in Chapter II.

Chapter V

The main application of the R-SQUID has been to search for stimulated emission from superconducting tunnel junctions. In this chapter a brief summary of the previous theoretical and experimental work is followed by a detailed description of the present system employed to duplicate these previous experiments.

Chapter VI

Details are given of the extensive experimental search for superconducting energy gap radiation from junctions of the form Ta - Oxide - Al under a variety of experimental conditions. The negative result of this search provided the impetus for a re-examination of the theory of tunnel junction maser. This analysis is contained in Chapter VI together with a critical discussion of the previous experimental work.

Chapter VII

The principal features of this thesis are summarised in this final chapter together with a number of suggestions for

further work on more fundamental studies of $NbSe_2$ and also its use in SQUID-type or other structures utilising the Josephson effects.

CHAPTER II

WEAK LINK DETECTORS REVIEW AND THEORY

2.1 Josephson Tunneling - A Brief Summary

The subject of Josephson tunneling has been extensively reviewed in the literature[5, 14-18] and only a brief survey of the principal results will be presented here. The initial theory of Josephson[3] was a microscopic theory involving the method of the tunneling Hamiltonian but the results of interest can equally well be derived on phenomenological grounds[4,5,19]. The system under consideration is shown in Fig. 2.1 where two superconducting regions A and B are separated by a thin insulating barrier I. Following Ginsburg, and Landau[20], the description of a superconductor is given in terms of a complex order parameter $\Psi = |\Psi| e^{i\phi}$ where ϕ is the phase of all pairs of the condensate. Thus one can ascribe phases ϕ_A, ϕ_B to superconductors A and B. The basic ideas of the Josephson effect involve studying the relation between the phases ϕ_A, ϕ_B as the barrier thickness d is reduced to zero i.e. the change when the system goes from two isolated superconductors to a single superconductor. As $d \to o$ the coupling energy E increases in magnitude (becomes more negative) until it is greater than the thermal fluctuation energy present, at which point the superconductors A, B become phase locked. Josephson[3] demonstrated that in this limit of

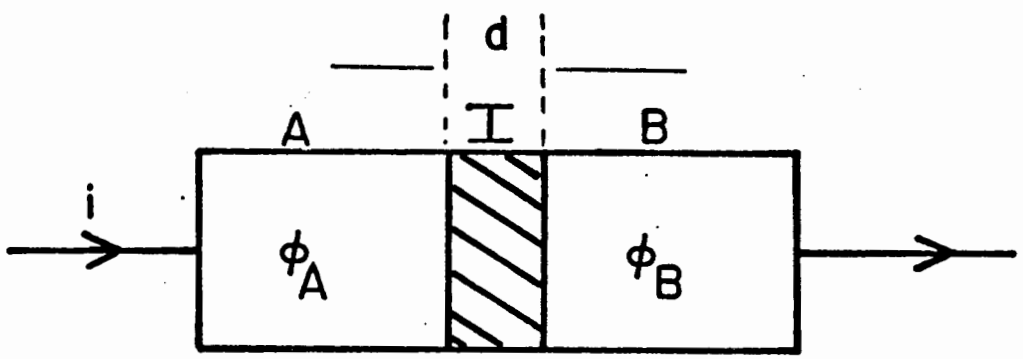

Fig. 2.1 Schematic Josephson Junction.

weak coupling a supercurrent of Cooper pairs could tunnel through the barrier. The coupling energy E, and supercurrent i, are given by[4,5,19]

$$E = -\frac{\hbar}{2e} i_c \cos\theta \qquad 2.101$$

$$i = i_c \sin\theta \qquad 2.102$$

where $\theta = \phi_B - \phi_A$ is the quantum phase difference across the barrier.

As the current i is increased from zero, θ increases and hence the coupling energy is reduced. When $i = i_c$ the critical current, the junction can no longer sustain a supercurrent, since E has been reduced to zero. As the current is further increased, a finite voltage V develops which causes θ to vary with time as[4]

$$\dot{\theta} = \frac{2e}{\hbar} V \qquad 2.103$$

More precisely V is the chemical potential difference (Fermi energy difference) of the two superconductors and not the electrostatic potential difference. Equation 2.103 in 2.102 thus gives an oscillating supercurrent $i = i_c \sin \omega t$ which may be regarded as the virtual tunneling of Cooper pairs through the barrier together with the emission and absorption of photons of energy 2eV. The precise reason for

the time dependence of θ with applied voltage stems from the fact that shifting the electron potential energy of a superconductor by $e\delta V$ produces a phase factor $\exp\left(-\frac{ie\delta Vt}{\hbar}\right)$ in the wavefunction of each electron.

The phase difference θ is also modified by the presence of a vector potential $\vec{A}$. From arguments of gauge invariance[4,5,19,21] one can generalise equation 2.102 by writing

$$i = i_c \sin\left[\theta_o + \frac{2e}{\hbar}\int^{t} V(t')dt' - \frac{2e}{\hbar}\int_{A}^{B} \vec{A}.\vec{dl}\right] \qquad 2.104$$

where θ_o is the value of θ at $t = o$, $\vec{A} = o$, and is a random phase difference which depends on the initial conditions when the junction was formed. The phenomenological theory does not allow for calculation of i_c but an explicit calculation[22] in the BCS approximation gives

$$i_c = \frac{\pi \Delta_A \Delta_B}{\Delta_A + \Delta_B} \cdot \frac{1}{R_N} \qquad 2.105$$

where $2\Delta_A$, $2\Delta_B$ are the temperature dependent energy gaps of A and B, and R_N is the barrier resistance in the normal state.

A point of interest in the practical utilisation of the AC Josephson effect is the frequency dependence of i_c. This was initially calculated by Riedel[23] and also by Werthamer[24] for the case of a Josephson junction consisting of two

identical superconductors at zero temperature. They predicted a logarithmic singularity in i_c (f) at a frequency

$$f_J = \frac{4\Delta}{h} \qquad 2.106$$

where 2Δ = energy gap. An appreciable Josephson current was also predicted to exist at frequencies $f \sim 10\Delta/h$, thus lending some hope for the utilisation of Josephson junctions as frequency sensors for energies many times the gap energy. The existence of the Riedel singularity has recently been confirmed by Hamilton and Shapiro[25].

2.2 Josephson Tunneling: Experiments and Applications

A large number of experiments has been performed on various aspects of the Josephson effects and no attempt will be made here to give a comprehensive review. Rather the major features only will be stressed. There are many structures which display the Josephson effects and they are collectively termed weak links. The latter include

(1) Tunnel junctions with oxide barriers[21].

(2) Superconductor - normal metal - superconductor (SNS) sandwiches[26].

(3) Metallic bridge of evaporated films[27,28] or single crystals[9].

(4) Metallic bridges of evaporated film with a normal metal overlayer[29,30].

(5) Point contacts[7,31].

(6) Crossed - wire weak links[31].

(7) Solder blobs (SLUG)[32].

The features of interest studied with these weak links are:

(a) The dependence of the dc critical supercurrent on temperature and magnetic field.

(b) The shape of the dc i vs v curve.

(c) Mixing effects between the AC Josephson current and external radiation.

(d) The emission of Josephson radiation.

(e) The accuracy of the voltage-frequency relation (equation 2.103).

(f) The validity of the current-phase relation (equation 2.102).

(a) Although all weak links (1-7) have a small dc critical supercurrent at zero voltage they do not all display the ideal behaviour. Oxide barrier junctions (1) are rather well understood and their properites are in good agreement with Josephson's theory both for large area junctions[21], and tiny area junctions[33]. On the other hand, weak link types 2, 3, and 5 generally show a small modulation of i with external magnetic field

possibly due to the presence of an appreciable normal current flow.

(b) The dc i vs v curve has been found to be strongly modified near zero voltage by the ac impedance seen by the junction and a complete analysis of this has been given by McCumber[34]. McCumber's theory has been recently verified in some detail by experiments on evaporated film junctions shunted by a low inductance loop of Copper[35]. This behaviour was also predicted by Aslamasov and Larkin[36], Stewart[37] and by Clarke et al[38]. The experiments and analysis by Sullivan and Zimmerman[39] on the mechanical analogue of a Josephson junction also gave a clear demonstration of this effect. This point will be discussed more fully in section 2.3. An additional effect in a metallic bridge has been examined by Zimmerman and Thiene[40] who allow for the formation and annihilation of vortices in the junction region of a metallic bridge.

(c) When an external signal of frequency ω is applied to a current biased Josephson junction, steps appear in the dc i vs v characteristic at the harmonic voltages $n(\hbar\omega/2e)$ corresponding to processes when n photons are absorbed and one condensed pair crosses the weak link[41]. This process has been extensively studied for point contacts[42] principally because these weak links are

readily made, and have the added advantage that their properties can be adjusted while operating at liquid helium temperatures. Details of the mixing process are given in section 2.5.

(d) The mixing process (c) provides indirect evidence for the AC Josephson current. Direct emission of the Josephson radiation has proved to be more difficult to detect[43], primarily because of the low powers available, and also the impedance mismatch between the junction and its environment. By mounting a voltage biased point contact at a low impedance point in a microwave cavity, Zimmerman et al[44] detected $\sim 10^{-11}$ watt for frequencies up to 10GHz.

(e) Considerable interest has revolved around the accuracy of the frequency - voltage relation (equation 2.103) which may be written as

$$f_J = \frac{2e}{h} \cdot V \qquad 2.201$$

where f is the frequency and V the voltage. Theoretically one expects it to be an exact universal relation independent of the experimental conditions. Taylor et al[45], in their re-evaluation of the fundamental constant $\frac{e}{h}$, measured the voltage positions of microwave induced steps in the i - v characteristics of various junctions.

They used oxide barrier and point-contact junctions made of five different superconductors under different experimental conditions. They found the value of $2\frac{e}{h}$ remained constant to within 2ppm. Using SNS sandwiches of lead, tin and indium Clarke[46] has also demonstrated that the relation 2.201 is constant to a precision of 1 in 10^8. The relation has also been shown to be frequency independent over a wide range by Finnegan et al[47].

At this point it is worth mentioning that frequency pulling effects were predicted for Josephson junctions by several authors[48,49], using as an analogy the coupling of an oscillator to a laser cavity. However, McCumber[50] has pointed out that frequency pulling will not affect the relation $hf = \delta\mu$ where $\delta\mu$ is the chemical potential difference. In an experiment where one measures the junction voltage drop V by potentiometric leads, one is in fact measuring $\delta\mu$. Thus equation 2.201 stands as a universal property of superconductors.

(f) On the other hand, a sinusoidal current phase relation (equation 2.102) may not be valid for some weak links since this depends critically on the mechanism of the transfer of condensed pairs across the weak link.

Bloch[51] has suggested that the current phase relation is more general and should be written

$$i = \sum_n i_{cn} \sin(n\theta) \qquad 2.202$$

One of the most direct measurement of the i - θ relation was carried out by Silver and Zimmerman[7] where the flux Φ in a point contact superconducting loop was measured as a function of the applied flux Φ_x. The experiments indicated that a sufficiently weak contact exhibits a single valued, reversible, 2π - periodic, but not necessarily sinusoidal current phase relation. In fact i was essentially linearly related to θ over a considerable range around integral multiples of 2π, although for very low critical currents the form $i = i_c \sin\theta$ was approached as expected by the theory of Aslamasov and Larkin[36].

A second direct determination of the i - θ relation was achieved by Fulton and Dynes[52] using the quantum interference effect between two Anderson - Dayem bridges operated near T_c. For critical currents $\lesssim$ 10μA, i(θ) was approximately sinusoidal but for temperatures a few % lower a distinctly saw-tooth behaviour was observed.

The most complete analysis of the current-phase relation

for weak links of the metallic bridge type has been developed by Baratoff et al[53] where the one-dimensional Ginsburg - Landau equations were applied to a weak link which was visualised as consisting of a small constriction in a region whose mean free path was shorter than the surrounding bulk material. This weak link region had a larger penetration depth, a smaller coherence length, and a smaller critical current density, but otherwise had the same thermodynamic properties. The results of the calculation indicate that the $i - \theta$ relation is 2π - periodic but not necessarily sinusoidal. The deviations from sinusoidal behaviour depend critically on the relative values of the mean free paths and hence coherence distances in the two regions. Distinctly skew forms are expected for some choice of parameters. Thus in general, Bloch's form of the $i - \theta$ relation (equation 2.202) is to be preferred.

The principal applications of weak link devices have been in computer memory elements, the determination of $\frac{e}{h}$, radiation emission and sensing, and flux detection. The switching time from the dc Josephson state to the voltage biased resistive state (for $i \geq i_c$) has been measured to be $\sim 10^{-10}$ sec and thus the junction can function as an exceptionally fast binary computer element. This avenue has been explored by Matisoo[54]. The determination of $\frac{e}{h}$ has been

previously encountered in the discussion of the validity of the frequency voltage relation and a review has been given by Taylor et al[45]. As mentioned earlier, a Josephson junction has the potential as a source of radiation, tunable over a wide range into the far infrared regime $\sim 10^{12}$ Hz. Although the power emission per junction is small ($\sim 10^{-12}$ watt) an array of coupled junctions can emit coherently, and the power output is significantly increased ($\sim 10^{-9}$ watt)[55]. An application to broad band radiation sensing at microwave and far infrared frequencies was provided by the techniques of Grimes et al[56] where a current-biased point contact was used as the detector in a Fourier Transform Spectrometer. An improvement in sensitivity (noise equivalent power $< 10^{-14}$ watt / $\sqrt{\text{Hz}}$) and selectivity was achieved more recently by Richards and Sterling[57] using a point contact junction strongly coupled to a cavity.

The application of major interest in this thesis is the development of flux detectors (M-SQUIDS) and sensitive frequency converters (R-SQUIDS). Since the initial study[7], a large effort has gone into understanding and developing these devices. Point contact versions have been the almost exclusive domain of J.E. Zimmerman and co-workers and the results of this research are contained in a series of Quarterly Technical Reports[58]. Most of the results in these reports are contained in references[8,59,60]. The evaporated thin film equivalent has been developed in parallel

and most information is contained in the articles by Mercereau[61], Nisenoff[30], and Goodkind and Stolfa[62]. In the following section (2.3) phenomenological models are presented to describe the behaviour of the M-SQUID. This analysis is extended to the R-SQUID in section 2.4 where mixing effects in Josephson junctions are also described. The problem of multiple quantum transitions and the generation of harmonics and subharmonics of the Josephson oscillation are analysed in section 2.5 by considering the effects of external reactance on a pure Josephson element.

2.3 Models for the Superconducting Ring (M-SQUID)

The study by Silver and Zimmerman[7] of quantised magnetic transitions in weakly connected superconducting rings combined two of the more fascinating aspects of superconductivity in one experiment - flux quantisation and Josephson tunneling. Two models have been proposed to explain the behaviour of the ring containing a single weak link Fig. 2.2:

(a) Supercurrent breakdown model

(b) Josephson model

The models are thus characterised by the behaviour of the current flowing in the weak link and the authors of reference 7 deduce that both models (a) and (b) give similar behaviour. Recently Simmonds and Parker[63] presented an analogue computer

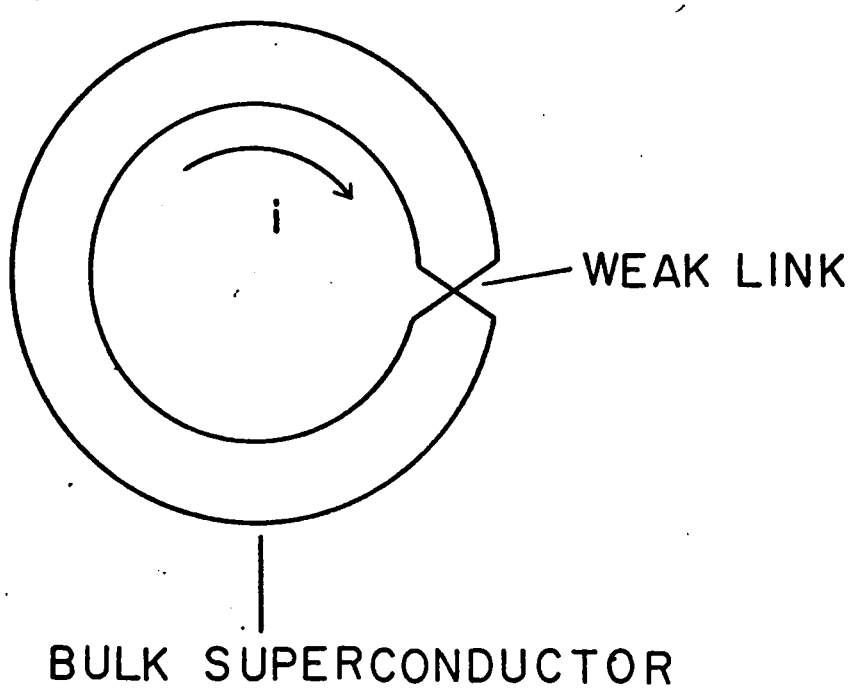

Fig. 2.2 Singly connected Superconducting Ring (M-SQUID).

simulation of the weakly connected ring using both models, which bears out the earlier analysis in remarkable detail. The latter authors favour the Josephson model since Josephson effects have been adequately demonstrated in point contact junctions. In the following the principal features of both models will be presented together with analogue computer simulations for three different values of the weak link critical current.

2.3.1 Supercurrent Breakdown Model

This model is characterised by a critical current i_c and transitions to adjacent magnetic flux states with $\Delta n = \pm 1$ where n is the number of flux quanta in the ring. The theory is based on the quantisation of the phase integral around the complete ring. Thus

$$\oint \vec{p} \cdot d\vec{x} = nh \qquad 2.301$$

where

$$\vec{p} = 2m\vec{v} + 2e\vec{A} \qquad 2.302$$

$\vec{p}$ is the canonical momentum of a condensed pair of electrons, $\vec{A}$ is the vector potential, h is Planck's constant, m and e the mass and charge of the electron, and n is an integer. Replacing the pair velocity $\vec{v}$ by the current density $\vec{j}$

$$\oint \frac{m}{\rho e} \vec{j} \cdot d\vec{x} + \oint 2e\vec{A} \cdot d\vec{x} = nh \qquad 2.303$$

Here ρ is the number of electron pairs per unit volume. Now the complete line integral of $\vec{A}$ round the loop is simply the enclosed flux Φ. Defining the quantity $\Phi_o = h/2e = 2.07 \times 10^{-15}$ weber, one finds

$$\oint \frac{m}{2\rho e^2} \cdot \vec{j} \cdot \vec{dx} + \Phi = n\Phi_o$$

The weak link is assumed to have a thickness small compared with the London penetration depth and thus a part of the line integral $\int \vec{j} \cdot \vec{dx}$ will be non-vanishing in the weak link region. The bulk portion of the ring is taken to be sufficiently thick compared with the penetration depth so that the integral vanishes there. Assuming that $\vec{j}$ is uniform across the weak link then

$$\int \frac{m}{2\rho e^2} \cdot \vec{j} \cdot \vec{dx} = \frac{m}{2\rho e^2} \cdot \frac{t'}{A'L} \cdot Li = \gamma L i \qquad 2.304$$

where t' = weak link thickness

A' = weak link cross-section

L - loop inductance

i = loop current

$\gamma = \frac{mt'}{2\rho e^2 A'L}$ = dimensionless parameter of weak link and ring geometry.

Thus

$$\gamma L i + \Phi = n\Phi_o \qquad 2.305$$

The total ring flux Φ consists of an ambient flux Φ_x and a self-generated flux Li:

$$\Phi = \Phi_x + L i \qquad 2.306$$

From equations 2.305, 2.306 one finds

$$Li = -(\Phi_x - n\Phi_o)(1+\gamma)^{-1} \qquad 2.307$$

$$\Phi = (\gamma\Phi_x + n\Phi_o)(1+\gamma)^{-1} \qquad 2.308$$

As the applied flux Φ_x is increased, the circulating current i decreases until it reaches $-i_c$, the weak link critical current. Then a quantised magnetic transition takes the system to a new magnetic state with $\Delta n = +1$, and the current i increases by $\Phi_o/(1+\gamma)L$. Similarily if the current i reaches $+i_c$, i decreased by $\Phi_o/(1+\gamma)L$. On this model single-valued transitions to adjacent states ($\Delta n = \pm 1$) are expected but experiments indicate that this is true only if $i_c \sim \Phi_o/L$. When $i_c >> \Phi_o/L$, multiple quantum transitions are possible. Also if $i_c < \Phi_o/2L$ the above description of quantised transitions no longer applies. When the weak link is driven normal for $i = i_c$, the quantisation condition (equation 2.301) is inapplicable and i then drops to zero.

2.3.2 The Josephson Model

A second model of the ring behaviour is obtained by using the current-phase relation $i = i_c \sin\theta$ (equation 2.101). If one writes the wave function of a condensed pair in the lowest energy state as

$$\Psi = \sqrt{\rho}\, e^{i\phi} \qquad 2.309$$

where ρ is the charge density and ϕ is the quantum phase, it is straightforward to deduce that the canonical momentum $\vec{p}$ may be written

$$\vec{p} = \hbar \vec{\nabla}\phi \qquad 2.310$$

Thus across the weak link there exists a phase difference

$$\phi_B - \phi_A = \theta = \hbar^{-1}\int_A^B \vec{p}.\vec{dx} \qquad 2.311$$

From equation 2.301

$$\hbar\theta + \int_A^B \vec{p}.\vec{dx} = nh \qquad 2.312$$

By neglecting the contribution to this integral from the vector potential $\vec{A}$ in the weak link region, one finds

$$\theta + 2\pi\frac{\Phi}{\Phi_o} = 2\pi n \qquad 2.313$$

where $\theta = \hbar^{-1} \sin^{-1}\left(\frac{i}{i_c}\right)$. 2.314

From equations 2.306, 2.313, 2.314 one finds

$$i = -i_c \sin \frac{2e}{\hbar}\left[Li + \left(\Phi_x - n\Phi_o\right)\right] \quad 2.315$$

$$\Phi = \Phi_x + Li_c \sin\left[\frac{2e}{\hbar}\left(\Phi - n\Phi_o\right)\right] \quad 2.316$$

In this model Φ and i are continuous functions of Φ_x whereas they were discontinuous in model (b). A further difference is that the states n, n + 1 are always connected at $\Phi = \Phi_x = (n + 1/2)\,\Phi_o$. Thus the ring can pass continuously from one state to the next. A comparison of the two models for three sets of parameters is given in reduced form in Fig. 2.3 by plotting Φ vs Φ_x for three values of $i_c = \Phi_o/2L'$, Φ_o/L', $2\Phi_o/L'$ with $L' = (1 + \gamma)L$. The behaviour of both models is noticeably different for $i_c = \Phi_o/2L'$ but becomes more nearly identical for $i_c > \Phi_o/L'$. The major difference between the two models for intermediate values of i_c is that for the Josephson-type weak link, the nominally trapped flux Φ increases slightly as a function of increasing external flux Φ_x.

Note also that there is a difference in critical currents at which hysteretic behaviour begins. On the Josephson model, this begins at $i_c \gtrsim \Phi_o/2\pi L'$ which is less than the value for

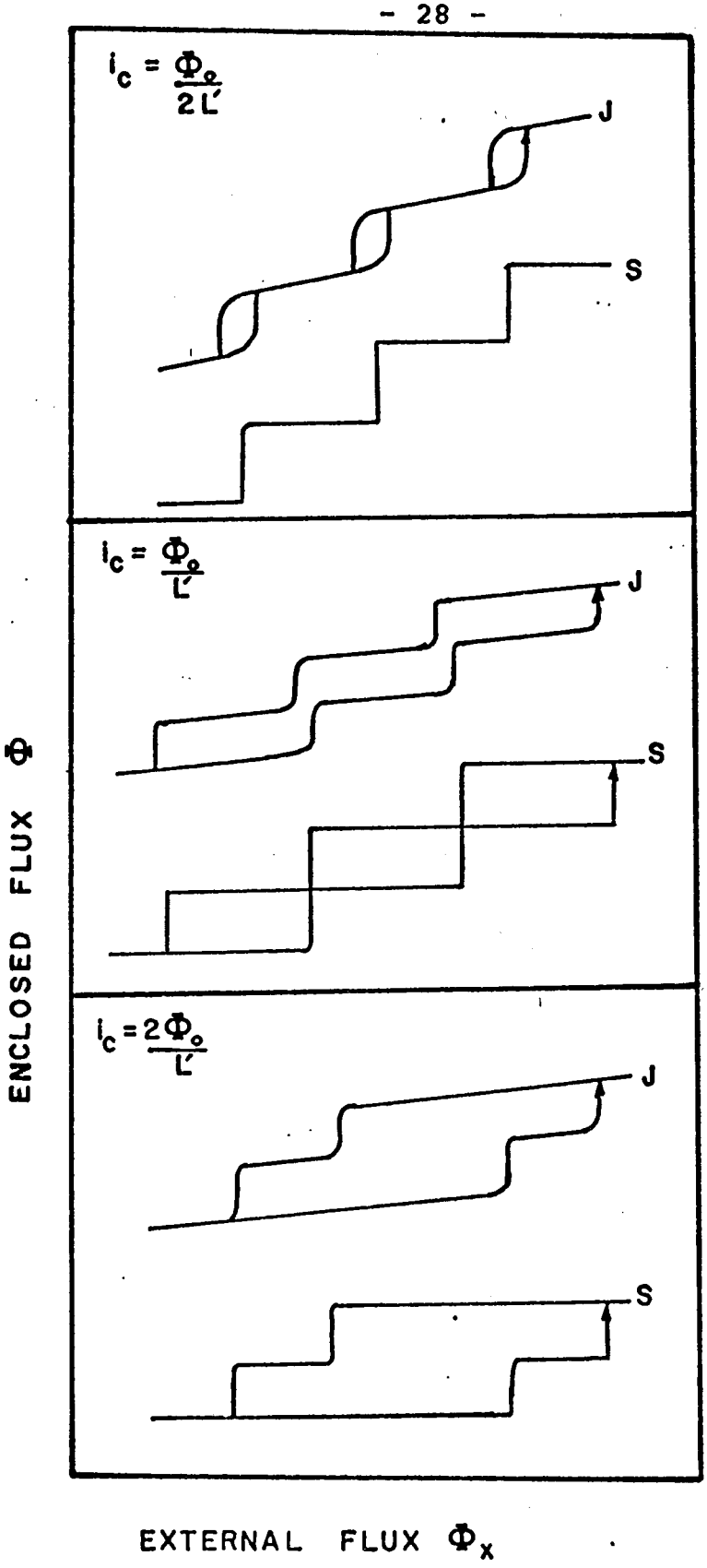

Fig. 2.3 Analogue simulation results for Φ vs Φ_x using different values of i_c (Reference 63). Although γ does not enter equations 2.315, 2.315, the same value of i_c is used for both models. (Note $\gamma << 1$ J = Josephson model, S = Super-current breakdown model.)

the supercurrent breakdown model where $i_c \gtrsim \Phi_o/2L'$.

The interesting feature of the foregoing analysis is that one need not have a weak link displaying Josephson effects in order to construct an M-SQUID. One merely requires a section of superconductor which has an appropriate critical current $i_c \sim \Phi_o/L$. The fact that Josephson effects are observed as in the R-SQUID (Chapter IV) arises because for practical purposes $L \sim 10^{-10}$H and thus $i_c \sim 20\mu A$, a region of weak link critical currents where i is often some 2π periodic function of the phase difference θ.

2.4 Equivalence of the Resistive and Superconducting Rings

The R-SQUID or resistive ring is essentially a variant of the M-SQUID where part of the bulk superconductor is replaced by a section of low resistance, Fig. 2.4. The resistance provides a means of voltage biasing the weak link using an external dc current I which is typically much larger than the weak link critical current. One can deduce the properties of the resistive ring from those of the purely superconducting ring with some important modifications which will be outlined in this section. The device itself has been used to examine the physics of the AC Josephson effect over a wide frequency range - both the mixing properties for external radiation[59] and the emission of radiation at Josephson frequencies controlled by the voltage bias[44,64]. Depending on the nature of the point contact critical current,

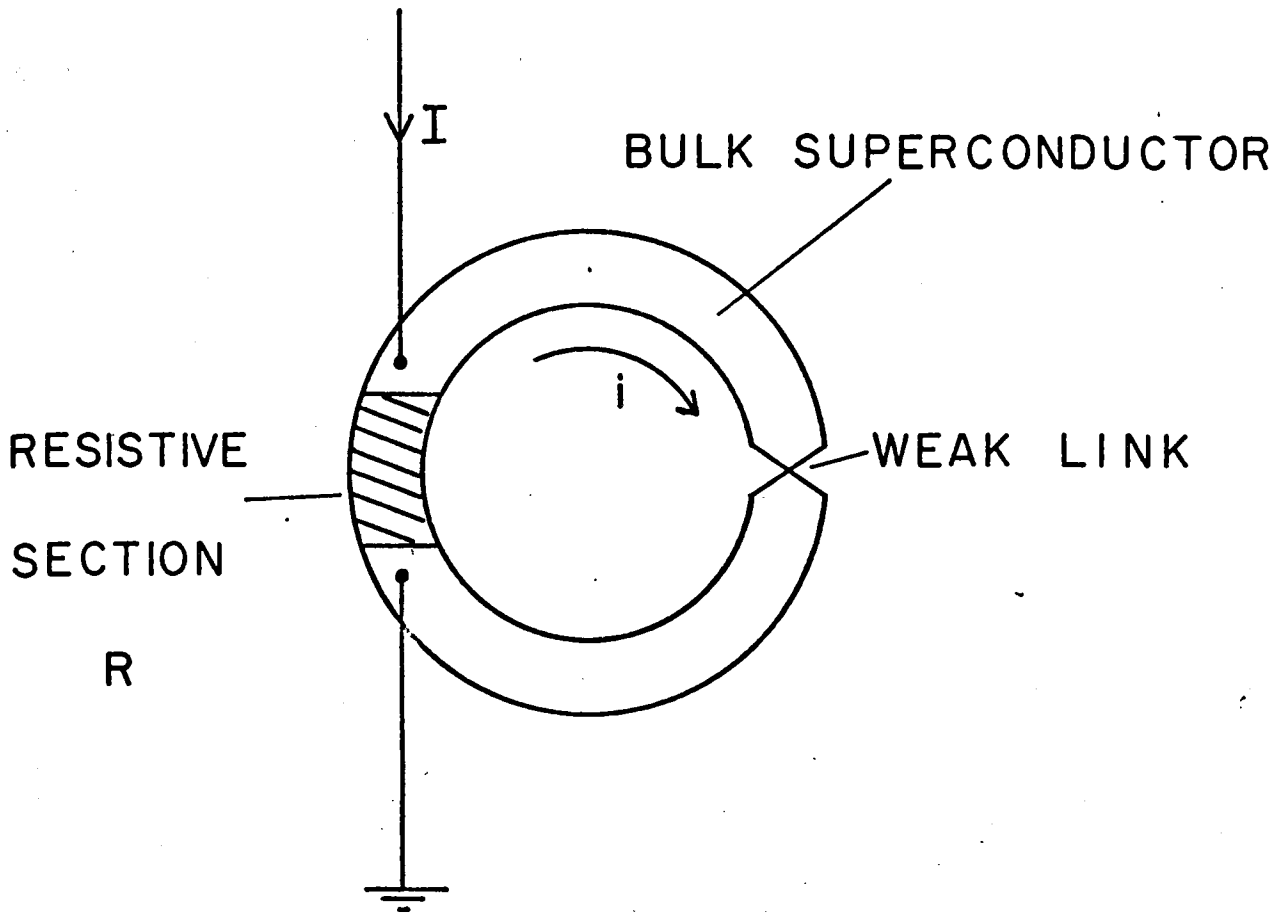

Fig. 2.4 Schematic of the R-SQUID.

single or multiple flux quantum transitions can take place and the R-SQUID geometry allows such effects to be studied.

In the voltage biased mode the R-SQUID can function as the superconducting input for a sensitive superheterodyne detector, the local oscillator and mixer being provided by the weak link. Sensitivities of at least 10^{-12} watt for incident radiation in the frequency range >dc to 10^{11} Hz have been reported[58]. Unlike the M-SQUID the R-SQUID is insensitive to dc or low frequency audio flux. One may also use the device as an NMR spectrometer[66], a voltmeter of ultimate sensitivity 10^{-16}V and as a parametric noise amplifier for low temperature thermometry in the range 0.075°K to 8°K[65,68]. An interesting survey of the latter applications is contained in a report by Kamper et al[69].

The phenomenological description of the R-SQUID has been given by Zimmerman and Silver[67] and the following equations are found to describe the resistive ring:

$$i = \frac{\Phi - \Phi_x}{L} \qquad 2.401$$

$$i(\theta) = -i(-\theta) = i(\theta + 2\pi n); \quad i \leqslant i_c \qquad 2.402$$

$$\theta'(t) + \theta + 2\pi \frac{\Phi}{\Phi_0} = 2\pi n ; \qquad 2.403$$

$$n = 0, \pm 1, \pm 2, \ldots$$

Equation 2.401 is classical and has been given previously (equation 2.306). The second equation is a statement that i is a 2π-periodic function of θ which may be the ideal Josephson case (equation 2.102) or the more general Bloch form (equation 2.202). Equation 2.403 takes account of the fact that the quantisation of the phase integral (equation 2.301) no longer applies since the wavefunction cannot exist in the resistive section. However one still makes use of the phase integral form by adding a (time dependent) phase $\theta'(t)$, for the phase difference across the resistor. There is no unique value for $\theta'(t)$ since it depends on initial conditions; however it changes with time according to the Josephson relation (equation 2.103)

$$\frac{d\theta'(t)}{dt} = \frac{2\pi}{\Phi_o} \cdot V'(t) \qquad 2.404$$

The voltage $V'(<2\Delta$, the energy gap) may have several contributions viz.

$$V' = V_o + V_N(T) + V_T - iR \qquad 2.405$$

$V_o \sim IR$ is the dc bias voltage produced by the applied bias current $I >> i_c$,

$V_N = \sqrt{4k_B TR\Delta f}$ is the Johnson noise voltage in R at temperature T,

V_T = any thermal emf across R.

The four terms in equation 2.505 generally all decrease with R so that for very small R, $|V'|$ is small and hence

$$\delta\theta' = \frac{2\pi}{\Phi_o}\int V' dt$$

will be negligible for some finite time t apart from the integration constant. During this interval the resistive ring will function precisely as the superconducting ring so that the magnetic response to external ac signals is precisely the same. Thus one can construct as in Fig. 2.5 a dynamic response curve which may be smoothly varying with Φ_x ($i_c \sim \Phi_o/L$) or be reversible and hysteretic for $i_c >> \Phi_o/L$.

If the dc bias voltage V_o gives the largest contribution to V' then $\delta\theta'$ will increase linearly with time according to equation 2.103 and thus Φ/Φ_o will decrease linearly with time. The net effect is to cause the magnetisation curve to slide along the diagonal $\Phi=\Phi_x$ at a rate governed by the Josephson frequency:

$$\omega_J = \frac{d\theta}{dt} = \frac{2\pi V_o}{\Phi_o} \qquad 2.406$$

The result of this motion along the line $\Phi=\Phi_x$ is that an external signal at frequency ω_1 is mixed with the frequency ω_J. Grimes and Shapiro[42] have analysed the mixing process in an ideal small-area Josephson junction where $i = i_c \sin\theta$,

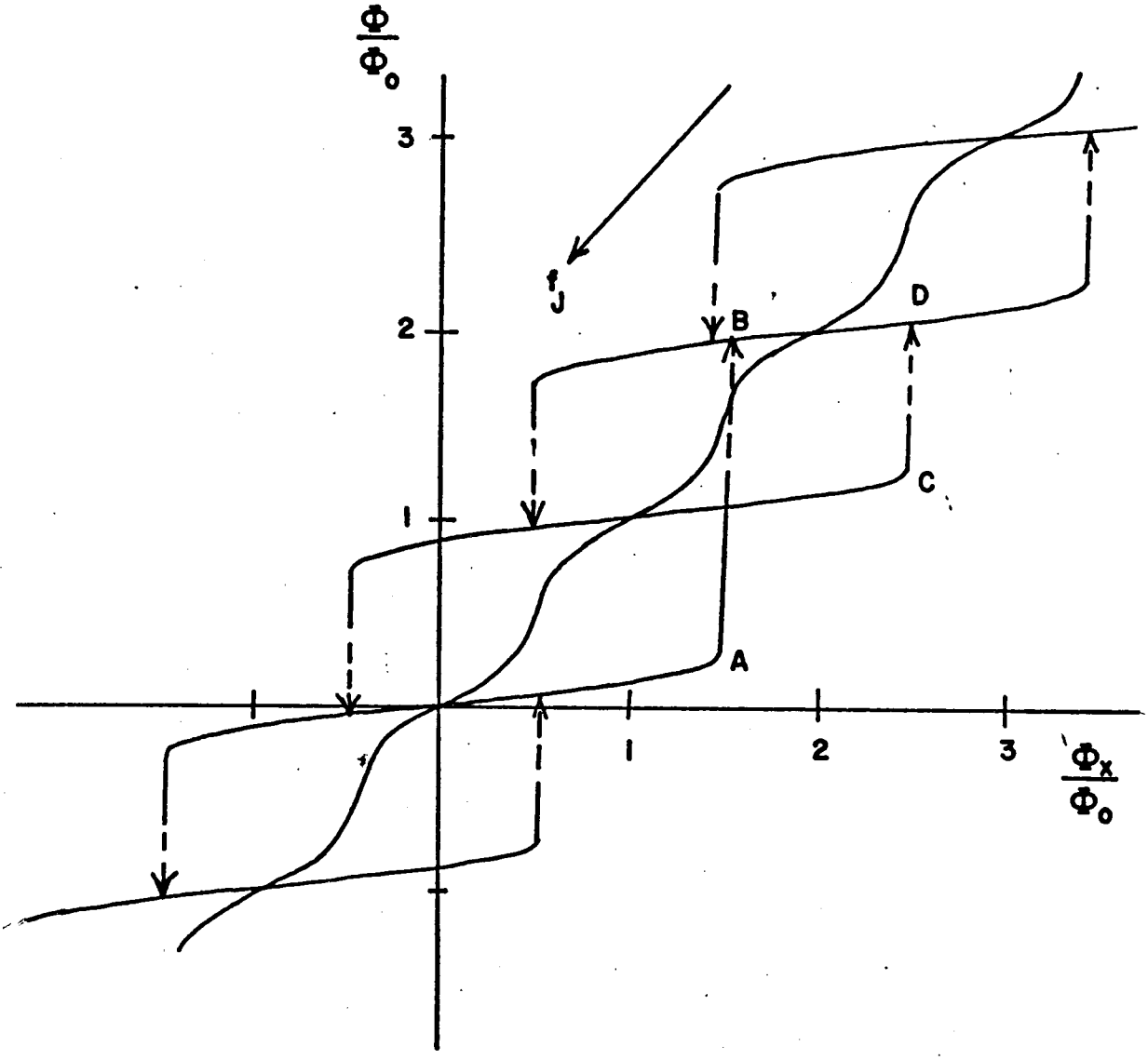

Fig. 2.5 Idealised R-SQUID magnetic response.

yielding the result

$$\frac{i}{i_c} = \sum_m J_m\left(\frac{2\pi v_1}{\Phi_o \omega_1}\right) \sin\left[\omega_J t + \theta_o + m(\omega_1 t + \theta_1)\right] \quad 2.407$$

where v_1 is the amplitude of the applied rf signal at frequency ω_1, θ_o is the initial value of θ, and θ_1 is the phase of the applied rf signal. If one uses the more general form (equation 2.202) the result is

$$i = \sum_{p,q} i_{cp} J_q\left(\frac{2\pi p v_1}{\Phi_o \omega_1}\right) \sin\left[p(\omega_J t + \theta_o) + q(\omega_1 t + \theta_1)\right] \quad 2.408$$

Equation 2.408 predicts the appearance of steps in the dc i vs v characteristic of weak links at voltages $v = \frac{\Phi_o}{2\pi} m\omega_1$ with Bessel function dependence on the amplitudes v_1. These predictions are in substantial agreement with experiments[25,42,75].

The experimental technique involved in using the R-SQUID as a frequency converter is to apply an rf flux $\Phi_1 \sin \omega_1 t$ to the loop thus introducing a voltage $v_1 = \Phi_1 \omega_1$ across the weak link. A suitable dc bias voltage V_o generates a frequency ω_J which mixes with ω_1 (equations 2.407, 2.408). The amplitudes of intermediate frequency Fourier components (say at 30MHz) of the loop magnetisation (-Li) are then measured using a narrow-band low noise rf amplifier inductively coupled to the SQUID via a tank circuit. In general one

expects signals whenever (equation 2.408)

$$p\omega_J + q\omega_1 = 30\,MHz \qquad 2.409$$

If equation 2.408 applies, then the dependence of the Fourier component amplitudes on v_1 will be rather complex since one does not know how the i_{cp} terms vary. If a saw-tooth variation of i with time is expected then the i_{cp} vary as p^{-1} and it should be possible to fit the amplitude dependence given v_1. This point will be discussed in more detail in Chapter IV section 4.5.

The high frequency behaviour of the R-SQUID is expected to be identical to that of the equivalent M-SQUID. Experimentally there is scant information on the behaviour of either SQUID at high frequencies where one expects to observe time constant effects of the SQUID loop. One can define a high frequency cut-off

$$\omega_c' = \frac{R_N}{L} \qquad 2.410$$

where R_N is the normal state resistance of the weak link. For conventional point contact weak links, estimates of R_N lie in the range 10Ω to 100Ω[70] and with a practical loop inductance $L \sim (10^{-9} - 10^{-10})$H, time constant effects should appear for frequencies in the range $10^{10} - 10^{12}$ Hz. Silver

and Zimmerman[7], and Mercereau[61] have shown that for an optimally adjusted ring with $i_c \sim \Phi_o/L$ one expects a time constant $\tau \sim 2 \times 10^{-12}$ sec.

The mixing process in a weak link junction has been shown to extend to at least $\sim 10^{12}$ Hz by McDonald et al[71] and Riedel[23] and Werthamer[24] have shown that the Josephson current can exist for frequencies many times the energy gap frequency. Thus the high frequency limitations for the present device appear to depend on the lumped circuit inductance L. At first sight a possible means of extending the frequency range would be to reduce L possibly along the lines suggested recently by Zimmerman[72]. This however is impossible since for an optimally adjusted SQUID ($i_c \sim \Phi_o/L$) an alternate form for ω_c' is[7] $\omega_c' \sim 2\Delta/\Phi_o$ where 2Δ is the energy gap and Φ_o the flux quantum.

The experimental low frequency behaviour of the R-SQUID has presented some surprises. On the basis of the foregoing model which was developed by Zimmerman and Silver[73] one expects a low frequency cut-off

$$\omega_L = \frac{R}{L} \qquad 2.411$$

where R is the bias resistance. A careful study of the ring behaviour as a function of external flux sweep frequency[60] has indicated that quantum transitions were observable in

such rings at frequencies much below ω_L and were ultimately limited by Johnson noise fluctuations in R. A low frequency cut-off ω_c may be defined in terms of the time taken for the quantum phase across R to execute an rms fluctuation of one radian. This occurs in a time

$$\tau_c = \frac{2\pi}{\omega_c} = \frac{\Phi_o^2}{8\pi^2 k_B T R} \qquad 2.412$$

where $k_B T$ is the Boltzmann factor at temperature T. For example, for R = 40μΩ and T = 4.2°k one obtains a cut-off limit of 7.3 KHz. This behaviour has been adequately substantiated in the resistance range $10^{-10}\Omega$ to 30μΩ. At this point it is worth noting that the fluctuations in phase due to noise voltage in R produce a line broadening of the Josephson oscillation which has had useful application as an absolute low temperature thermometer[68]. The subject of frequency modulation of the Josephson oscillation by random noise is complex, but using an expression for the power spectrum of a single frequency modulated by white noise, Zimmerman and Harding[60] calculated an effective linewidth

$$\delta\omega = \frac{8\pi^2 k_B T R}{\Phi_o^2} = 4.05 \times 10^7 RT(MKS) \qquad 2.413$$

The relation between 2.412, and 2.413 is evident since the correlation time τ_c for a mean square phase fluctuation

of one radian is simply the reciprocal of the linewidth i.e. $\delta\omega\tau_c = 1$.

The fact that low frequency time constant effects were never observed, has led the authors of reference 60 to conclude that the quantum interference effects which are observed with superconducting loops are a consequence of the weak link properties and do not necessarily depend on the spatial coherence of the superconducting wavefunction. There the matter rests for the present with some authors preferring to use the quantisation of the phase integral to describe single and double junction ring behaviour. It is difficult to see how the phase integral description is to be avoided in the case of the double junction ring where one observes quantum interference between dc currents as a function of a dc external flux. (For example see reference 74.) Zimmerman and Harding[60] have managed to show that quantisation of the phase integral may be unnecessary only in the case of ac signals, by utilising the Josephson relation, (2.103) and the classical law $V = \frac{d\Phi}{dt}$ where the time dependence of the flux Φ is implicit.

The foregoing analysis (sections 2.3, 2.4) does not give a complete description of the behaviour of the devices especially when multiple quantum transitions are present. In the following section (2.5), the effects of external reactance are explicitly taken into account. Solutions for

the loop currents in the M- and R-SQUIDS are given where possible, indicating in the case of the R-SQUID that the Josephson oscillation is strongly distorted for relatively tiny resistances and inductances.

2.5 Interaction of Josephson Current with External Reactance

In 1963, Anderson[5] pointed out the analogy between the Josephson coupling energy (equation 2.101) and the energy of a rigid pendulum in a gravitational field. Since then, several authors[51,76,77] have shown that the interaction of the Josephson oscillation with external circuit elements (reactances, distributed or otherwise) leads to equations which are idential with those of a damped driven pendulum. (In any practical study of the Josephson effects, reactances will always be present.) Perhaps the most fascinating study has been the recent development of mechanical analogues of time dependent Josephson phenomena by Sullivan and Zimmerman[39]. Using a Lagrangian formalism, these authors developed one-to-one correspondences between various mechanical elements of a damped driven pendulum (moment of inertia, torsional drive, viscous drag etc) and the corresponding electrical elements (capacitance inductance and resistance etc). The value of this approach lies in the fact that the Josephson oscillation can be strongly distorted from a purely sinusoidal form, merely by the influence of external reactances, and the experimental

mechanical analogue allows a systematic study of such effects.

The equivalent circuits for the M-SQUID, and R-SQUID are given in Fig. 2.6. The Josephson junction is represented by the three circuit elements shown: an element which has pure Josephson behaviour with $i = i_c \sin\theta$, a conductance G to account for quasiparticle flow in the non-ideal cases, and a capacitance C which is a combination of both the junction capacitance and the lumped capacitance of the circuit elements. The Hamiltonian for the junction in a loop of inductance L is

$$H_1 = \frac{-\Phi_o i_c}{2\pi} \cos\theta + \frac{1}{2} L i^2 + \frac{1}{2} C V^2 \qquad 2.501$$

where the first term is the junction coupling energy (equation 2.101). If the loop contains flux Φ with a voltage V across the inductance L then $\Phi = -\int V dt$.

Hence using equation 2.103

$$\frac{\Phi}{\Phi_o} = -\left(\frac{\theta + \theta_o}{2\pi}\right) \qquad 2.502$$

where θ_o is an initial arbitrary phase difference. For an external flux θ_x one has the purely classical relation $i = L^{-1} (\Phi - \Phi_x)$ therefore

$$i = -\left(\frac{\theta - \theta_x}{2\pi L}\right) \qquad 2.503$$

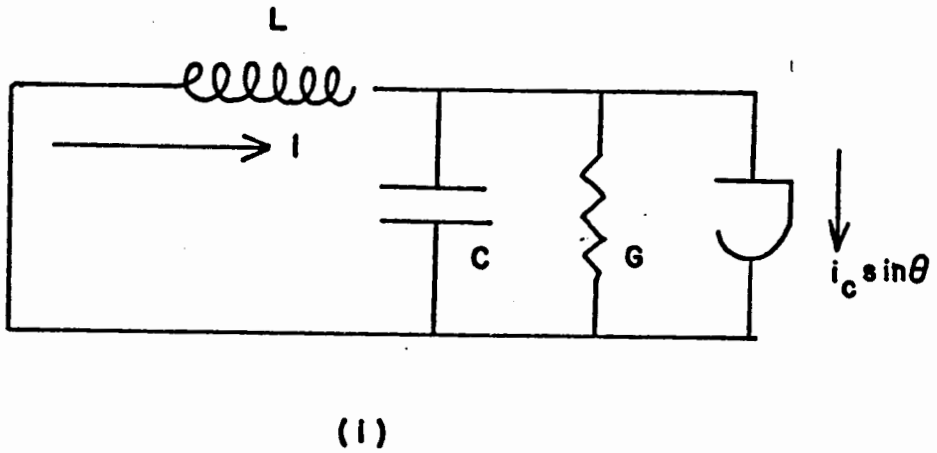

(I)

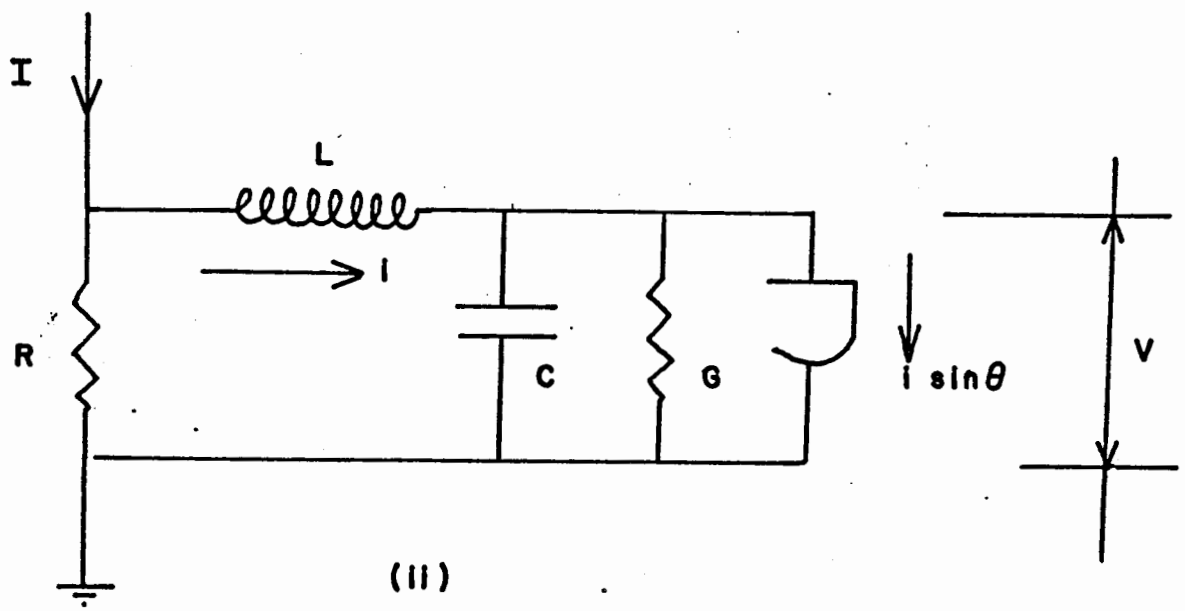

(II)

Fig. 2.6 Equivalent circuits for
(i) M-SQUID Fig. 2.2.
(ii) R-SQUID Fig. 2.4.

where θ_x is the phase difference appropriate to an applied external flux Φ_x. Inserting 2.503 in 2.501,

$$H_1 = -\frac{\Phi_o i_c}{2\pi}\cos\theta + \frac{\Phi_o^2}{8\pi^2 L}(\theta-\theta_x)^2 + \frac{\Phi_o^2 C}{8\pi^2}\dot{\theta}^2 \qquad 2.504$$

with loop current

$$i = i_c \sin\theta + \frac{G\Phi_o}{2\pi}\dot{\theta} + \frac{C\Phi_o}{2\pi}\ddot{\theta} \qquad 2.505$$

An identical equation can be derived for a rigid pendulum mass m, length l, attached at right angles to a torsion bar of force constant K whose angular displacement θ_x can be varied. For this sytem the Hamiltonian is

$$H_2 = -mgl\cos\theta + \frac{1}{2}K(\theta-\theta_x)^2 + \frac{1}{2}I'\dot{\theta}^2 \qquad 2.506$$

with torque

$$\Gamma = K(\theta-\theta_x) = mgl\sin\theta + f'\dot{\theta} + I'\ddot{\theta} \qquad 2.507$$

where f' is the damping constant and $I' = ml^2$ the moment of inertia. The following analogies can be strictly made between the mechanical and electrical systems:

Torque	Γ	$\leftrightarrow$	Loop current	i
Angular Velocity	$\dot{\theta}$	$\leftrightarrow$	Voltage	v
Angular Displacement	θ	$\leftrightarrow$	Flux (quantum phase)	Φ (θ)
Torsion Bar	K	$\leftrightarrow$	Inductance	L
Flywheel	I'	$\leftrightarrow$	Capacitance	C
Viscous Drag	f'	$\leftrightarrow$	Resistance	R

The technique of Zimmerman and Sullivan[39] was to build a damped rigid pendulum with a torsion bar driven by a suitable motor, and then measure on this mechanical model various quantities such as Γ, $\dot{\theta}$, θ, as a function of various values of K, I', f'. For example, a measurement of $\bar{\Gamma}$ vs $\bar{\dot{\theta}}$ (where the bar denotes average value) should give the analogue dc i vs v curve for the junction. The effects of L, C, R on the i vs v curve can be readily demonstrated merely by changing the values of K, I', or f'.

Using the mechanical analogue, it is possible to examine the SQUID behaviour, both the quantised flux states and the transitions between them. Insight into the conditions under which multiple quantum transitions appear can be obtained from this model. The angle θ_x is the mechanical analogue of the applied flux and θ is related to the ring flux. Thus from equation 2.502 a change in θ of 2π corresponds to a change of flux inside the ring of one flux quantum. This change in θ is accompanied by a change in torque (loop current) since from equation 2.507, $(\theta-\theta_x)$ is proportional to the torque.

The system potential energy may be written (2.504, 2.506)

$$P.E. = -\beta\left[\cos\theta - \frac{1}{2\beta}(\theta-\theta_x)^2\right] \qquad 2.508$$

where

$$\beta = \frac{2\pi L i_c}{\Phi_o} = \frac{mgl}{K} \qquad 2.509$$

For fixed θ_x which gives $\theta<\pi/2$, $\dot{\theta} = \dddot{\theta} = 0$, and

$$\beta = \frac{(\theta_x-\theta)}{\sin\theta} \qquad 2.510$$

Hence $\beta = 1$ when θ_x, the applied angle leads θ by one radian at $\theta = \pi/2$. For $\theta > \pi/2$ sufficient torque has been applied to bring the pendulum over the top and thus a transition will take place. A single transition only occurs since insufficient torque has been applied to bring the pendulum over the top more than once.

The case for $\beta >> 1$ is completely different, since many twists have to be put into the torsion rod (i.e. $\theta_x >> 2\pi$) before $\theta > \pi/2$. In Fig. 2.7 the potential energy (2.508) is given for $i_c = 10^{-3}$A, $L = 10^{-10}$H: thus $\beta = 10\pi$. Two values of θ_x have been chosen: $\theta_x = 0$, and $\theta_x = 10\pi$. According to equation 2.508, which applies to the case of winding up the pendulum, a transition will commence when $\theta > \pi/2$ and

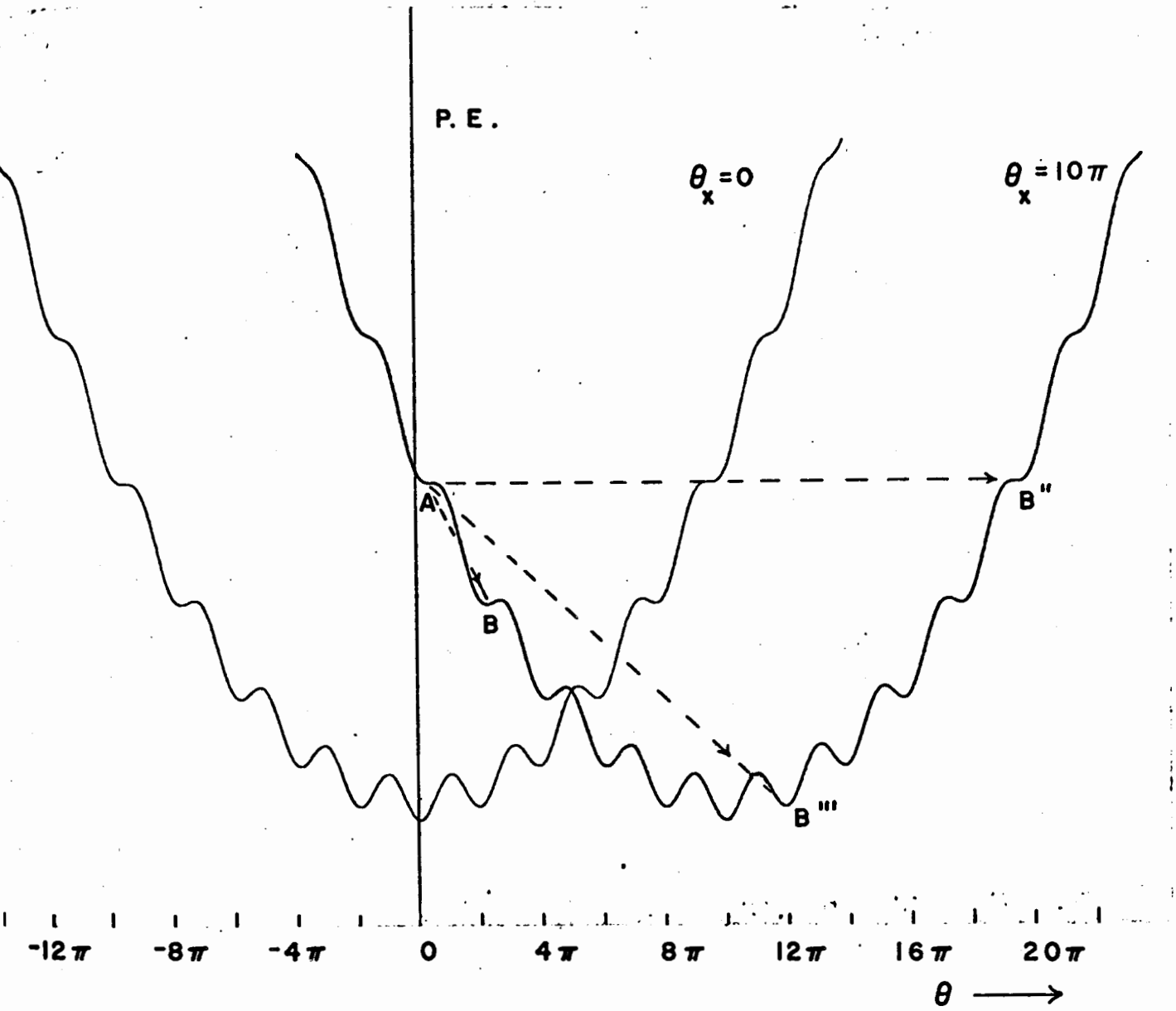

Fig. 2.7 Potential Energy Function (Equation 2.508) for i_c = 1mA, L = 10^{-11} H, using two different values of θ_x.

$\theta_x > 10\pi$. Figure 2.7 is useful in that it allows one to obtain some idea of the subsequent motion of the system. Once the pendulum flops over the top, the motion is governed by the inertia term (capacitance) and the damping (junction conductance) and these terms determine the final state. If there is no inertia (capacitance) the system moves to the adjacent minimum A → B. This is also true with large damping even in the case of non-zero inertia. On the other hand low damping allows several minima to be traversed before the system comes to rest[39] eg A → B'''. Thus multiple pendulum revolutions correspond to the multiple quantum transitions in the SQUID and it is clear from the above considerations that for a single flux quantum device one must utilise a weak link with low values of G and C if for practical reasons a large value of β is employed. This point will be reconsidered in the discussion of the $NbSe_2$ SQUIDS (section 3.5). Note also that since the R-SQUID (Fig. 2.6(ii)) has been shown to have identical behaviour to the M-SQUID (section 2.4) at least for frequencies above the Johnson noise limit (equation 2.408), the above arguments also apply.

In the above discussion only a qualitative idea of the factors governing the order of the quantum transition has been given. The complete solution can be obtained by solving the following equation for θ:

$$\frac{1}{\alpha}\frac{d^2\theta}{d\xi^2} + \frac{1}{\alpha}\frac{d\theta}{d\xi} + \sin\theta + \frac{1}{\beta}(\theta-\theta_x) = 0 \qquad 2.511$$

This is obtained by substitution of 2.503 in 2.505 where

$$\xi' = \omega_o t$$
$$\omega_o = GC^{-1}$$
$$\alpha = 2\pi i_c (G\omega_o \Phi_o)^{-1} \qquad 2.512$$

In the case of the M-SQUID θ_x is related to the external flux (equation 2.502). In the case of the R-SQUID one takes θ_x to include the external flux and also the effect of the dc bias voltage $V_o \sim I_{DC} R$. Thus $\theta_x = \frac{\omega_J}{\omega_o} \xi' + \theta_x'$ where ω_J is the Josephson frequency appropriate to V and θ_x' is produced by external flux. (In section 2.4 it was shown that the voltage bias was equivalent to an external flux linearly changing with time. By equation 2.502 this is equivalent to an advancing phase θ_x.)

Equation 2.511 has no analytic solution due to the sine term,but is conveniently solved on the mechanical analogue[39]. Of interest is the variation of the loop current i with time and analytic solutions to 2.511 can be obtained provided one ignores the effects of junction capacitance and loss. In this limit the solution is[44,64]

$$\frac{i-\alpha' i_c}{|i_c-\alpha' i|} = \sin\left[\omega_J \sqrt{1-\alpha'^2}\left(t+\frac{L}{R}\ln\left(1-\frac{\alpha' i}{i_c}\right)\right)\right] \qquad 2.513$$

where

$$\alpha' = \left(1+(V_o/i_c R)^2\right)^{-1/2}$$

Sullivan et al[77] studied this equation in detail and generated a series of solutions for various values of α', ω_J, L, R, which clearly demonstrated the strong influence of external circuit parameters on the Josephson oscillation.

2.5.1 Harmonic Generation by Resistive Feedback

This distortion can be determined by setting L = 0 in equation 2.513 and generally manifests itself as a change from the ideal in the dc i vs v characteristic of weak links. This distortion is strongest near zero bias and tends to zero for large bias (small α'). It has already been discussed in the review of the Josephson effects (section 2.2)[34-38,78].

2.5.2 Harmonic and Subharmonic Generation by Inductive Feedback

For very small inductance L, such that $i_c L << \Phi_o/2\pi$ one obtains a well-behaved sinusoidal solution; however as L is increased keeping all other parameters fixed, the current i(t) becomes multivalued in time for $i_c L > \Phi_o/2\pi$ where the oscillation is irreversible and develops a sawtooth behaviour whose frequency can be at submultiples of the fundamental frequency ω_J. To adequately describe this irreversible behaviour one must of course include the junction capacitance C and the losses G in the method previously described using the mechanical analogue.

In Fig. 2.8, there is generated a solution to equation 2.513 using the following parameters $i_c = 10^{-5}$A, $R = 40\mu\Omega$, $L = 10^{-11}$H, $\omega_J/2\pi = 70$GHz, $V_o = 145\mu$V. Thus $\alpha' = 2.8 \times 10^{-4}$. This low value of α' indicates that there will be very little resistive distortion, but it is evident from Fig. 2.8 that even a tiny inductance ($\sim 10^{-11}$H) has a drastic effect on the oscillation. (For L = 0, and all other parameters as above, one obtains an almost pure sinusoid.) The dashed transition A → B′ corresponds to three flux quanta crossing the weak link and if continued in time as in C → D, this transition corresponds to a sawtooth oscillation of frequency one third that of the fundamental ω_J. By extending the order of the transition, lower frequency subharmonics can be produced. The minimum oscillation frequency in Fig. 2.8 corresponding to the transition A → B'' is $\omega_J/10$. (Note that one obtains a single quantum transition for $i_c = \Phi_o/2\pi L$)

The above arguments of course give no indication of the conditions governing the order of the transition. Again one has to consider the solution to the full pendulum equation where capacitance and loss are included (equation 2.511). For example, if one considers Fig. 2.7, the transition A → B'' is highly unlikely since it corresponds to zero damping. The system is much more likely to stop at one of the intermediate minima.

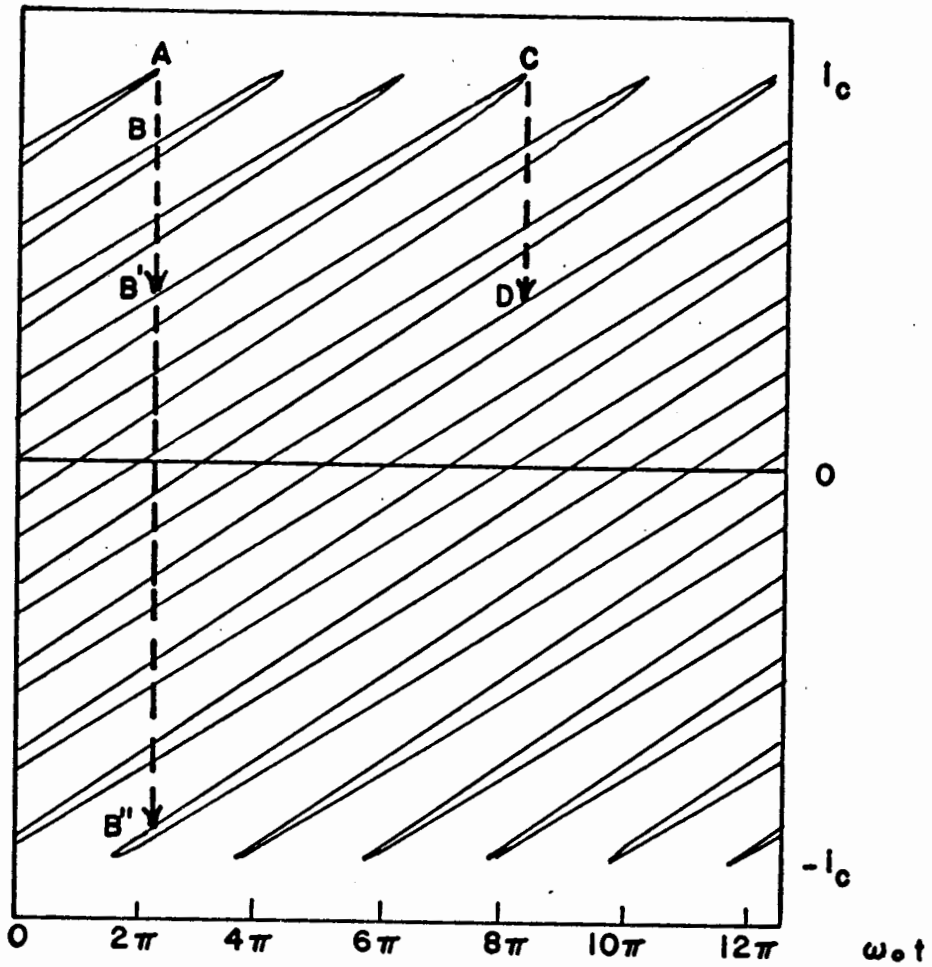

Fig. 2.8 Solution to equation 2.5 13 for i_c = 1mA, L = 10^{-11}H, V_o = 145 μv, $\omega_o/2\pi$ = 70GHz, R = 40μΩ. For those parameters, equation 2.513 reduces to i ~ Sin ($\omega_o t$ - 30.8i) mA.

The mechanical analogue also allows a qualitative description of the effects of fluctuations. As already mentioned, internal or external noise frequency modulates the fundamental oscillation ω_J (equation 2.409). Besides this frequency modulation, the noise produces uncertainty in the order of the transition and also uncertainty in the time at which the transition occurs. Noise in the system corresponds to a random motion in one of the potential minima, which causes a transition to occur at an indeterminate time. Thus the starting potential energy and momentum have indeterminate values which result in an indeterminate final potential energy. Both of these factors will tend to frequency broaden the subharmonic oscillation (Fig. 2.8) which, because of its sawtooth nature, will contribute to the width of the fundamental oscillation at ω_J.

Thus to summarise this section one cay say that reasonable behaviour can be expected from the R-SQUID provided one has a weak link with reasonable properties i.e. high resistance (G^{-1}) low capacitance (C), and a critical current $i_c \sim \Phi_o/L$. Straying outside these bounds result in complex behaviour which manifests itself in high order quantum transitions and hence a Josephson current containing harmonics and subharmonics of the fundamental oscillation. The R-SQUID should function well in a shielded environment at low frequencies where a low value of the bias resistance may be employed (i.e. low noise). At higher frequencies of operation

where for practical reasons the bias currents are limited to a few amperes, one expects noise to broaden the oscillation both for the ideal current $i_c \sim \Phi_o/L$ and additionally for the case $i_c >> \Phi_o/L$.

The generation of harmonics of the fundamental Josephson frequency (equation 2.201) is expected to be extremely complicated in any real experimental situation where one finds departures from the ideal Josephson relation $i = i_c \sin \theta$. A non-sinusoidal behaviour leads to harmonic terms for the phase (equation 2.202). In the presence of an external flux of frequency ω one obtains the complex current phase relation (equation 2.408). This solution will be further complicated in the experimental situations where one has to consider the effects of external reactance on the Josephson oscillation as in the R-SQUID. For this case, the solution to the differential equation for θ vs t (equation 2.511) is inserted into equation 2.408 yielding a sequence of harmonics whose amplitudes may vary in a very irregular way depending on the precise nature of the current phase relation (equation 2.202).

CHAPTER III

WEAK LINK DETECTORS: THE M-SQUID

In this chapter experimental details are given of the design and study of M-SQUIDS - both a point contact version using niobium screws, and a similar structure where the point-contact was replaced by a metallic bridge of $NbSe_2$, a superconducting layer structure. The bulk of the discussion in this chapter is concerned with the M-SQUIDS of $NbSe_2$ since they represent a new development in the technique of making such devices (section 3.2). The point contact versions, two of which were built and tested, were identical in design to the symmetric hole structures recently described by Zimmerman et al[8] and only a brief description of the design is given (section 3.1).

In section 3.3 details are given of the SQUID detection electronics which together with the devices of sections 3.1, and 3.2 form the basis of a magnetometer system of ultimate sensitivity $\sim (10^{-9} - 10^{-10})$ gauss.

A number of tests and measurements on the $NbSe_2$ devices were carried out and these are presented in section 3.5 together with suggestions for further experiments and improvements on the existing devices.

3.1 Point Contact M-SQUID

The design for a symmetric hole structure with point contact screws is given in Fig. 3.1. A double hole structure is more useful for measurements than the previously described single loop (section 2.3) since the device is insensitive to magnetic flux uniform over both holes but will respond to flux difference between the holes. The bulk metal was Niobium supplied by Fansteel(*) and the screws were 080 or 000-120 of Niobium. Two 2mm diameter holes were first drilled symmetrically off-axis along a 1cm diameter Niobium rod. A countersunk hole was drilled and threaded perpendicular to the rod axis for the point contact screws. The paraxial holes were then connected by an 0.005" wide spark-cut slit. The point contact consisted of one microscopically sharp screw (tip radius < 1μm) and a screw with a flat mechanically polished end. Screws of gauge 080 were preferred since they were less likely to shear off during adjustment of the contact. The contact was positioned at the centre of the spark-cut slit and could be locked in place at room temperature or in liquid He^4 using a dip stick with a screwdriver and wrench. Locknuts were essential for some measure of stability, but care had to be exercised during the adjustment, since

---

*Fansteel Metallurgical Corporation, Michigan, U. S. A.

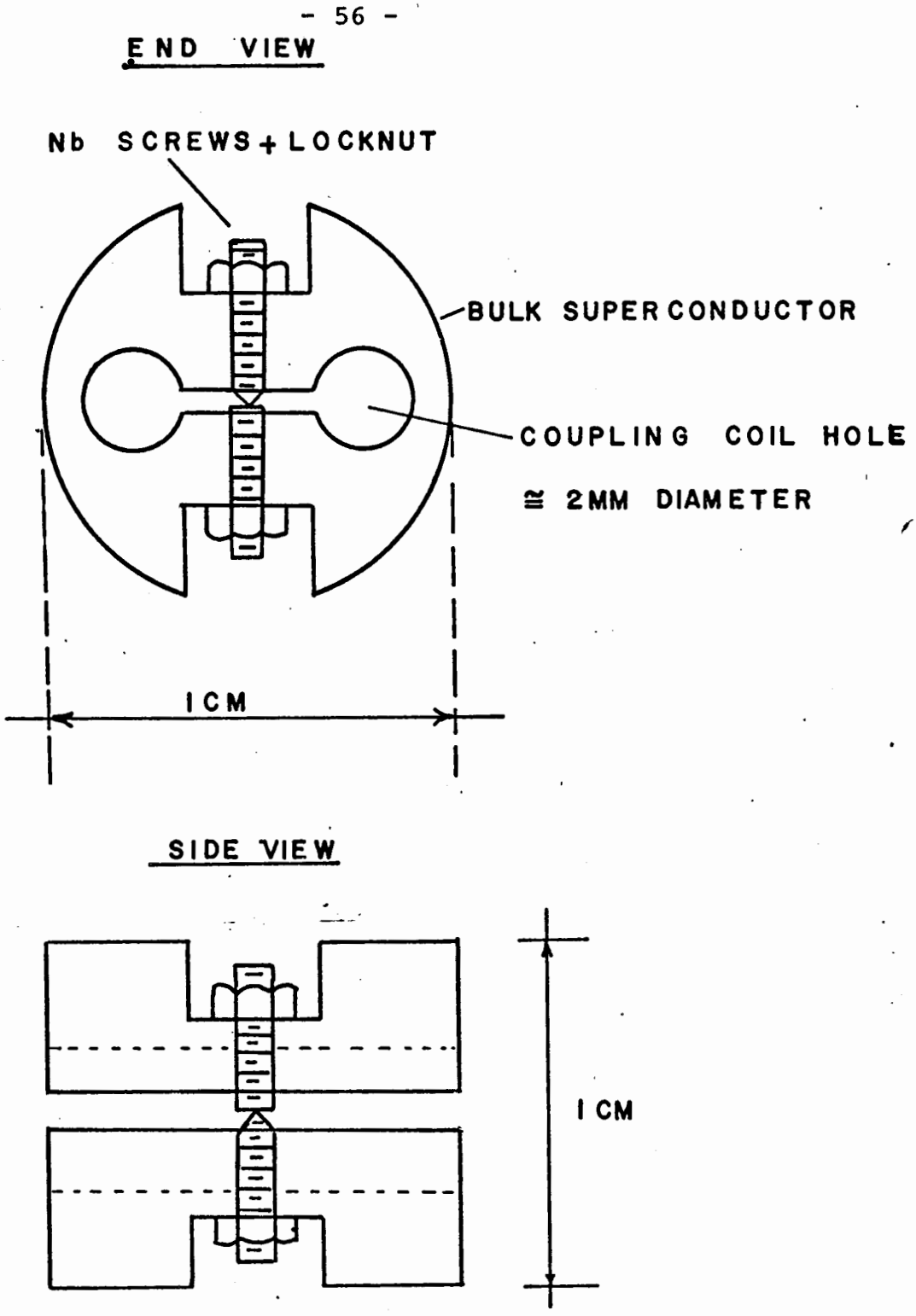

Fig. 3.1 Point contact M-SQUID (i) End view
(ii) Side view.

tightening the locknut often eased the contact apart. The precise technique for testing with the detection electronics will be considered later (section 3.3).

3.2 $NbSe_2$ M-SQUID

The point contact M-SQUID (section 3.1) is a relatively simple structure and is suitable for many laboratory purposes. The only disadvantage is that the point contact tends to be rather delicate and has to be protected from excessive vibrations and atmospheric corrosion. The research effort of Zimmerman et al[8] culminated in devices of relatively long life (> 1 year), rugged enough to be taken out into the field.

There has also been some recent success with thin-film devices[30,61,62] formed by evaporating a superconductor on a rotating quartz or sapphire rod. A neck approximately 1μm wide is produced by cutting the cylinder along one side with a sharp point. Such structures are expected to be more mechanically stable than the point contact system and Mercereau[61] has stated that such devices have successfully survived hundreds of cycles to helium temperatures over a three year period.

More recently Consadori et al[9] have had some success in making M-SQUIDS where the weak link has been of $NbSe_2$, a superconducting layer structure. These devices and their properties will now be described in some detail.

$NbSe_2$ is one of the transition metal dichalcogenides which crystallises in a hexagonal layer structure[79], and has a pronounced cleavage plane perpendicular to the c-axis. The crystals used were the two layer modification of $NbSe_2$ with a transition temperature of $7.0\,^{\circ}K$[79]. The crystals were grown by R.F. Frindt and F. Consadori of this laboratory using the techniques of chemical vapour transport by iodine, generally following the procedure of Kershaw et al[80]. The method yielded platelets typically 0.01 - 0.1 mm thick and $\sim 2\ cm^2$ in area. The purity of the elements used was 99.93% for the Niobium and 99.999% for the Selenium.

In making a weak link, a single crystal platelet of $NbSe_2$ was fixed to a suitable substrate such as quartz, epoxy or mica (Fig. 3.2). (Provided the $NbSe_2$ layer is sufficiently thin, it will strongly adhere to a smooth surface by means of surface forces alone.) Since there was great interest in developing a stable reliable device, many substrates were tested. The two most reliable systems were found to be

(a) A thin platelet of $NbSe_2$ adhering to a clean mica sheet by surface forces alone.

(b) A thin platelet of $NbSe_2$ fixed to a quartz substrate by means of a clear epoxy - Stycast 1269A(*)

---

*Available from Emerson and Cumming, Canton, Massachussetts.

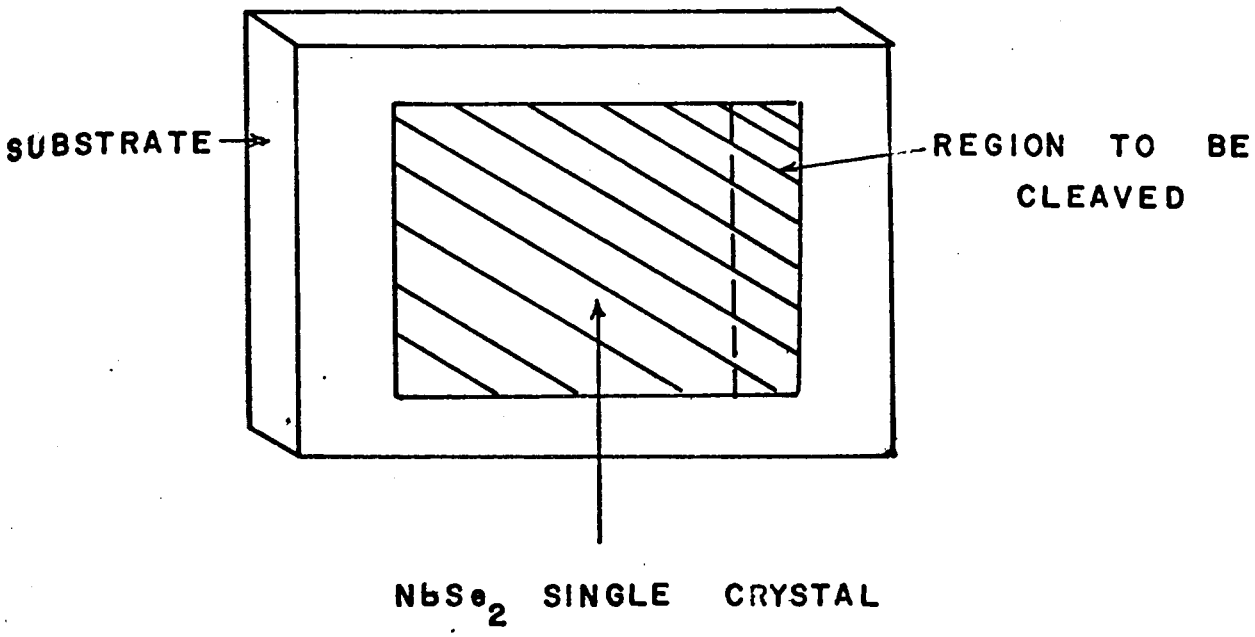

Fig. 3.2 $NbSe_2$ Single crystal fixed to insulating substrate. Crystal platelet dimensions typically 5mm x 5mm, thickness 0.1mm.

About ten other glues or epoxies were tried with little or no success. What is required is a substrate whose thermal expansion matches that of the metal $NbSe_2$. Quartz-filled epoxies such as Stycast 2850GT which has a bulk expansion similar to Copper, were found to be unsuitable since the quartz filling particles were often larger than the weak link dimensions and thus locally the epoxy expansion coefficient was similar to the unfilled medium.

The steps in constructing a weak link are shown in Figs. 3.2 - 3.4. A small region of the $NbSe_2$ platelet on its substrate was repeatedly cleaved or stripped down to a few unit cell layers ($\sim 10^{-6}$ Å thickness)[81]. A simple method for doing this is to use adhesive tape which is laid over a small fraction of the platelet area and the tape then removed. Due to the weak forces holding the layers together, the tape strips off some of the crystal. (Mica sheets exhibit similar behaviour.) This process is repeated until a sufficiently thin region is obtained. (Note: this thin region need not be at the platelet edge.)

A slightly different technique had to be employed with a mica substrate where surface forces alone were used[82]. With a pair of fine tweezers it was possible to strip off very thin layers of $NbSe_2$ from a platelet. As these strips were carefully removed they gradually became thinner until at the final contact, regions of $\sim$ 100Å - 200Å thickness remained.

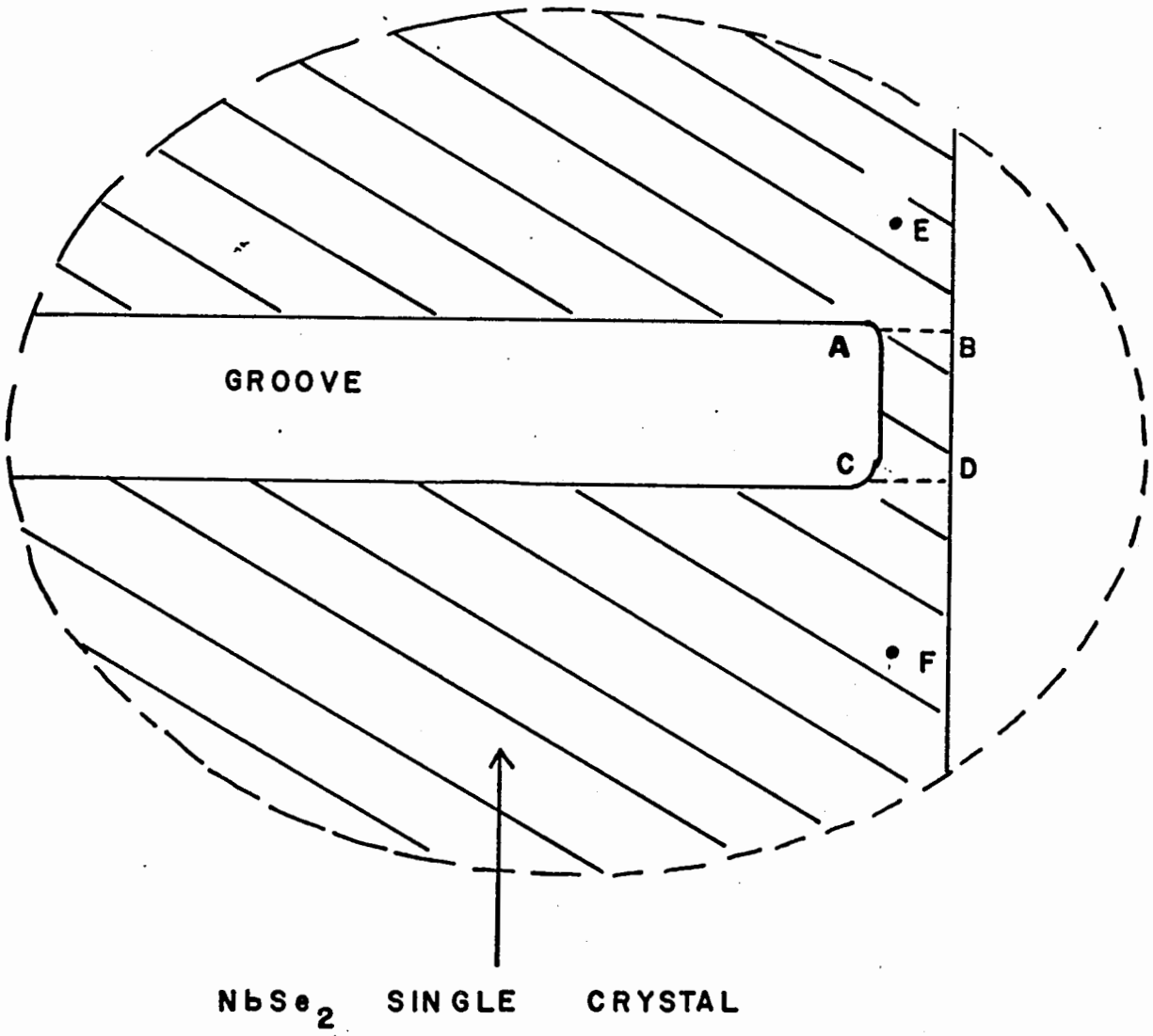

Fig. 3.3 Weak Link Region. AB ~ 5 μm, AC ~ 5μm. Crystal thickness at weak link region ~ 200 Å.

This approximately wedge shaped strip was then carefully placed on a freshly cleaved piece of mica sheet to which it adhered strongly.

The weak link region was then formed by cutting away sections of the crystal to the geometry shown in Fig. 3.3, where a narrow ($\sim$ 20μm) groove was cut to within a short distance of the crystal edge. The groove was cut by a chemically etched Tungsten point operated by a three dimensional micromanipulator(*) and the operation was viewed in transmission with the $NbSe_2$ plus substrate mounted on a microscope stage. The Tungsten tip was formed in the following way. A Tungsten wire of diameter 0.060" functioned as the anode in a sodium hydroxide bath[83] of concentration 100gm/litre. With a Carbon cathode $\sim$ 1cm distant, a current of $\sim$ 100mA was allowed to flow until the Tungsten section below the etchant surface dropped off. A tip of radius < 1μm resulted from this procedure.

Typical weak link dimensions formed by the above process were (Fig. 3.3)

$$AB \sim 5\mu m$$

$$BC \sim 5\mu m$$

for a 200Å thick crystal layer. An enlarged view of an

---

*Kuhlicke, Soffa, Manufacturing Co., 135 Commerce Drive, Fort Washington, Penn.

actual weak link made by the above method is shown in Fig. 3.4, where the dark regions represent the crystal. The crystal thickness for this weak link was $\sim$ 500Å in order to make the section visible. $NbSe_2$ crystal layers of thickness < 100Å are almost invisible in transmission, and have to be viewed in reflection.

A variety of structures was developed in this study and they can be classified according to whether single loop or multiple loop geometries are involved.

(i) Single loop planar geometry.
(ii) Single loop (bulk) cylindrical geometry.
(iii) Multiple loop geometry (planar or bulk).

3.2.1 Single Loop Planar Geometry

Planar devices are relatively easy to make once the weak link region (Fig. 3.3) has been formed. One merely chips away the crystal until the ring structure in Fig. 3.5 results. This ring geometry consists of a narrow groove of the desired length leading to a circle of diameter $\sim$ 2mm. In order to minimise the loop inductance, the groove should be as short as possible. To complete the device and make it ready for measurements electrical leads can be fixed to points E and F in Fig. 3.3 on either side of the weak link. An equivalent but more practical scheme is inductive coupling via a small flat coil of wire of diameter slightly

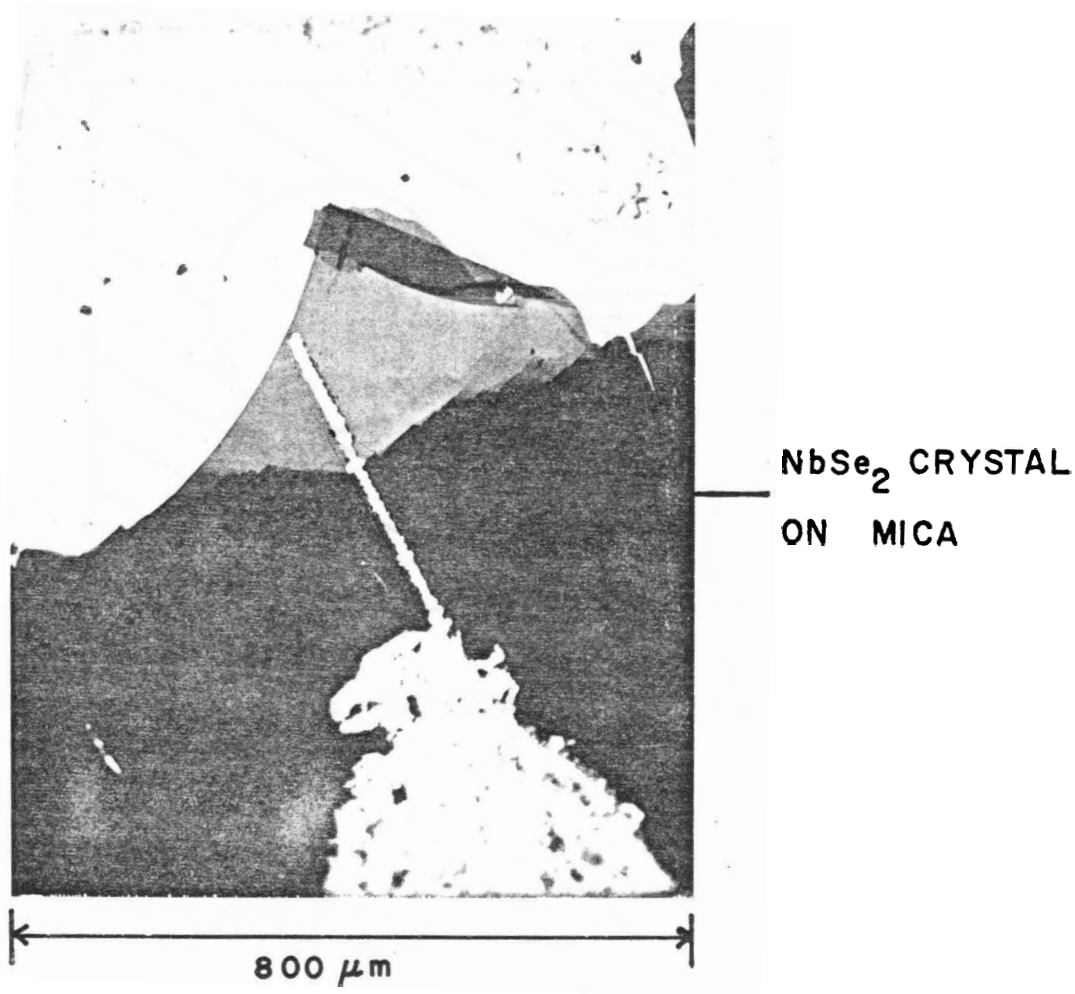

Fig. 3.4 Polaroid photograph of actual $NbSe_2$ weak link on mica. The weak link dimensions and crystal thickness have been scale up for clarity. (Courtesy R.F. Frindt)

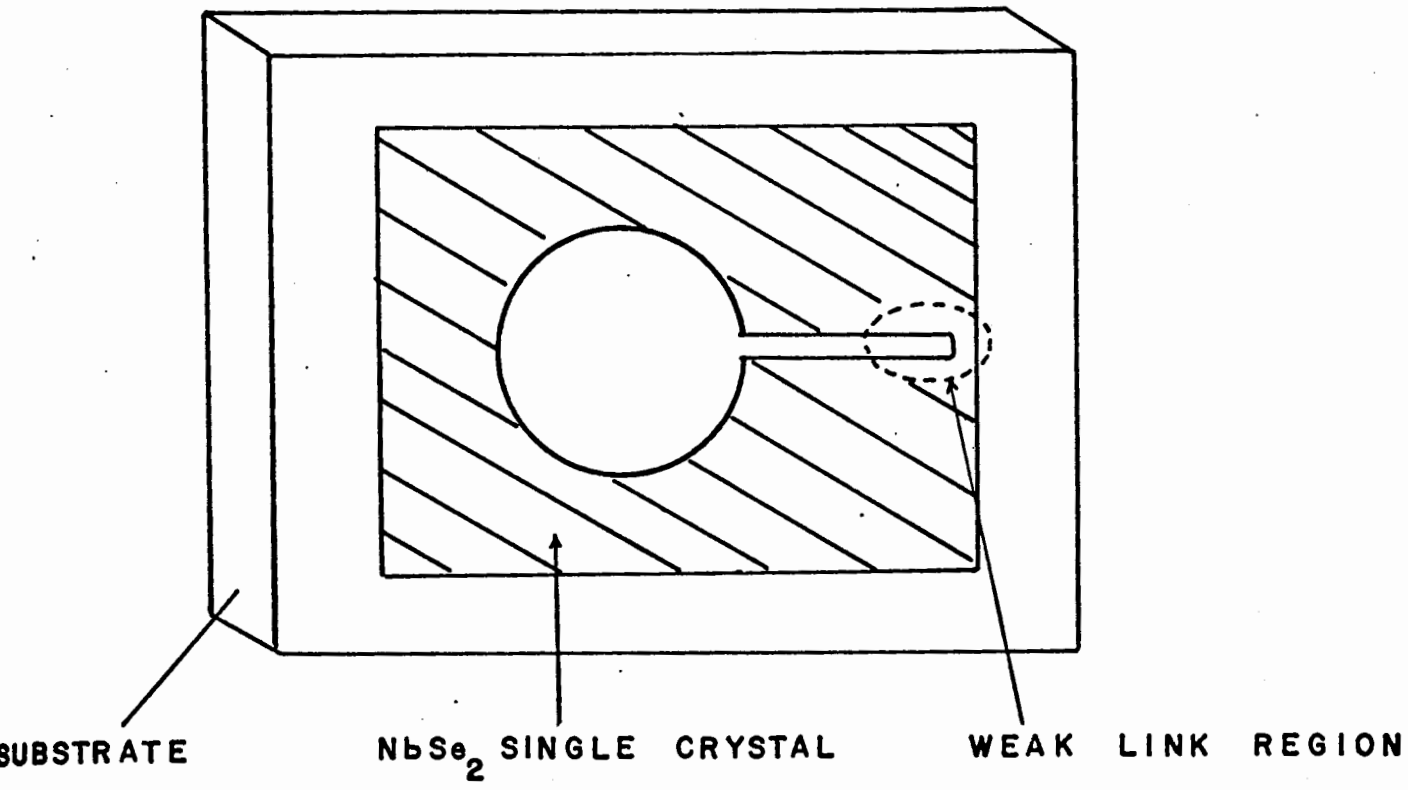

Fig. 3.5 Single loop planar geometry.

less than 2mm. For this purpose ten turns of fine copper wire, AWG 44, were wound in a flat tight spiral and then epoxied into the hole of Fig. 3.5. To stabilise the device against thermal shock and to prevent atmospheric corrosion the weak link region could be sealed using a thin layer of the epoxy Stycast 1269A.

This structure was the first one to be studied and had the advantage that after the initial dip-test at 4.2°K, the ring could be cut open and the weak link critical current measured by a four-probe technique. The results of such experiments will be presented later in section 3.4.

3.2.2 Single Loop Cylindrical Geometry

The single loop planar geometries were found to be less sensitive to magnetic flux changes than the bulk point contact devices (section 3.1) and this was attributed partly to the poor coupling between the planar loop and the pickup coil (section 3.2.1). Thus there was some interest in developing a bulk geometry similar to section 3.1 where the point contact was replaced by a weak link of $NbSe_2$. This was suggested initially by B. Heinrich[84] and subsequently developed by F. Consadori, R.F. Frindt and S. Gygax in collaboration with the author[9].

One of the bulk geometries is shown in Fig. 3.6. The idea is to take a preformed weak link (Fig. 3.3) on a suitable insulating substrate e.g. mica, and clamp it to a superconducting metal cylinder which has a narrow slit of width 0.005" along the axis. The substrate is clamped to the bulk metal in such a way that the weak link region is situated directly above the slit (Fig. 3.7). There was sufficient area of crystal on either side of the weak link such that superconducting contacts resulted between the crystal layer and the bulk superconducting metal. Superconducting contacts resulted when sufficient pressure was applied to the substrate via the pressure plates of Fig. 3.7. Thus again there was a completely superconducting loop interrupted by a narrow constriction. The device was then inductively coupled to the external circuitry via a cylindrical 15 turn coil of AWG 30 inserted in the hole.

3.2.3 Multiple Loop Geometries

One is not confined to using single loop geometries in magnetometers and certain multiple loop configurations have inherent advantages over the single loop counterpart. Figures 3.8 and 3.9 show symmetric hole structures sensitive only to the gradient of the external magnetic field. Figure 3.8 indicates the planar geometry where two identical holes are cut in the same crystal platelet and are separated by a weak link region similar to Fig. 3.3. Figure 3.9, a bulk geometry, shows a weak link on

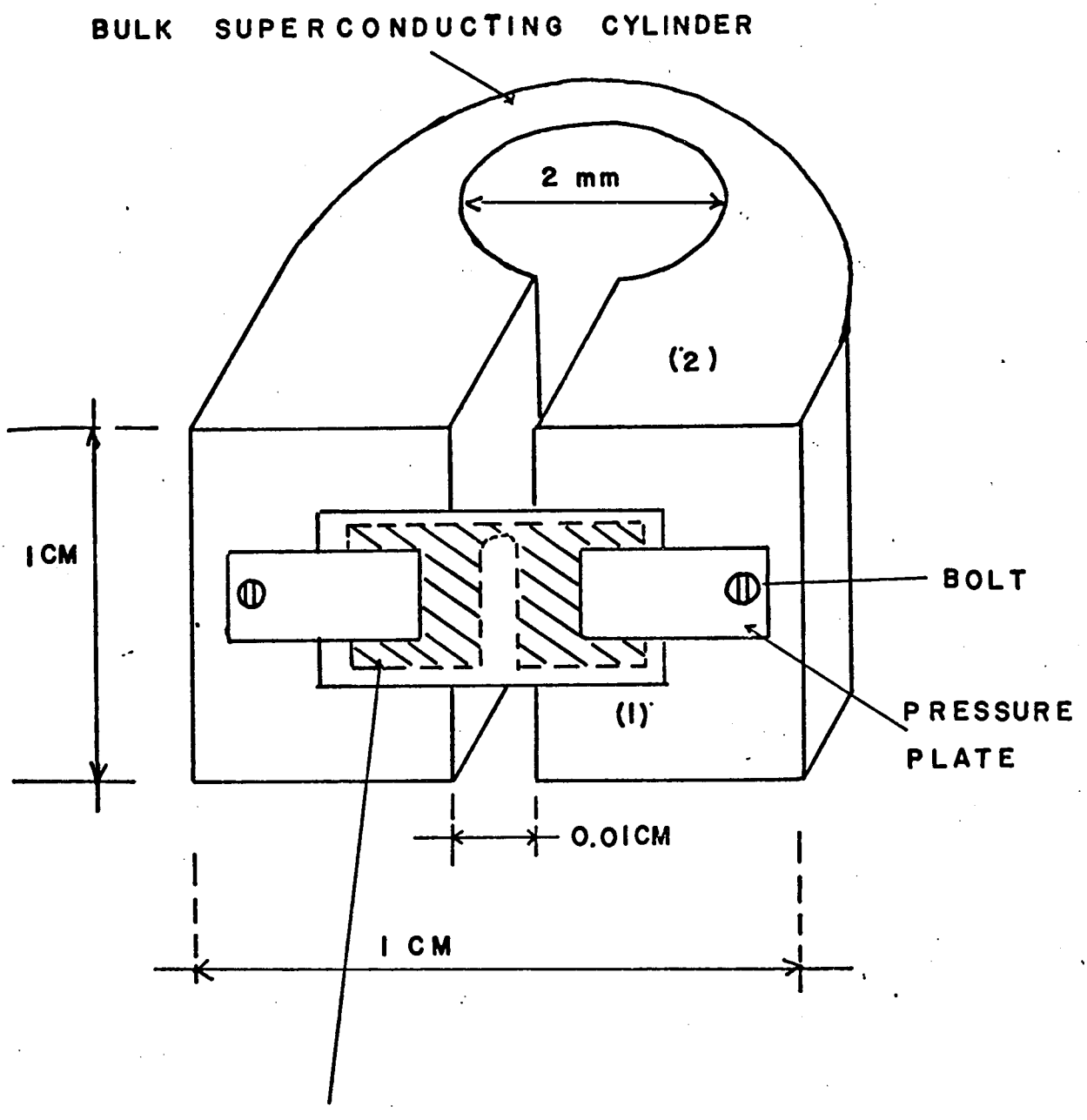

Fig. 3.6 Single loop cylindrical geometry (bulk) with weak link clamped in position.

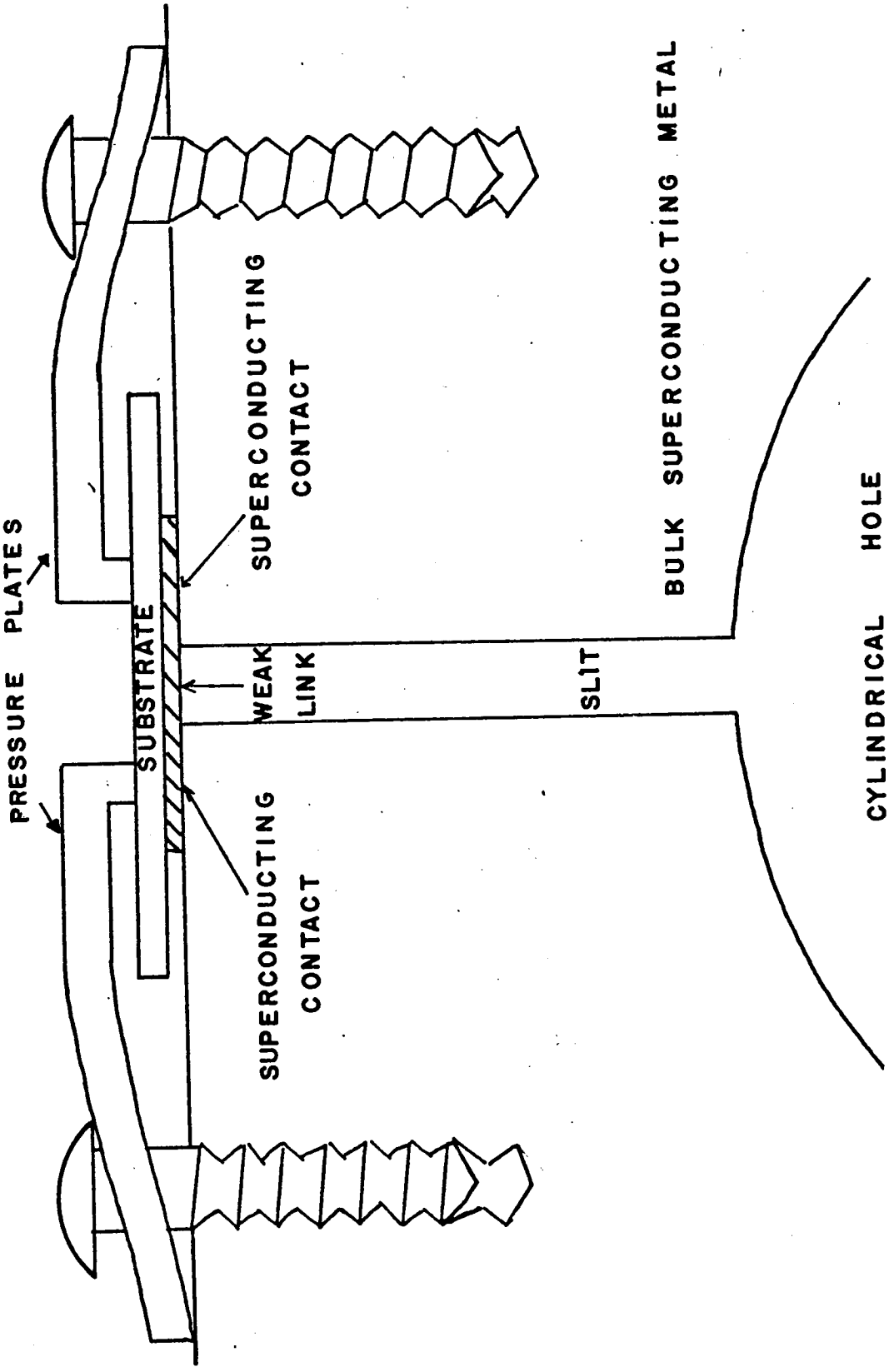

Fig. 3.7. $NbSe_2$ Weak link clamping system. Top view of Fig. 3.6.

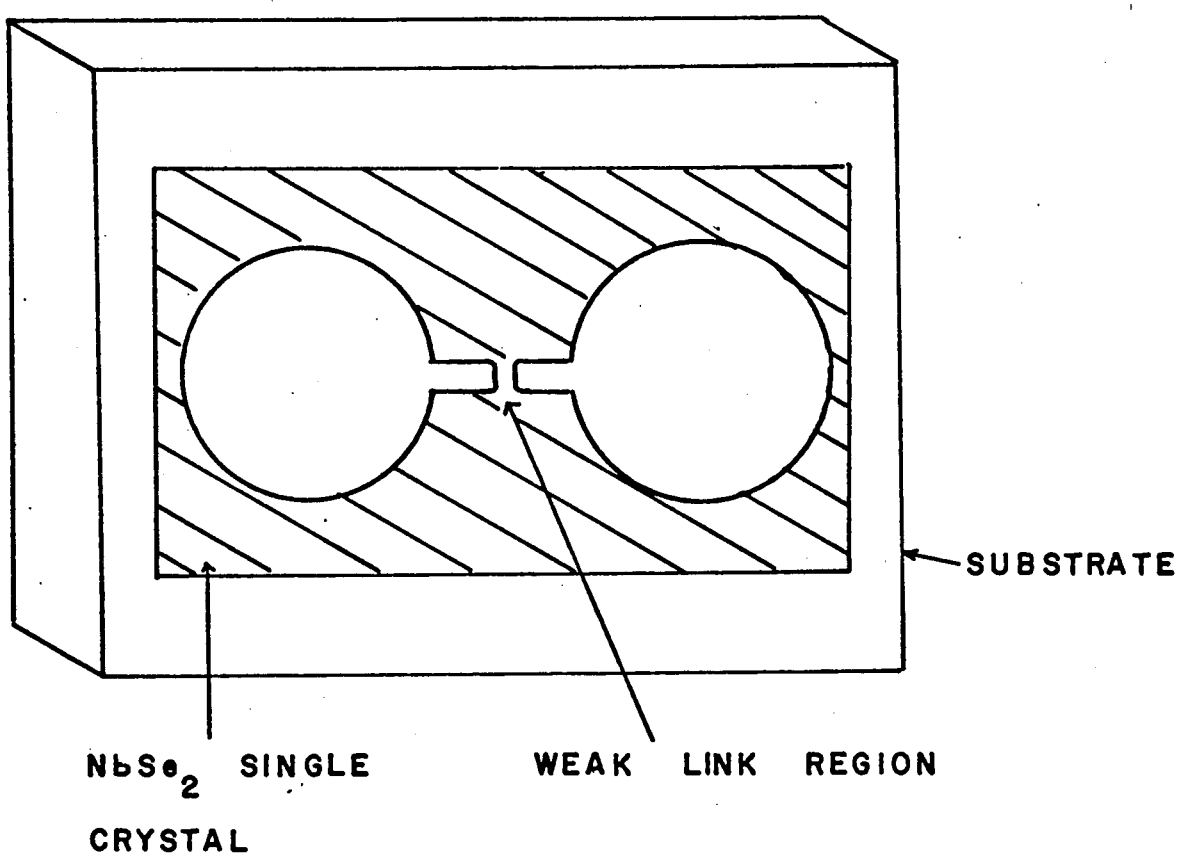

Fig. 3.8 Symmetric double hole planar M-SQUID. Hole diameters ~ 2 mm.

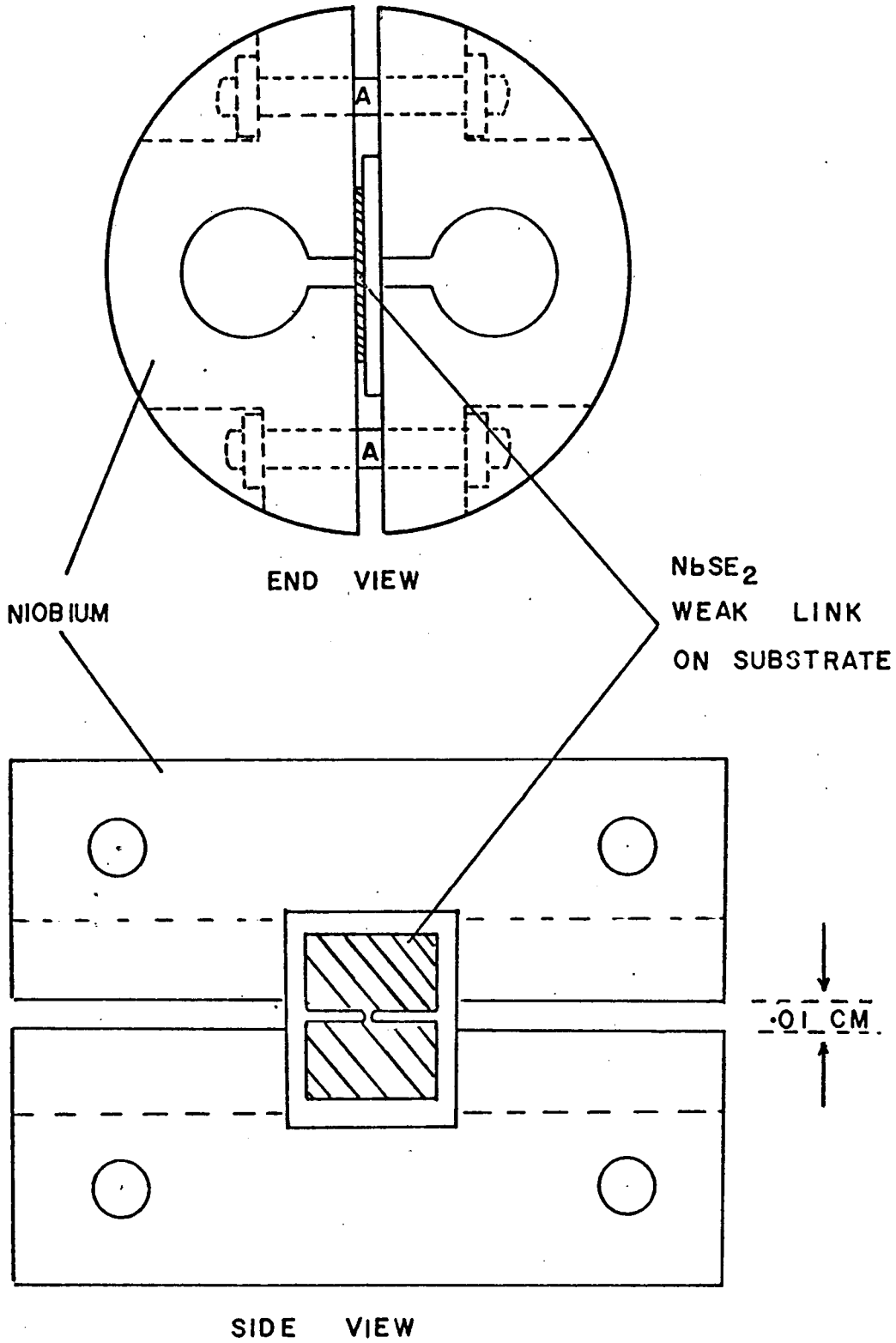

Fig. 3.9 Symmetric double-hole bulk M-SQUID. Hole diameters ~ 2mm, slit width ~ 0.01 cm. Clamping bolts (A) are superconducting.

a substrate clamped between the mirror image halves of a symmetric hole structure.

By designing a multiple loop structure of N identical loops where self inductances add in parallel, one can use weak links whose cross sectional area is N times greater[72]. This considerably eases the problem of making weak links as in Fig. 3.3 where the cross dimension AB could be N times greater. This results from the fact that the optimum value of critical current for the SQUID operation is $i_c \sim \Phi_o/L$.

3.3 Detection Electronics

Thus far various theoretical models of the M-SQUID have been discussed together with some practical details of how the devices are constructed. In order to utilise the peculiar properties of the superconducting ring, one inductively couples the M-SQUID to a tank circuit resonant at an rf frequency of say 30MHz. In this mode, the tank circuit acts as a voltage source and the weak link current is free to adjust to flux changes occurring within the ring. The basic point is that the rf impedance of such an inductively coupled ring is a sensitive periodic function of the applied flux. This last statement has been justified analytically[8,61] and also by analogue computer simulation[63].

In the theoretical model of the M-SQUID (section 2.3)it was shown that the magnetic flux enclosed by the superconducting ring was a steplike function of the applied flux (Fig. 2.3). As the applied flux is increased from zero up to some critical level, the flux in the ring remains fixed (Supercurrent breakdown model). For applied flux greater than critical, flux enters the ring in quanta. The persistent current shielding the flux drops by Φ_o/L where one quantum enters the ring, and hence the external flux has to be increased again by Φ_o to reach the critical condition at which point the process repeats. If a single flux quantum transition takes place in a transition time τ then an emf

$$E = \frac{\Phi_o}{\tau} \qquad 3.301$$

is generated where $\tau = \hbar(2\Delta)^{-1}$ with 2Δ = energy gap. Thus if $i_c = \Phi_o/2L$ one obtains the pulse train shown in Fig. 3.10 as a function of the applied flux, where the pulse height depends on τ and the pulse period is Φ_o in flux. Following Mercereau[61], it is possible to derive an approximate analytic expression for the generated emf E(Appendix A)

$$E = \frac{2\omega\Phi_{rf}}{\pi} + \frac{4\omega\Phi_{rf}}{\pi} J_1\left(\frac{2\pi\Phi_{rf}}{\Phi_o}\right)\cos\left(\frac{2\pi\Phi_{dc}}{\Phi_o}\right)\sin\omega t \qquad 3.302$$

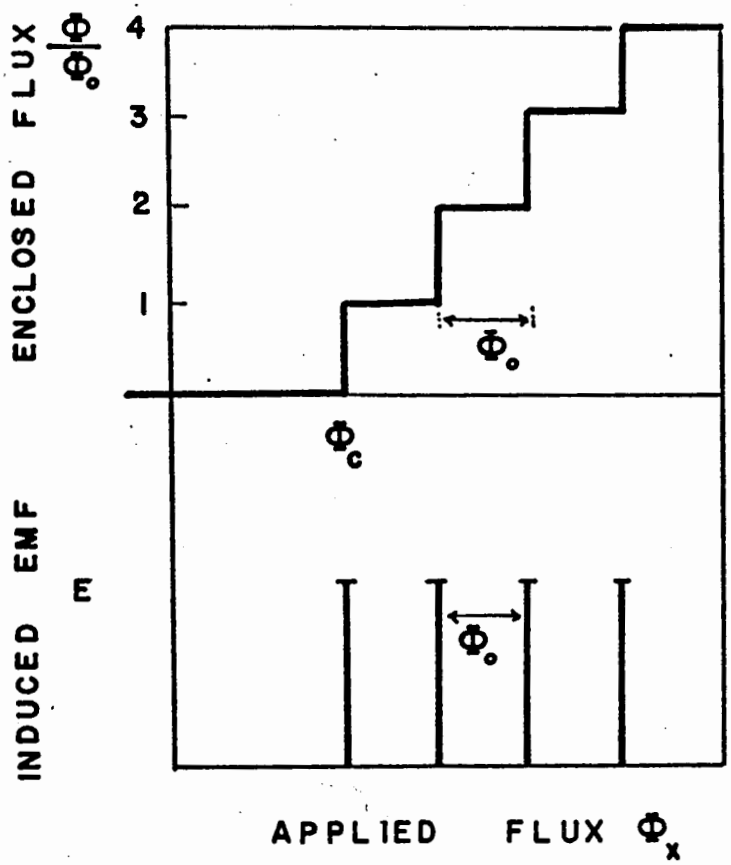

Fig. 3.10 (i) Magnetic response for the M-SQUID, Φ vs Φ_x.
(ii) Emf E generated when flux is transferred into the ring.

where the applied flux is

$$\Phi = \Phi_{DC} + \Phi_{rf} \sin \omega t \qquad 3.303$$

In 3.302 only the fundamental component of the generated emf is given, and Mercereau[61] and Nisenoff[30] demonstrate that this gives good agreement with the experimental data despite neglect of higher harmonics.

Zimmerman et al[8], again using the fact that emf pulses are generated when the weak link goes normal, use a hysteretic model of the Φ vs Φ_x curve to derive a similar result displayed in graphical form.

The electronic circuit used to measure the emf (equation 3.302) is given in schematic form in Fig. 3.11, with the circuit diagram of the rf preamplifier and rf demodulator given in Figs. 3.12, 3.13. Much of the initial SQUID circuitry in tube form was brought to the department in 1969 by Dr. J.E. Zimmerman. The transistorised versions of the battery operated preamplifier and demodulator were respectively developed by Dr. S. Gygax, and Mr. P.A.M. Garnett. The 40db rf amplifier was a broad band Hewlett Packard Model 461A. The rf oscillator was a General Radio Model 1001-A.

Using equation 3.302, the voltage V appearing across the

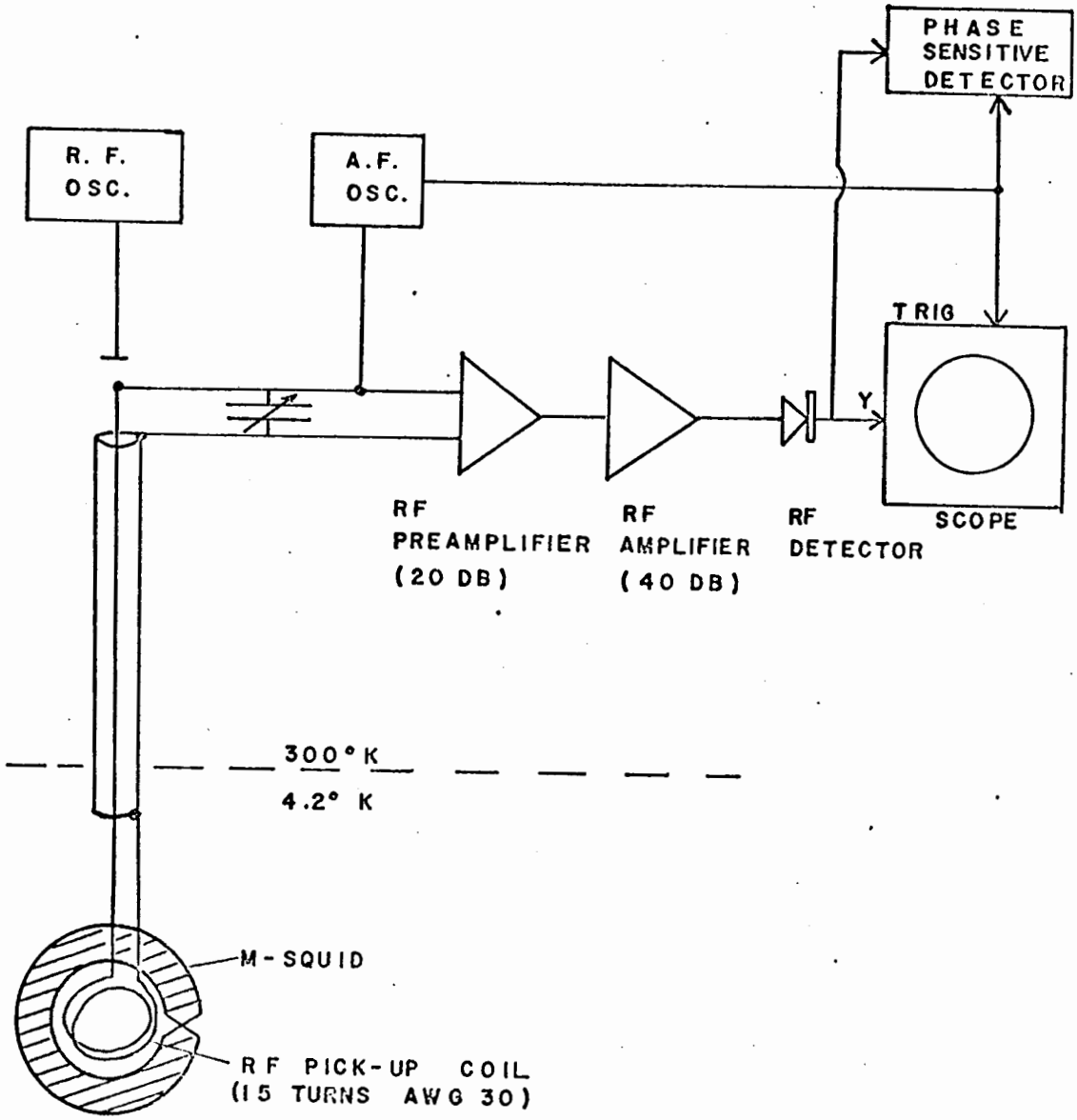

Fig. 3.11 Schematic of the detection electronics coupled to the M-SQUID. RF preamplifier : Fig. 3.12; RF amplifier Hewlett Packard 461A; RF detector Fig. 3.13; RF Oscillator General Radio 1001A; Phase Sensitive Detector : Princeton Applied Research Model HR-8; Oscilloscope Tektronix Model 547, with types 1A1, 1A7A plug-in units; AF Oscillator : Hewlett Packard Model 204B.

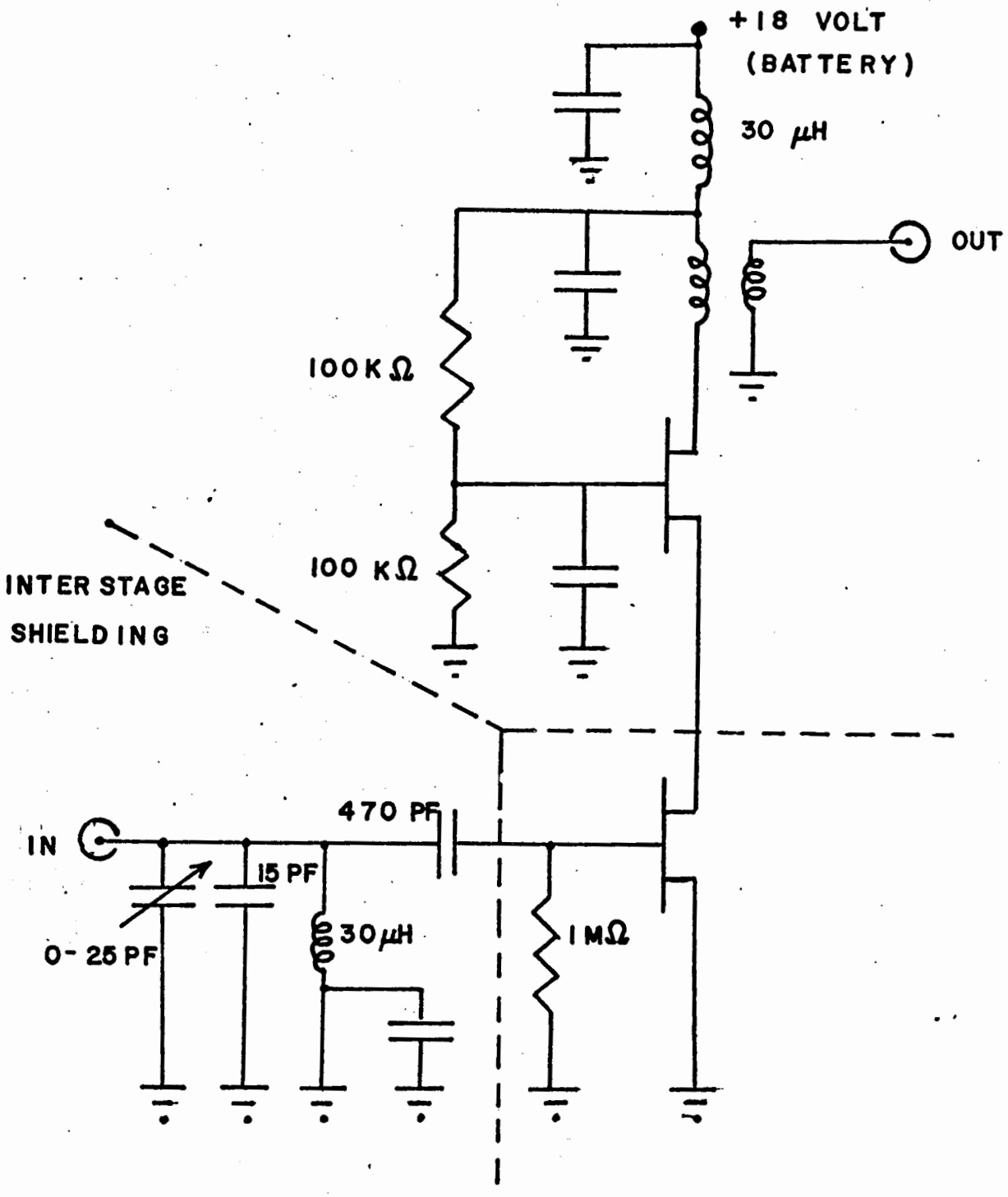

Fig. 3.12 Circuit diagram for the low noise preamplifier. The transistors were field effect 2N3819. All capacitors are 1500 pf unless otherwise indicated.

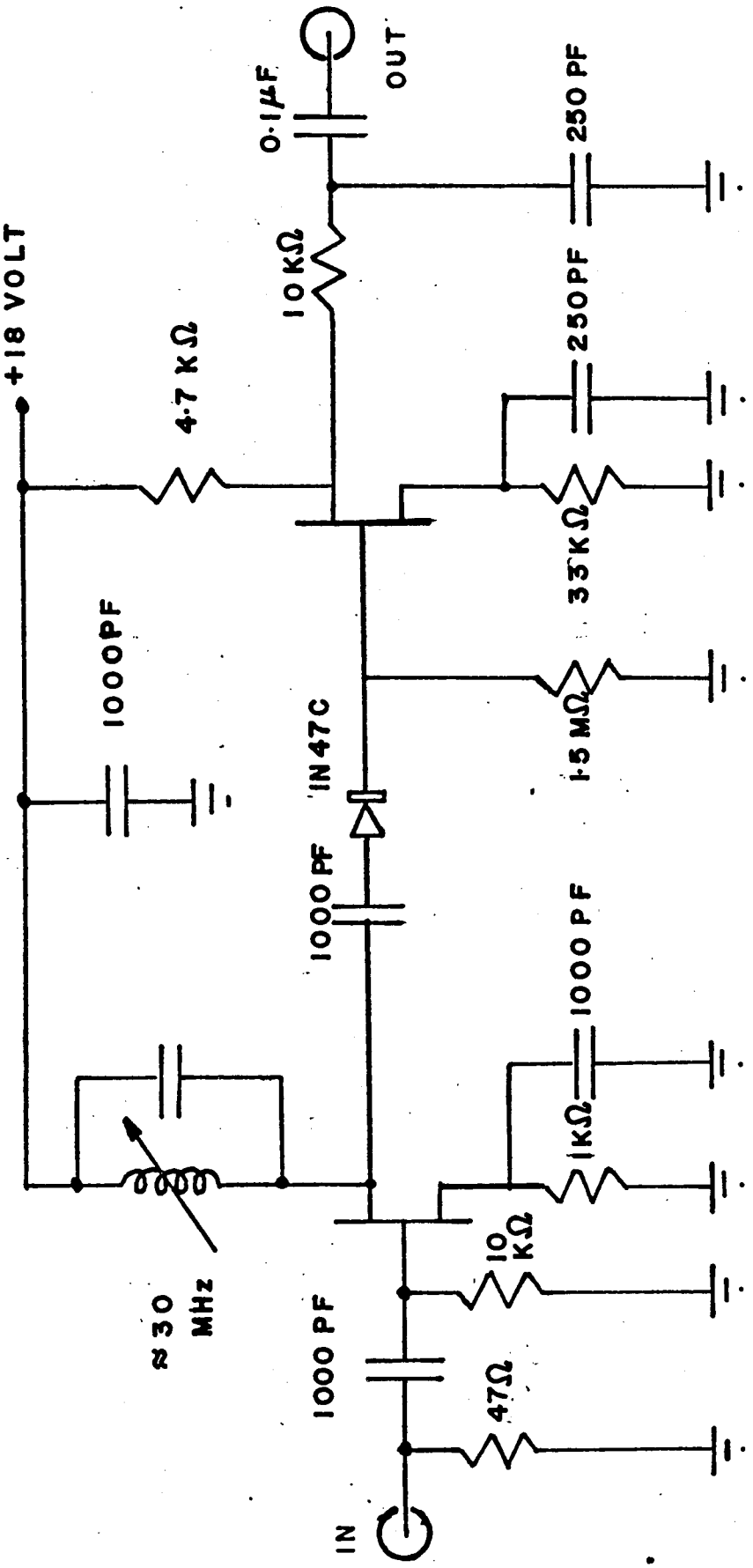

Fig. 3.13 Circuit diagram for the transistorised rf demodulator. The transistors were field effect 2N3823.

coil is

$$V = \left[\omega\Phi_{rf} + A''\omega\Phi_{rf}\, J_1\left(\frac{2\pi\Phi_{rf}}{\Phi_o}\right)\cos\left(\frac{2\pi\Phi_{dc}}{\Phi_o}\right)\right]\sin\omega t + \cdots \qquad 3.304$$

where the first term is the Faraday induction voltage ($V = -d\Phi/dt$) in the coil, and the factor A'' is determined by the mutual inductance between the drive coil and the SQUID. The Φ_{DC}- dependent part of the voltage has a maximum amplitude $\sim \omega\Phi_{rf}$ which is $\sim 5\mu V$ where $\Phi_{rf} \sim \Phi_o$ at 30MHz. According to this formula (equation 3.304) there is some interest in operating the device at 300MHz or higher and hence increasing the modulation amplitude by a factor ten or more over the 30MHz operation[72].

3.4 Flux Patterns and Sensitivity

Detected flux patterns obtained with the present electronics system are shown in Fig. 3.14 for the $NbSe_2$ bulk M-SQUIDS and in Fig. 3.15 for the $NbSe_2$ planar devices. In Fig. 3.14(i) the rectified rf voltage is plotted vertically on the oscilloscope in time-base representation, where a low-frequency audio flux of magnitude approximately five flux quanta is held constant. This audio signal is superposed on the oscilloscope for clarity. According to the previous analysis no oscillating signal should be observed as the amplitude Φ_{rf} is increased, until the current induced in the SQUID ring exceeds the critical

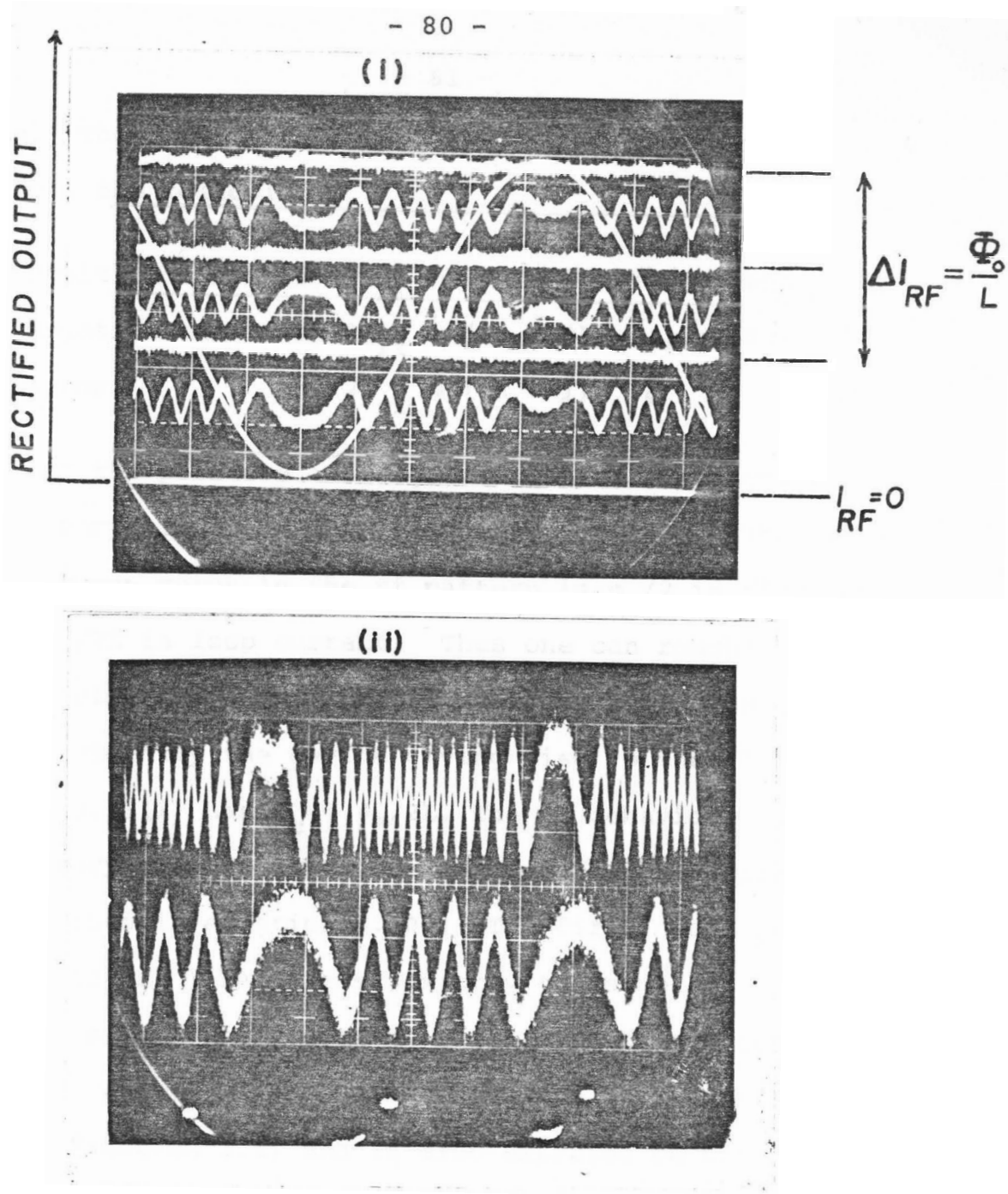

Fig. 3.14 Response of a bulk single ringe $NbSe_2$ M-SQUID with $i_c \sim \Phi_o/2L$.

(i) The demodulator dc output is presented for seven values of the applied rf flux increasing vertically. The external af sweep triggers the oscilloscope in time base representation. This audio flux is superposed on the trace for clarity.

(ii) Oscilloscope traces for two different values of the audio flux for fixed rf flux.

value. The Bessel function behaviour of the ring emf predicts the following:

Positive maxima at $2\Phi_{rf} \sim (4n + 3)\phi_o/4$, n even;

Negative maxima at $2\Phi_{rf} \sim (4n + 3)\phi_o/4$, n odd;

Zeros at $2\Phi_{rf} \sim (4n + 1)\phi_o/4$

For the positive and negative maxima, the amplitudes should vary sinusoidally with the dc flux Φ_{DC}. The separation between zeros in the rf pattern is $\Phi_o/2$ in flux and hence $\Phi_o/2L$ in loop current. Thus one can roughly characterise the weak link critical current i_c in terms of Φ_o/L. Evidently the device giving rise to the flux pattern in Fig. 3.13(i) has $i_c \sim \Phi_o/2L$. The rf behaviour although oscillatory, was not quite Bessel function behaviour (J_1) as described in equation 3.304. The first oscillation (Fig. 3.13 (i)) had almost exactly the same amplitude as all others up to at least the fifth. This evenness of amplitude with Φ_{rf} is observed with the point contact devices (section 3.1) and is also expected on the hysteretic model of the ring response[8,63]. (Note that equation 3.304 predicts the flux dependent amplitude will <u>increase</u> after the first few oscillations since $J_1(x)$ decreases as $x^{-1/2}$ for large x.)

For some $NbSe_2$ bulk devices particularly those with

$i_c > \Phi_o/L$ the rf pattern was amplitude modulated. Figure 3.14(iii) is a plot of the rectified output signal versus the rectified drive signal (Φ_{rf}), for a single ring M-SQUID with $i_c \sim 8\Phi_o/L$. This was obtained by plotting the phase sensitively detected output from the demodulator (Fig. 3.13 AC o/p) versus a rectified signal proportional to the rf flux. This modulation may be due to a weak link loop of area much smaller than the main loop. Such multiple contacts are easily envisaged, due to the complex construction of the bulk devices.

Figure 3.14(ii) shows two flux patterns (again in time-base representation) for two different values of audio bias at a fixed rf flux bias. To determine the accuracy of the period, a carefully shielded device was subjected to slow (10 seconds/cycle) sawtooth flux of amplitude $\sim 5\Phi_o$. The SQUID signal after amplification and detection was fed to a phase-sensitive detector(*) phase-locked at the external audio frequency used to produce the flux pattern($\sim$ 200Hz). The PAR output was plotted on a Moseley X-Y recorder Model 6001 and the periodicity in flux measured. The period (Φ_o) was found to be constant to one part in 1000. This plot is shown in Fig. 3.11.

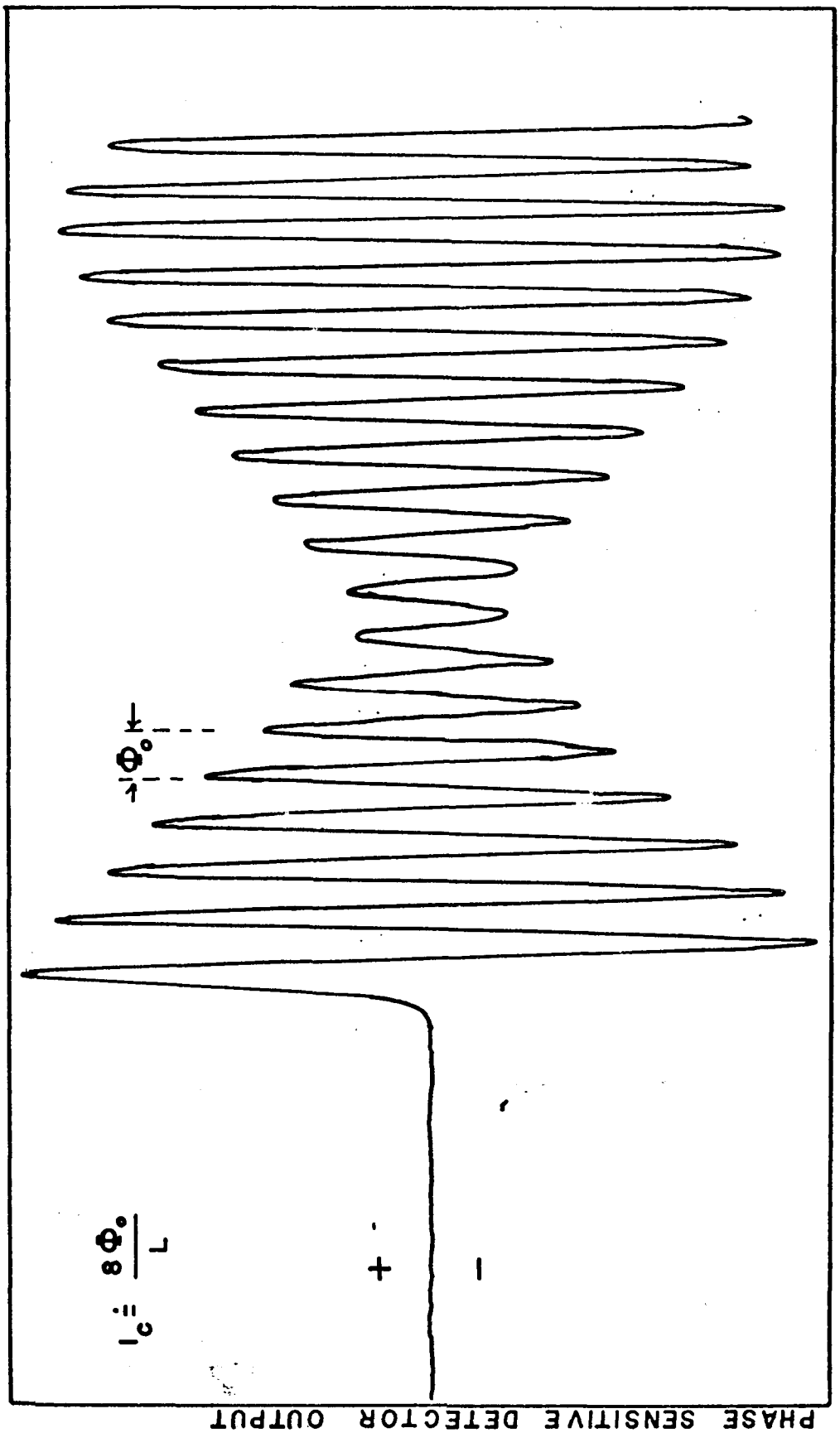

Fig. 3.14 (iii) A plot of the phase detected demodulated signal vs the applied rf flux Φ_{rf} for $i_c \sim 8\ \Phi_o/L$.

It is well known[7] that multiple flux quantum transitions are possible with M-SQUIDS especially when $i_c >> \Phi_o/L$. These have been observed with the present bulk $NbSe_2$ devices and cases where two flux quanta crossed the weak link per transition often occurred. The number of flux quanta per transition was determined by measuring the number of quantum oscillations (Fig. 3.14(ii)) corresponding to a known external flux. Where $i_c >> \Phi_o/L$, the pattern often became very irregular and these weak links were usually discarded.

In order to examine the device sensitivity with respect to the orientation of the weak link in the external magnetic field, the single ring structure of Fig. 3.6 was utilised (following a design by F. Consadori). The weak link could be clamped with the plane of the $NbSe_2$ layers either parallel (position 1) or perpendicular (position 2) to the applied field. The device sensitivity was found to be identical in the two orientations. Of course, this experiment is not entirely conclusive since the dynamics of flux flow in these metallic bridges of $NbSe_2$ is not known.

The flux patterns obtained with a double hole planar device (Fig. 3.8) are shown in Fig. 3.15(i) and (ii). These multiple oscilloscope traces were taken in the same way as those for the bulk devices (Fig. 3.14). The planar devices

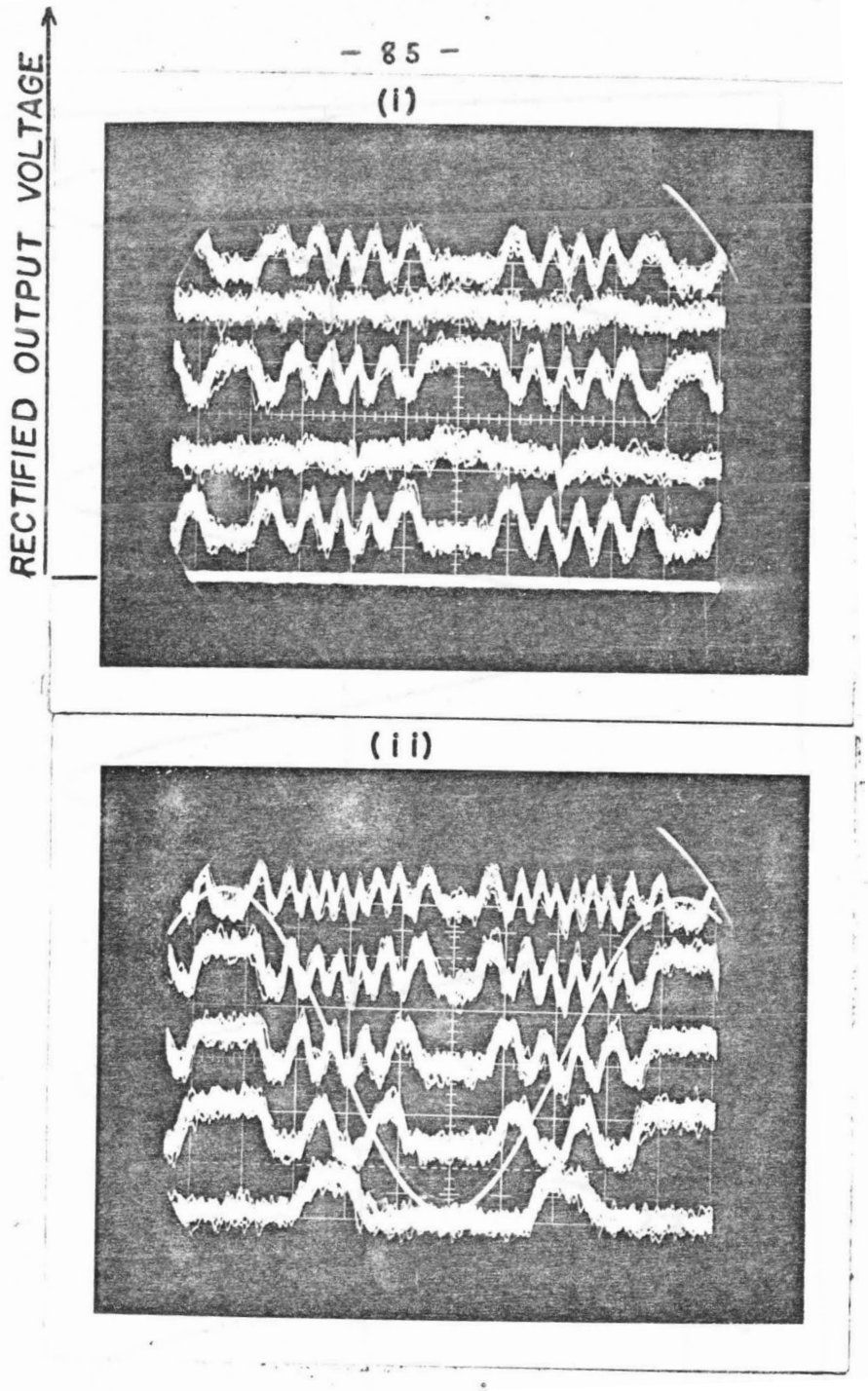

Fig. 3.15 RF (i) and af (ii) response of a double loop planar $NbSe_2$ M-SQUID using the same detection electronics as in Fig. 3.11. In (i) the dc zero has been shifted downward between successive traces to compensate for the small modulation amplitude.

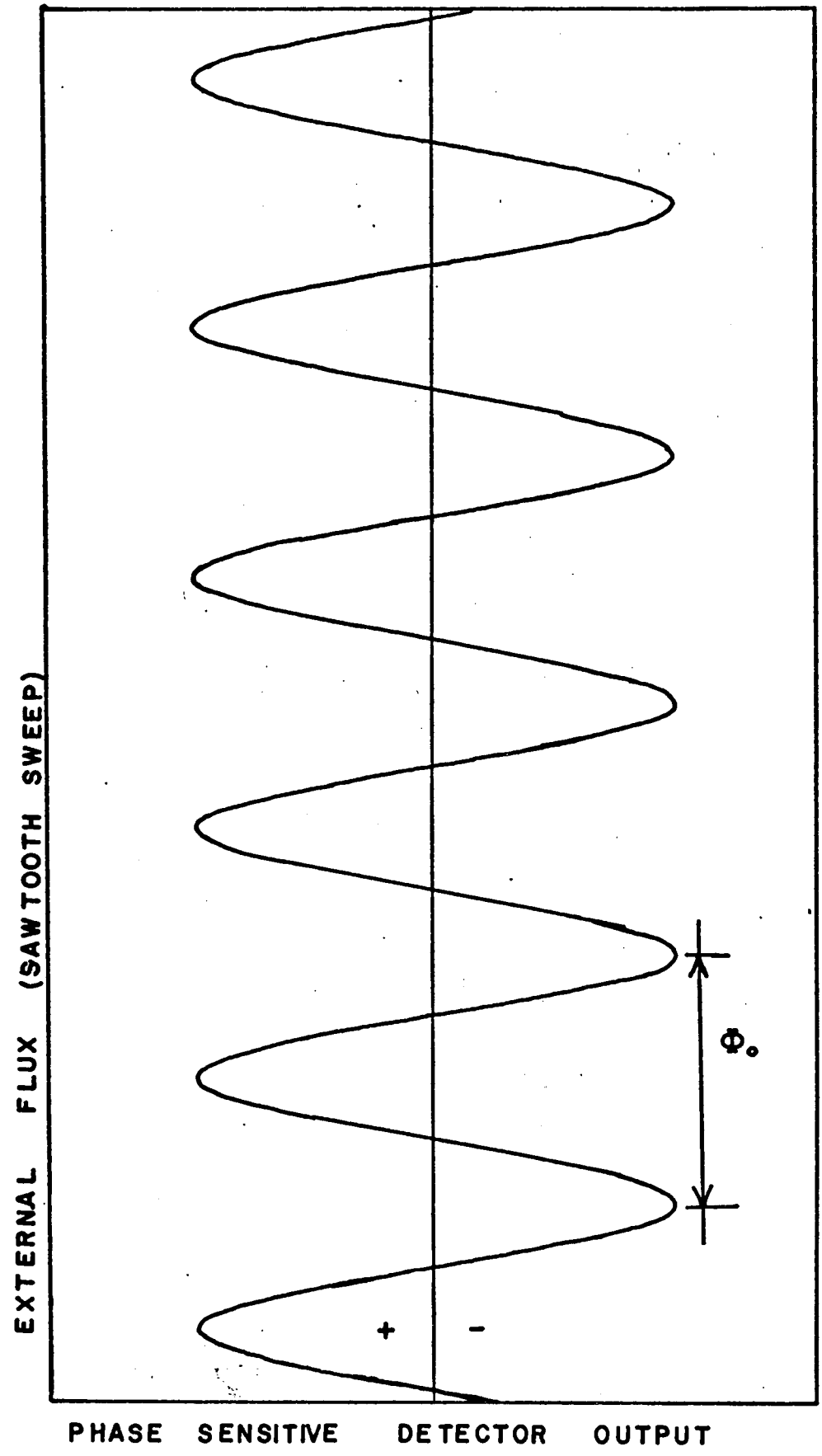

Fig. 3.16 Reproductibility of the af flux quantum periods for a bulk $NbSe_2$ M-SQUID.

were the first type to be studied mainly because their construction is straight forward once the weak link has been formed. Their main disadvantage was that their sensitivity to external flux changes was much lower than that of the corresponding bulk devices (by at least a factor of ten). This was principally due to the poor mutual inductance coupling between the pickup coil and the device. This small coupling had three main effects:

(i) Much larger rf bias than normal had to be applied in order to induce sufficient ring current to exceed i_c. This tended to introduce noise from the rf oscillator.

(ii) The modulation of the applied rf flux by the audio quantum oscillations tended to be smaller than normal. (Normal here refers to the bulk device behaviour.)

(iii) The shape of the quantum oscillations (Fig. 3.15 (ii)) tended to be trapezoidal rather than sinusoidal or triangular (Fig. 3.14 (ii)).

Simmonds and Parker[63] have presented an interesting analysis of the effects of the strength of the inductive coupling between the drive coil and the ring. The important parameter in determining how tightly the ring is coupled to the coil is the term $K_I^2 Q$ where Q is the Q-value of the drive coil, and the coupling constant $K_I^2 = M^2 (L_R L_T)^{-1}$ for

an inductance M between the ring inductance L_R and the drive coil inductance L_T. The analogue simulation indicated that a value $K^2Q \sim 1$ was sufficient to obtain the full amplitude of the quantum interference signal. For values of $K^2Q >> 1$ the system was found to become slightly unstable. In any practical measurement, improvement of coupling would tend to increase the flux noise from room temperature sources.

In order to understand how the coupling affects the triangular flux pattern one has to consider the response of the ring in a slightly different way. In Fig. 3.17(i) and (ii), the peak rf voltage appearing across the tank circuit coil is plotted as a function of the rf flux amplitude for two values of the coupling parameter K^2Q. (The technique for measuring the response curve is indicated in reference 8, and the present curves are taken from reference 63.) On each plot, the response is given for two values of ambient dc flux differing by $\Phi_o/2$.

If one uses an rf drive amplitude corresponding to the point A of Fig. 3.17(i) then a linear increase of the ambient dc flux causes the voltage plateau to shift downward to point A′ in a linear manner. At A′ the rf voltage starts to increase and the amplitude returns to A. Thus as a function of Φ_{DC} a triangular flux pattern emerges. If

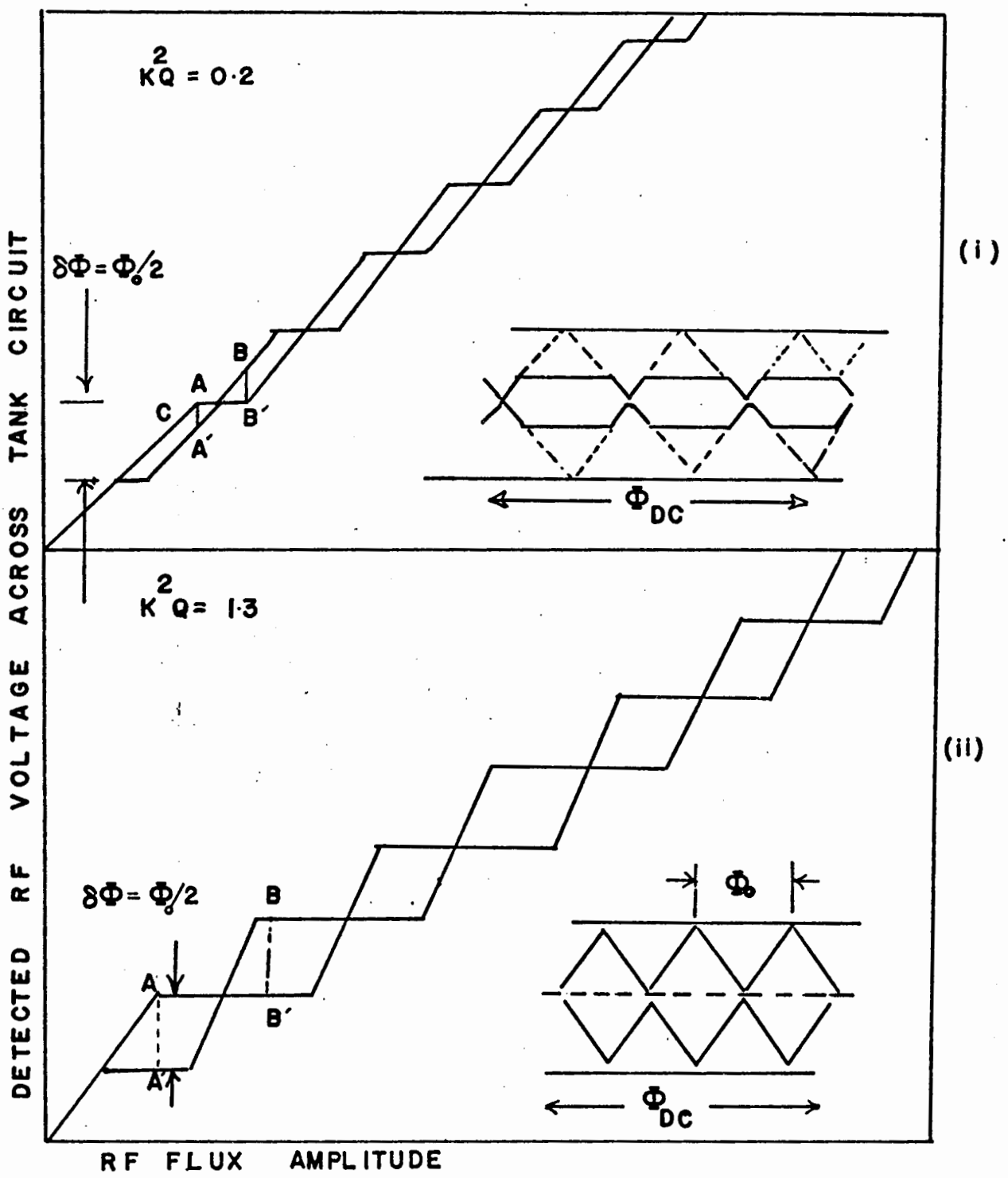

Fig. 3.17 The effect of coil-SQUID coupling on the detected flux pattern. Detected rf voltage appearing across tank circuit for two values of the coupling parameter K^2Q : (a) $K^2Q = 1.3$ (b) $K^2Q = 0.2$

one starts at point B, the rf voltage increases and thus a pattern 180° out of phase with the first pattern, is swept out.

The resultant pattern is quite different if one considers the case $K^2Q = 0.2$ (Fig. 3.17(ii)). Here, if one starts at A and increases Φ_{DC}, one obtains a linear decrease until A' is reached at which point there is no further change in the signal until Φ_{DC} has been increased sufficiently for the curve to cross A' again, where the rf voltage again increases until A is reached. A similar argument in reverse applies to the case of point B. Thus one obtains a curve of triangles with alternate vertices clipped. A curve with every vertex clipped is obtained by starting from point C. The lower traces of Fig. 3.15(ii) clearly display this behaviour.

As mentioned earlier, the planar devices tended to be a factor of at least ten times less sensitive than the corresponding bulk device. There was some interest in determining if the periodicity in flux was reproducible, and a similar experiment to that of Fig. 3.16 produced the curve on Fig. 3.18 where a flux pattern with alternate vertices clipped was obviously present. Superposed on the trace is a linear ramp magnetic field used to produce the flux changes. This field was supplied by a small Helmholtz coil pair with the single ring planar SQUID loop

placed between the coils. An approximate calculation of the flux threading the SQUID loop indicated that the periodicity in flux of Fig. 3.18 was $\sim 25\Phi_o$. This periodicity was accurate to better than 1% for 25 repeated sweeps of which only one is shown.

3.5 Weak Link Critical Current

The weak link critical current was measured for eight of the planar devices constructed. After the first He^4 dip where a satisfactory flux pattern was obtained (i.e. as in Fig. 3.15), the $NbSe_2$ ring was cut open at a point opposite the weak link and voltage and current leads were attached to the $NbSe_2$ crystal with silver conducting epoxy(*) as shown in Fig. 3.19. A simple dc sweep circuit (Fig. 5.12) was used to measure the I vs V curve for the $NbSe_2$ weak link and a typical result is shown in Fig. 3.20 where $i_c \sim 2mA$. Values of i_c ranging between 150μA and 10mA were obtained with most of the values in the 1mA range. By any standards, the curve in Fig. 3.20 is complex, but the hysteretic load line switching between the different parts was quite reproducible. A qualitative explanation of this behaviour is that different parts of the layer structure weak link are driven normal as the current is increased.

---

* See page 164

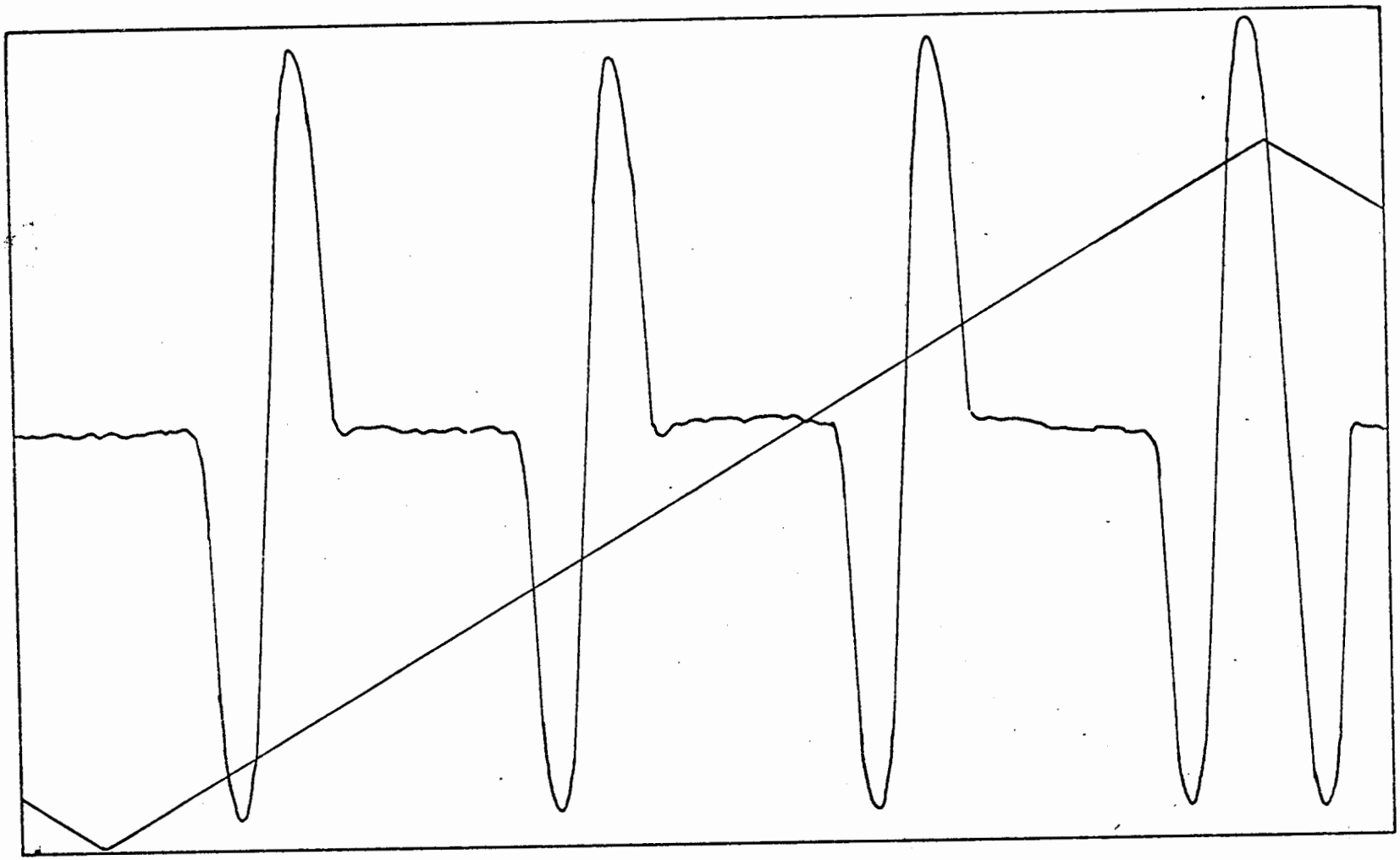

Fig. 3.18 Reproducibility of the af flux quantum periods for an $NbSe_2$ planar M-SQUID. The discontinuous nature of the signal is due to the clipping action of the weak coupling Fig. 3.17 (b). Superposed is the sawtooth external flux.

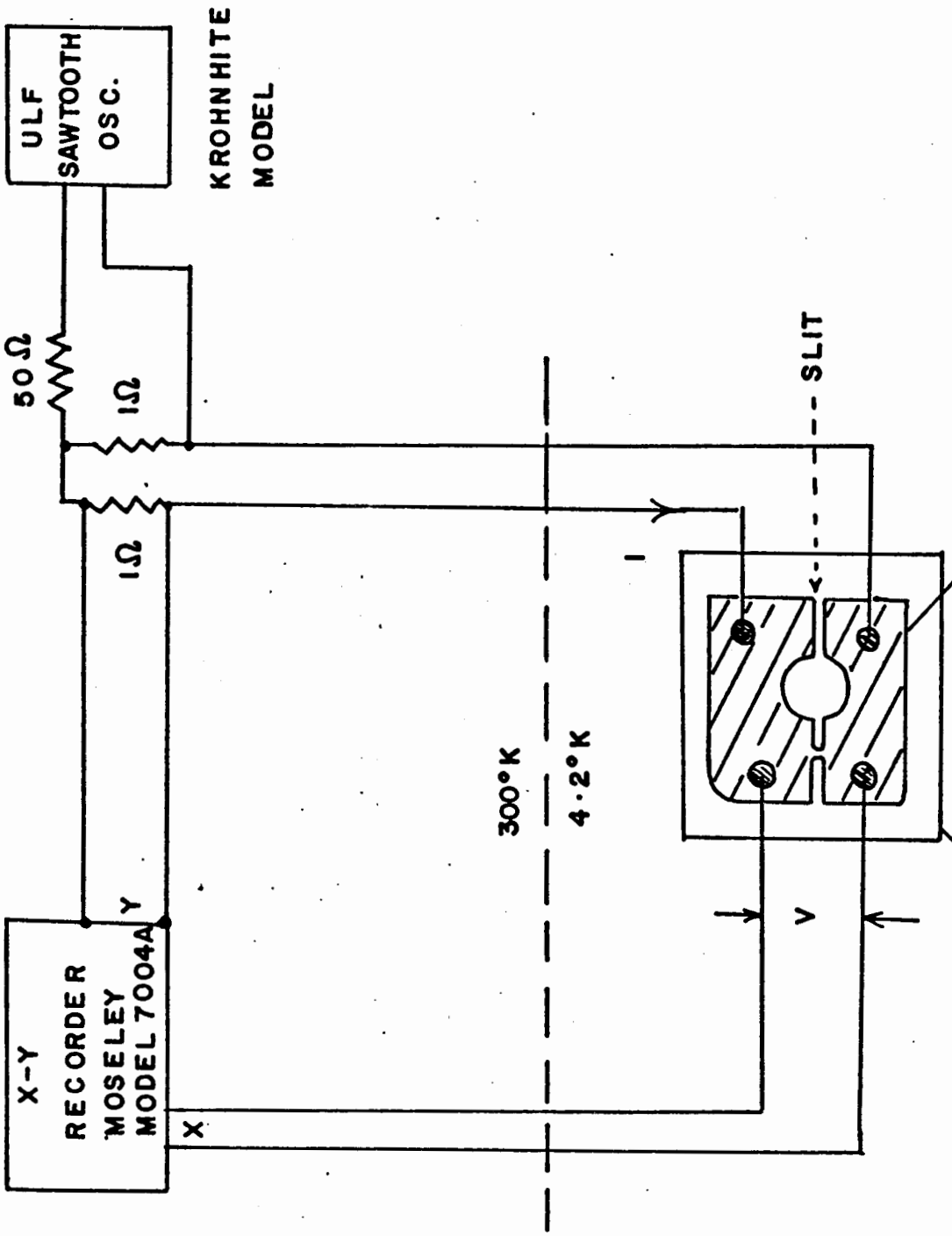

Fig. 3.19 Circuit for measuring the critical current of the weak link of an $NbSe_2$ M-SQUID.

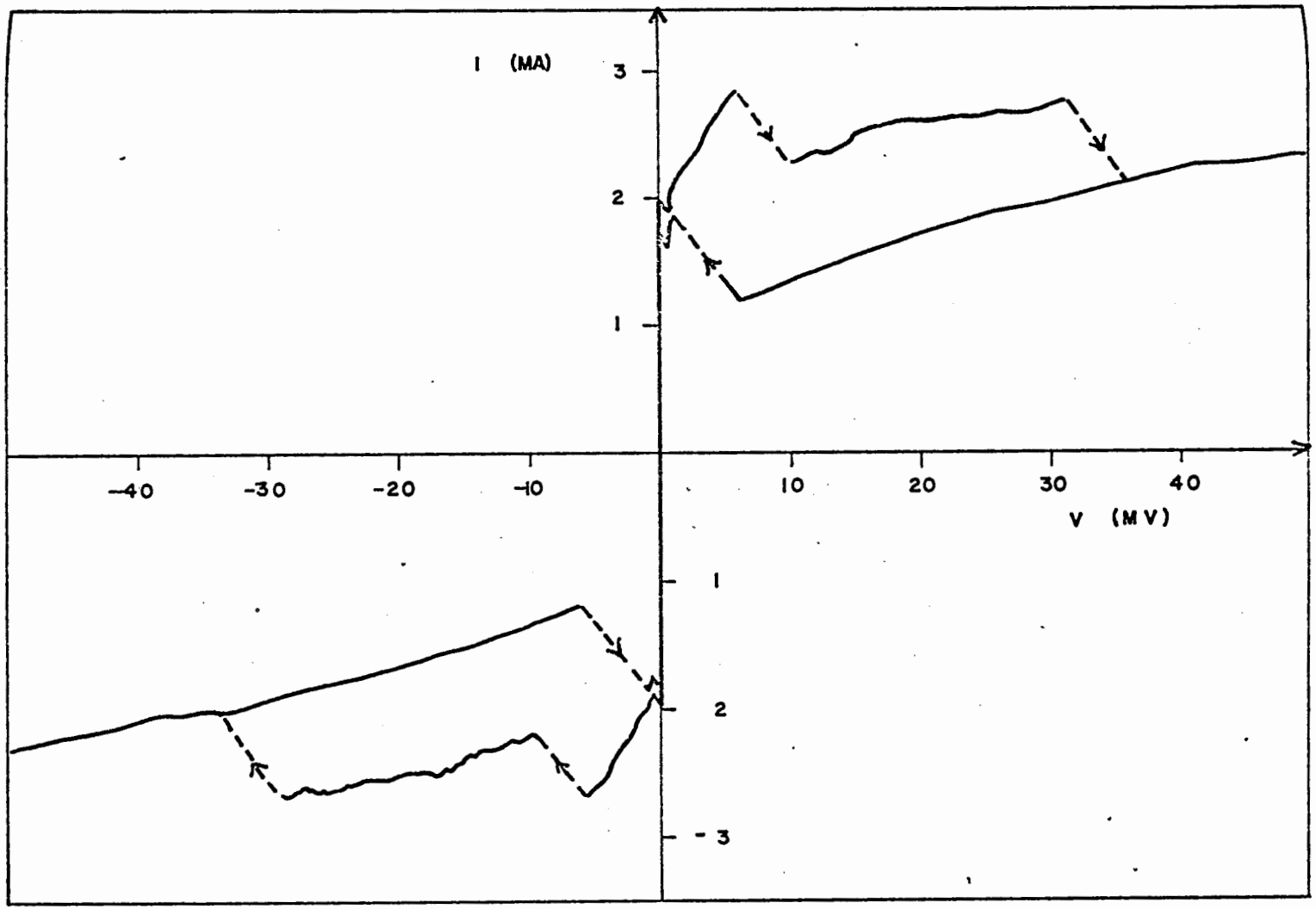

Fig. 3.20 DC I vs V plot for the weak link of a planar $NbSe_2$ M-SQUID. The arrows give the sweep directions and the dotted lines are for the discontinuous switching along the circuit load line.

The I vs V curves for lower critical current tended to be smoother although some hysteresis was usually evident near the voltage origin.

These values of critical current are high if one considers the fact that for optimum SQUID operation $i_c \sim \Phi_o/L$. The calculation of the inductance L is complicated since one does not know the distribution of current around the ring. A cylinder, area S, length l has an inductance

$$L = \mu_o \frac{S}{l} \qquad 3.501$$

if end effects are neglected. For a ring diameter 2mm length 1cm this gives $L \sim 4 \times 10^{-10}$H. Considering point contact devices one obtains a small contribution ($< 10^{-10}$H) from the conical point contact and the slit[72]. An approximate calculation of the loop inductance for a planar device consisting of a ring diameter 2mm and weak link dimensions 5μm x 5μm gives a value $L \sim 5 \times 10^{-10}$H if the current is assumed to be uniform across the link. For both planar and bulk devices one obtains an expected $i_c \sim 5\mu A$. For the planar devices the measured values ranged between 30 and 200 times the expected value. The estimates of L cannot be in error by as much as this and the only reasonable explanation of this discrepancy is that the dc measurement of i_c does not constitute the criterion for the inset of flux flow across the weak link. In fact, the motion of flux vortices can

produce a resistive transition in $NbSe_2$ layers for applied dc magnetic fields much below the critical value[153]. A similar behaviour for applied flux of amplitude much less than the critical value necessary to destroy the weak link superconductivity may account for the operation of the M-SQUID in the single flux quantum mode.

Note that one of the difficulties in making weak links of $NbSe_2$ with low critical currents is that the critical current density j_c along the crystal planes is observed to increase as the film thickness is decreased. Data from R.F. Frindt of this laboratory give a bulk j_c at 4.2°K of $\sim$ (0.5 - 1.0) x 10^5 A/cm^2 and for a 100Å thick film, j_c $\sim$ 5 x 10^5 A/cm^2.

In all, some thirty-five planar SQUIDS were constructed with varying degrees of success. Of these, about half were found to be suitable for flux measurements and the critical currents of eight of the most sensitive were measured as outlined. As regards stability, many of the unprotected devices ceased to function after about ten dips to He^4 temperatures possibly due to frozen moisture vapour disrupting the crystal layers. By coating the weak links with the epoxy Stycast 1269A the lifetime could be considerably extended. One such coated planar device is still functioning 9 months and some 70 dips after construction.

The bulk $NbSe_2$ devices were also found to be extremely

robust and stable. Prior to cooldown, dry He^4 gas was usually blown through the SQUID slot for $\sim$ 3 minutes. One difficulty which did arise with the bulk devices was the lifetime of the superconducting contacts between the weak link crystal and the bulk Niobium metal. On several occasions, particular devices ceased functioning and the loop appeared to be open circuited. However, if the weak link plus its substrate were removed and the contact area carefully cleaned or chemically etched the magnetic flux pattern often returned indicating that the pressure contacts were at fault. For the study of the bulk devices, six bulk bodies and about thirty weak links on mica substrates were made. Many of these weak links failed after repeated dips to He^4 temperatures, the main culprit probably being moisture, either at the pressure contacts or on the weak link. However, many weak links survived indefinitely and it is safe to say that a stable rugged device can be constructed using $NbSe_2$ weak links provided the weak link is protected from moisture and a better method is developed for making superconducting contacts to the crystal layers.

Some success was achieved in reducing the critical current of $NbSe_2$ weak links by anodisation[85] where the $NbSe_2$ was chemically oxidised in a weak organic acid bath. Starting with a moderately large weak link where $i_c \sim 50mA$ it was possible to reduce this to $\sim$ 300μA. The weak link was made the anode and the cathode was Carbon. The experimental

oxide growth rate was monitored by measuring the dc resistance of the weak link. After a few minutes with a cell voltage of 4 volts the dc resistance had reached $\sim 500\Omega$ at room temperature. Although this technique was a successful way of reducing i_c, the resultant structures were very fragile and were invariably destroyed after two or three dips in liquid helium. Microscopic examination of the weak link indicated a large number of fine cracks open-circuiting the link. From this evidence it was concluded that the thermal expansion of the oxide and the underlying metal were incompatible. Similar experiments on 200μm diameter NbZr wires also met with failure. This anodic technique has been used by Goodkind and Stolfa[62] on weak links of Lead, but the Lead oxides were found to be unstable at room temperature.

A final point with regard to the I vs V curves was that the normal state resistance at 4.2°K was found to be between $\sim 5\Omega$ and $\sim 150\Omega$ with most values $\sim 20\Omega$. Thus in general, the resistance was much greater than the source resistance ($\sim 1\Omega$). (This resistance is large for metallic bridges which normally have resistances $< 1\Omega$,[70] and may account in part for the appearance of single quantum transitions in a ring structure containing a $NbSe_2$ weak link. As mentioned in section 2.5, a large value of R_N (low value of G) acts as a strong damping constant and tends to limit transitions to adjacent magnetic flux states.

CHAPTER IV

WEAK LINK DETECTORS: THE R-SQUID

The more interesting of the two detectors studied in this thesis has been the R-SQUID where the frequency conversion properties of the AC Josephson effect have been exploited by using a low inductance resistive loop containing a weak link. This chapter is essentially a complete report of the construction and properties of the R-SQUID at frequencies in the mm microwave regime.

4.1 Design of the Resistive SQUID

The theory calls for a partially resistive loop of low inductance interrupted at one point by a weak link section. To obtain optimum sensitivity one has to design a structure which will readily couple the external radiation into the weak link to provide maximum interaction with the supercurrent. For frequencies in the mm wavelength regime, a cat's whisker or point contact type of junction is expected to be a more sensitive coherent detector than a thin film junction or an evaporated metallic bridge[70]. The reason for this is that for frequencies in the GHz range, tunnel junctions present a large reactive mismatch and reflect most of the incident radiation since they generally have a large junction capacitance (100 pf - 1000 pf). On the other hand,

although they have low capacitance, metallic bridges generally have large conductance and thus most of the radiation is absorbed as Joule heating. Grimes et al[86] and Zimmerman et al[44] have demonstrated that coupling into a Josephson junction is significantly improved by locating a point-contact at a low impedance position in a microwave cavity. However, in the mm microwave regime, suitable closed cavity resonators tend to be smaller than the resistive SQUID dimensions. One could of course design a system where the bulk of the R-SQUID was external to the cavity and the contact was situated at a field maximum in the cavity. An alternative scheme might be to design a resistive SQUID with the point contact at a low impedance point of an open resonator[87] whose dimensions are much larger than the incident radiation wavelength. In this way the device dimensions could be retained and also the coupling to the external field significantly improved.

For this study, a device of reasonably broad band sensitivity (10^9 - 10^{12} Hz) was required, and it was decided to avoid the use of resonators which require tuning in favour of antennae or tapers which would concentrate the radiation on the point contact. The interaction of a Josephson junction strongly coupled to a resonant cavity has been shown to be rather complex, and it was felt that this might affect the interpretation of the R-SQUID spectrum.

The basic design followed that described by Zimmerman

et al[8] with certain modifications introduced to improve the stability and sensitivity at the microwave frequencies of interest. The R-SQUID (Fig. 4.1) was machined from a composite block of material of dimensions 1cm x 0.8cm x 0.8cm. The superconducting sections were of Niobium and the resistor R an alloy of Copper and Germanium ($\sim$ 10% by weight). A good bond was formed between the alloy and Nb by rf induction melting in an Argon atmosphere at 1200°C. Early attempts to bond Copper to Niobium by electrodeposition proved to be unsuccessful despite thoroughly etching and cleaning the Nb surface prior to the deposition. Although it proved possible to Copper-plate the Nb, the Copper tended to peel off in layers after a few hours.

The R-SQUID body was prepared as follows. Alloy powder of the proper proportions was poured into a rectangular mould cut into the end of a 6cm diameter Carbon rod. A chemically etched rectangular Nb block (3cm x 1cm x 1cm) was then placed on top of the powder in this mould, providing a snug fit to prevent any liquid from escaping during the melting process. The Carbon rod was then placed in an rf induction furnace with an inert atmosphere of Argon gas, and the temperature raised to 1200°C. At this point, the alloy melted and the Nb block settled evenly in the mould. A good bond was formed between the alloy and the Nb in this way. The block was then machined approximately into two symmetrical halves, which were then

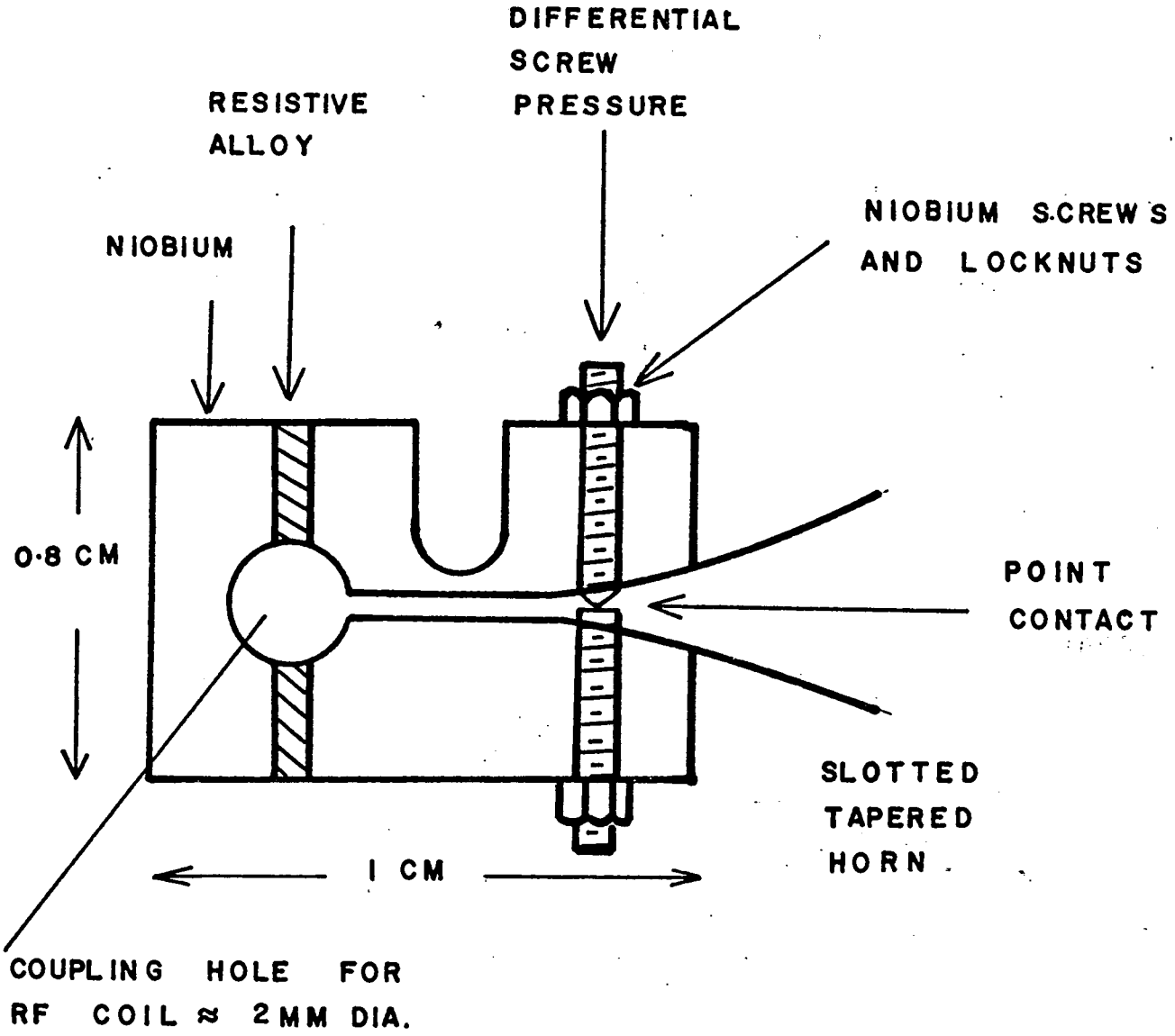

Fig. 4.1 R-SQUID section with dimensions.

soldered together along the alloy faces. The block was finally machined into the form shown in Fig. 4.1 where a hole ∿ 2mm diameter was drilled through the resistive section dividing the resistor into two parts. An 0.005" wide slit was then spark-cut, connecting the hole to one edge.

The screws forming the weak link were either 080 or 000-120 of Niobium and were locked in place at room temperature with the screw ends separated in the spark-cut slot by ∿ 50μm. The pointed screw was mechanically polished to microscopic sharpness with tip radius ∿ 1μm. Contact was then made at liquid helium temperatures, by exerting pressure on the top section by means of a differential screw assembly having an equivalent pitch of 350 threads/inch (Fig. 4.2). The reason for introducing a screw adjustment mechanism of this type rather than using a permanently adjusted contact[8] is that point contacts tend to be rather delicate, and there was some interest in investigating the response of the device to microwave power using a variety of point contact critical currents. The differential screw assembly proved to be an ideal way of adjusting the critical current and the device generally remained stable and transient-free during any particular run. For subsequent thermal cycles to helium temperatures, the contact usually had to be readjusted but it was found possible to use the same pointed screw many times before the tip was sufficiently dulled to warrant replacement.

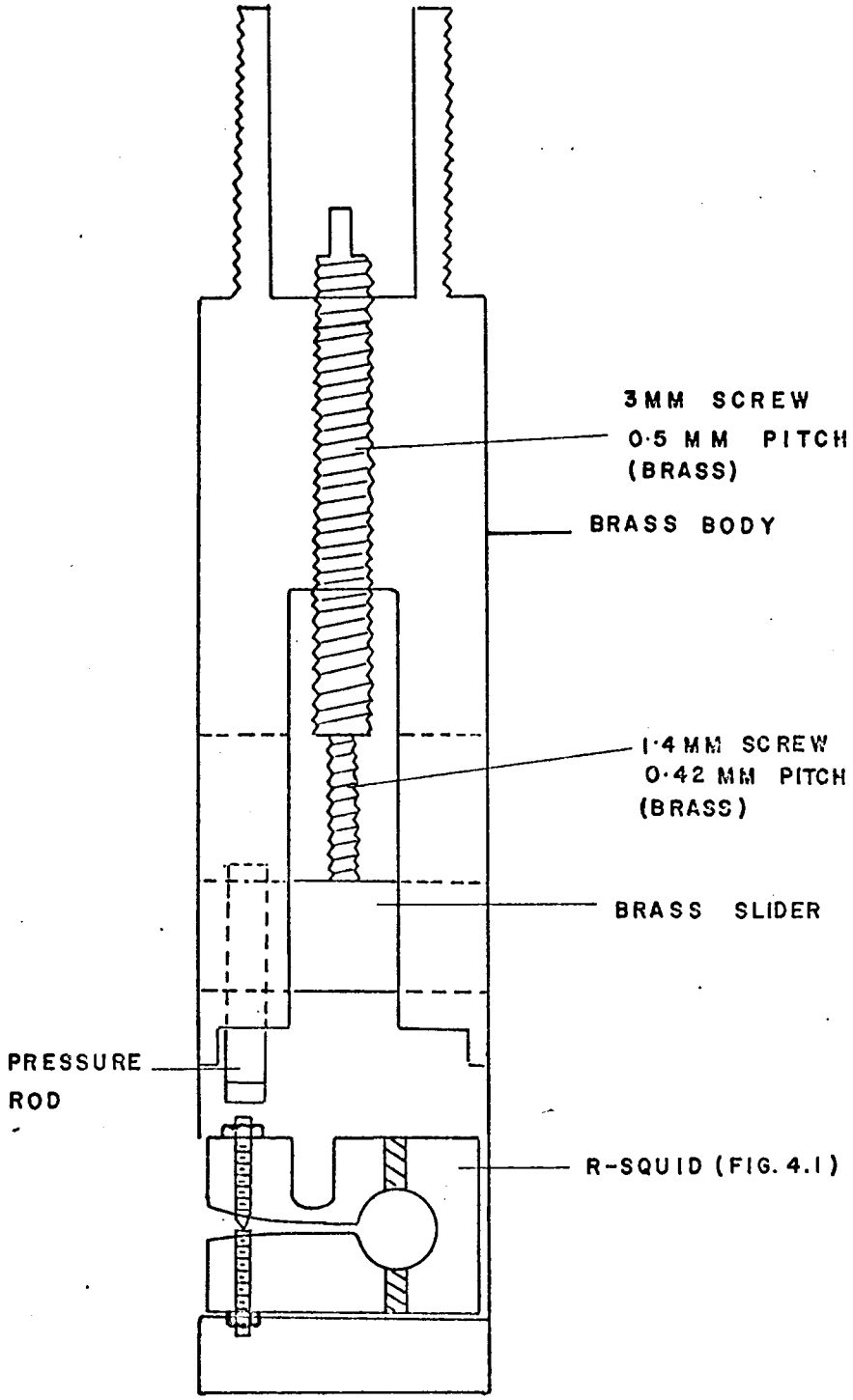

Fig. 4.2 Differential screw assembly for adjusting R-SQUID.

Preliminary attempts at making R-SQUID devices involved adjusting an 080 Nb screw in a similar resistive ring by means of a screwdriver operable from outside the cryostat. This technique however proved to be extremely crude and the contact invariably needed adjustment during any one run. It was also extremely sensitive to vibrations and even to the bubbling of Helium liquid.

The differential screw assembly is shown in Fig. 4.2 with the R-SQUID in position. This technique is similar to the one employed by Contaldo[88] and provides a means of reducing the mechanical coupling between the screw contacts and the room temperature control. A similar approach to forming spring-loaded contacts has been described by Kamper et al[69]. This differential screw assembly was designed to be used both in the main cryostat (see Fig. 6.11), and also for mounting on a 1/2" dip-stick version to provide a rapid study of the R-SQUID behaviour for a variety of point contacts.

An alternate scheme for adjusting the R-SQUID which was also developed for dip-stick tests at 4.2°K is shown in Fig. 4.3 where an 080 stainless steel screw controlled by a long rod from room temperature, exerts pressure at point B in the device and bends the section A, thus bringing the Nb screws together. This scheme proved more crude than the differential system (Fig. 4.2) but again it was possible to

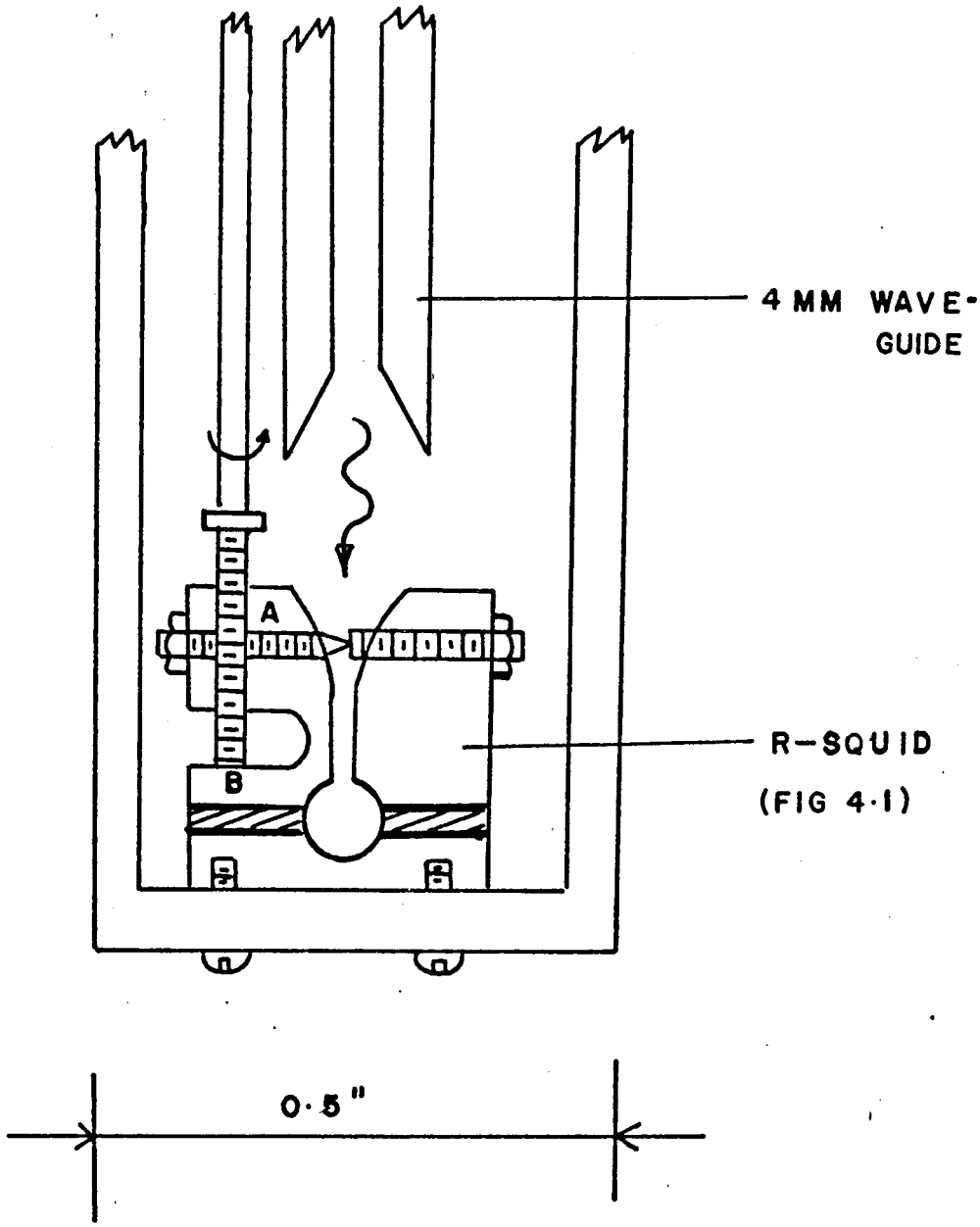

Fig. 4.3 Alternative scheme for adjusting R-SQUID on a 1/2" dip stick assembly.

obtain stable transient-free contacts which demonstrated the desired behaviour.

The resistance R of the alloy section was chosen as a compromise between two mutually inconsistent requirements. The Josephson frequency f_J is given by the voltage bias $V_o \sim IR \sim \Phi_o f_J$. Thus the dc power dissipated in R is $I^2R = \Phi_o{}^2 f_J{}^2/R$. For a given frequency of operation this varies as R^{-1}. The linewidth of the Josephson oscillation is given by $\delta f = 4.05 \times 10^7$ RT at temperature T (equation 2.413). Thus for spectral purity a low value of R is desirable and for low power dissipation a large R. A value $R \sim 40\mu\Omega$ is a reasonable compromise for frequencies up to $\sim 10^{11}$ Hz where the power dissipation is $\sim 10^{-3}$ watt and the linewidth is $\sim 10^4$ Hz for $I \sim 5A$.

The R-SQUID resistances used in the present study were in the range $20\mu\Omega$ - $160\mu\Omega$. Prior to using a device, the resistance was measured at 4.2°K using a four-probe technique, where the contacts were made to the superconducting regions containing the Nb screws (Fig. 4.1). The resistance was easily adjusted by machining away sections of the alloy until the required value was obtained.

To couple the radiation into the point contact, the latter was located roughly at the apex of a rectangular taper section formed partly by the SQUID slit and continued by means of a slotted horn fixed to the front face of the

SQUID facing the incoming radiation. A significant improvement in sensitivity was achieved using such taper sections over the cases where no taper was employed. Conical tapers were used for some devices but it was found that the gradual rectangular taper indicated in Fig. 4.1 gave better sensitivity.

In an attempt to extend the weak link lifetime, both niobium screws were hardened prior to assembly of the device. After mechanical polishing the screws were enclosed in a dry nitrogen atmosphere at 1200°C for about two days and then quenched. This technique was suggested by A. Arrott[90]. Niobium is hardened in this way by the formation of NbN and Nb_2N and also by the interstitial trapping of nitrogen atoms[91]. Both NbN, Nb_2N are superconducting with critical temperatures 14°K - 17°K[92,93]. This technique met with only partial success and it was found that the tips of both hardened and non-hardened screws tended to flow on contact by roughly equal amounts.

4.2 Initial Adjustment of the R-SQUID

As shown in section 2.4, the R- and M-SQUIDS should have identical behaviour for applied frequencies above the Johnson noise limit (equation 2.412). Thus one can use the same M-SQUID detection electronics (Figs. 3.11, 3.12, 3.13) and one should be able to observe similar quantum interference patterns

(Fig. 3.14(i)). Figure 4.4 gives the general schematic for both the initial point contact adjustment (switch position (a)) and subsequent microwave experiments (switch position (b)).

After the device had been cooled to 4.2°K, the differential screw assembly was adjusted forcing the R-SQUID jaws together until the point contact was formed. After suitably adjusting the pressure, signals as in Fig. 4.5 were obtained.

The oscilloscope patterns for the R-SQUID tended to be rather noisy and for clarity Fig. 4.5 represents the phase detected signal at the applied audio frequency (normally > 10KHz) versus the applied rf flux Φ_{rf}. The latter signal was measured by taking the dc rectified rf signal from the demodulator (Fig. 3.13). A similar plot for the M-SQUID has already been displayed (Fig. 3.14(iii)).

The preliminary detection patterns on the oscilloscope (switch position (a) Fig. 4.4) generally did not display quantum oscillations in the audio period, although on the basis of previous experiments by Zimmerman they should have been visible. Part of the problem, was circuitry, since at the af sweep rates employed (> 10KHz), the quantum oscillations tended to become washed out when using the M-SQUID. The second problem was the Johnson noise and any thermal emfs associated with the R-SQUID bias resistance. These resistances (20μΩ - 160μΩ) were larger than the values

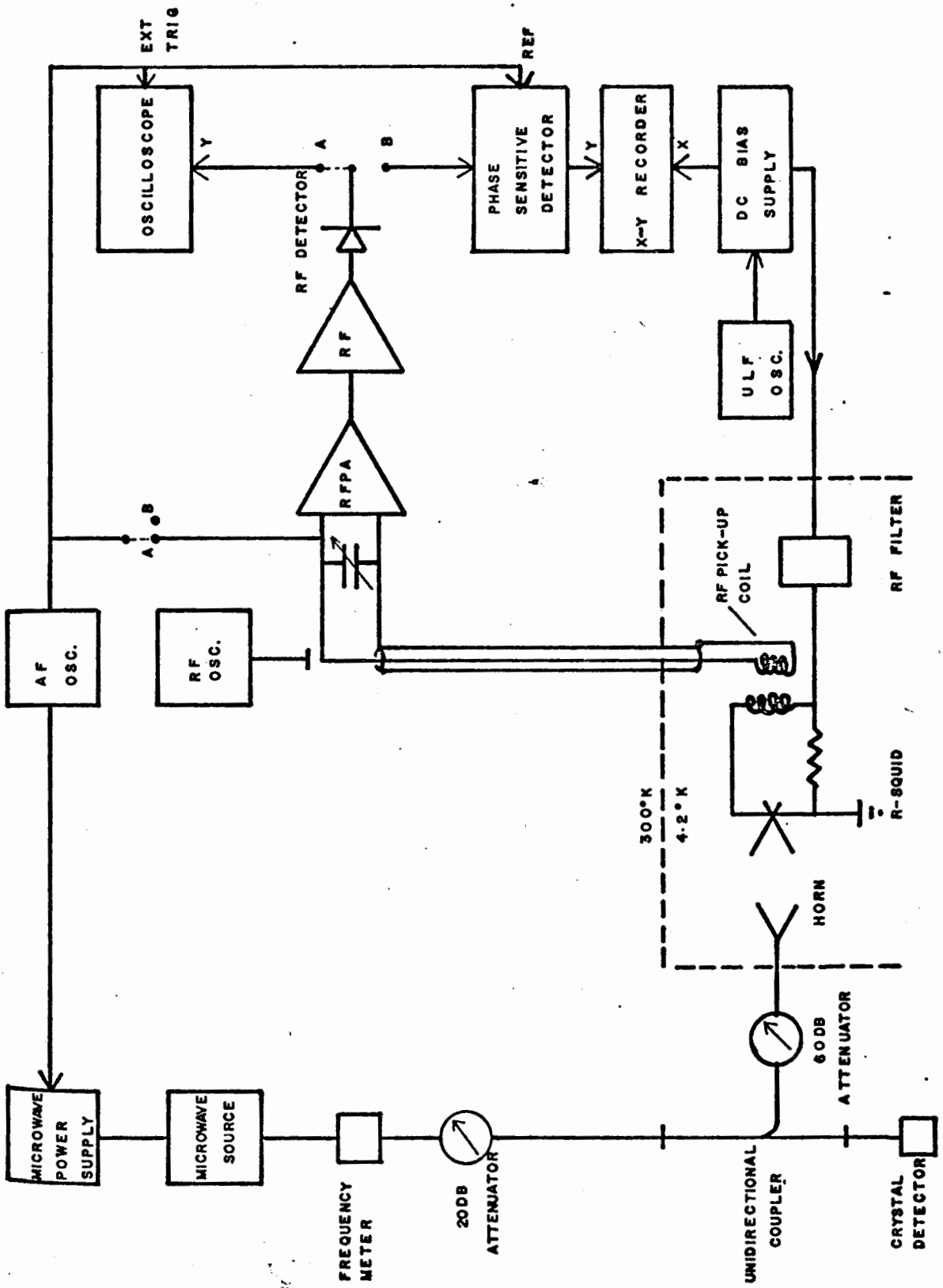

Fig. 4.4 Schematic of the electronics for the initial R-SQUID adjustment (switch position (A)) and microwave experiments (switch position(B))(Fig. 3.11). The microwave sources were: (i) Varian klystron VC705 for (67-73) Ghz (ii) Backward Wave Oscillator Model 650 for (26.5-40) Ghz.

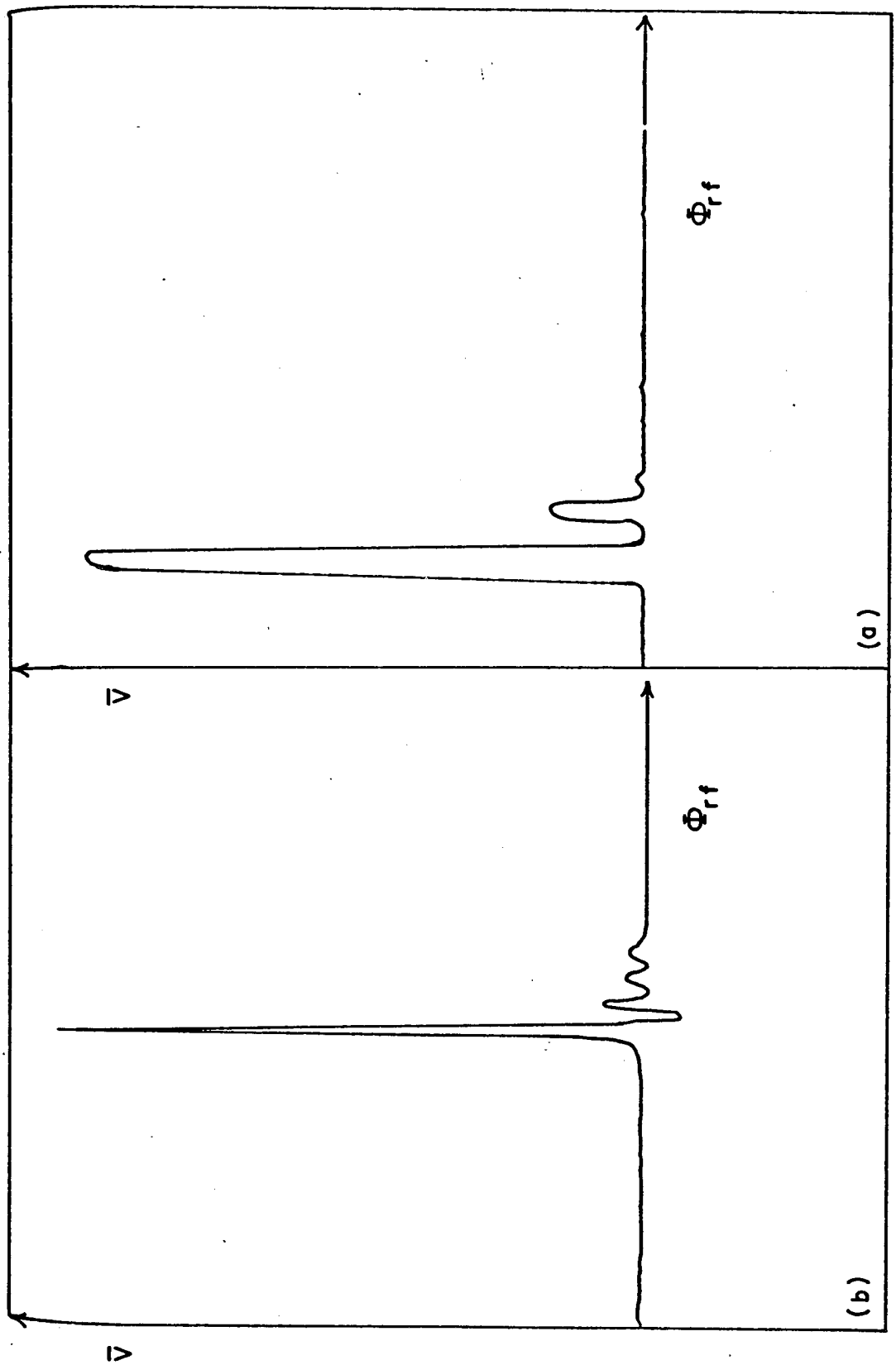

Fig. 4.5 RF detection signals for the R-SQUID. The amplitude of the audio modulation signal $\bar{V}$ (at 12 KHz) vs the amplitude of the applied rf flux Φ_{rf} (at 27 MHz) for two different adjustments of the same point contact of an R-SQUID with R = 39.3μΩ.

employed by Zimmerman and Harding[60] ($10^{-10}\Omega$ - $2\mu\Omega$) and this fact coupled with the circuitry may have caused the audio quantum oscillations to disappear.

On some occasions quantum oscillations were clearly observed in the audio period and displayed none of the fluctuations in phase observed by the authors of reference 60. In this mode the device was sensitive to dc magnetic fields although the sensitivity was a factor of several hundred below that usually observed with the purely superconducting rings. This behaviour was attributed to multiple contacts at the point contact and was usually observed with screws which had been used a number of times.

The most common feature of the detected signals was a mixing between the applied audio and rf fluxes. This mixing could generally be observed for audio frequencies much below the cut-off limit of $\sim$ 7KHz where R= 40$\mu\Omega$. In fact mixing has been observed for audio frequencies as low as $\sim$ 200Hz before the pattern became obscured by noise.

The curves in Fig. 4.5 represent this audio mixing signal at 12KHz versus the rectified rf at 27MHz appearing at the demodulator output. This response differed considerably from the equivalent M-SQUID curve (Fig. 3.14(iii)). Generally the first oscillation was very large relative to subsequent oscillations which tended to be few in number. Contact (a) was the first light contact at which an audio signal could

be detected. The curve for contact (b) was taken after increasing the point contact pressure and hence the weak link critical current. Often only a single large peak in the output could be observed especially with contacts which had been used many times.

The foregoing behaviour could be only qualitatively explained on the basis of the theory in Chapter II. From curves such as Fig. 4.5 it was estimated that the device was generally operated with $i_c >> \Phi_o/L$. Referring to Fig. 2.5 for the case where multiple quantum transitions are possible, transition A → B can be much larger than successive transitions C → D. Thus one can obtain a correspondingly larger output emf for the first transition.

One of the reasons that $i_c >> \Phi_o/L$ operation was more usual, was probably due to the fact that the inductance L of the structure in Fig. 4.1 was somewhat larger than that estimated for the M-SQUIDS. The point contact for the R-SQUID was further from the pick-up loop and there was an increased contribution to L from the slit.

It must be stressed at this point that the non-ideal behaviour for $i_c >> \Phi_o/L$ does not limit the usefulness of the device as a frequency converter. Rather, as the next section will show, this behaviour may be exploited to yield better signal-to-noise from the system. Using point contacts, mixing effects associated with the AC Josephson effect have always been observed over a wide range of values of i_c,

although for large values, care had to be exercised when interpreting the spectra.

4.3 Microwave Circuits

Thus far the devices have been tested in two microwave frequency regimes (67-73) GHz and (26.5 - 40) GHz. In all, four devices were constructed whose resistances varied between 20μΩ - 160μΩ and which used a variety of tapers and horns to optimise the coupling to the external radiation. All the devices used point-contact screws and the most sensitive radiation coupling scheme was found to be the shallow taper system indicated in Fig. 4.1.

The microwave circuit employed in the measurements is outlined in Fig. 4.4. The (67-73) GHz source was an oil cooled 4mm klystron (Varian VC705) whereas a Backward Wave Oscillator (Alfred Sweep Oscillator Model 650) with a (26.5 - 40) GHz plug-in was used for the other frequency regime. The repeller voltage of the 4mm klystron was externally modulated at audio frequencies in the range 30Hz - 10KHz. The modulation sensitivity of the VC705 in the particular mode used (n = 6 3/4) was 4MHz/volt and from the manufacturer's tables the modulation was estimated to generate a line of width $\sim$ 20MHz. The microwave power was fed through a frequency meter, a variable 20 db attenuator into an unidirectional coupler. The direct power was monitored in a crystal detector while the power in the isolated arm of

the coupler was fed through a 50 db calibrated attenuator to the cryostat where it was directed towards the SQUID slit by means of a rectangular horn. The output horn SQUID distance was about 1 cm.

The schematic for the Backward Wave Oscillator tests at (26.5 - 40) GHz was similar, although for this case, the directional coupler and crystal detector were specially designed for broad band application. There was also the facility of levelling the output power by a feedback control using signals from the crystal detector. External square wave audio modulation was used with this source.

Intermediate frequency signals at $\sim$ 30MHz were amplified and demodulated as before (section 4.2) and the demodulator output was then fed to a phase sensitive detector (Princeton Applied Research Model HR-8) externally referenced at the source modulation frequency. The PAR output was then fed to the Y-axis of the recorder. The X-axis gave a measure of the dc current I used to voltage bias the point contact. This current was supplied by two 12-volt batteries whose output was controlled by the transistorized dc amplifier shown in Fig. 4.6. This power supply underwent several stages of evolution before reaching the system of Fig. 4.6 where the operational amplifier A stabilised the voltage at B to better than 1 in 10^4. At 5A output current into the R-SQUID the current did not drift by more than $\sim$ 0.25mA per minute.

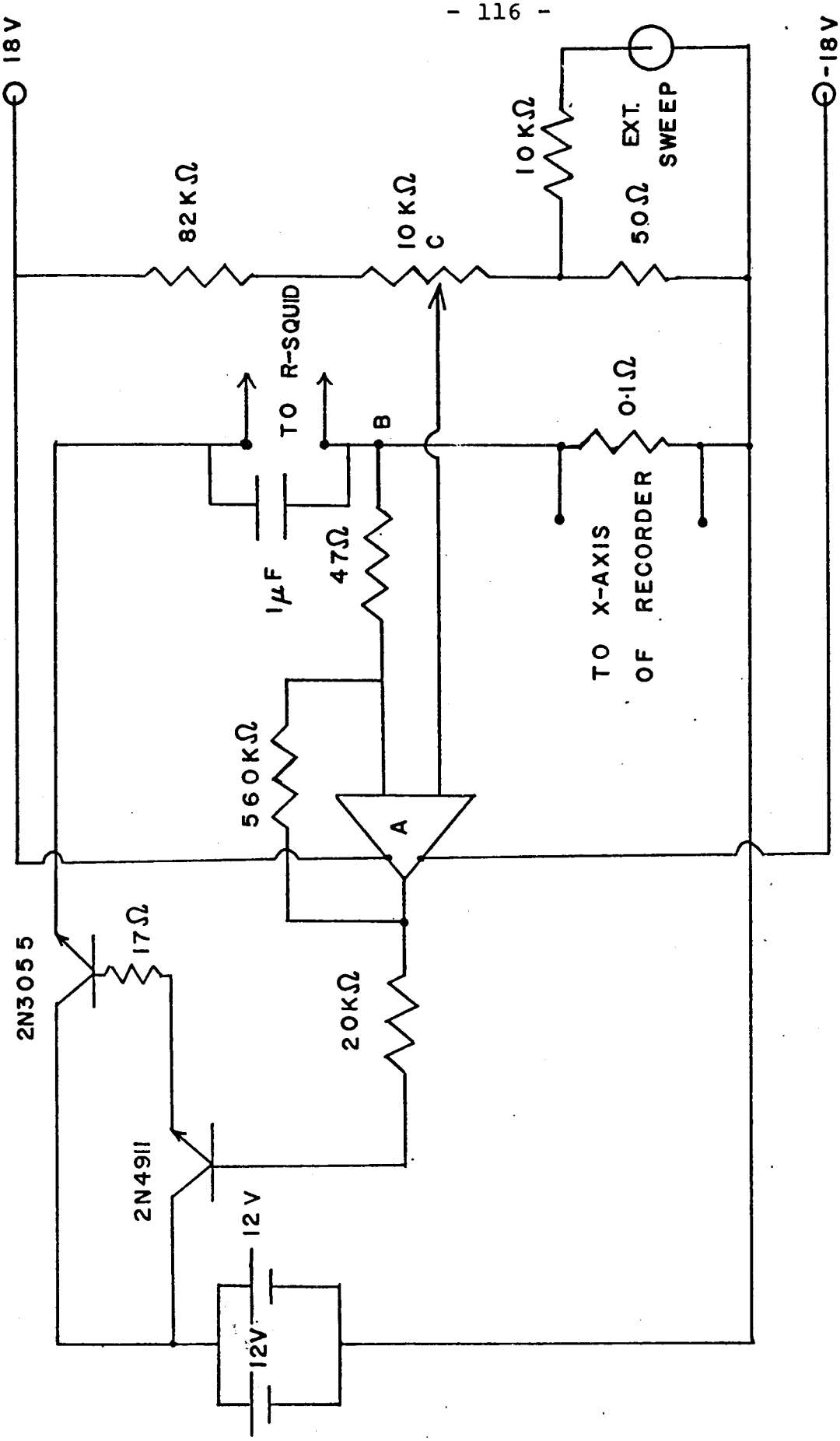

Fig. 4.6 Battery operated voltage stabilised current supply (0 → 10) amps. A is a Fairchild operational amplifier UA 741 C.

Attempts at improving the stability by increasing the open loop gain with two amplifiers in series, caused the output current to oscillate. The output current could be swept either mechanically using a motor driven potentiometer C or electronically with an ultra-low frequency ramp voltage from a Krohnhite Generator Model 5100. The supply could be safely operated up to 10A output. (The power transistors were mounted on large heat sinks cooled by an air fan.) For a 40μΩ R-SQUID the minimum Josephson frequency sweep rate was ∿ 250 KHz/sec. This circuit was designed by Mr. P.M. Garnett.

To reduce the noise reaching the R-SQUID via the dc bias leads, twin chokes of inductance ∿ 3mH were inserted into the low temperature current leads. These chokes were completely enclosed in superconducting lead foil for shielding purposes. (At 30MHz they have an impedance ∿ 400KΩ.) To shield the R-SQUID from spurious external signals the low temperature end of the cryostat was completely enclosed in a bucket-shaped superconducting shield of Lead foil (see Fig. 5.10).

From a foreknowledge of the microwave source frequency and the SQUID resistance R, it was possible to compute the exact dc current value at which to expect the microwave fundamental. The SQUID was biased at this value of current and then the microwave power level was adjusted until a line was observed.

A typical spectrum taken with one of the present detectors is shown in Fig. 4.7, which indicates klystron frequencies at 68 GHz, 69.4 GHz and 72.2 GHz superposed on the same graph. Using the Josephson relation $I = \Phi_o \omega_J / 2\pi R$ dc biases computed for the microwave frequencies were found to agree within the limits of error of those observed. A feature which is immediately apparent from the spectra of Fig. 4.7 is that a single line only appears at the fundamental, f_1. According to equation 2.409 one should expect at least two strong lines separated by twice the intermediate frequency; i.e., $\sim$ 60 MHz. This has been observed in mixing experiments with the resistive SQUID at f_1 = 120 MHz but to date, a single line only has been observed associated with the fundamental. Of course, there was not a sufficiently accurate knowledge of either the klystron frequency or the SQUID resistance to determine precisely the current bias at which the line(s) should appear.

The data from the detection of low level ($\sim 10^{-10}$ watt) microwave power from the Backward Wave Oscillator are presented in Fig. 4.8. Spectra were taken at $\sim$ 1 GHz intervals in the range (26.5 - 40)GHz using a microwave track similar to that in Fig. 4.4. There was a problem with standing waves in the microwave track - R-SQUID system and for some positions of the R-SQUID the signal output oscillated rapidly. However, it was possible to position the R-SQUID to obtain a reasonably uniform output over the entire tuning range of the oscillator.

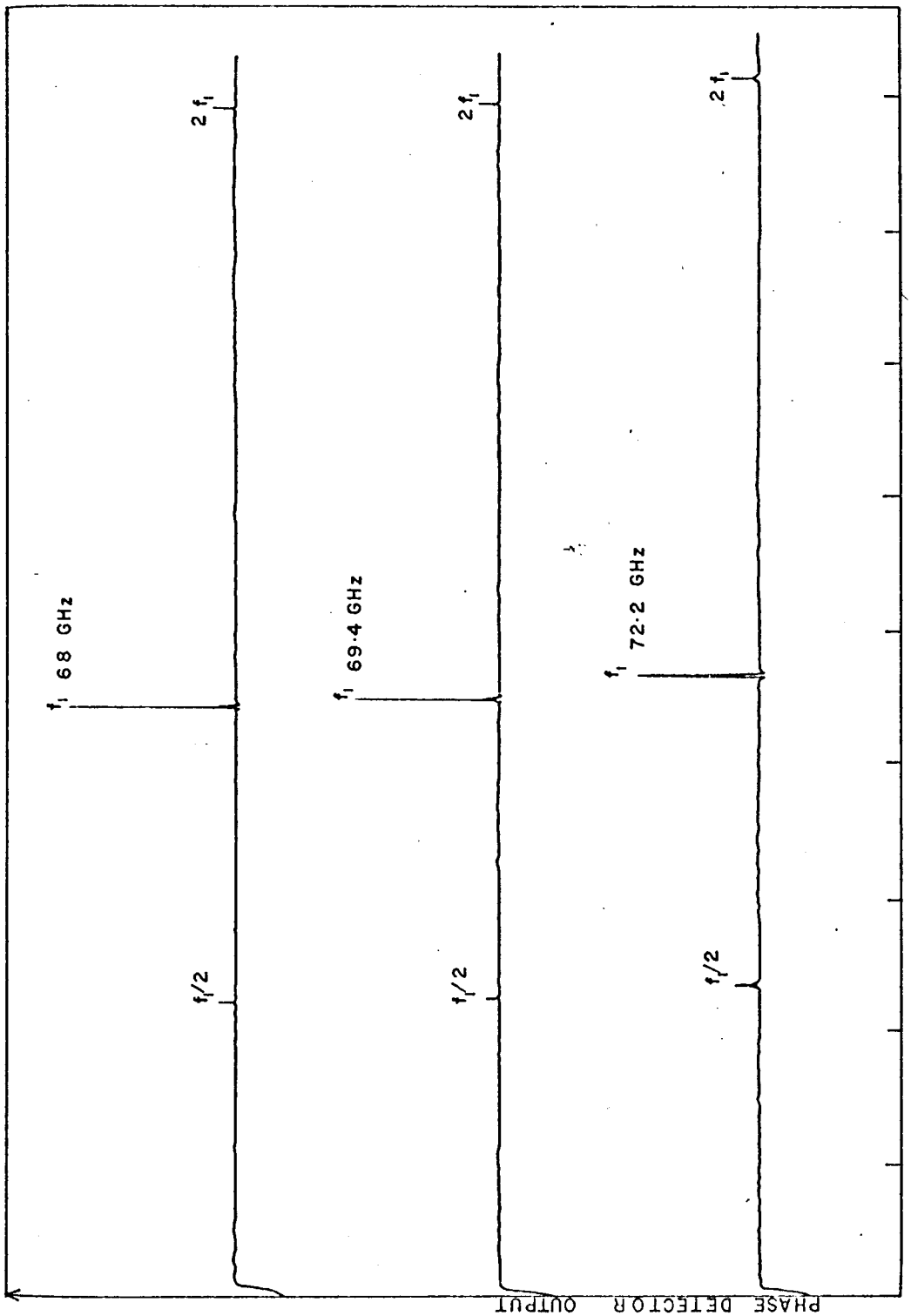

Fig. 4.7 Typical microwave spectrum detected by an R-SQUID (R_n = 160.1μΩ) in the range (68 - 72) Ghz for incident power ~ 10^{-10} watt.

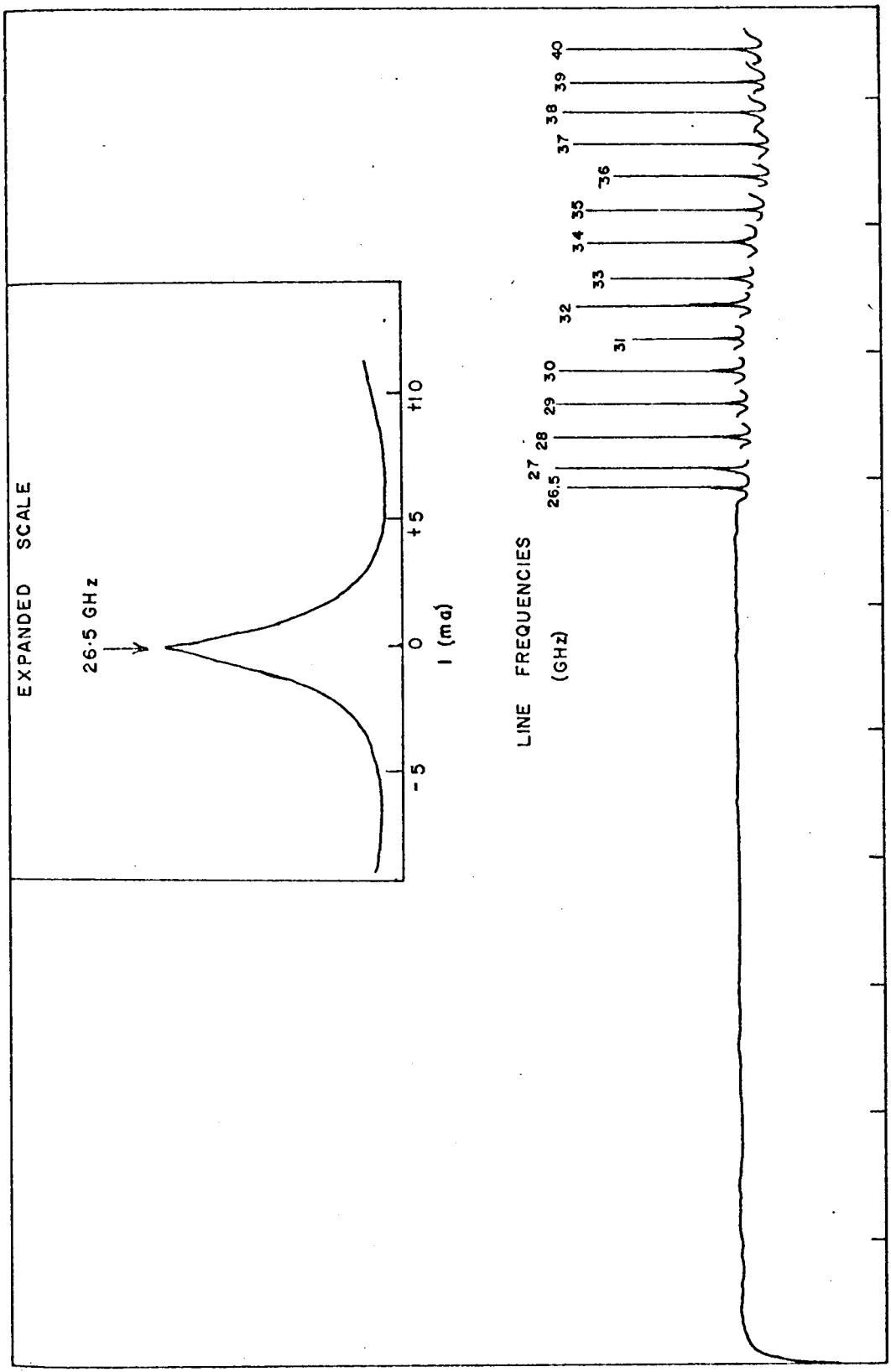

Fig. 4.8 Typical microwave spectrum detected by an R-SQUID (R = 39.3μΩ) in the range (26.5 - 40) GHz. Spectra were taken at 1 GHz intervals using power from the backward wave oscillator. Insert is shown an expansion of the line at 26.5 GHz.

The sensitivity achieved was similar to the 70 GHz experiments although the linewidth was somewhat broader.

For many of the R-SQUID critical current adjustments it was found advantageous to apply an rf bias current of suitable amplitude. This was particularly true for large critical currents when multiple quantum transitions were present. An increase in sensitivity of several hundred could be achieved from the detection electronics using this method which will be discussed in greater detail in the next section (4.4). For example, the data of Figs. 4.7, 4.8, were taken using this rf bias technique. The features of particular interest studied in the spectra besides this amplification effect were:

§ 4.5 : Response as a function of critical current

§ 4.6 : Sensitivity to microwave power

§ 4.7 : Harmonic content

§ 4.8 : Measurement of linewidths

§ 4.9 : Spurious lines

4.4 RF Bias-Amplification and Lineshape

Initial studies with the resistive SQUID at 70 GHz were rather disappointing as it was found that the mixing signals appearing at the demodulator o/p were extremely small ($\sim$ 50μV), despite amplification of the initial R-SQUID emf by $\sim$ 60db. The rf bias technique has, however, produced signals as large as 20mV - 50mV with the same incident

radiation power levels as before.

The features of the amplification effect are as follows: in Fig. 4.9 are shown plots of the line shape at 70 GHz both with (b), and without (a), rf bias current. The amplitude of a suitable rf bias current is approximately two to five times less than that required to give the first rf quantum oscillation in Fig. 4.5. The lineshape itself is rather curious, consisting of broad wings punctuated at the peak by a sharp spike of opposite phase. The lineshape appeared to be a characteristic feature for all the detectors constructed and for both frequency regimes studied. The line thus appeared to have two components and surprisingly, either one could be amplified by selecting the rf bias frequency. With the present system of electronics, the rf bias frequency for amplifying the spike appeared to be $\sim$ 0.4 MHz higher than the frequency for the broad line. The widths of the resultant amplified lines differed by as much as a factor of ten to twenty. The effect of rf bias on linewidth will be discussed in more detail in section 4.8.

For zero rf bias one obtained the line shown in Fig. 4.9a. As the bias current was increased, the amplitude increased rather slowly for low rf biases and then approximately linearly up to a maximum where a saturation effect appeared to set in (Fig. 4.10). Further rf bias current caused the amplitude to decrease. A further feature of interest was that the peak of the line position did <u>not</u> shift by a detectable

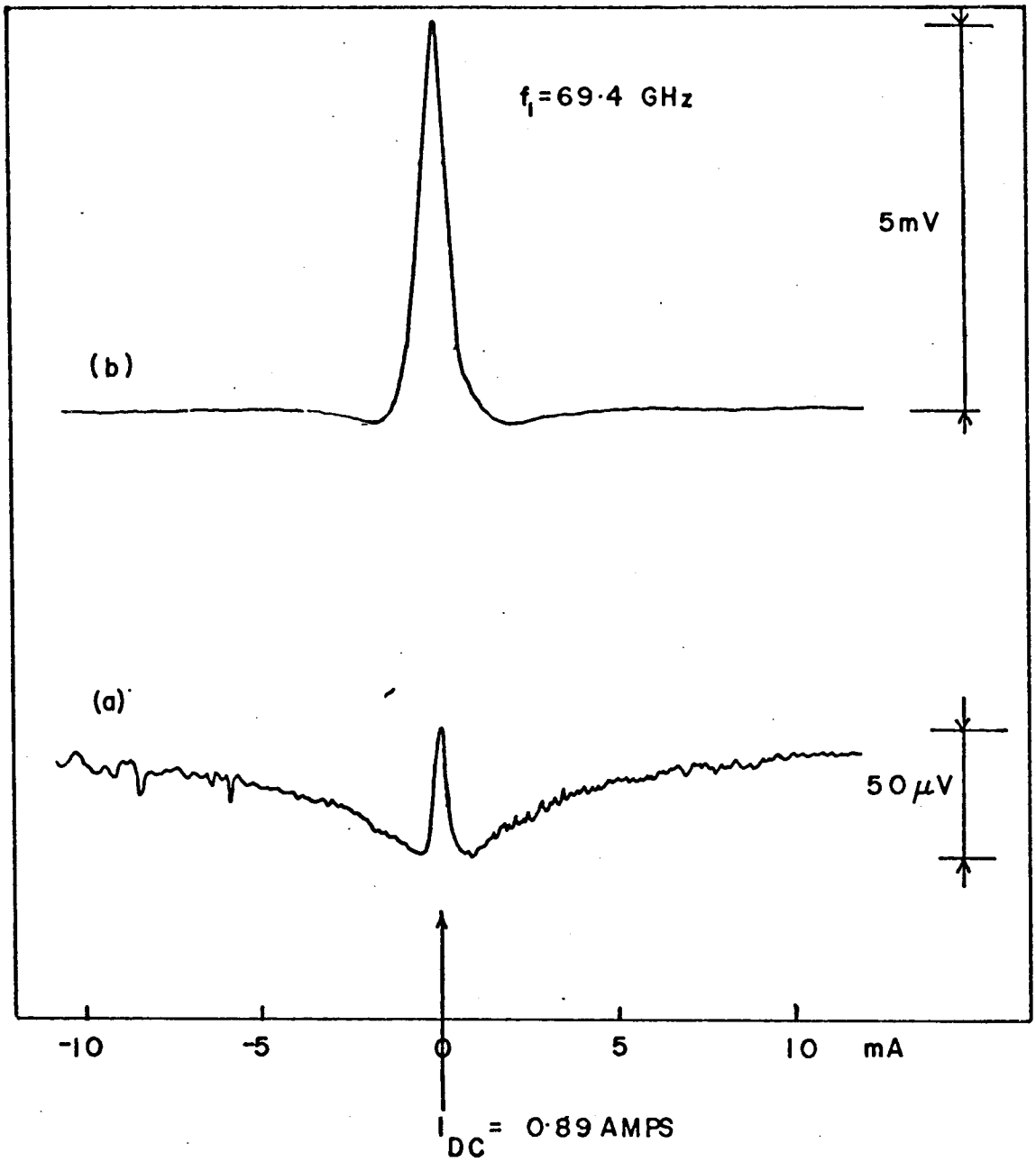

Fig. 4.9 The effects of rf bias on detected signal amplitude. Unbiased (a) and biased (b) line shapes for f_1 = 69.4 GHz, R_{SQUID} = 160.1μΩ. Identical line shapes were obtained for all R-SQUIDS constructed.

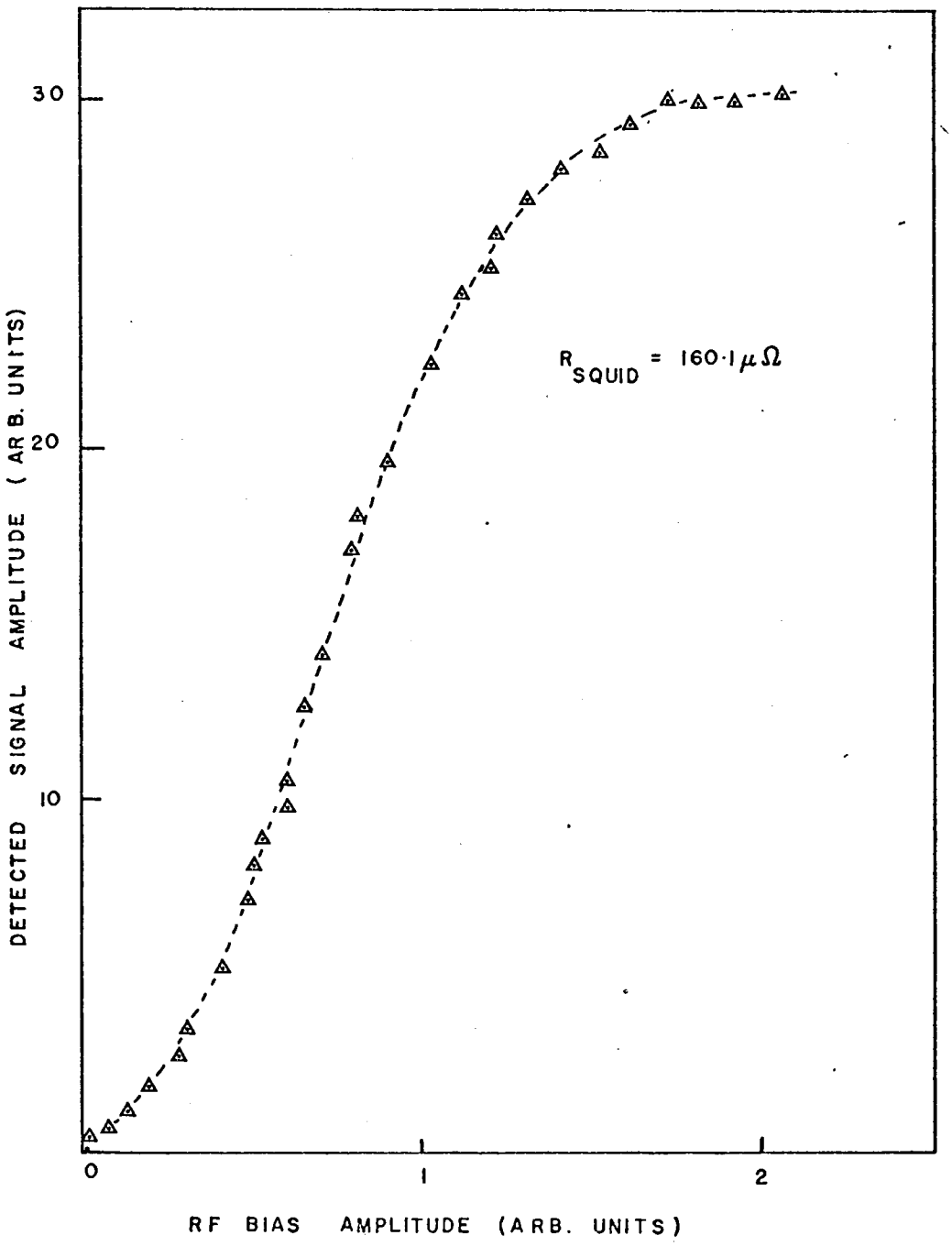

Fig. 4.10 The detected line amplitude at f_1 = 70 GHz vs applied rf bias amplitude.

amount when the rf bias was applied. The only effect of the rf bias was to broaden the line about the central position. Also no detectable change in the amplification factor could be determined for klystron modulation frequencies in the range 30 Hz - 15 KHz.

Some explanations of these effects are as follows. If the weak link critical current $i_c >> \Phi_o/L$, then the magnetic response curve appears as in Fig. 2.5, and multiple-quantum transitions A → B take place as well as the regular single quantum transitions C → D etc. As pointed out in Section 2.4, the effect of the bias voltage V_o is to cause the Φ vs Φ_x response to slide along the line $\Phi = \Phi_x$ at the rate $\omega_J = 2\pi V_o/\Phi_o$. However it is well known that for large critical current point contacts, only part of the dc supercurrent displays Josephson effects. The major part of this current may be due to direct metallic contact. Thus application of a dc bias voltage will have no effect on the position of most of this initial vertical step, and it will remain <u>stationary</u> on the Φ vs Φ_x curve. If an external signal $\Phi_x(\omega_1) << L\, i_c$ is now applied, then a very small mixing signal between ω_1 and ω_J is possible depending on the magnitude of the voltage $v_1(\omega_1)$ induced across the contact (equation 2.407). Application of a suitable rf bias flux is now seen to shift the signal $\Phi_x(\omega_1)$ through the A → B step at least twice per rf cycle and thus greatly enhance the mixing between ω_1 and ω_J. This technique can be viewed as the rf equivalent of the dc biassing scheme of Grimes et al[56]. Thus what appears to be a device defect (multiple quantum transition may

be exploited to improve signal-to-noise.

The above theory is only tentative since it gives no explanation of the lineshape, or the magnitude of the amplification effect. The tuning of the applied rf is expected to be rather critical since one is dealing with a circuit at resonance. An increase in the linewidth may be expected from the fact that the Josephson oscillation will be frequency modulated to form sidebands at frequencies $\omega_J \pm m\omega_{rf}$ where $\omega_{rf} \sim 30$ MHz. If the system resolution is worse than 30 MHz or if external noise is present, (e.g. from the rf bias oscillator,) then these extra sidebands will appear as an addition to the linewidth since the noise will smear the sidebands together.

The use of Josephson junctions for parametric amplification is well documented[65,68,89,94,95]. The scheme of Kamper et al[68] involved parametric up-conversion of low frequency noise ($\omega_1 \lesssim$ 1KHz) to $\omega_2 \sim 30$ MHz where the Josephson oscillation acts as the pump frequency and the output (idler) frequency is at the resonance of the coupling tank circuit. The ideal power gain of such a system is $(\omega_2/\omega_1) \sim 3 \times 10^4$. In the analogue simulation of a Josephson junction coupled to a cavity, Werthamer and Shapiro[89] indicate frequencies generated by parametric interaction of the applied rf, the resonant cavity and the Josephson ac current. Cases where the Josephson ac current, and the applied rf act as pump and input and the reverse where they act as input and pump respectively, were recorded. The analysis of Russer[95] describes amplifiers where the Josephson ac current acts as the pump frequency source.

For the present case, it is difficult to see where the ideas of parametric amplification apply. Using equation 2.407 with the application of two signals:

(i) the klystron voltage $v_k \cos \omega_k t$ and

(ii) the 30 MHz rf voltage $v_{rf} \cos \omega_{rf} t$

one obtains:

$$\frac{i}{i_c} = \sum_m \sum_n J_m\left(\frac{2\pi v_k}{\Phi_o \omega_k}\right) J_n\left(\frac{2\pi v_{rf}}{\Phi_o \omega_{rf}}\right) \sin\left(\omega_J t + (m\omega_k + n\omega_{rf})t\right) \qquad 4.401$$

Thus the effect of the rf bias is to produce 30 MHz sidebands of the Josephson oscillation ω_J. The amplitude v_{rf} is incorporated into the Bessel function $J_n(v_{rf}/\omega_{rf})$. With the experiments in the rf biased condition, one is measuring Fourier terms with amplitudes such as $J_{-1}(v_k/\omega_k) \cdot J_0(v_{rf}/\omega_{rf})$ or $J_{-1}(v_k/\omega_k) \cdot J_2(v_{rf}/\omega_{rf})$ etc., where $\omega_J - \omega_k = \pm 30$ MHz. Thus for all $v_{rf} > 0$, one obtains an amplitude <u>less</u> than the case without rf bias.

4.5 Response as a Function of Critical Current

As part of a general study of the device the response to microwave radiation was investigated as the point contact pressure was gradually increased after making a tiny contact where the critical current $i_c << \Phi_o/L$. As mentioned earlier there was some estimate of the critical current range since the electronics and pick-up coils were identical to the M-SQUID system. Thus the statements $i_c < \Phi_o/L$, $i_c \sim \Phi_o/L$, $i_c >> \Phi_o/L$ are generally made with reference to the purely superconducting counterpart.

For the first tiny contact no signal was observed in the non-rf biased condition, but when the rf bias was applied a spectrum as in Fig. 4.11 was obtained. The peak of the enormously broad signal occurred at the expected position for 70GHz signals, and the wings extended on either side $\pm \sim$ 20GHz. This behaviour was observed for several very tiny contacts and seemed to be a characteristic phenomenon. As the microwave power was increased the response oscillated approximately in a Bessel function manner $J_1 (v_1/\omega_1)$. At present there is no explanation for this curious behaviour.

As the value of i_c was gradually increased one could observe on the oscilloscope the beginnings of an rf interference pattern which became more distinct with increasing i_c. A small-amplitude narrow line was obtained at 70GHz with this adjustment. The pressure was then increased to give the largest signals, resulting in spectra as in Fig. 4.7. As the contact pressure was increased still further, the signals became smaller until for very large critical current neither oscilloscope pattern nor signals at 70GHz could be detected.

4.6 Sensitivity to Microwave Power

To obtain the optimum sensitivity and narrowest linewidth it is absolutely crucial to have a stable current bias supply. With regard to this point it is worth noting that a current fluctuation of 1mA where R=40μΩ represents a

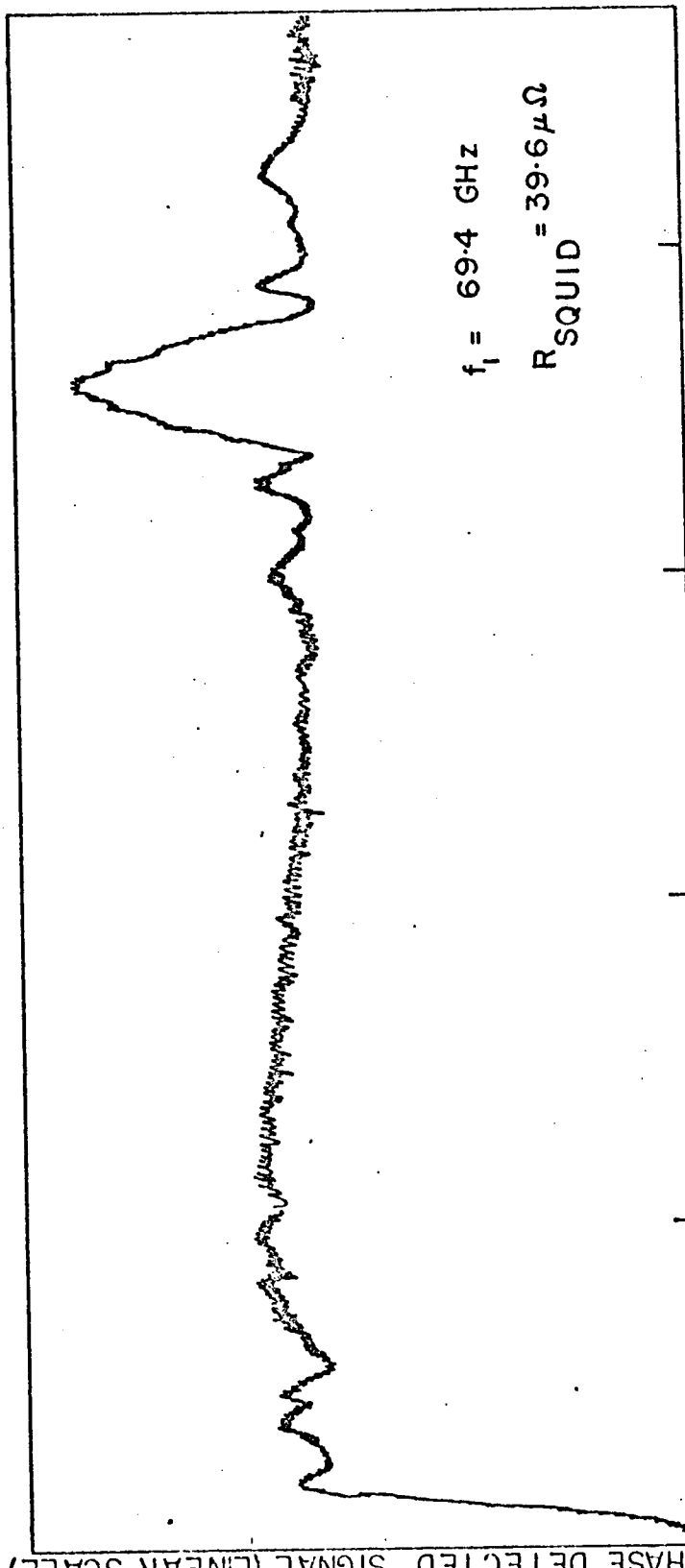

Fig. 4.11 The spectral output for a tiny contact $i_c << \Phi_0/L$ for incident power at 70 GHz.

Josephson frequency fluctuation of $\sim$ 20MHz. Similarly a voltage fluctuation of 10^{-9}V is equivalent to a frequency uncertainty of 0.48MHz.

A rough estimate of the sensitivity of the R-SQUID to external microwave power at $\sim$ 70GHz was measured using a calibrated vane attenuator. The latter was calibrated in a separate experiment using a Carbon bolometer of sensitivity at least 10^{-10} watts of the type described by Boyle and Rogers[96]. The calibration was rechecked at a later date using a Silicon bolometer(*) similar to those described by Bachmann et al[97]. (For bolometer details see section 5.3.) The bolometer, which had approximately the same sensing aperture as the R-SQUID, was placed at the R-SQUID position and was heated by various levels of microwave power controlled by the 50 db attenuator. The change in the bolometer ac resistance (33 hz) was then duplicated by Joule heating the bolometer by means of an external dc current. By this technique it was possible to measure the absorbed power in the bolometer and from a knowledge of the transmittance and reflectance one could arrive at a crude estimate of the total power reaching the R-SQUID for a given attenuator setting.

The sensitivity appeared to depend on the critical current employed for the weak link. One of the most convenient ways of optimising the sensitivity was to voltage bias the

---

* See page 173

R-SQUID at the microwave fundamental and then to carefully adjust the point contact pressure until the maximum signal was obtained. Care had to be exercised while making this adjustment since the detector output tended to be an oscillating function of the applied rf power. This technique worked well when low levels of power were used, e.g. $\sim 10^{-11} - 10^{-12}$ watts. While using the rf bias technique optimum sensitivity generally occurred for critical currents $> \Phi_o/L$. There was a range of contact critical currents which yielded good signal-to-noise over a wide range of power. From the above measurements it was estimated that the R-SQUID was sensitive in the range $\sim 10^{-5}$ to $\sim 10^{-12}$ watt. Similar sensitivities were obtained for measurements in the (26.5 - 40) GHz regime. At the high power end some form of saturation effect set in and the signal vanished, and at the low power end the signal amplitude decreased monotonically until it was masked by noise. It was discovered that a large part of the noise was produced by the rf bias oscillator and presumably the sensitivity could be improved by using a battery operated rf bias. The sensitive power range appeared to depend on the weak link critical current. For low critical currents the device tended to saturate with less power incident than for high critical currents although the minimum detectable powers were about the same for the two values of i_c. In some cases an oscillating behaviour with power was observed for the PAR o/p signal; in other cases the oscillations were absent. An examination of the demodulator o/p as a function

of the crystal detector signal indicated an extremely complex behaviour (Fig. 4.12). Trace 12a represents the 70GHz signal from the diode-detector and trace 12b is the output from the demodulator over one cycle of the klystron output. The oscillations in the R-SQUID o/p as a function of incident signal level tended to be rather irregular and changed drastically as a function of the incident power level. For low power levels only one or two oscillations were evident, for intermediate power levels the oscillation number increased and for high power levels the signal at the centre of the klystron pulse had dropped to zero leaving a double spiked output for each pulse(12ii(b)). The PAR in fact averages over the oscillations in each pulse since it is phase-locked at the modulation frequency and thus an interpretation of the PAR output signal is rather meaningless given these irregularities.

The only other reported measurement of sensitivity was conducted by Zimmerman[59] at a frequency of 110MHz where he indicated a NEP of $\sim 10^{-16}$ watts, although a minimum detectable power of $\sim 10^{-20}$ watts was expected. More recently, intrinsic noise measurements of purely superconducting rings conducted by Wheatley[98] have indicated that some loss mechanism is operating which may account for this discrepancy.

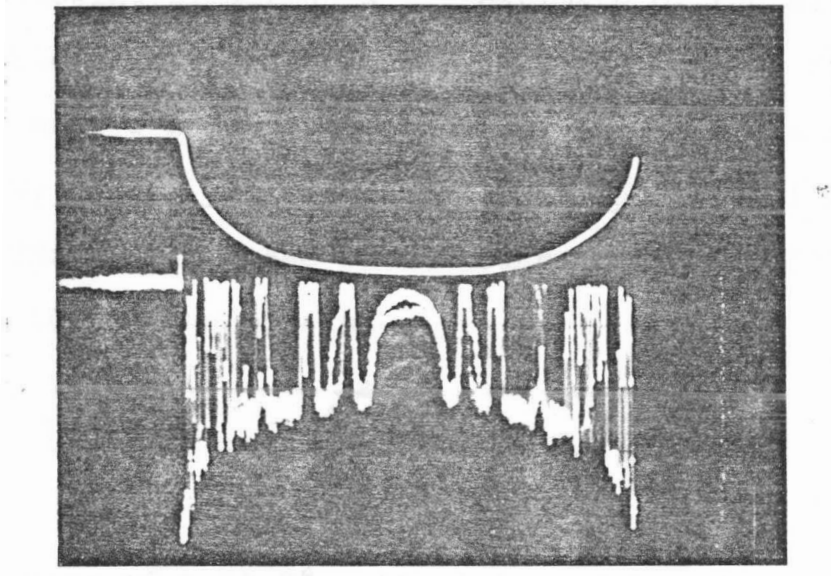

(i)

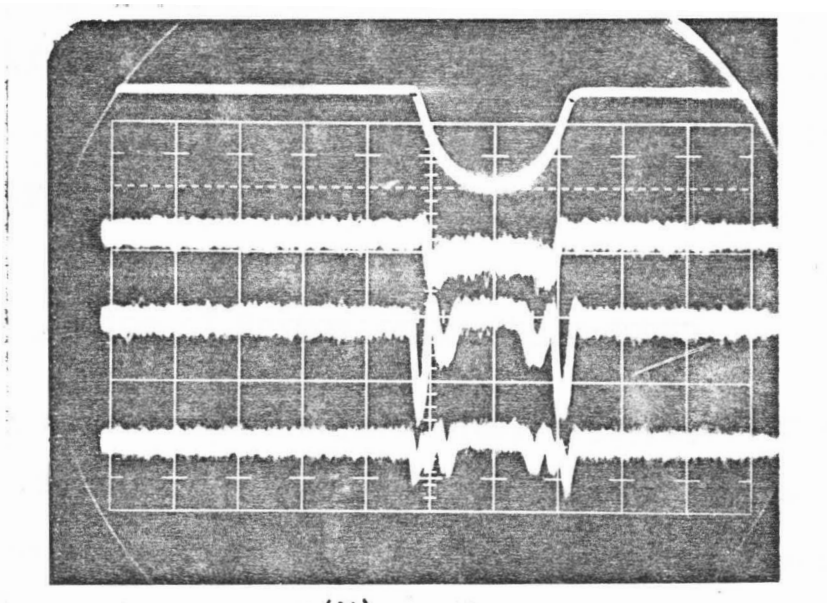

(ii)

Fig. 4.12

(i) Simultaneous microwave crystal detector output (top trace) and rf demodulator output (bottom trace) for $\sim 10^{-10}$ watt of 70 GHz radiation incident on an R-SQUID R = 39.3μΩ.

(ii) Same as (i), with decreasing microwave power starting from the bottom trace.

Following Zimmerman's[99] estimate of the minimum detectable power for a heterodyne experiment at f_1 = 120MHz one can make a rough estimate based on the minimum detectable flux, say $\Phi_o/50$. If the signal voltage $V_M = \Phi_o f_1/50$ (where f_1 = 70GHz) is in phase with a current $I_M = \Phi_o/50L$ and with $L \sim 4 \times 10^{-10}$H one obtains

$$P_{MIN} = V_M \cdot I_M = \frac{\Phi_o^2 f_1}{2500 L} = 3 \times 10^{-13} \text{ watt} \qquad 4.601$$

The estimate of $\sim 10^{-12}$ watt minimum detectable power is thus fairly close to the limit. From the above formula, it is evident that P_{MIN} increases linearly with frequency and thus at $\sim 10^{12}$Hz, the estimated upper limit cut-off frequency, one expects $P_{MIN} \sim 4 \times 10^{-12}$ watts.

4.7 Generation of Harmonics in the R-SQUID

For some contact adjustments, e.g. Fig. 4.7 signals at f_1 and $f_1/2$ only were observed. Other adjustments, Figs. 4.13, 4.14, yielded a richly intricate sequence of lines at harmonic and subharmonic positions relative to the fundamental. Again, only single lines are apparent at each position. This behaviour is fully expected on the basis of equation 2.409 but it must be stressed that the signals can only be clearly distinguished when using the rf bias technique (section 4.4). Without the rf bias, the lines at harmonic and subharmonic positions were virtually indistinguishable from the background

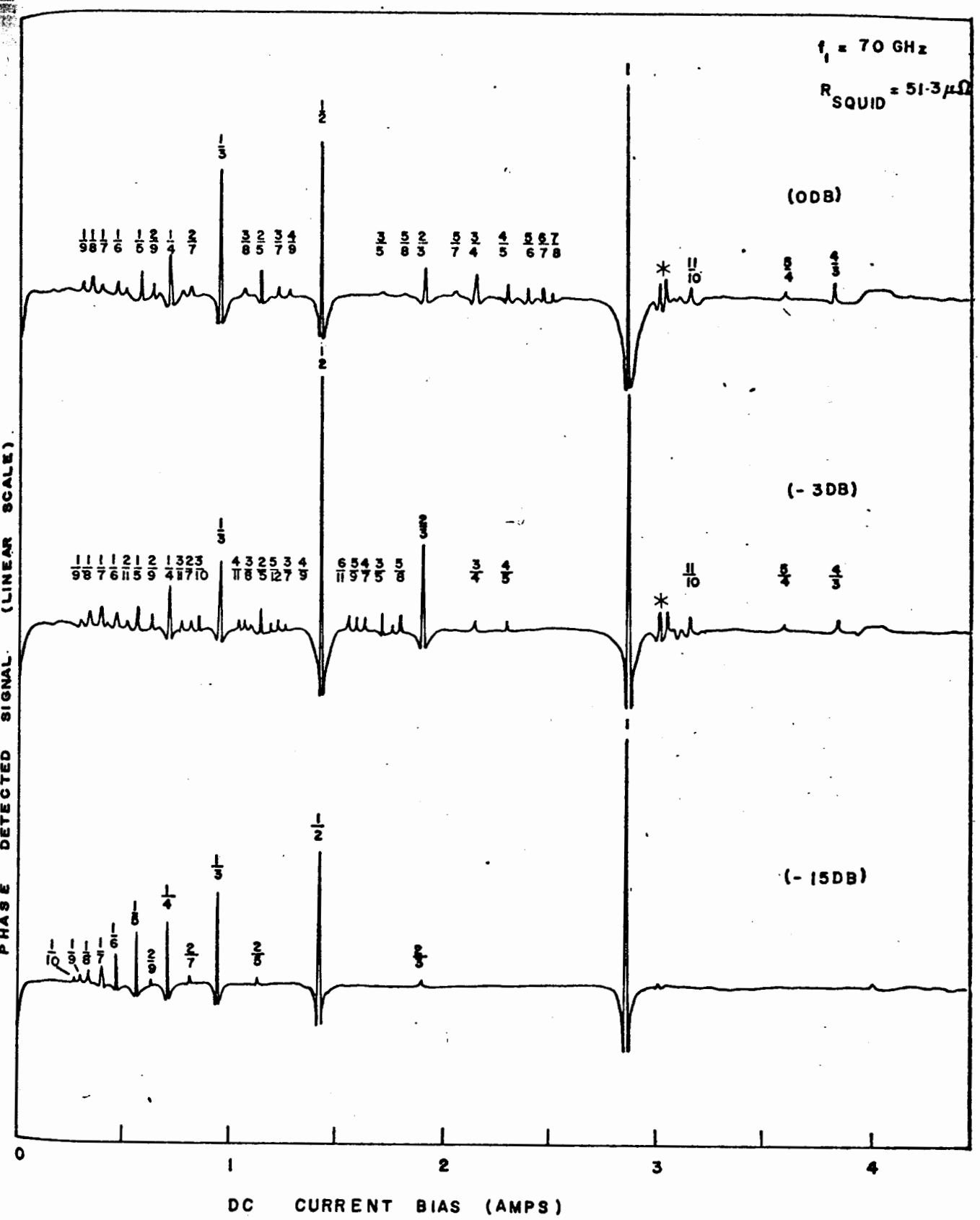

Fig. 4.13 Harmonic spectrum as a function of microwave power at 70 GHz (-15 db $\approx 10^{-10}$ watt). The fractions refer to the ratio p/q (equation 2.409. The lines marked with an * could not be identified.

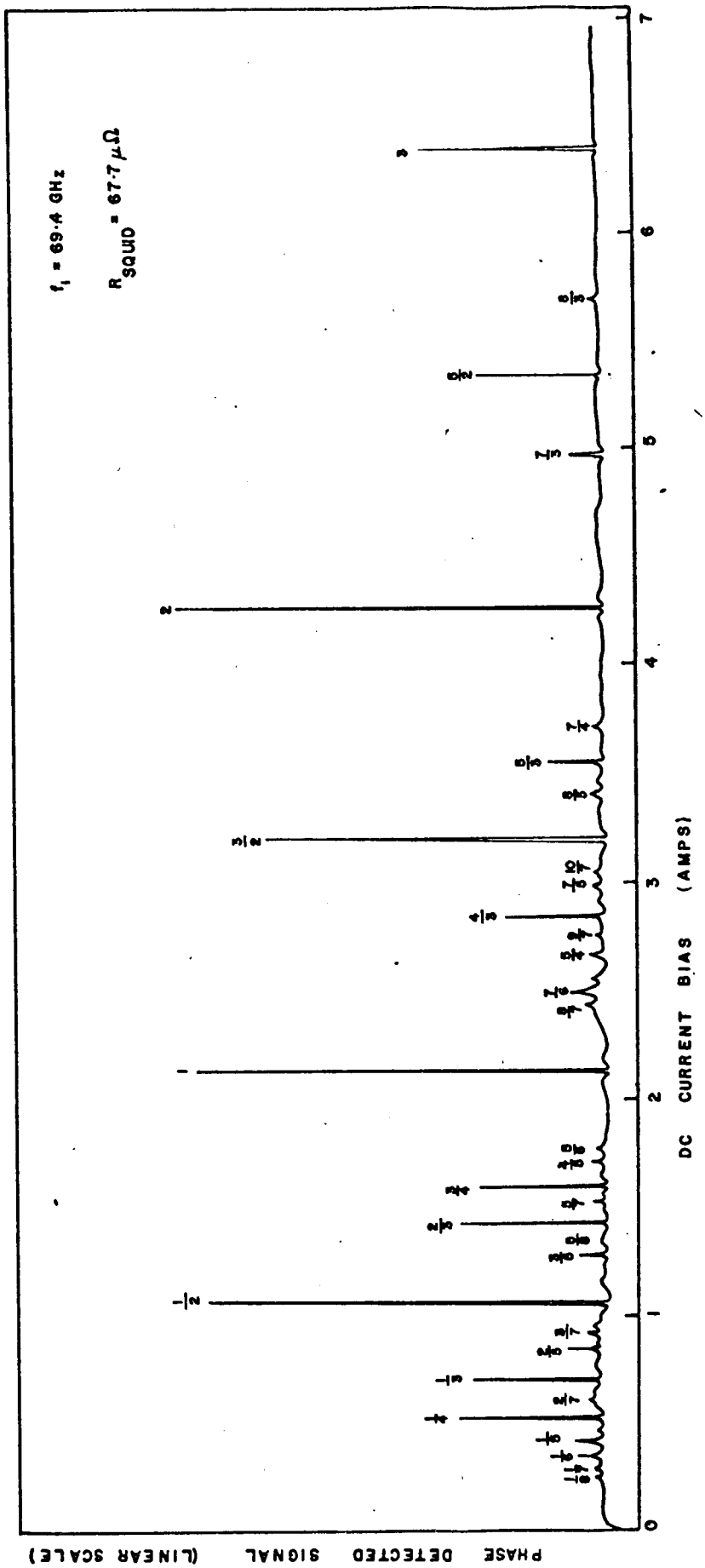

Fig. 4.14 Harmonic spectrum in the range (0 - $3f_1$) for f_1 = 69.4 GHz, R_{SQUID} = 67.7μΩ. Again the fractions refer to the ratios p/q. Incident power was $\sim 10^{-10}$ watt.

noise. It was impossible to determine the nature of the contact where extensive harmonic structure was evident although one was more likely to obtain a rich harmonic content using screws which had flattened tips. Microscopic examination of the tips after contact indicated that the Nb metal had flowed to form a flattened circular region of diameter $\sim$ 15 - 20μm.

The sequence of harmonics in Figs. 4.13, 4.14 fits the matrix presented in Table 4.1 for two different SQUID resistances but using the same incident frequency f_1= 70GHz. The spectra are characterised by the ratio p/q where $I \equiv f_J = |p/q| f_1$; and the spectrum was swept out up to the Josephson frequency $f_J \gtrsim 3\ f_1$.

According to equation 2.408 the amplitude of the pq_{th} harmonic is given by $(i_{cp} J_q(2\pi\ pv_1/\omega_1\Phi_o)\ )$. The power dependence of many of the spectral lines was plotted in an attempt to obtain some information on the form of i_{cp} assuming that a Bessel function dependence was accurate. However it was discovered that the power dependence of the amplitude could not be correlated from run to run using different point contact adjustments. For any one particular spectrum the harmonic amplitudes often oscillated in a very irregular manner and nothing systematic could be deduced about the behaviour of i_{cp}. This amplitude irregularity has already been noted in a discussion of the device sensitivity.

TABLE 4.1

OBSERVED HARMONICS

Signals are expected at $f_{pq} = 30$ Mhz $= pf_1 + qf_J$. Since we have never observed double lines $2f_{pq}$ apart, we specify the observed harmonics as occurring at Josephson frequencies $f_J = |p/q| f_1$. The bracketed spectra refer to degenerate assignments.

$\|p/q\|$							
1	2	3					
1/2	(2/2)	3/2	(4/2)	5/2	(6/2)		
1/3	2/3	(3/3)	4/3	5/3	(6/3)	7/3	8/3
1/4	(2/4)	3/4	(4/4)	5/4	(6/4)	7/4	(8/4)
1/5	2/5	3/5	4/5	(5/5)	6/5	7/5	8/5
1/6	(2/6)	(3/6)	(4/6)	5/6	(6/6)	7/6	(8/6)
1/7	2/7	3/7	4/7	5/7	6/7	(7/7)	8/7
1/8	(2/8)	3/8	(4/8)	5/8	(6/8)	7/8	(8/8)
1/9	2/9	(3/9)	4/9	5/9	(6/9)		
1/10	(2/10)	3/10	(4/10)	(5/10)	(6/10)		
	2/11	3/11	4/11		6/11		
				5/12			

4.8 Linewidth Studies

It has been shown previously in equation 2.413 that the device should measure linewidths to the limits imposed by the Johnson noise fluctuations in the resistor R. Experimentally this behaviour has been demonstrated, at least for incident signals of frequency less than a few hundred MHz[65]. At higher frequencies up to 36GHz, Zimmerman[59] has stated that bias current fluctuations increase the apparent linewidth.

For the present 70GHz microwave experiments the narrowest linewidth achieved has been $\sim$ 7MHz (FWHM) indicating a Q of $\sim 10^4$. This figure represents a lower limit, and linewidths up to 250MHz have been obtained in other experiments. The linewidth referred to is the one obtained by suitably rf biasing the device to amplify the spike Fig. 4.9. This linewidth depends on a number of factors independently of the source linewidth:

(a) RF bias amplitude

(b) magnitude of i_c

(c) RF filtering of bias leads and suitable shielding from external noise.

RF bias amplitude generally increases the apparent linewidth as shown in Fig. 4.15 where the bias amplitude is plotted versus the measured linewidth at 70 GHz.

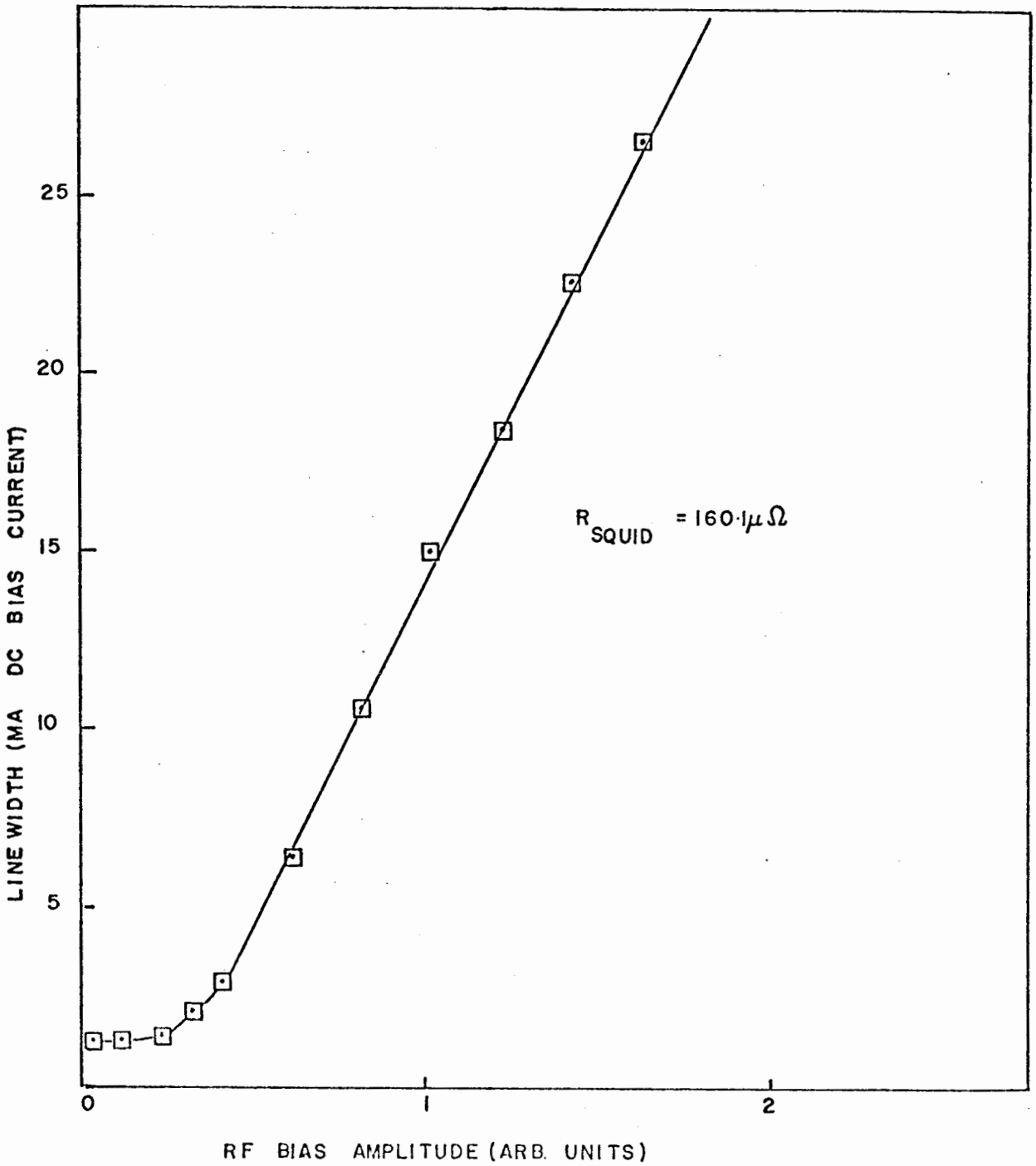

Fig. 4.15 RF biased linewidth at 70 GHz as a function of the rf bias amplitude with R_{SQUID} = 160.1μΩ.

The effect of i_c on the linewidth is difficult to assess although one would generally expect that as i_c increases, the value or R_N, the normal state resistance, decreases since a broader contact is involved. Using equation 2.410, one thus expects time constant effects to be more effective for larger i_c. Qualitatively the linewidth has been observed to increase as a function of contact pressure but nothing systematic could be deduced as no estimate of the values of i_c or R_N were available.

Initially the R-SQUID was operated without shielding and without rf filters on the bias leads. Invariably linewidths $\geq$ 250MHz were obtained. Subsequent efforts to eliminate the noise and rf pickup reduced the linewidth considerably. The effects of noise on the Josephson mixing effect has been studied in some detail by Kose and Sullivan[100], at least for the case of the induced voltage steps in the I-V characteristic when external radiation is present.

As mentioned earlier (section 2.5), in the case where multiple quantum transitions occur ($i_c > \Phi_o/L$), noise increases the linewidth by frequency modulating the fundamental and also by causing fluctuations in the frequency of the subharmonic oscillation (section 2.5.2). For good signal-to-noise with the present system, the R-SQUID was generally operated with $i_c > \Phi_o/L$ and one hence expects contributions to the linewidth from these noise effects. Since there was more interest in obtaining the narrowest possible line, no

systematic investigation of the effects of noise was undertaken. It was observed however that the linewidth of the harmonics was broader than that of the fundamental. This latter effect follows from an equation such as 4.401.

4.9 Spurious Lines

Sometimes while using the R-SQUID the output spectrum was confused by the presence of spurious lines. For example, there was no identification for the lines marked with an asterisk on Fig. 4.13. For other spectra, lines were often present, whether or not microwave power was incident and their spectral position varied considerably over the current bias range as the point contact was adjusted. In some cases, particularly at low current biases, e.g. (0 - 200)mA, groups of these lines were periodic in frequency, but generally these lines were scattered throughout the entire bias range (0 - 9) amps. The spurious lines were sometimes a function of temperature but no systematic study of this dependence was undertaken. (There was a brief study of the temperature dependence of the spectral line positions with the result that no shift could be detected for the temperature range $2^{\circ}K$ to $5^{\circ}K$.)

A possible interpretation of this phenomenon is obtained from the generation of harmonics and subharmonics of the Josephson oscillation[64,77]. Zimmerman and Silver[64] have

observed for appropriate contact adjustment ($i_c > \Phi_o/L$) a regular power spectrum at voltage bias:

$$V = \frac{N}{n} \cdot \Phi_o \cdot \frac{\omega_J}{2\pi} \qquad 4.901$$

where n, N, are integers and ω_J is the Josephson oscillation at the tank circuit frequency ($\sim$ 30MHz). The authors of reference 77 point out that at times, a very irregular output is observed and attribute this to multiple contacts in the weak link. The exact mechanism for the 30MHz output is not clear. However one expects that harmonics or subharmonics of the Josephson oscillation will coincide with geometrical LC resonances of the R-SQUID structure. This might enhance certain harmonic outputs over others. For the R-SQUIDS constructed one can estimate the value $L \sim 4 \times 10^{-10}$H and for the slit region with area $\sim$ 1 cm^2 and width 150μm, one obtains a slit capacitance $\sim$ 6pf. The point contact has a capacitance $\sim$ 2pf, say, and thus the structure has a resonant frequency at

$$f_c = \left(2\pi\sqrt{LC}\right)^{-1} = 2.5\,GHz \qquad 4.902$$

Multiple contacts in the weak link may also introduce a large number of additional resonances. The Q of the resonance is given by $Q \sim R^{-1}\sqrt{L/C}$, where R is the R-SQUID bias resistance. (Note $R << R_N$ the normal state point contact resistance. Thus

for R = 40μΩ, the resonance (equation 4.903) has a Q-value $\sim 10^5$. Internal and external noise voltages will broaden this Q-value. Generally, the spurious lines had Q-values $\sim$ 20 - 100, so that some further loss mechanism is necessary to explain the spurious line-width.

For the 40μΩ R-SQUID, this resonance frequency (equation 4.902) occurs at a current bias of $\sim$ 130 mA. The value of C is very uncertain and estimates vary between 1pf and 1000pf[70]. For the higher capacitance values, one would obtain f_c < 1 GHz and Q $\sim 10^4$.

With the present R-SQUID design, a strong continuous 30MHz output was usually observed in the 0 - 100 mA bias range. This output was often a function of the point contact pressure. The interaction of the Josephson oscillation and the geometric LC resonance may account for some of this output.

4.10 Summary

Although a considerable part of this chapter has been devoted to the broad range of behaviour which can be observed with the R-SQUID, it must be stressed that good behaviour is generally the rule rather than the exception. If one uses a sharp Nb point and a contact resulting in rf behaviour such as in Fig. 4.5, the rf biased R-SQUID response generally results in spectra as in Fig. 4.7. Good signal-to-noise and narrow linewidths are usually obtained with very few harmonic or subharmonic lines appearing.

Narrower linewidths than those obtained with the present system may be possible by improved design of such features as the dc bias supply, bias lead filtering, shielding etc. and also by operating the device at much lower temperatures (equation 2.413). Higher sensitivity can be achieved by mounting the point contact in a suitable tunable cavity thus providing greater interaction between the supercurrent and the incident radiation. The main reason for not following the latter approach was because a free space radiation detector was desired. The next two chapters contain an account of an application of such R-SQUIDS to the problem of detecting stimulated emission of radiation from superconducting tunnel junctions.

CHAPTER V

APPLICATION OF THE R-SQUID: SEARCH FOR STIMULATED EMISSION FROM SUPERCONDUCTING TUNNEL JUNCTIONS

5.1 Historical Introduction

The millimeter and submillimeter regions of the wavelength spectrum present special problems to the experimenter. The main problem is the lack of a sufficiently powerful coherent source of radiation, tunable over a wide range of frequencies. Leopold et al[101] made the attractive suggestion of constructing a maser using as the source, energy gap radiation from superconductors. Such a maser should have a reasonable output power ($\sim 10^{-7}$ watt) and should be tunable, merely by changing an ambient magnetic field or the superconductor temperature. The highest critical temperature superconductors should have a maximum output frequency $\sim 10^{12}$Hz. In what follows a summary of the previous work will be presented.

The theory of Leopold et al[101] was closely patterned on the theory of p-n junction lasers[11,102] with suitable modifications to describe the superconducting state. The type of device under consideration (Fig. 5.1) is a superconducting tunnel junction where quasiparticles are injected into empty states above the superconducting energy gap by tunneling from a normal metal through an insulating barrier B.

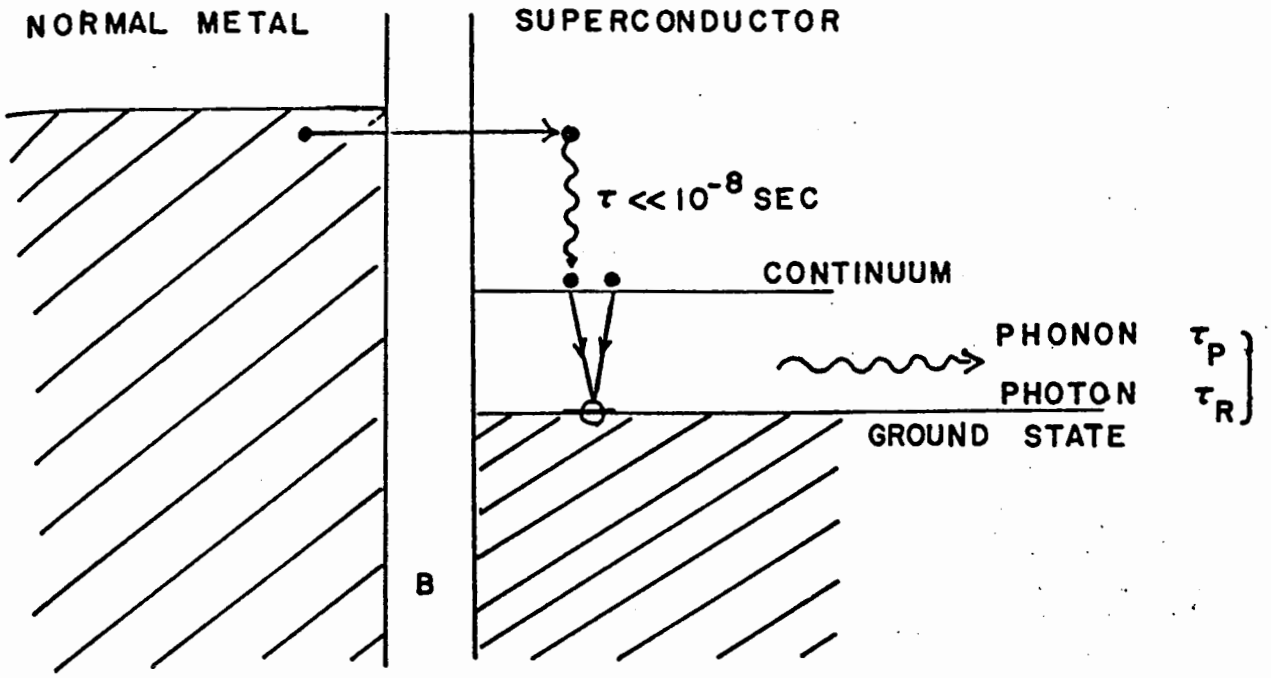

Fig. 5.1 Electron excitation representation of quasiparticle injection by tunneling.

Experimentally these quasiparticles are known to relax first to the gap edge in a time much less than the quasiparticle recombination time[108]. The processes of recombination have been examined both theoretically[103-105] and experimentally[106-110]. Quasiparticle recombination is predominantly via phonon emission with experimental lifetimes 10^{-8} sec - 10^{-6} sec, and the generation and detection of these phonons has been elegantly demonstrated by Eisenmenger and Dayem[108], and Dynes et al[111]. The theory and experiments yield a lifetime τ_p for phonon emission which behaves as $\sim \exp(2\Delta/k_B T)$ where 2Δ is the energy gap at temperature T. Size effects in thin films may cause a marked increase in the experimental lifetimes as $T \to T_c$[112].

A second mode of decay is via photon emission, but here the lifetime is much longer. Using the radiative recombination theory of van Roosbroeck and Shockley[113], Burstein et al[114] derived a lifetime $\tau_R = 0.4$ sec for Lead at 2°K. This lifetime decreases as $T \to T_c$ but the precise temperature dependence is rather complicated, since τ_R depends on the density of excited quasiparticles and the complex conductivity σ of the superconductor. This point will be enlarged on later.

Once emitted in the bulk metal, the photon may be reabsorbed by breaking up condensed pairs, or by further excitation of quasiparticles, or it may stimulate the

emission of more photons of the same frequency. Macroscopically one can describe the photon propagation by solving London's[1] electromagnetic equations for the bulk superconductor, (see section 6.3). Leopold et al[101] suggest that one can incorporate a resonator for the emitted photons into the tunnel junction, thus enabling stimulated emission to occur. The situation studied both theoretically and experimentally[10,12,13] consisted of a cylindrical cavity for the photons provided by the superconducting part of the tunnel junction itself. This is made possible by the very high refractive index of a superconductor ($n \sim 1000$). A further point is that one is more likely to form a cavity for photons rather than phonons, due to the differences in the photon and phonon wavelengths. This follows from analysis of scattering from rough surfaces by Beckmann[115].

The calculation of the threshold injection current j_T for masing action to occur follows by direct comparison with the case of semiconductor injection lasers. One calculates the stimulated gain and equates this to the losses. Thus

$$j_T(A/cm^2) = 1{\cdot}35\times10^7\,\eta^2 d(2\Delta)^3(z\zeta)^{-1}\cdot\frac{\delta E}{2\Delta}\cdot\sum_i k_i \qquad 5.101$$

where η = real part of the refractive index (n);

2Δ = energy gap in eV;

δE = spontaneous radiative linewidth in eV;

z = quantum efficiency (= 50% for pair production);

ζ = fraction of decays which are radiative = τ_p/τ_R;

Σk_i = Total loss in terms of absorption coefficients $k_i (cm^{-1})$

The total quantum efficiency ($z\zeta$) is expected to be extremely small ($\sim 10^{-7}$) due to the tiny fraction of decays which occur via photon emission. The large losses and small quantum efficiency for superconductors result in a rather large threshold current density which must of course be smaller than the current density necessary to destroy superconductivity. Taking into account in a self-consistent way the effects of a strong overpopulation on the energy gap itself, Leopold et al[101,116] have calculated the threshold current density and power output for a number of parameters and have concluded that stimulated emission was possible for Tantalum. For a Ta tip of diameter 25μm at 4.26°K one expects a threshold current density for stimulated emission of $\sim 10^5 A/cm^2$. For this case, one expects a total power output at $\sim$ 100GHz of $\sim 10^{-7}$ watts.

To facilitate comparison with the experiments to be described in section 5.2, a summary of the experimental conditions and data in references 10, 12, 13 will now be given. The previous experiments were conducted with tunnel junctions consisting of a specially formed cylinder of Tantalum, $\sim$ 25μm in diameter and 75μm in length, making light contact with the oxidised surface of an Aluminium plate. The diameter was chosen for practical purposes and the length represents a

mean distance through which the quasiparticles drift prior to recombination[110]. Current to the junction was supplied by an audio oscillator at 33hz and radiation was measured with a Ga-doped Ge bolometer some distance away from the tunnel contact. The junction and the bolometer were mounted in a vacuum can filled with exchange gas and a Carbon resistance thermometer was mounted on the junction support. It was necessary to attach a heater to this support in order to keep the thermometer reading the same temperature for the whole range of tunnel currents used. The experimental results can be summarised as follows:

(i) The observed radiation showed a threshold behaviour: beyond a certain tunnel current, the absorbed power on the bolometer started to increase with increasing current. Approximately 10^{-7} watts of radiation have been observed, allowing for the solid angle open to the bolometer. The signal was above the noise level by a factor of about 1000.

(ii) The radiation wavelength was investigated in two ways: introduction of short pieces of waveguide between the source and the bolometer to act as cut-off filters[10] and a separate arrangement[12,13] where a wavemeter of Q $\sim$ 18 was mounted in a waveguide system containing the source and bolometer. The temperature dependent output appeared to follow a BCS-type behaviour.

(iii) The observed radiation disappeared when the temperature of the junction support was heated above 4.4°K as measured by the attached Carbon resistor. No radiation was evident when the Ta was replaced by a normal metal.

From these measurements, it was deduced that some form of stimulated process was taking place in the tunnel junction. The radiation appeared to have roughly the correct temperature-dependent frequency and it proved possible to fit the power output versus current density curve for some reasonable parameters where the threshold density was $\sim 10^5 A/cm^2$. The frequency measurements[10,12,13] did not conclusively prove that a stimulated process was occurring. For this, one has to observe line-narrowing of the spontaneous emission as the injection current is increased[11]. Thus there was some interest in studying the junction radiation with a tunable spectrometer and for this purpose the R-SQUID of Chapter IV would appear to have ideal properties. The R-SQUID can be positioned close to the radiating junction in the Helium bath, and it is possible to operate both the R-SQUID and the junction in He^4 liquid to improve heat conduction. Excellent sensitivity ($\sim 10^{-12}$ watt) and narrow linewidth at the frequencies of interest (Q's of $\sim 10^4$ at 70GHz) are available with this device. Actually, the R-SQUIDS were developed primarily for the purpose of detecting this stimulated emission.

The sections which follow (sections 5.2 - 5.4) give details of the expermental system used to search for stimulated emission from Tantalum metal tunnel junctions. The results of an extensive search presented in Chapter VI have been completely negative and this disappointing result caused a critical re-evaluation to be made of the theory of the tunnel junction maser. This analysis is presented in section 6.2 and gives some explanation of the negative result. The final section of Chapter VI discusses the earlier experiments in the light of the present investigation.

5.2 Preparation of the Tunnel Junctions

The initial observations of radiation were achieved using tunnel junctions formed as follows. The Ta tips were constructed by machining the end of a piece of Ta wire on a jeweller's lathe to a cylindrical form of diameter $\sim$ 25μm and length $\sim$ 100μm. The oxide on the Aluminium plate completing the junction was grown using an anodic technique[117] to form a film $\sim$ 1500Å thick.

At the outset, it was decided to duplicate the tunnel junction system used by Gregory et al[10] to test their conclusion that stimulated radiative emission had occurred. The majority of the experiments were conducted using Ta tips which had been chemically polished and cut to the required geometry. Fourteen experiments were also conducted using

four Ta tips supplied by Dr. W. Gregory . The latter tips had been machined and polished on a jeweller's lathe.

The exact technique for making the chemically etched tips is as follows. A 3cm length of Ta wire diameter 0.03" supplied by Fansteel[*] was mounted in the jaws of a small hand drill, and using files and emery paper, machined into the form shown in Fig. 5.2a. The final form after the electrochemical etching (Fig. 5.2b) was found to depend rather critically on this starting shape. The narrowest neck formed during this preliminary machining was $\sim$ 200μm. The Ta wire was then mounted in a vertical rotating brass holder driven by a 60rpm motor. It was found essential to rotate the tip during polishing to obtain a cylindrical shape. The experimental arrangement for the electrochemical polishing is shown in Fig. 5.3 where the Tantalum tip formed the anode in a suitable acid bath and the cathode was a graphite rod. After some experimental work the following bath composition was chosen for all subsequent electropolishing:

25 ml Concentrated Hydrofluoric Acid (HF);

25 ml Concentrated Sulphuric Acid (H_2SO_4);

50 ml Lactic Acid

(Tegart[83] recommends a 9:1 mixture of H_2SO_4 and HF for Ta.)

---

*See page 55

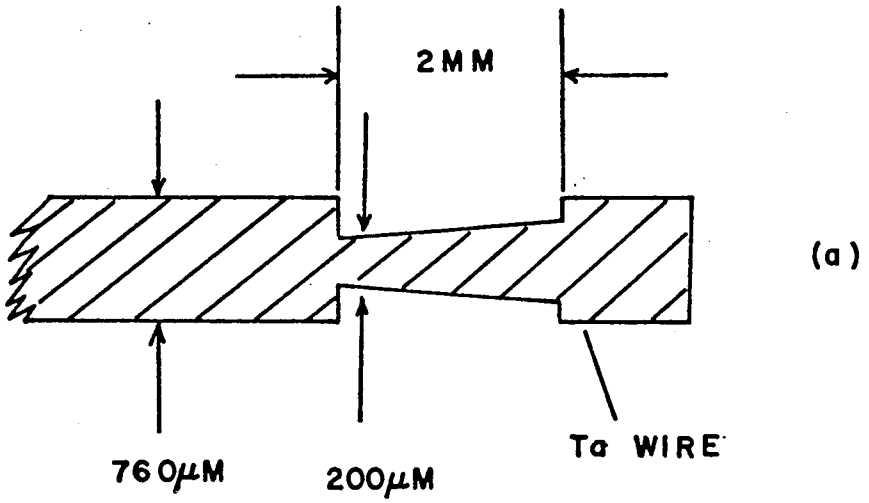

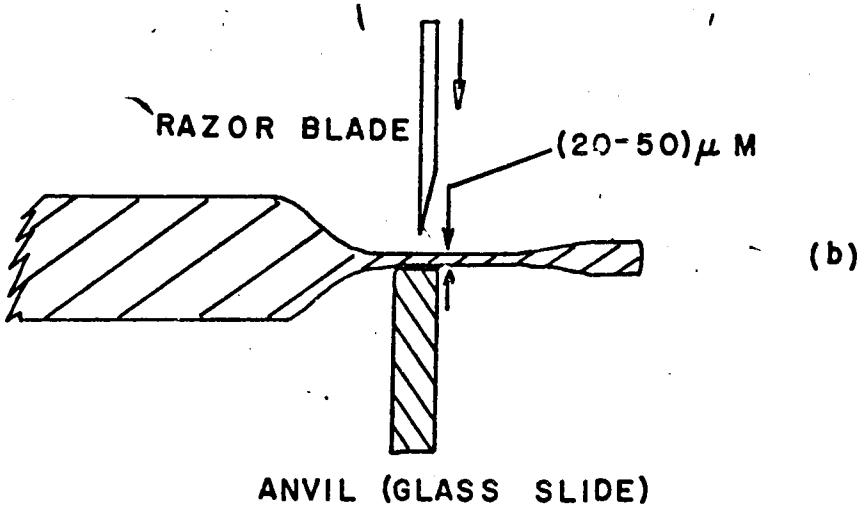

Fig. 5.2 Preparation of Ta needle by electropolishing

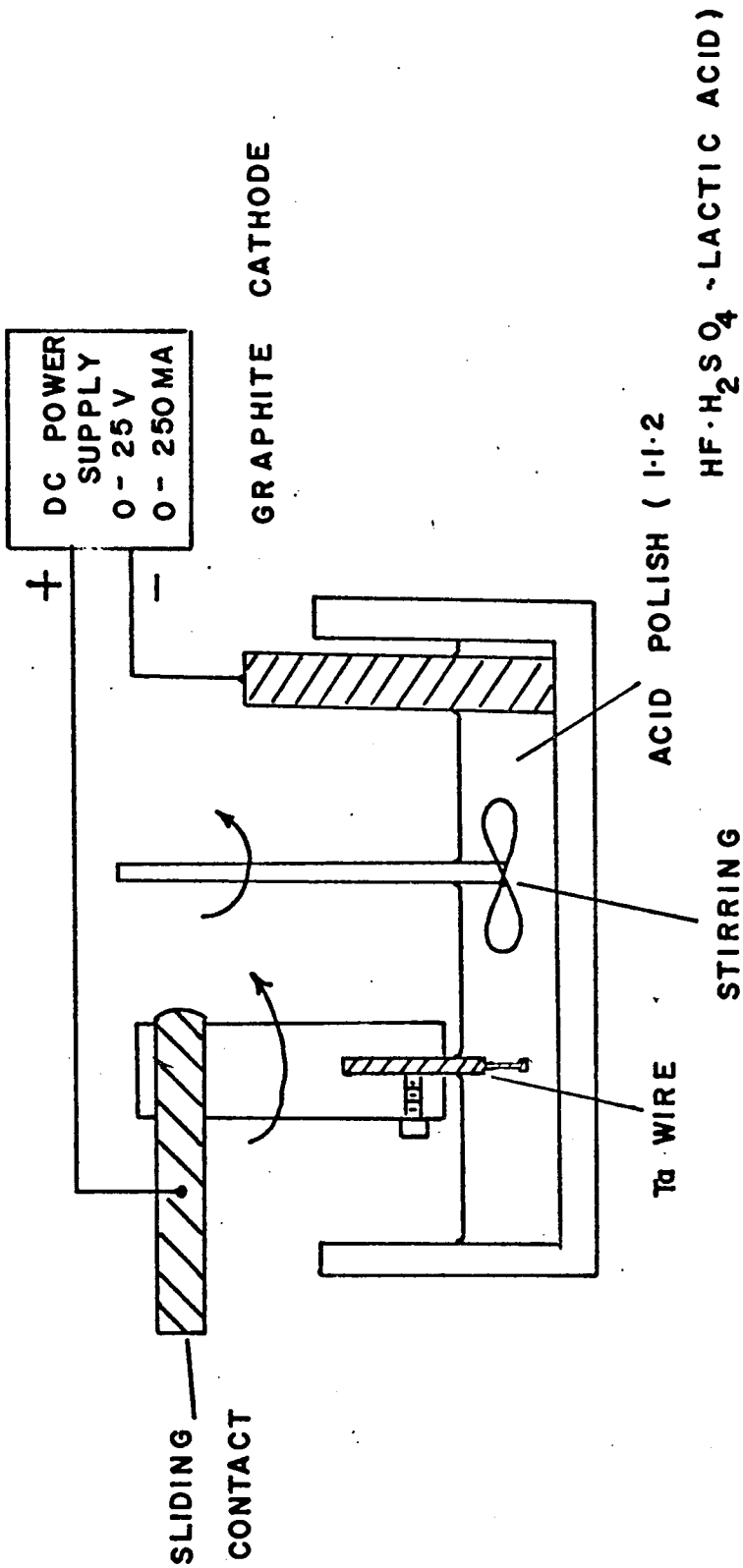

Fig. 5.3 Electropolishing apparatus

The HF and H_2SO_4 acids were mixed at room temperature in a plastic container inside a fume hood. The temperature of the mixture immediately rose to $\sim 70^{\circ}C$ with a strong fuming action apparent. Addition of Lactic acid cooled the solution to $40^{\circ}C$ - $50^{\circ}C$. This warm solution was then used immediately for the polishing. The rate of polishing for the Ta wires used was found to depend strongly on the solution temperature, the current passed through the cell, and also the solution age. For hot solutions, the metal surface became quickly pitted, perhaps by more rapid etching at impurity sites, or at cleavage planes of microcrystallites. The ideal temperature, resulting in the smoothest Ta surfaces, was found to be $\sim 30^{\circ}C$. As the voltage drop across the cell was increased, the current rose and the polishing action became very rapid. By driving large current (> 250mA) through the cell during the preliminary polish, the tip diameter could be reduced from $\sim$ 300μm to $\sim$ 60μm in $\sim$ 3 minutes. The voltage across the cell was then reduced to 4 volts for a total current of 40mA to produce a final polish to $\sim$ 25μm leaving a mirror-like finish. The graphite rod was 1cm in diameter with a 2cm length in the solution and the anode-cathode distance was $\sim$ 4cm.

After the polishing was deemed complete, the Ta needle was mounted in a holder operated by a three-dimensional

micromanipulator(*). Using the latter, the polished needle was carefully positioned so that one edge rested on a narrow vertical anvil as shown in Fig. 5.2b. A suitable anvil was a 1/5 mm thick glass slide. A razor blade, mounted vertically in an adjustable micrometer, was gradually lowered until the Ta needle was sectioned at the anvil position. These proceedings were viewed through a X50 microscope located nearby.

A typical cylindrical Ta tip obtained by the above procedures is shown in the microscope picture 5.4a for a tip of diameter $\sim$ 20μm. One of the mechanically ground tips supplied by Dr. W.D. Gregory is shown in Fig. 5.4b.

To provide electrical connection for passing current through the junction, a copper lead was spot welded to the Ta wire about 1cm from the polished tip. The Ta wire was then mounted in a differential screw assembly used to make contact with the anodised Al plate, Fig. 5.5.

The adjustment mechanism consisted of a differential screw of equivalent pitch = 350 threads per inch, attached to a slider constrained to move vertically by means of a groove channeled into the section B. All moving parts were of brass, in order to eliminate any difficulties during operation in liquid He^4. When the movement was examined in an optical microscope, it was found to be relatively smooth and the delicate Ta tip could be adjusted to make contact to the oxide surface with minimal damage incurred. There

*See page 62

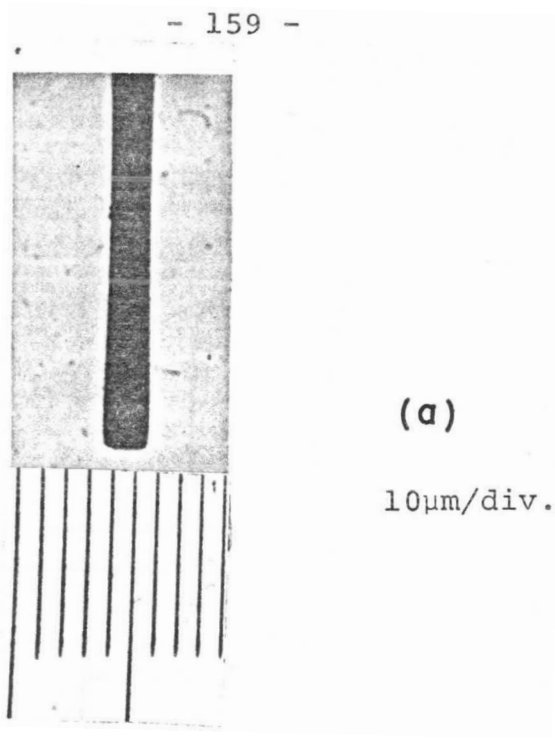

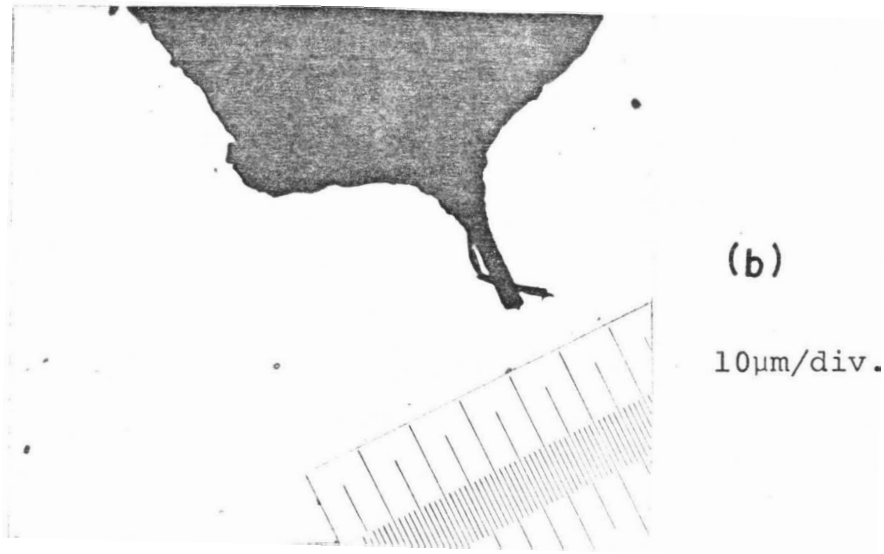

Fig. 5.4 (a) Electropolished Ta needle d ∿ 20μm.

(b) Mechanically milled Ta needle d ∿ 30μm. (Courtesy Dr. W.D. Gregory)

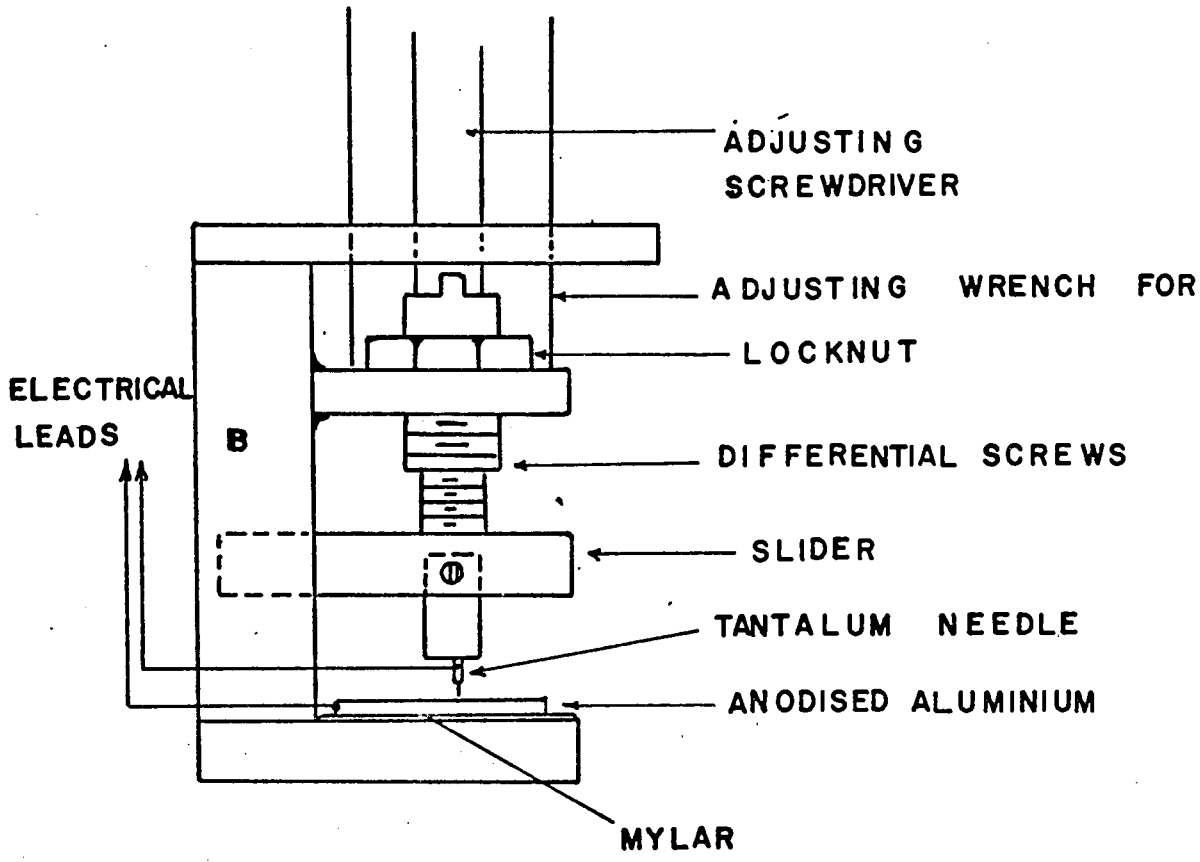

Fig. 5.5. Differential screw assembly for adjusting Ta tunnel junction contact.

was of course the possibility of buckling the needle with excess contact pressure and care had to be taken to avoid this.

To ensure that the Ta tip end was parallel to the oxide surface and also perpendicular to the direction of travel, the Al plate was replaced by an exactly parallel glass slide and the tip very carefully adjusted to make light contact with the slide surface. Any irregularities or asperities at the tip end tended to be eliminated by this technique.

The aluminium plates used in these experiments were supplied by W. Gloor of this laboratory and had been spark-cut from an ingot of Cominco 69's grade Aluminium. These plates were then subsequently electropolished in a phosphoric acid bath[83] to a mirror surface finish. An anodic oxide layer was grown on these plates using the techniques outlined in reference 121. The Aluminium plate functioned as the anode in a suitable bath (Fig. 5.6) and the cathode was a second pure Aluminium plate. The recommended bath was a solution of Tartaric Acid and Ammonium Hydroxide with a ph $\sim$ 5.5.

A second solution which was also used was formed as follows:

20 gms	Boric Acid
8 gms	Borax
500 cc	distilled deionised water.

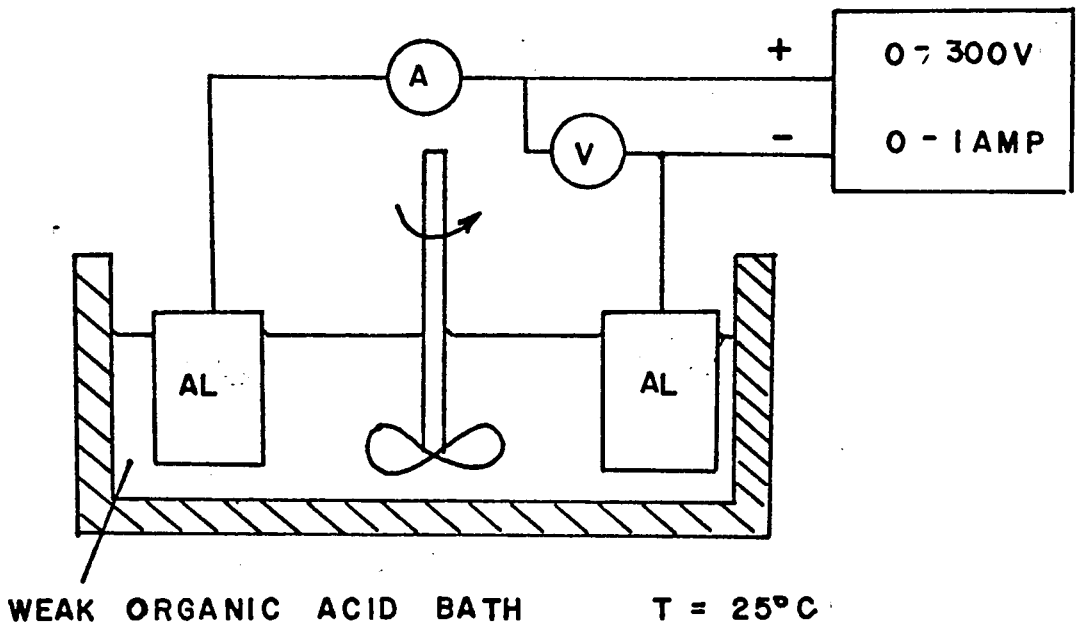

Fig. 5.6 Apparatus for anodic oxidation.

Both these solutions have been found to give similar growth rates of oxide[117]. Weak organic acid solutions tend to give very uniform films with ideal properties. The commercial anodisation process for Aluminium which uses a Sulphuric acid bath, results in porous films of much greater thicknesses. The growth rate is given in Å/Volt and for both the above solutions a voltage drop of 100 volts across the cell should result in an oxide thickness $\sim$ 1400Å, when fully grown. Prior to the anodisation process, the Al plates were placed in a beaker of boiling deionised water for 30 minutes. Young[85] has found that this technique results in oxide layers which bond strongly to a metal substrate such as Ta. Presumably boiling water helps to remove adsorbed layers of the acidic etch.

The diagram of Fig. 5.6 shows the aluminium anode and cathode in a weak organic acid bath. To obtain the requisite oxide thicknesses the voltage across the cell was manually increased at a slow rate while maintaining a reasonably constant current through the cell ($\sim$ 20mA). When the desired voltage was reached the current dropped roughly exponentially with time as the oxide grew thicker. The growth was stopped when the current at the applied voltage had reached $\sim$ 50μA. In the subsequent parts of this report, the oxide thicknesses quoted are then deduced using a growth rate of 14Å/Volt. Experiments have shown that the

growth rate is a function of the applied voltage tending to be larger for lower voltages ($\lesssim$ 50 volts) and reducing as the voltage increases. However the final quoted oxide thicknesses are expected to be in error by no more than 20%.

The most convenient way to form electrical contacts to the Aluminium plate was to drill a small hole at the plate edge prior to anodisation, and then thread a stripped Copper wire (AWG 26) several times through the hole. The mechanical Cu-Al contact was then sealed using silver conducting epoxy(*). Repeated thermal cycling between 300°K and 4.2°K had little effect on the contact.

The anodised Al plate was then expoxied(**) to a brass flange located directly below and at right angles to the Ta needle axis (Fig. 5.5). It was insulated from the brass by a 0.005" Mylar sheet. The Ta needle was also insulated from the metal differential screw assembly by means of a Celaron holder.

5.3 The Radiation Detectors

As mentioned earlier two types of radiation sensors have been employed in this study namely bolometers for broad band detection purposes and the sensitive frequency

---

*Starnetics Silpox, 10639 Riverside Drive, North Hollywood, California 91602

**Easipoxy K235 (Clear) CONAP INC., Alleghany, New York, U. S. A.

converter (R-SQUID) to investigate typical stimulated radiative effects such as line narrowing etc. R-SQUIDS as previously described were used for the narrow band sensitivity, and the reader is referred to Chapter IV for further details. In the following sections (5.3.1 - 5.3.7) a detailed account of bolometers is presented with descriptions of some of those built.

5.3.1 Bolometers

In recent years there has been a considerable improvement in the sensitivity available from far infrared spectroscopic systems, due partly to the development of bolometers operating at liquid He^4 or liquid He^3 temperatures. The most useful detectors for the frequency regime $1cm^{-1}$ - $100cm^{-1}$ are the Carbon resistance bolometer, the doped Silicon or Germanium bolometer and the Indium Antinomide detector. The latter detectors are now available commercially.

The Carbon resistance bolometers of Boyle and Rogers[96] developed from the use of Carbon resistors on thermometers at liquid helium temperatures. The latter bolometers tend to be rather noisy and limit the absolute power sensitivity to $\sim 10^{-10}$ watts. A considerable reduction in noise and hence increase in sensitivity was achieved by Low[118] with the use of Germanium doped with Gallium. These Germanium bolometers were extensively studied and developed by

P. Richards[119] and the He^3 cooled version provides the mainstay detector for much modern research in astronony and far infrared spectroscopy. More recently[97] it has been possible to exploit to superior properties of Phosphorous-doped Silicon to achieve a faster response time and better signal-to-noise ratio.

5.3.2 Theory

A relatively simple model may be employed to describe the optimum operating conditons for such a bolometer. A far infrared or microwave signal modulated at the frequency ω is incident on a bolometer of heat capacity C'. The bolometer is connected to a bath at temperature T_o by leads of thermal conductance K'. The heat balance equation for the bolometer element may be written for a constant bias current I as

$$C' \frac{dT}{dt} = I^2 R(t) + W_0 e^{i\omega t} - K'(T(t) - T_o) \qquad 5.301$$

R = bolometer resistance

$W_0 e^{i\omega t}$ = radiation power absorbed by the bolometer.

The solution to equation 5.301 neglecting transients is[121]

$$T(t) = T_B + \frac{W_0 \tau^*}{C'} \cdot \frac{e^{i\omega t}}{\sqrt{1 + \omega^2 \tau^{*2}}} \qquad 5.302$$

where

$$\tau^* = \frac{C'}{(K' - \delta' I^2 R_B)} \qquad 5.303$$

$$\delta' = \frac{1}{R} \cdot \frac{dR}{dT} \qquad 5.304$$

$$R_B = R(T_B) \qquad 5.305$$

T_B satisfies

$$I^2 R_B = K'(T_B - T_o) \qquad 5.306$$

Thus the Joule heating due to the dc bias current I raises the bolometer temperature to the value T_B; the absorbed power $W_o e^{i\omega t}$ causes a harmonic zero average heating of the bolometer element. This results in a harmonic variation of the bolometer temperature:

$$T = T_B + T_1 e^{i\omega t} \qquad 5.307$$

where

$$T_1 = \frac{W_o \tau^*}{C' \sqrt{1 + \omega^2 \tau^{*2}}} \qquad 5.308$$

and a harmonic variation of the resistance

$$R = R_B + R_1 e^{i\omega t} \qquad 5.309$$

The temperature dependent resistance for Carbon, Germanium and Silicon is well approximated in the liquid helium temperature range by

$$R = R_o e^{\chi/T} \qquad 5.310$$

Thus expanding the exponential we find

$$R_1 = - \frac{R_B T_1 \chi}{T_B^2} \qquad 5.311$$

It is convenient to define a facter termed the responsivity S'[120] where

$$S' = \frac{dE}{dW} = \frac{\delta' E}{K' - \delta' I^2 R_B} \qquad 5.312$$

(E = voltage across the bolometer, W = radiation power described by the bolometer.) To obtain the maximum signals one has to optimise S' by adjusting the various bolometer parameters C', K', R, δ', χ and also the operating conditions T_o, T_B, I. Blackburn et al[121] have analysed this problem and have generated computer solutions to obtain the optimum operating bias current I and lead conductance K for a given bolometer. An intuitive idea of how the parameters affect S' is obtained by writing S' as[119]

$$S' = \frac{I R_1}{W_o} \qquad 5.313$$

When the constant bias I is applied, the ac signal voltage R_1, will increase with I until T_B begins to rise appreciably due to the I^2R_B contribution. Thus χ and R_B must be large, and T_B small to obtain optimum responsivity. Form (equation 5.312), it is evident that a large value of S' involves having large δ' and small K' leading to relatively slow bolometers (equation 5.306). Note however that K' is subject to the condition $K' = (I^2R_B/(T_B - T_o))$. In practice C' is made as small as possible and K is adjusted to obtain a convenient operating frequency $\omega = (\tau^*)^{-1}$. Since the heat capacity for Silicon is less than for Germanium, Silicon bolometers are to be preferred. For a given bolometer size and time constant, Silicon should be superior to Germanium in signal-to-noise by at least a factor of five.

The noise equivalent power (NEP) is a figure of merit for a bolometer and is the signal which produces unity signal-to-noise ratio for unity bandwidth. The NEP in the absence of photon noise is the sum of the equivalent Johnson noise power and the phonon noise power. Low[118] showed that

$$NEP \sim T_o\sqrt{k_B K'} \qquad 5.314$$

and is thus dependent only on the bath temperature T_o, and the lead conductance K (k_B = Boltzmann's constant). The

NEP is independent of the detector dimensions. A comparison is made in Table 5.1 of the three varieties of bolometers using published data.

5.3.3 Carbon Resistance Bolometer

A number of Carbon resistance bolometers were constructed according to the following system. A slice of Carbon was cut from a 2 watt Allen Bradley resistor whose nominal value ranged from 10Ω to 470Ω. The rectangular slab of carbon was then ground to final dimensions 5mm x 7mm x 0.1mm. The leads were attached to the Carbon along the 5mm slab edges using either Silver Dag dispersion(*) or Silver conducting epoxy(**) and the leads provided the support as well as the thermal conductance to the bath. The leads consisted of 2cm of 0.007" NbZr wire Copper plated at both ends with a 1cm section of the Copper etched away in Nitric acid to provide a purely superconducting conductance to the bath. About thirty such bolometers were constructed and dip-tested at liquid He^4 temperatures until a resistance of ∿1MΩ was obtained for an ac measuring current of 10^{-8}A at 30Hz. The optimum dc bias current was selected by optimising the signal voltage during an actual experiment

---

*Silver Dag Dispersion 415 (Acheson).

**See page 164

TABLE 5.1

TYPE	R (4.2°K) (Ω)	S $\left(\frac{\text{Volts}}{\text{Watt}}\right)$	τ^* (Sec)	NOISE (Volts)	NEP (Watts/$\sqrt{\text{HZ}}$)
Carbon[124]	1.2×10^6	2.1×10^4	10^{-2}	1.6×10^{-7}	1×10^{-11}
Germanium[125]	1.2×10^4	4.5×10^3	4×10^{-4}	2×10^{-9}	5×10^{-13}
Silicon[127]	7.2×10^4	7.9×10^4	1.6×10^{-4}	1×10^{-9}	3×10^{-13}

TABLE 5.2

TYPE	R (4.2°K) Ω	S $\left(\frac{\text{Volts}}{\text{Watt}}\right)$	τ^* (Sec)	K' (μW/°K)	NEP (Watts/$\sqrt{\text{HZ}}$)
Si 4.2R	8.42×10^5	4×10^4	2.5×10^{-3}	16	$< 3 \times 10^{-13}$

using 70GHz incident radiation.

5.3.4 Germanium Bolometers

Some Indium-doped Germanium bolometers were constructed using wafers of Ge roughly 5mm x 5mm x 0.2mm in dimension. The wafers were carefully etched with suitable chemicals(*) and fine copper leads (AWG 42) were attached by means of pure Indium solder. Good electrical contact to the Ge was obtained by first heating melted Indium wire (99.999% purity) for about 30 minutes prior to the actual soldering. This technique was found to improve the wetting properties of Indium(122).

The wafers of Ge, supplied by Dr. L.H. Palmer, were found to have both a relatively low resistance ($< 20K\Omega$) and also a low temperature coefficient of resistance (α') for a temperature of $4.2^{\circ}K$. This Ge was more suitable for temperatures $\sim 1.2^{\circ}K$ or lower. However some of these bolometers were tested at $4.2^{\circ}K$ but were found to be less sensitive than the best Carbon bolometer constructed.

5.3.5 Silicon Bolometers

Eventually a Phosphorus-doped Silicon bolometer was obtained and this proved to have excellent properties for

*CP 4 Etch

operation at 4.2°K(*). The specifications are given in Table 5.2

5.3.6 Bolometer Vacuum Chamber and Detection Electronics

For temperature stability it was decided to operate the superconducting maser and the R-SQUID in liquid He^4. Accordingly a suitable vacuum chamber with a quartz window was constructed as in Fig. 5.7 to house the bolometer. The design was suggested by Dr. B. Clayman, and T. Templeton of this laboratory and was extremely successful. Once the leaks had been eliminated the vacuum chamber remained vacuum tight for an indefinite number of cycles from 300°K to 4.2°K.

The important feature of the design is the use of a phosphor-bronze washer of suitable dimensions to absorb the differential thermal contraction during cooling and subsequent warm-up to room temperature. The Indium o-ring was made by forming a tight flat spiral of approximately four turns of 1mm diameter pure Indium wire. The fine Gold leads of the bolometer were soldered on AWG 22 Copper leads using a special Indium based solder supplied by the bolometer manufacturer. The Copper leads were then fed through hermetic seals into the liquid He^4 bath. A vacuum outlet

---

*Available from: Far-Infrared Inc., a division of Molectron Corp., 930 Thompson Place, Sunnyvale, California, 94086 U. S. A.

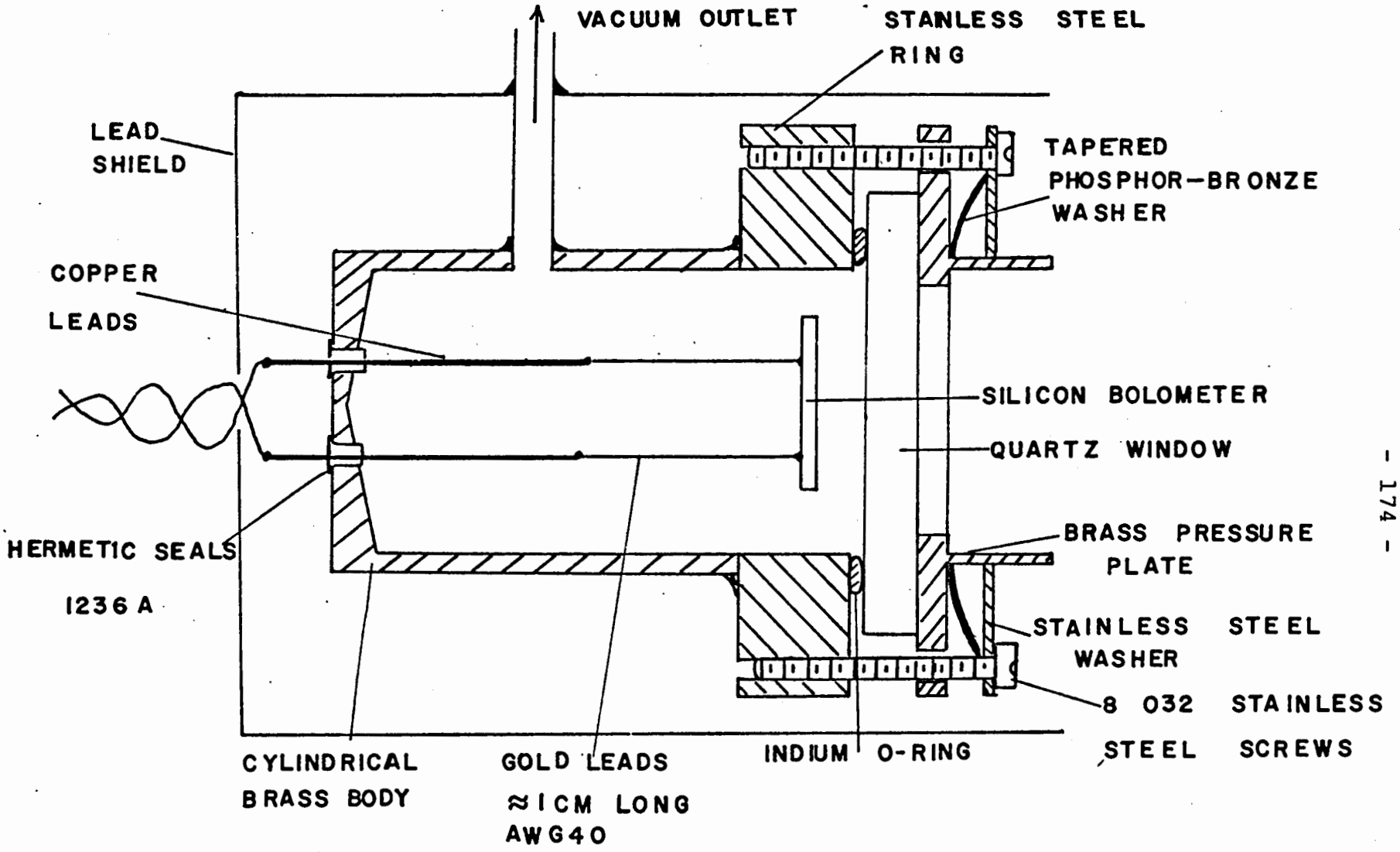

Fig. 5.7 Vacuum chamber for bolometer.

allowed for periodic checks of the chamber pressure.

To reduce the noise in the bias source circuit to an absolute minimum, the bias resistor was immersed in liquid He^4 at 4.2°K (Fig. 5.8). After some experimentation, a metal film resistor with a value of 7.5MΩ at 4.2°K was chosen. The bolometer bias current was supplied by a 7 volt Mercury cell as shown. The bias current could not be increased beyond about 1μA for the Silicon bolometer, since one had to avoid producing a dc voltage drop across the bolometer of greater than 1 volt. Higher voltages produced a breakdown effect which interfered with the response. The output voltage was detected differentially by a phase-sensitive detector (Princeton Applied Research Model HR-8) with a type A plug-in preamplifier. This was externally referenced to the modulation frequency of the incident signal. The shield for the three leads which were twisted together and which extended to within ∿ 1" of the bolometer, was carefully grounded to the case of the measuring circuit which had the same ground potential as the input to the PAR preamplifier. The bolometer itself was not at ground potential.

To measure the absorbed power sensitivity of the bolometer at the microwave frequencies of interest the change in the bolometer ac resistance (33Hz) produced by an unknown microwave power at 70GHz was duplicated by a known Joule heat

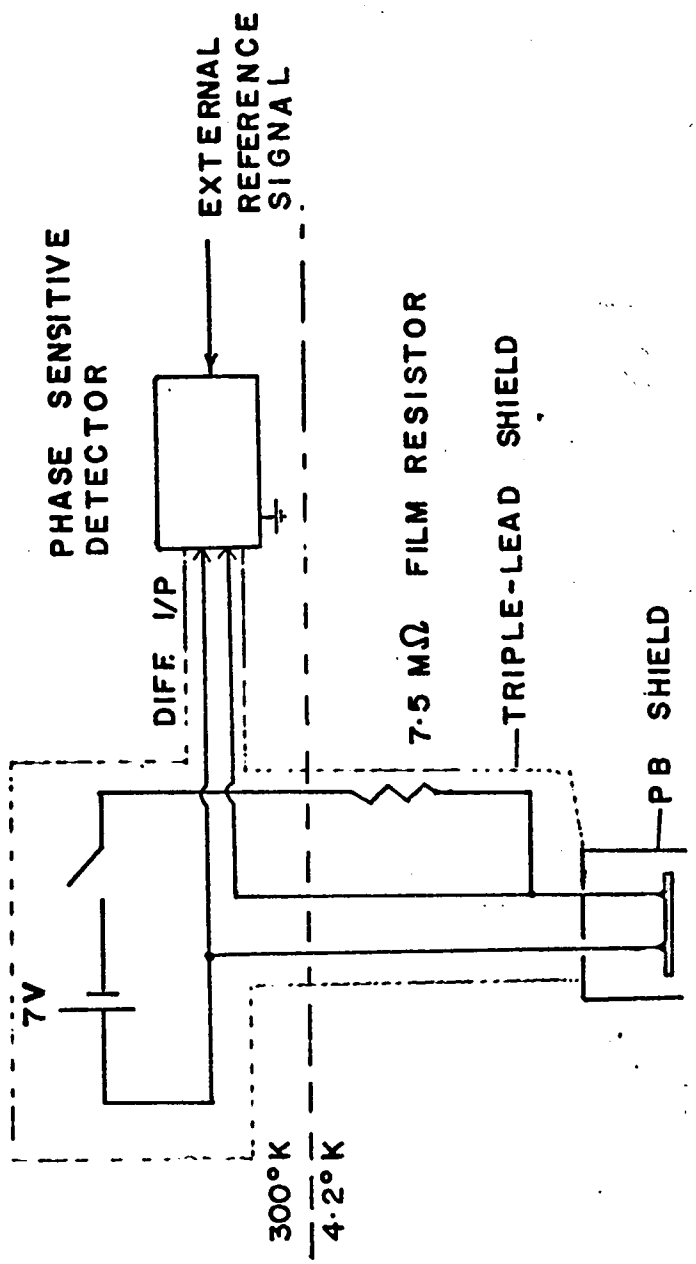

Fig. 5.8 Bolometer detection circuit.

produced by a steady current through the bolometer. For this purpose the circuit of Fig. 5.9 was employed. The bolometer ac resistance was measured by passing a small ($\sim 10^{-8}$A) current at 33Hz through the bolometer and detecting the voltage appearing across the bolometer by means of the differential i/p to the PAR. The reference source was isolated from the bolometer circuit by a low impedance transformer. The ac current was determined from the ac voltage appearing across a precision (1%) 10KΩ resistance. A calibrated Hewlett Pachard Model 214 oscilloscope was used here, operated in the differential input mode. The bolometer was first biased with a dc current of about 0.8μA selected by means of the ten-position rotary switch. The dc current was then measured as well as the ac resistance. The dc bias current was reduced by approximately 10% and the ac resistance then restored to its original value by externally heating the bolometer with 70GHz microwave power. The microwave power was modulated at 15KHz, a frequency the bolometer could not follow - thus the bolometer responded as it would to a dc average power. Using this technique one could obtain a rough idea of the amount of power absorbed. The bolometer transmittance varied with frequency - generally reducing with frequency. Discussion of the transmittance and reflectance of the Silicon bolometers with the manufacturers(*) led to the conclusion that at a frequency of $3cm^{-1}$ there was a transmittance of $\sim$ (55 - 60)% and a roughly constant reflectance

---

* See page 173

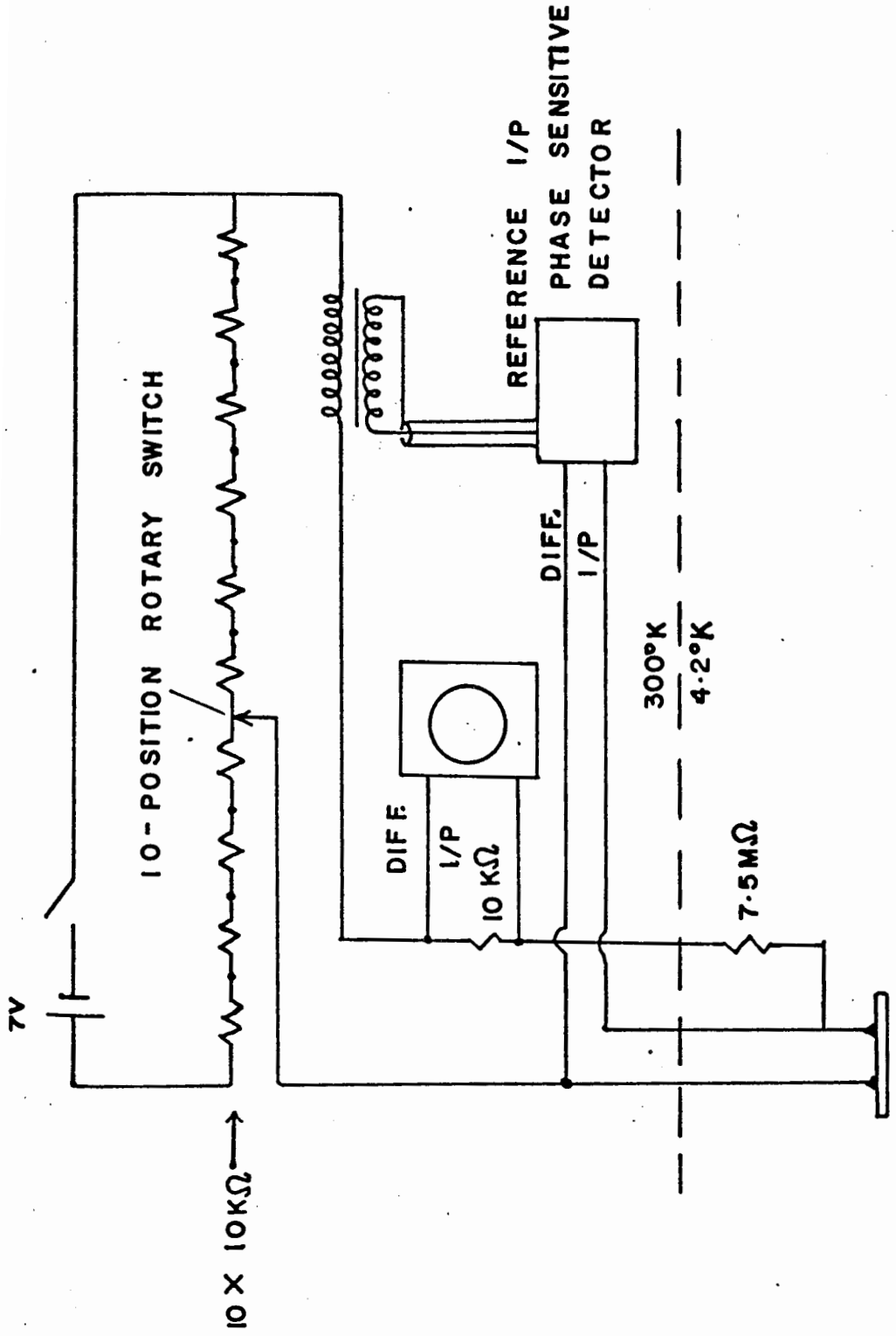

Fig. 5.9 Bolometer power calibration circuit.

of $\sim$ 28% leaving $\sim$ (12 - 15) % absorption.

5.3.7 Noise Considerations

The bolometer is ultimately limited by noise and the sources which will affect the sensitivity are:

(i) Noise in the bias battery.

(ii) Noise in the bias resistor.

(iii) Noise in the contact between leads and the bolometric element.

(iv) Extraneous black body radiation.

(i) Battery noise has been investigated by Knott[123]. He concluded that a dry Leclanche cell at 300°K has an intrinsic rms noise voltage $\sim 10^{-9}$V. (No information on the Mercury cells was found.)

(ii) If one applies the Nyquist formula for the noise in a bias resistance R at temperature T one finds an rms noise:

$$\sqrt{\overline{V_N^2}} = \left(\int 4k_B T R \, df\right)^{1/2} \qquad 5.315$$

For a bandwidth of 0.2Hz, (which is reasonable for a risetime of 5 secs in the PAR with a Q-value $\sim$ 10 at 33Hz), one obtains for R $\sim$ 8MΩ at 4.2°K:

$$\sqrt{\overline{V_N^2}} \sim 5 \times 10^{-8} \text{ volts}$$

(iii) Noise in the lead contact to the bolometric element was lowest for the Silicon bolometers. The technique of manufacture involved diffusing Gold into the semiconductor to form a truly degenerate region and then bonding the Gold leads to this diffused region.

(iv) Black polyethylene was taped in front of the quartz window for some runs but no appreciable reduction in the noise reaching the PAR input was observed. For no external radiation to the bolometer, the PAR could be operated on the most sensitive scale (100nV sensitivity) with an rms noise approximately 15% full scale.

5.4 Cryostat and System Electronics

During the preliminary studies of the R-SQUID it became evident that the detector output was strongly affected by spurious external signals especially those containing appreciable megacycle components. For example, the operation of a 5MHz excitation circuit for an Argon-ion laser in a nearby laboratory tended to swamp any signals which could be detected from the 70GHz klystron. Shielding the R-SQUID with Lead foil did not help appreciably, and it appeared that many signals were picked up at the tank circuit input. The presence of these external signals hastened the dismantling of the vacuum and dewar system for removal to a screened room facility available in the department. For

certain frequencies eg in the 100MHz range, this room when sealed had a measured attenuation factor of > 100db.

The main cooling system was a conventional liquid nitrogen-liquid helium pair of glass dewars. The liquid nitrogen level was controlled within three inches of a constant level near the dewar top by utilising the level sensing circuit outlined in Appendix B. For temperatures below 4.2°K the station could control the Helium bath temperature to within 0.01°K. Above 4.2°K the control was less efficient and the temperature fluctuation larger ($\sim$ 0.05°K).

The physical arrangement of the tunnel junction, R-SQUID and silicon bolometer is shown schematically in Fig. 5.10 with a vertical plan view in Fig. 5.11. The Ta needle - SQUID separation was $\sim$ 2cm, whereas the Ta needle-bolometer separation was $\sim$ 3cm. Not shown is a microwave horn used to direct 70GHz radiation towards the R-SQUID and the bolometer for sensitivity checks prior to searching for radiation from the tunnel junction.

To reduce the effects of external noise on the R-SQUID and bolometer responses, a bucket shaped superconducting shield of lead foil completely enclosed the tail end of the cryostat extending to at least six inches above the top of the vacuum can flange (Fig. 5.10).

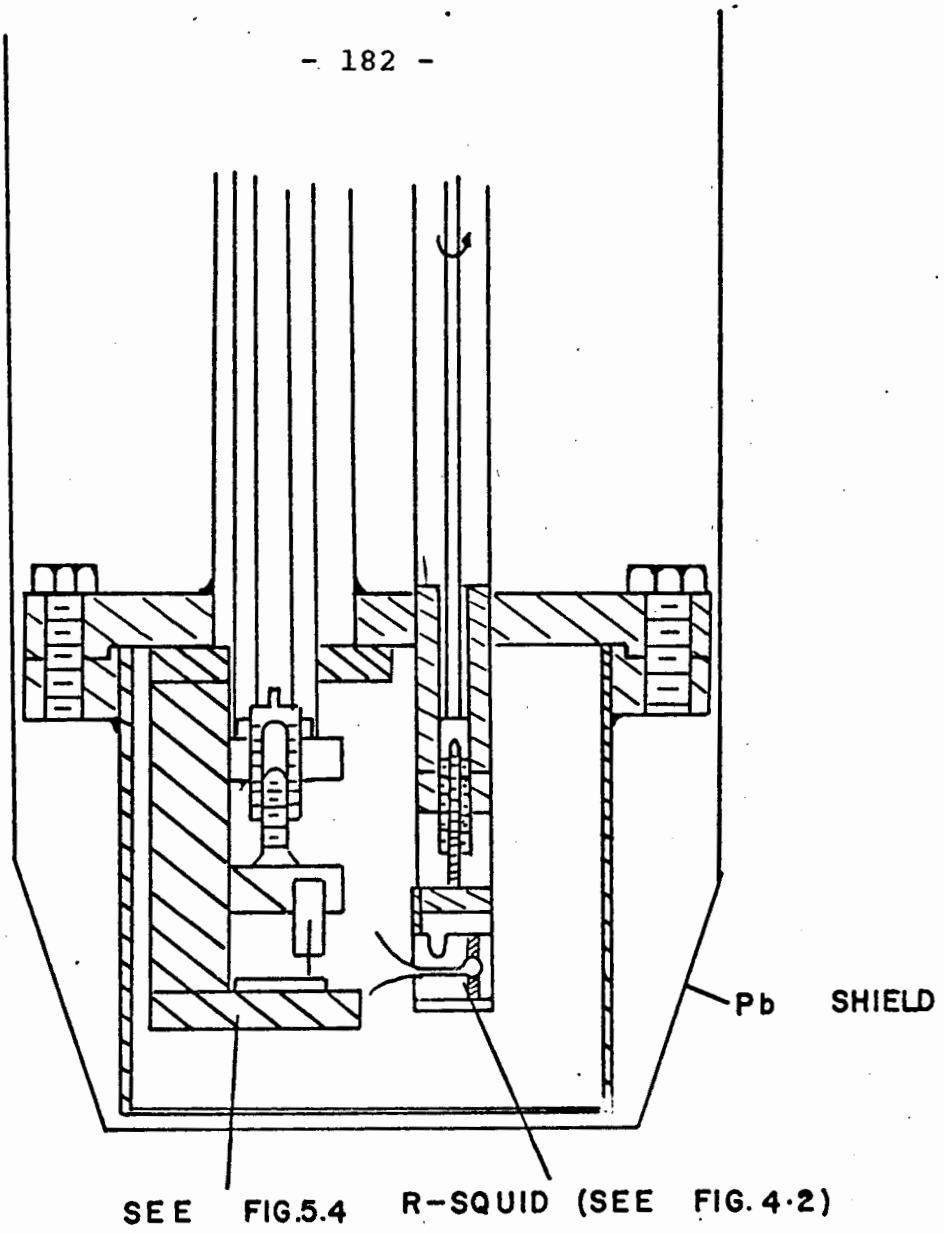

Fig. 5.10 Cryostat vacuum chamber showing R-SQUID system and Ta tunnel junction.

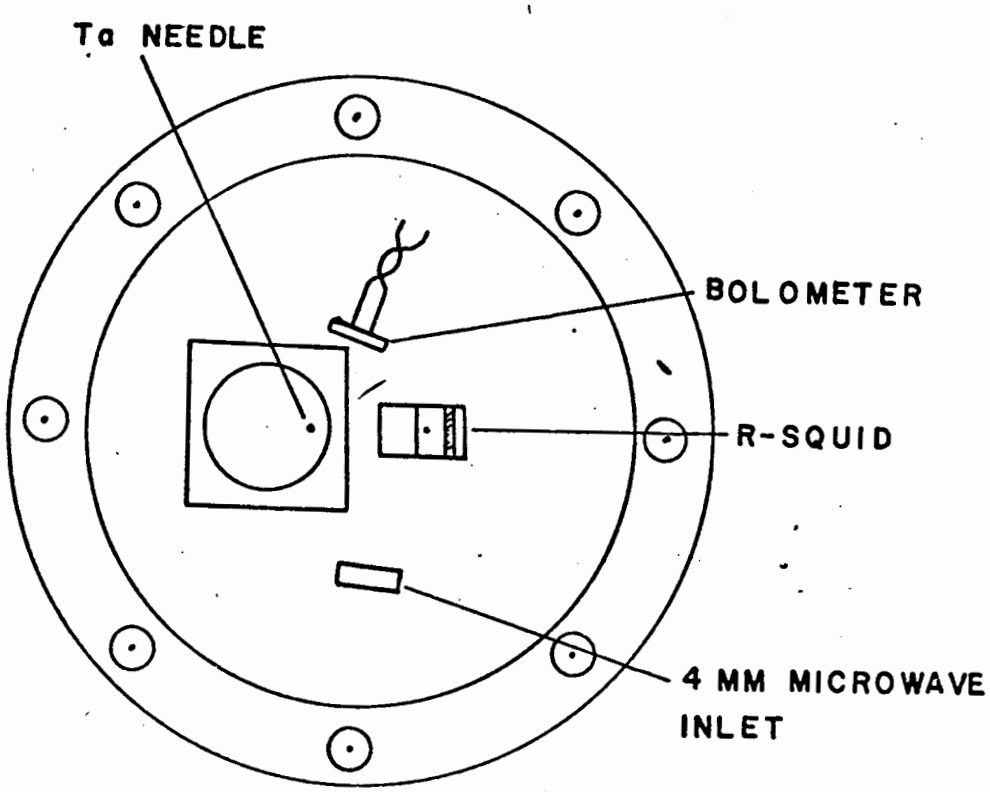

Fig. 5.11 Vertical view of geometrical arrangement of R-SQUID, Ta needle, and bolometer.

The complete electronics for the superconducting maser experiments is shown in schematic form in Fig. 5.12. The R-SQUID system of electronics was identical to that employed already (Fig. 4.4), and the bolometer bias and detection circuit has already been described (Fig. 5.8).

The tunnel junction could be driven from either pulsed or continuous current sources. In Fig. 5.12, a low frequency current (33Hz) could be obtained from a Dynakit power amplifier with peak amptitude ranging between zero and three amps. Since the tunnel junction impedances were normally $\sim 1\Omega$, these large currents often had a destructive effect due to excess Joule heating at the Ta tip. Accordingly, for many runs, the pulse circuit of Fig. 5.13 was used to drive the junction. The Tektronix Model 214A pulse generator could supply pulses of variable amplitude, duration, and repetition rate into a load of 50Ω. This generator had an internal oscillator which could be used to externally reference the bolometer and R-SQUID phase sensitive detectors (Fig. 5.12). For most of the experiments, pulses of amplitude 0 - 2 amps, duration 10 - 20 μsec, and repetition rate 1KHz were employed. The current amplitude was measured by passing the central lead of the pulse-carrying coaxial cable through a calibrated transformer loop (Tektronix CT-1 015-040, sensitivity 5mV/mA). The induced voltage in this transformer, as well as the voltage appearing across the tunnel junction

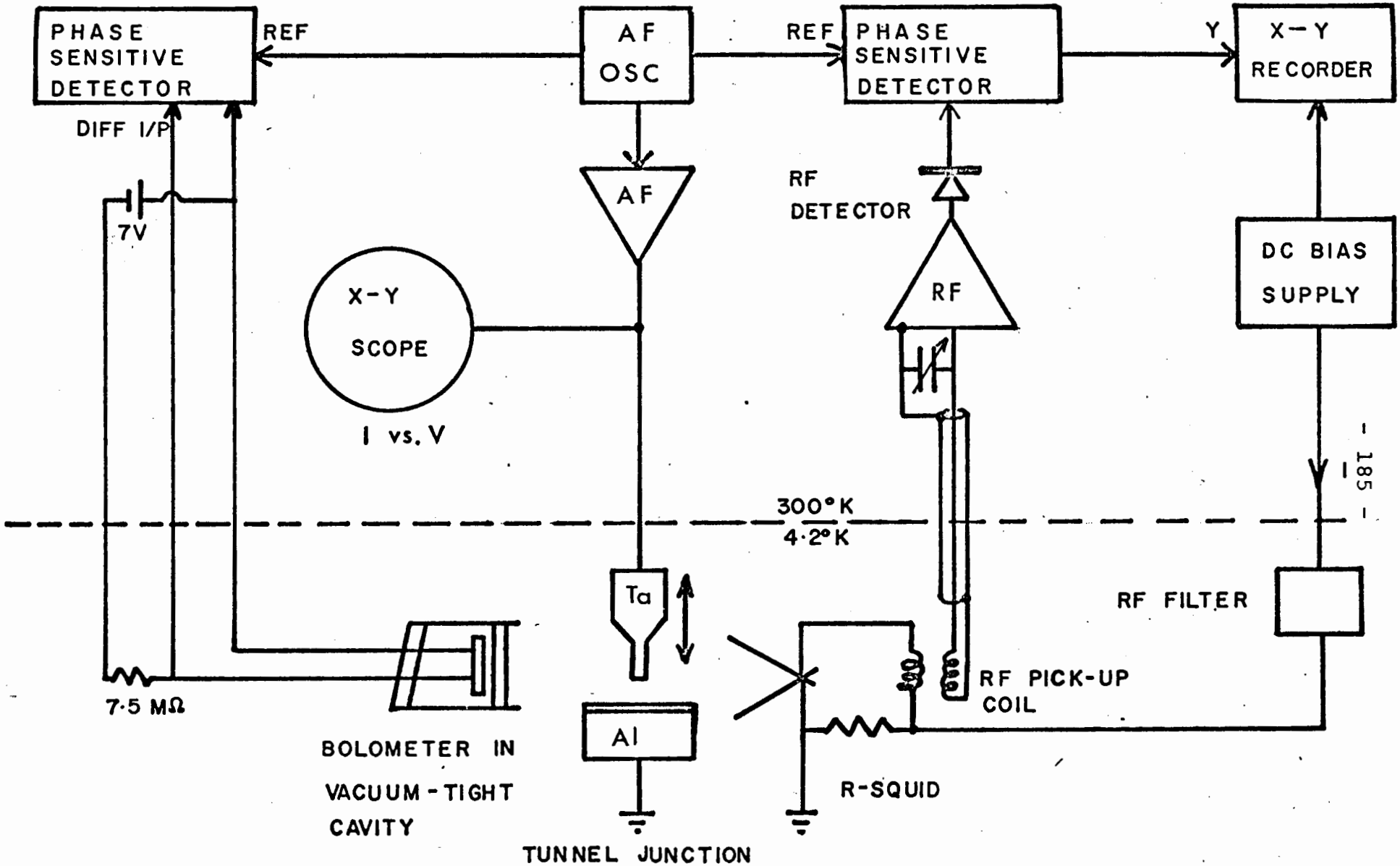

Fig. 5.12 Electronic Schematic for simultaneous detection of tunnel junction radiation by the R-SQUID and bolometer.

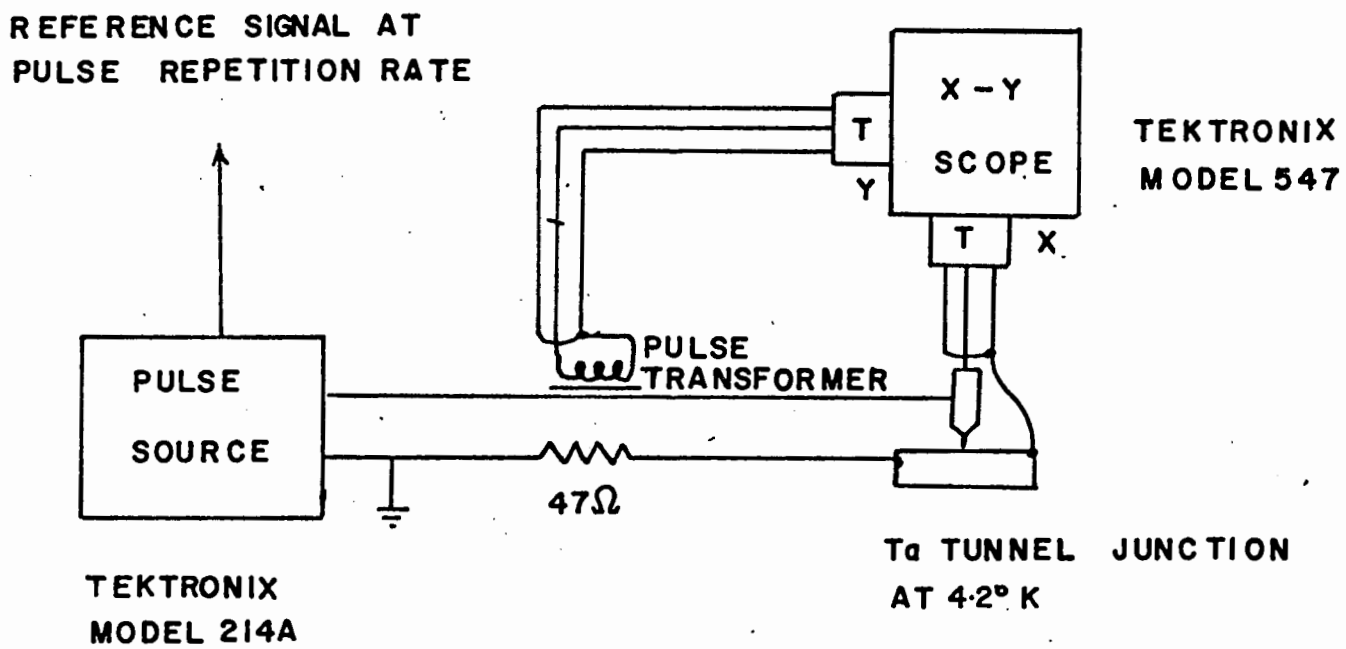

Fig. 5.13 Pulse circuit for driving Ta tunnel junction. T= 50Ω coaxial termination.

contact could be measured with a Tektronix oscilloscope Model 547 with a type 1A1 plug-in unit. For observing the pulse edges, a fast risetime sampling plug-in unit Tektronix type 1S1, was also available.

In order to improve the coupling between the expected junction radiation and the R-SQUID, many experiments were performed using the waveguide system sketched in Fig. 5.14. A short length of 4mm waveguide, type RG98/u, was positioned on the differential screw assembly (Fig. 5.5) in such a way that the Ta needle could be adjusted vertically through a small hole in the centre of the broad section of the waveguide. Inside the waveguide, the Ta tip made contact with a thin anodised Al plate electrically insulated from the guide walls. The needle was positioned approximately $5\lambda_g/4$ from the guide end away from the R-SQUID where $\lambda_g = \lambda \ (1-(\lambda/\lambda_c)^2)^{-1/2}$, λ is the free space wavelength and λ_c is the cut-off guide wavelength. For Ta at 4.26°K, with T_c = 4.39°K, one expects energy gap radiation where $\lambda \sim$ 3mm assuming the BCS theory applies. Thus for the lowest TE_{01} mode where $\lambda_c = 2a$ = 7.5mm (40GHz) one has λ_g = 3.3 mm. Of course the best system would consist of mounting the tip at a low impedance point in a tunable cavity (eg as in reference 44,) and then adjusting the tuning for each wavelength of interest. However the system of Fig. 5.14 should be an improvement over the isotropic situation Fig. 5.12 merely by directing more of

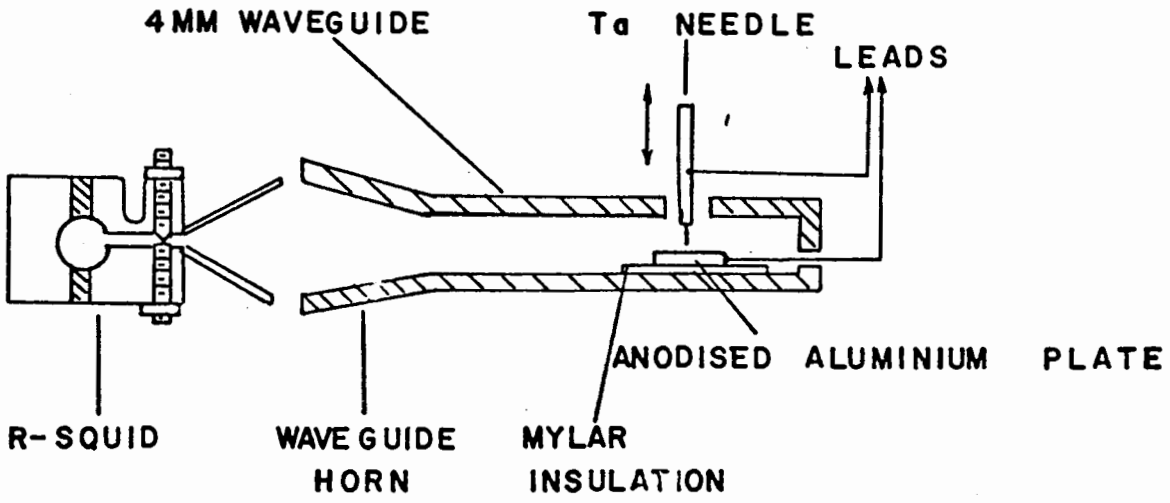

Fig. 5.14 Waveguide experiments with Ta tunnel junctions.

the emitted radiation towards the SQUID point contact via the guide output horn.

In order to determine if there was any tunneling structure present, the sweep circuit of Fig. 5.15 was employed. This circuit was completely battery operated and the voltage sweep (in the mV range) was provided by driving one of the 10-turn potentimeters by a multigear motor.(*) Either d.c. I vs V or the derivative $\frac{dI}{dV}$ vs V could be measured. The latter measurement involved applying a small ($v_1 \sim 10\mu V$) a.c. voltage at 1 KHz across the tunnel junction plus 1 Ω load. The voltage appearing across the 1 Ω was then measured using the differential input to a phase-sensitive detector, Princeton Applied Research model HR-8. To first order in v_1 this voltage was proportional to dI/dV.

---

* Insco Motor Corporation
Groton, Massachussetts, U.S.A.

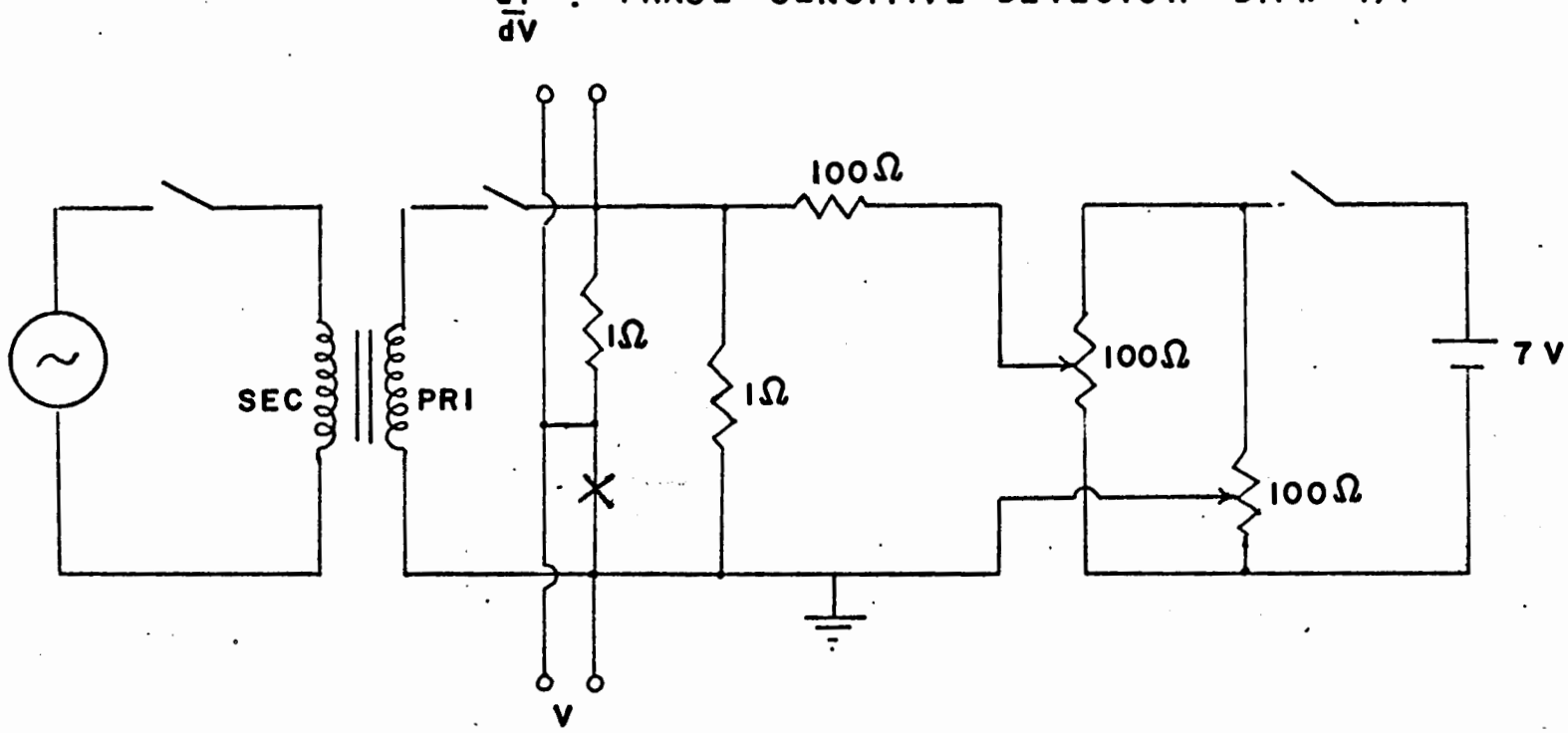

Fig. 5.15 Battery operated I vs V, dI/dV vs V sweep circuit.

Oscillator : Hewlett Packard Model 204B

Transformer : Geoformer Model G-10

✳ : Tunnel Junction

CHAPTER VI

EXPERIMENTAL RESULTS AND ANALYSIS

6.1 Superconducting Properties of Tantalum Metal

Some preliminary measurements were made on the Ta metal used to construct the tunnel junctions. These included estimates of T_c — the superconducting transition temperature, σ_N— the normal state conductivity just above T_c, and j_c— the critical current necessary to destroy superconductivity. Tabulated values for T_c vary between 4.39°K and 4.46°K depending on the purity of the sample, and also whether or not films or single crystals of Ta are employed.

To measure T_c and σ_N, the resistance of a Ta wire sample was measured (by a four-probe technique) as a function of temperature in the variable temperature dewar system. Four copper leads were spot-welded to a piece of 0.03" diameter Ta wire with 2 cm separating the voltage leads. Current was supplied by a Hewlett Packard dc power supply Model 6200B, and the voltage drop across the Ta sample measured using a Keithley Model 147 Nanovolt Null Detector. Various measuring currents were employed ranging from 50 mA to 500 mA. A plot of the wire resistance (R) as a function of temperature (T) is shown in Fig. 6.1 where a relatively broad transition is indicated. The transition temperature T_c was taken to be at the point of maximum $\frac{dR}{dT}$ where a sharp jump in the sample voltage was observed. The measurements gave an averaged value

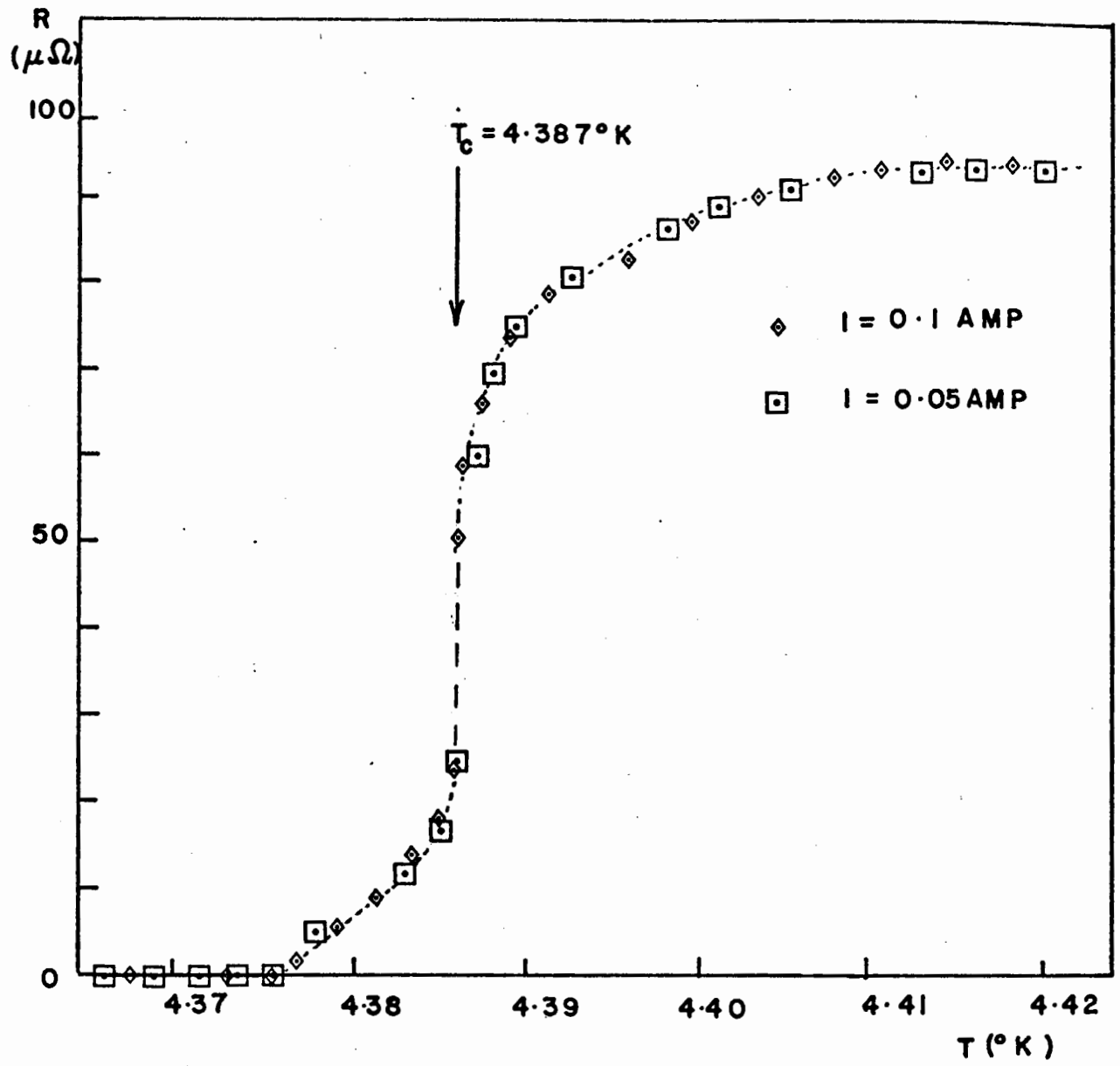

Fig. 6.1 Determination of the critical temperature T_c for Ta.

T_c = (4.387 ± 0.003)°K, in agreement with published data (4.39 - 4.46)°K. The normal state resistivity was $\sigma_N = 6.3 \times 10^{-11}$ Ω - m leading to $\sigma_N = 1.42 \times 10^{20}$ sec^{-1}.

An estimate of the critical current density necessary to destroy superconductivity was obtained as follows. A 3 cm length of 0.03" Ta wire was machined as before to the shape shown in Fig. 5.2, with approximately equal lengths on either side of the milled section. Copper leads were carefully spot-welded to the Ta wire and the Cu-Ta contact areas then sealed with epoxy. The Ta wire was then mounted in the electropolishing apparatus (Fig. 5.3) and the neck diameter reduced to a value in the range 20μm - 70μm. This etched wire was then mounted on a dip-stick and cooled to 4.18°K. The dc current at which resistance first disappeared was determined by using a four-probe technique. The measured values of the critical current, I_c, are given in Table 6.1 for a number of Ta wire diameters together with a theoretical estimate of I_c and j_c. The wire diameter quoted is the smallest one obtained during the etching process. The theoretical estimate of I_c is obtained from Silsbee's rule[124] where, for a wire of diameter 2a, the critical current is

$$I_c(T) = 5 H_c(T).a \qquad 6.101$$

with I_c in amps, a in cm, and $H_c(T)$, the critical field, in gauss. $I_c(T)$ was measured and calculated using equation 6.101 at T = 4.18°K for comparison with the experiments of Gregory

et al.[10]. The value of $H_c(T)$ can be found from the parabolic temperature law for the critical field, $H_c(T) = H_c(0)(1 - T/T_c)^2)$ with $H_c(0) \sim 800$ gauss or from experimental data[125]. A value $H_c(T) = (50 \pm 10)$ gauss was used for the calculation of j_c at $T = 4.26°K$.

The first point to note is that the experimental critical currents are approximately 40% lower than the theoretical values for the same temperature. This discrepancy may have several sources including: an overestimate of $H_c(T)$, geometrical effects, or the influence of the electrochemical etch on the Ta metal in the skin depth region where the current flows.

In order to determine if there was an appreciable difference for wires which had been machined, three wires were prepared with neck diameters 100μm, 120μm, 140μm, by grinding and polishing the Ta wire on a jeweller's lathe. The data for these wires is given in Table 6.1 and it is clear that the agreement with Silsbee's rule is somewhat better although the measured values are again lower than expected.

In the final column of Table 6.1 estimates of the critical current density are given assuming a uniform distribution of current ($j_c = I_c/\pi a^2$). This assumption is known to be inaccurate since the current flows in the London skin depth. However it is useful since these values give some idea of when the Ta wire will go normal. Also Gregory et al.[10] appear to have assumed a uniform current distribution when they determined

Table 6.1:Ta Critical Current Data

2a μm	I_c(Exp) T = 4.18°K (Amp/cm^2)	I_c(Theory) T = 4.18°K (Amp/cm^2)	J_c(Theory) T = 4.26°K (Amp/cm^2)
Etched Wire			
20	0.16	0.42	8×10^4
25	0.28	0.52	6.4×10^4
40	0.55	0.84	4×10^4
42	0.56	0.89	3.8×10^4
65	0.88	1.35	2.5×10^4
70	0.95	1.47	2.3×10^4
Machined Wire			
100	1.86	2.09	1.59×10^4
120	1.93	2.51	1.33×10^4
140	2.20	2.92	1.14×10^4

the threshold current density for masing action in Ta.

6.2 Experimental Search for Radiation

A typical experimental run involved first adjusting the R-SQUID point contact using the system in Chapter IV and then testing the device sensitivity by directing microwave radiation at 70 GHz towards the R-SQUID slit (Fig. 4.4). Using the present system, a linewidth $\sim$ (10-20) MHz and sensitivity $\sim(10^{-11} - 10^{-12})$ watt were obtained for 70 GHz radiation. The geometrical arrangement allowed a fraction of the microwave beam to fall on the bolometer in its vacuum chamber and this detector could be tested simultaneously.

After obtaining satisfactory behaviour from both detectors, the Ta tunnel junction was adjusted. The preliminary contact adjustment involved sweeping out the dc and ac (33 Hz) I vs V curves for voltages in the mV range. For most contacts the I vs V curves were linear with resistances varying between 0.1Ω to 50Ω depending on the contact pressure and the junction oxide thickness. Since the contact was rather ill-defined it was impossible to correlate junction resistance with parameters such as oxide thickness or Ta tip diameter. Following Gregory et al[10], resistances in the neighbourhood of 1Ω were generally chosen.

On a few occasions slight nonlinearities were observed in the I vs V curve near zero voltage bias and dI/dV vs V curves

measured with the circuit of Fig. 5.15 yielded structure which could be interpreted as due to an energy gap $2\Delta \sim 0.5$ meV at $T = 4.20^{\circ}K$. However even with the derivative circuit, this structure was very weak and usually disappeared for injection currents exceeding 100 mA. The lack of a good tunneling characteristic is hardly surprising considering the oxide thicknesses usually employed (> 1000Å).

The initial experiments were carried out with the tunnel junction and detectors inside the vacuum chamber (Figs. 5.10, 5.11) containing a low pressure of Helium exchange gas. With this system however, it was found impossible to maintain the junction temperature constant while using continuous current injection. The initial experiments[10] and theory[101] indicate that for the emission threshold one requires a critical current density $j_c \sim 2 \times 10^5$ A/cm^2. For a cylindrical tip, diameter 25μm, this represents a peak current ∿ 1A through the junction (assuming a uniform distribution of current).

With only exchange gas present, heating of the Ta tip was inevitable and experimentally this was found to be the case. For 0.4A peak current at 33 Hz flowing in the junction at $T = 4.2^{\circ}K$ and an exchange gas pressure of 100 microns of He^4 gas in the main vacuum chamber, an equilibrium pressure increase of $\Delta p \sim 10$ microns was observed. For 500 microns exchange gas $\Delta p \sim 40$ microns. Application of Charles' Law indicates an ambient gas temperature increase of $\Delta T/T \sim 10\%$, which would drive the Ta tip normal. Thus heating of the Ta

tip at high injection currents is a crucial problem with this device, and similar effects were probably present in the system of Gregory et al[10]. No heating effect was observed in the exchange gas when the injection current was pulsed, but in order to duplicate the continuous current operation at 33 Hz, it was decided to operate the junction in liquid Helium. The vacuum chamber of Fig. 5.7 was then used to house the bolometer.

After suitable Ta contact adjustment, the tunnel junction ac current (33 Hz) was systematically increased in 20 mA steps up to a maximum of 2.5 - 3.0 amps peak, while continuously monitoring the outputs from the bolometer and the R-SQUID detection systems. The bolometric output was usually phase-sensitively detected at 33 Hz and 66 Hz. For each value of the junction injection current, the dc bias current through the R-SQUID was swept linearly with time covering a Josephson frequency spectrum of $\sim$ dc to $\sim$ 140 GHz. During the dc current sweeps $\sim 10^{-11}$ watt of 70 GHz radiation was usually incident on the R-SQUID to provide a marker frequency. The junction ac resistance (33 Hz) was monitored continuously during each run and provided a useful check on the junction behaviour as a function of injection current.

In conducting the search for radiation the tip diameter was systematically varied from 15μm to 50μm and the anodic oxide film from $\sim$ 500Å to $\sim$ 2500Å. Table 6.2 lists the

Table 6.2 Variation of Tunnel Junction Experimental Parameters

Tip Diameter μm	Oxide Thickness Å	Junction Injection Current Pulsed (0-2) A.	Junction Injection Current Continuous (33Hz) (0-3) A.	IN wave-guide	IN Liquid He^4	IN Exchange Gas	Results
15	1200		✓		✓		Negative
20	2000	✓	✓		✓		"
20	2500	✓	✓		✓		"
22	1500		✓		✓		"
25	1000		✓		✓	✓	Pressure change in gas
25	1500		✓	✓	✓	✓	" " " "
28	1500	✓	✓		✓		"
30	500		✓		✓		"
30	1000	✓	✓	✓	✓		Tip melted
30	1500	✓	✓		✓		"
33	1200	✓	✓		✓		"
33	1500	✓	✓		✓		"
35	500		✓	✓	✓		Tip melted
35	1500	✓	✓	✓	✓	✓	Pressure change in gas
35	2500		✓		✓	✓	" " " "
35	1500		✓		✓		Tip incandescent for ~30 secs.
40	500		✓		✓		"
40	1500		✓		✓		"
45	600		✓	✓	✓		"
45	800		✓		✓		"
45	1500		✓		✓		"
45	2500	✓	✓		✓		"
48	800	✓	✓		✓		"
50	1400		✓		✓		"
50	2000		✓		✓		"

variation of the tip diameters and oxide thicknesses together with the R-SQUID frequency spectrum sweep and the result of each combination. Many more runs were attempted with tips of diameter (25 - 30)μm and oxide thicknesses ∿ 1500Å.

For several of the tips constructed and operated in liquid Helium, the bath temperature was systematically varied from ∿ 4.10°K to 4.45°K in 0.02°K steps using the variable temperature dewar system. Also in some cases the bath temperature was pumped to below the λ-point to improve the heat conduction from the tip. However since from equation 5.101 the threshold current varies as $(2\Delta)^3$ this approach may be of dubious advantage. The increase in the Joule heat due to the increased threshold current density may in fact offset the improved conductivity.

Typical I vs V curves for dc and ac (33 Hz) currents are shown in Fig. 6.2 (i) and (ii) respectively. For bias voltages (0.3 - 0.5) volts, one generally observed a breakdown effect which was often reversible, but which occasionally led to a systematic decrease in the junction resistance as the junction current was increased. It must be stressed that this breakdown effect was not related to the superconductivity of Ta and was present both at liquid Nitrogen and room temperatures.

The effect is possibly associated with the high electric field gradient $(10^4 - 10^5)$ volts/cm across the oxide layer.

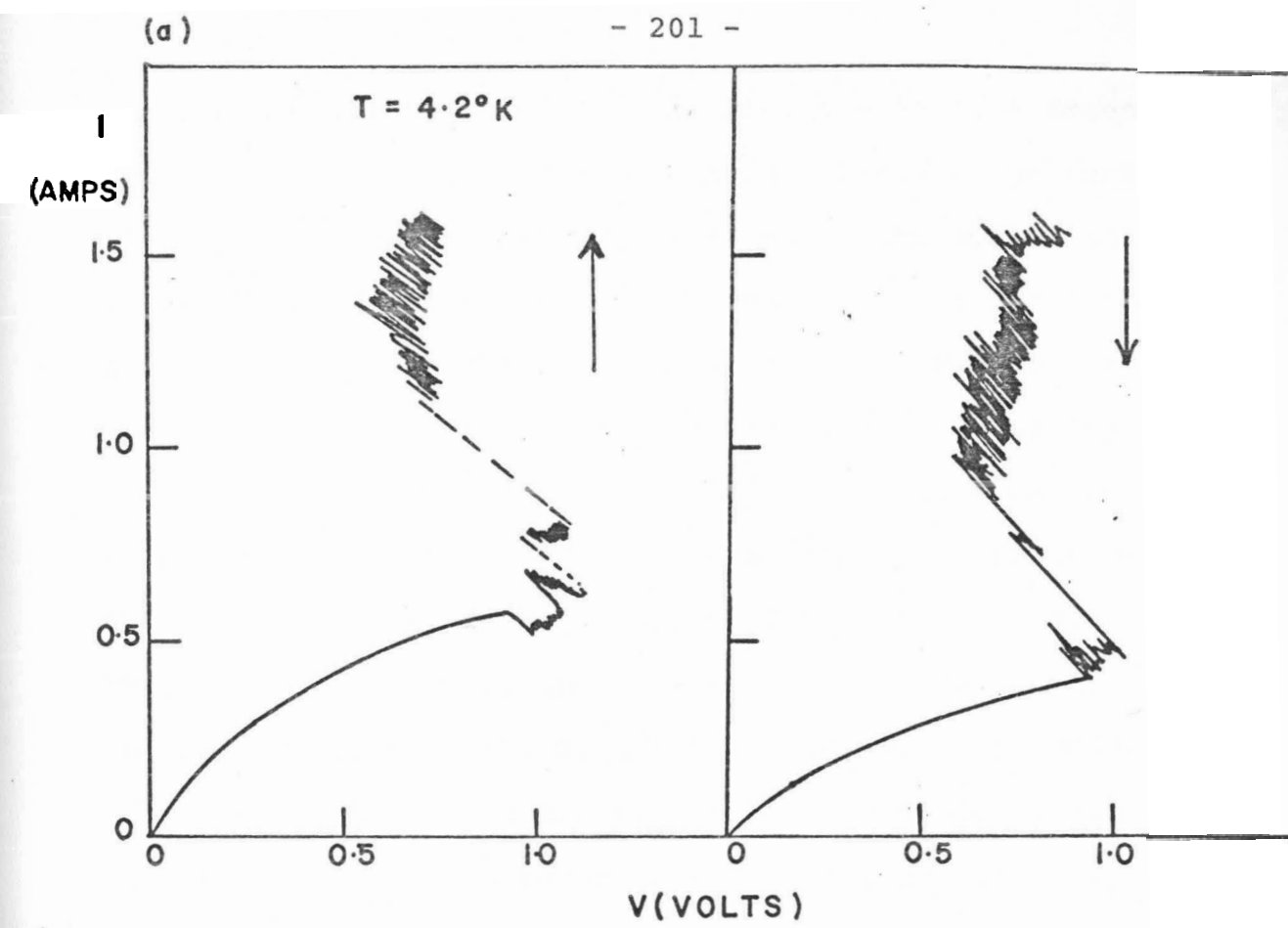

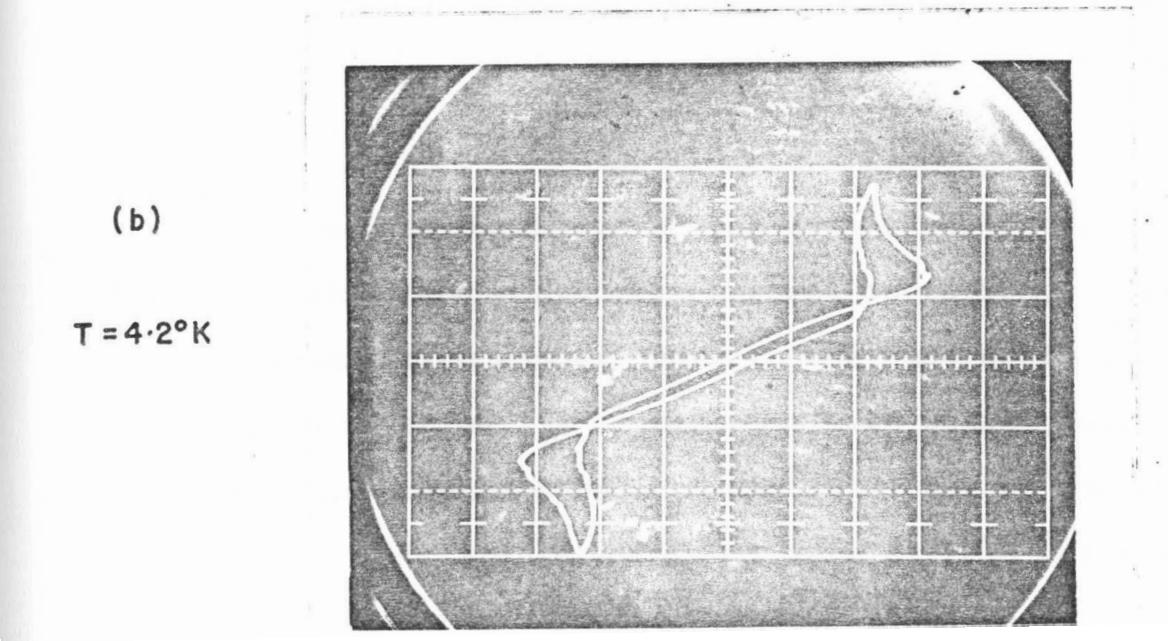

Fig. 6.2 (i) DC I vs V sweeps for Ta tunnel junction d = 30μm. Oxide thickness 1500 A.

(ii) AC I vs V sweep (33Hz) for Ta tunnel junction d = 25μm oxide thickness 1500 A.

I = 400 mA/div.
V = 500 mV/div.

For the experiments conducted in liquid Helium, a second explanation of the non-ohmic behaviour lies in the nucleation of gas bubbles at the contact where the Joule heating is greatest. Assuming that say 1 watt of heat has to be dissipated through the walls of a Ta cylinder diameter 30μm, length 100μm, one obtains a power density $\sim 10^4$ watts/cm^2. This greatly exceeds the threshold of 0.5 watts/cm^2 measured by Eastman and Datars[126] for formation of a Helium gas sheath at the surfaces of samples of Sb and Bi at 4.2°K. This gas sheath around the sample greatly reduces the thermal coupling to the liquid bath and causes a sudden increase in the sample temperature at threshold, which may result in a sudden increase in the sample resistance. However this boiling effect cannot represent a complete description since the non-ohmic behaviour in the I vs V curve is observed when exchange gas only is present.

Despite this extensive search summarised in Table 6.2 for both pulsed and continuous current operation, no narrow linewidth radiation associated with the superconductivity of Ta has been observed. The junctions were usually operated well into the breakdown region (Fig. 6.2) but no radiation was evident. It is interesting to note at this point that the radiation observed by the authors of reference 10 appeared at injection currents of similar magnitude to the values required for breakdown.

A number of effects did occur however. On some occasions, for ac peak currents $\sim$ 0.5A through a tip of diameter $\sim$ 30μm in contact with liquid Helium, the contact was suddenly broken. Post-experimental examination of the tip indicated that the Ta had melted leaving a small globule of metal at the end of the Ta needle (Fig. 6.3).

On one occasion when the tip could be viewed from outside the dewar, an incandescent white light suddenly appeared emanating from the tip region. This occurred for an injection current of $\sim$ 1A at 33Hz with the tip in liquid Helium. Unfortunately, this effect lasted only $\sim$ 30 secs and then extinguished. Despite repeated attempts no such effect was observed again.

6.3 Theoretical Analysis

As mentioned earlier, the theory of Leopold et al[101] relied heavily on the analogy with semiconductor lasers such as the p-n junction injection devices of GaAs etc. This approach is somewhat unsatisfactory since the resulting conditions for masing action depend closely on the superconducting material parameters, many of which were unknown for their experimental situation (Ta). While investigating the parameters chosen by the authors of references 10, 101, it became evident that their agreement with experiments was more than somewhat fortuitous. Thus there was an interest in improving the theory and deriving more general conditions

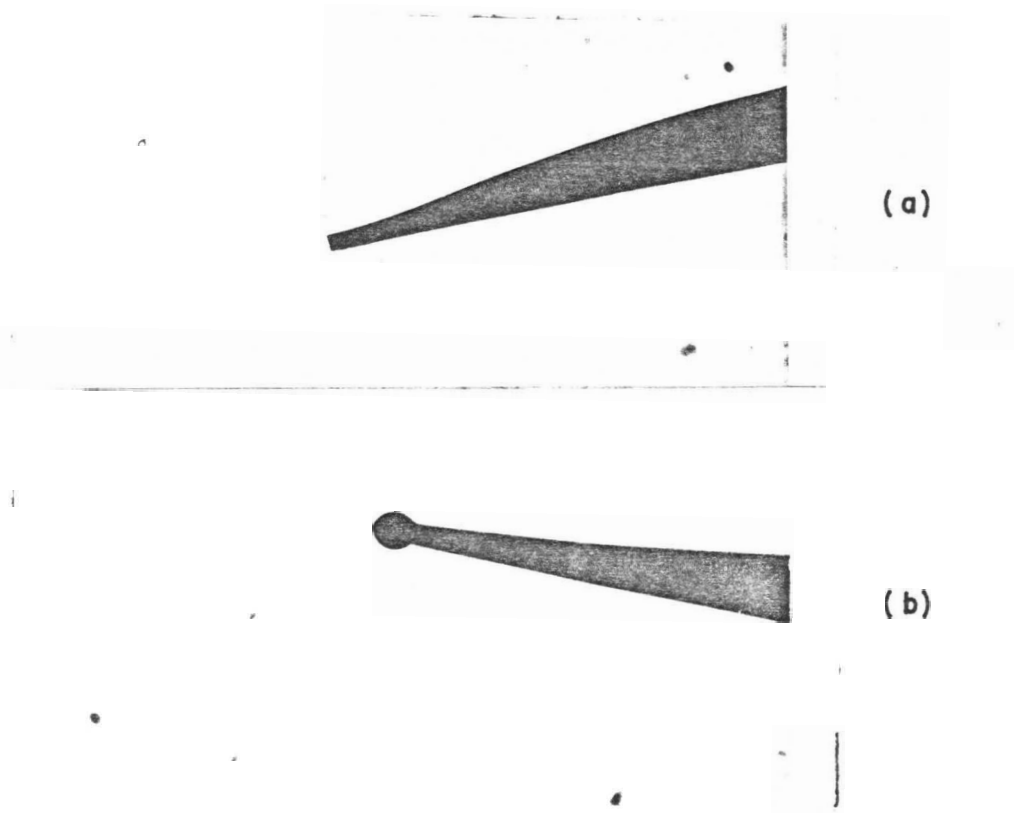

Fig. 6.3 Evidence for excessive heating at Ta contact:

(a) Before contact d ∿ 32μm.

(b) After contact with I ∿ 0.5 Amp at 33 Hz flowing.

for masing action in superconductors. (For example, there are the Bernard-Duraffourg relations for semiconductor lasers [127]. These may be shown to be necessary conditions for a superconducting maser system but they are insufficient.)

For the superconducting maser one can begin with the treatment for a two-level system where the intensity gradient per unit frequency may be written as[11]:

$$\frac{dI}{dz} = h\nu\left[N_2 A + (N_2 - N_1) B u(\nu)\right] \qquad 6.301$$

A^{-1} is the spontaneous recombination time for forming pairs from quasi-particles at the gap edge, and $(Bu(\nu))^{-1}$ the corresponding time for stimulated processes with $u(\nu)$ the energy density per unit frequency of the radiation field. A and B will contain the coherence factors which normally appear in the coefficient for absorption of electromagnetic radiation. (See for example the analysis by BCS[2], Tinkham[128], or Ginsberg and Hebel[129].) N_2 is half the number of quasi-particles within $h\delta\nu$ of the gap energy $2\Delta = h\nu$, and N_1 is the number of pairs within $h\delta\nu$ below the gap. The use of this simple model is based on the observation that quasi-particles injected into states above the gap will decay rapidly via phonon emission to the gap edge before they recombine. One then finds the usual expression for the gain g due to stimulating monochromatic radiation:

$$g = \frac{c^2 h^2}{8\pi\eta^2 (2\Delta)^2} \cdot A.(N_2 - N_1).\Xi \qquad 6.302$$

Where η is the real part of the refractive index of the superconductor ($\hat{n} = \eta + ik$), and $\Xi \sim (\delta\nu)^{-1}$ is the normalised line-shape function connected with the energy spread $h\delta\nu$ at the gap edge. Analytic expressions commonly used for Ξ are the Gaussian and Lorentzian distributions, which give the same magnitude for Ξ as the one expressed above.

In order to achieve maser action, the gain has to exceed the combined system losses, and the threshold current necessary to maintain this gain may thus be calculated. This approach leads directly to equation 5.101. It was stipulated that as long as the threshold current was smaller than the critical current necessary to destroy superconductivity, maser action was possible[101]. Although this is of course a necessary condition, it may not be sufficient.

In order to see this, A can be expressed in terms of some absorption process, generally following van Roosbrock and Shockley[113] in their calculation of the electron-hole recombination time in Ge. This was the procedure adopted by Burstein et al[114] to calculate a thermally averaged lifetime for Lead at 2°K, using the calculation by Mattis and Bardeen[130] and Miller[131] for the complex conductivity of the superconductor. For the present case, A is required for radiative recombination within $h\delta\nu$ of the gap edge rather

than a lifetime averaged over thermal energies. To obtain A, the principle of detailed balance is applied to the two-level system used before, and in thermal equilibrium one can equate the rate of radiative recombination of broken pairs to the rate of pair breaking due to absorption of black body radiation. The recombination rate may be written:

$$\frac{dN_2}{dt} = N_{2t}\left[A + B\,u(\nu)\right] f_{FD}\left(\Delta/k_B T\right)$$
$$= \frac{1}{2} N A\left[1 + f_{BE}\left(2\Delta/k_B T\right)\right] f_{FD}^2\left(\Delta/k_B T\right) \qquad 6.303$$

This rate must equal the pair-breaking rate:

$$\frac{dN_1}{dt} = N_{1t}\, B\, u(\nu)\left[1 - f_{FD}\left(\Delta/k_B T\right)\right]$$
$$= P(\nu)\, u(\nu)\, \delta\nu / h\nu$$
$$= \alpha_o \frac{8\pi\,(2\Delta)^2 \eta^2}{h^2 c^2} f_{BE}\left(2\Delta/k_B T\right)\delta\nu \qquad 6.304$$

Here $N_{2t} = 1/2\ N\ f_{FD}\ (\Delta/k_B T)$ is the number of broken pairs in thermal equilibrium within $h\,\delta\nu$ of the gap edge, and N is the number of available quasi-particle states within the same energy interval. Similarily $N_{1t} = 1/2\ N\ (1 - f_{FD}\ (\Delta/k_B T))$. $f_{BE}\ (x)$ and $f_{FD}\ (x)$ are the Bose-Einstein and Fermi-Dirac distribution functions respectively, $P(\nu)$ is the probability of photon absorption leading to pair breaking and α_o the corresponding absorption constant. From equations 6.302, 6.303, 6.304 one finds:

$$\frac{g}{\alpha_o} = \frac{2\,(N_2 - N_1)}{N}\left[\frac{\left(1 + e^{\Delta/k_B T}\right)}{e^{\Delta/k_B T}}\right]^2 \qquad 6.305$$

The largest overpopulation is achieved with $N_2 = 1/2\ N$ i.e. all available states filled. Charge neutrality in the superconductor then requires $N_1 = 0$. If α_o were the only loss present (pair breaking), then maser action would be possible as long as the temperature dependent factor in equation 6.305 is greater than unity. This factor is plotted in Fig. 6.4(a) and indicates a value of 1 at $T = 0$, and a value 4 at $T = T_c$. (The energy gap $2\Delta\ (T)$ was assumed to be given by Sheahen's empirical result[132]:

$$\Delta(t) = \Delta(0)\sqrt{\cos(\pi t^2/2)} \qquad 6.306$$

where $2\Delta\ (0) = 3.6\ k_B T_c$ and $t = T/T_c$. This formula agrees with the BCS energy gap curve to within 1%.)

At $T = 0^\circ K$, the only loss is due to pair breaking, since there are no quasi-particles which have been thermally excited. For this case with complete overpopulation, one obtains $g = \alpha_o$ and hence the maser cannot function.

For $T>0$, conditions appear to be more favourable especially as $T \to T_c$. However for this regime one must include the additional loss due to absorption by excited quasi-particles, which should become increasingly important as $T \to T_c$. The total loss has already been calculated by Mattis and Bardeen[130] for the anomolous skin effect in superconductors. The latter theory yields an expression

for the complex conductivity of a superconductor, and thus provides some connection between the microscopic processes involved in photon absorption and the Maxwell equations which define the macroscopic response.

Of interest are the following two Maxwell equations for the fields $\vec{B}$ and $\vec{E}$ (c.g.s. units).

$$\nabla \times \vec{B} = \frac{1}{c}\frac{\partial \vec{E}}{\partial t} + \frac{4\pi}{c}\cdot\vec{J} \qquad 6.307$$

$$\nabla \times \vec{E} = -\frac{1}{c}\cdot\frac{\partial \vec{B}}{\partial t} \qquad 6.308$$

In equation 6.307, the total current has been split into a vacuum displacement current and a term $\vec{J} = \hat{\sigma}\,\vec{E}$, where $\hat{\sigma}$ is the complex conductivity. On solving 6.307, 6.308 using fields of space - and time - dependence exp $(i\,(\vec{q}.\vec{r} - \omega t))$, one finds:

$$q = \frac{\omega}{c}\,\hat{\epsilon} \qquad 6.309$$

where $$\hat{\epsilon} = \left(1 + \frac{4\pi i \hat{\sigma}}{\omega}\right) = \hat{n}^2 \qquad 6.310$$

is the complex dielectric constant for a complex conductivity $\hat{\sigma}$ and complex refractive index $\hat{n}$. The present sign convention dictates that one must write:

$$\hat{\epsilon} = \epsilon_1 + i\epsilon_2 \qquad 6.311$$

$$\hat{\sigma} = \sigma_1 + i\sigma_2 \qquad 6.312$$

$$\hat{n} = \eta + ik \qquad 6.313$$

Solving for η, k in terms of σ_1, σ_2 one finds:

$$\eta = \sqrt{\frac{2\pi\sigma_N}{\omega}}\sqrt{\sqrt{\left(\frac{\sigma_1}{\sigma_N}\right)^2+\left(\frac{\sigma_2}{\sigma_N}\right)^2}+\frac{\sigma_2}{\sigma_N}} \qquad 6.314$$

$$k = \sqrt{\frac{2\pi\sigma_N}{\omega}}\sqrt{\sqrt{\left(\frac{\sigma_1}{\sigma_N}\right)^2+\left(\frac{\sigma_2}{\sigma_N}\right)^2}-\frac{\sigma_2}{\sigma_N}} \qquad 6.315$$

Here σ_N is the normal state conductivity.

The total absorption coefficient α'' is given for frequency ω by:

$$\alpha'' = 2k\omega/c \qquad 6.316$$

Mattis and Bardeen's theory allows one to calculate the normalised ratios σ_1/σ_N, σ_2/σ_N and hence α'' from equation 6.316.

The approach taken by Leopold et al[101] in determining the losses expected in the bulk superconductor, was to use the two-fluid model approach of F. London[1] (see also Werthamer[24]). However the two-fluid model leads to the Mattis-Bardeen result only in the limits of frequencies $\omega << 2\Delta/\hbar$, and long mean free paths $l >> \xi_o$, the Pippard coherence length[133].

Prior to the actual analysis, it is worth considering whether or not the anomolous limit is applicable to the Ta metal used in the experiment. Table 6.3 lists the appropriate parameters, and the relevant quantity is the ratio of the coherence distance ξ to the penetration depth λ. For a temperature $T/T_c = 0.975, \xi/\lambda|_{Ta} = 0.5$ which is certainly outside the anomolous limit ($\xi/\lambda >> 1$). However most experiments on the far-infrared absorptivity of superconductors have been conducted under circumstances where $\xi/\lambda \lesssim 1$[138]. Norman[134] quotes a value $\xi/\lambda = 0.05$ for a Ta film at $1^{\circ}K$ and yet obtains good agreement with the theory of Mattis and Bardeen[130]. Thus the latter theory appears to apply for situations outside the prescribed conditions and will be used in the present case.

Miller[131] has calculated the complex conductivity components σ_1/σ_N, σ_2/σ_N for various temperatures in the range $(0 - T_c)$ and for frequencies spanning the energy gap frequency. The ratio $\sigma_1/\sigma_N = 0$ for frequencies $\omega < 2\Delta/\hbar$

Table 6.3 : Tantalum Parameters.

Critical Temperature		$T_c = 4.39^{\circ}K$
Normal Conductivity		$\sigma_N = 1.42 \times 10^{20}/sec$
Fermi Velocity[134]		$v_F = 10^8 cm/sec$
Atomic Volume		$V = 10.1 cm^3$
Electron Density		$n' = 2.76 \times 10^{23}/cm^3$
Effective Mass[136]		$m^* = 1.65m$
Mean Free Path		$l_F = (m\, v_F \sigma_N / ne^2)$
		$= 3.4 \times 10^{-4} cm$
Scattering Time	$\tau' = l_F / v_F$	$= 3.4 \times 10^{-12} sec$
Coherence Distance ($l_F = \infty$)[136]		$\xi_o = 900\text{Å}$
Coherence Distance ($l_F \neq \infty$)[136]	: $\xi = (\xi_o^{-1} + l_F^{-1})$	$= 880\text{Å}$
London Penetration Depth (t = 0)		$\lambda_o = 540\text{Å}$
$\lambda(t = 0.975) = \lambda_o (1 - t^4)^{-1/2} (1 + \xi_o / l_F)$		$= 1730\text{Å}$
Density of States at the Fermi Surface[137]		$N(0) = 4.2 \times 10^{22}/eV/cm^3$
Specific Heat Coefficient[137]		$\gamma' = 5.8 mJ/mole/^{\circ}K^2$
Diffusion Constant for Quasiparticles		
$D = 1/3 \langle l_F v_F \rangle$		$= 3.4 \times 10^3 cm^2/sec$

where T = 0 and thus from equations 6.315, and 6.316, there is zero absorption until the gap frequency is exceeded. For $T > 0^{\circ}K$ there is a significant increase in the values of σ_1/σ_N for $\omega < \omega_g$ whereas σ_2/σ_N does not change appreciably. On the microscopic picture this implies that the single quasi-particle absorption process will begin to dominate the pair-breaking absorption at $T \to T_c$.

Using the values obtained by Miller it is possible to calculate the ratio of the total absorption $\alpha''(t)$ at reduced temperature $t = T/T_c$ to the pair breaking absorption $\alpha_o(t)$. Since the latter absorption is proportional to the number of condensed pairs (n_s) in the ground state, it is expected to scale appropriately with temperature becoming vanishingly small as $T \to T_c$. The temperature dependence used in the calculation was:

$$n_s(t) = n_s(0)(1 - t^4) \qquad 6.317$$

The ratio $\alpha''(t) / \alpha_o(t)$ is plotted versus t in Fig. 6.4 (b) for a BCS superconductor using a frequency width $\delta\omega = 10^{-5}\ \omega_g$ above the energy gap. (The reason for choosing such a small width is to maintain the current threshold for masing action (equation 5.101) below the current necessary to destroy superconductivity. The value of j_c increases linearly with $\delta\omega$.) The slope of the σ_1/σ_N curve at T = 0 near $\omega = \omega_g$ was taken to be $d(\sigma_1/\sigma_N)/d(\omega/\omega_g) = \pi/2$ [139].

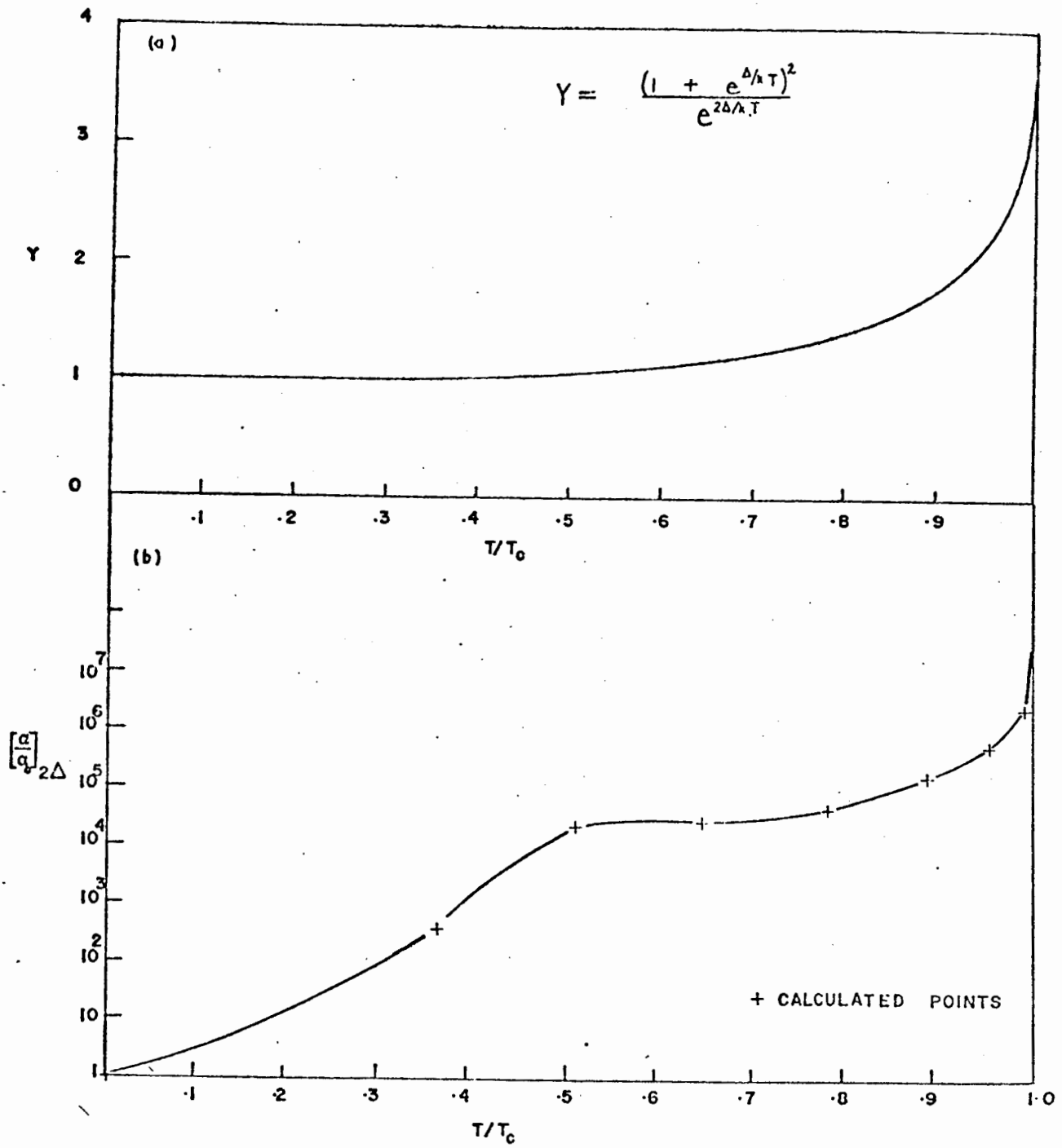

Fig. 6.4 Plots of (a) $Y = (e^{\Delta/k_BT} + 1)^2/e^{2\Delta/k_BT}$ vs T/T_c.

(b) $(\alpha/\alpha_o)_{2\Delta}$ vs T/T_c.

The significant feature of Fig. 6.4 is that the single quasi-particle absorption appears to dominate the pair-breaking absorption by several orders of magnitude in the range ($0.3 < t < 1$) a range most likely to produce masing action (Fig. 6.4 (a)). Of course the ratio $\alpha''(t)/\alpha_o(t)$ is much reduced by increasing the frequency width $\delta\omega$. However for values of $\delta\omega$ up to $\sim 10^{-2}\ \omega_g$ the ratio $\alpha''(t)/\alpha_o(t) >> 1$. For this latter frequency width, the value j_c greatly exceeds the value necessary to destroy superconductivity.

From the present analysis which is quite general, it appears that the superconducting tunnel junction maser cannot function. The flaw in the arguments of Leopold et al[101] is that there are only a limited number of states above the energy gap for obtaining stimulated gain. A formula such as in equation 5.101 is open-ended, and implies that if one pumps the system hard enough, the stimulated gain will eventually exceed the losses. The calculation in this section shows this to be a false interpretation, and the stimulated gain will saturate at a value less than the value necessary to overcome all the system losses.

Also evident are the limitations of using a two-fluid model to describe wave propagation in superconductors at energy gap frequencies. The two-fluid model leads to a so-called "Meissner damping loss", a macroscopic quantity which gives no hint of the complex processes taking place in the

superconductor during absorption. Leopold et al[101] deduce a loss $k_M \sim 10^4$ cm^{-1} for Ta at $\omega \sim \omega_g$. On the other hand, equation 6.316 yields a value $\alpha'' \sim 7 \times 10^5$ cm^{-1} for Ta at 4.26°K using the measured conductivity σ_N.

6.4 Criticisms of Earlier Experiments

The main criticisms which can be leveled at the previous experimental work revolve around the question of whether or not the Ta tip was superconducting while radiating. The two main factors which will destroy the superconductivity of the Ta are the high injection current and the Joule heating at the contact.

Leopold et al[101] state that the critical current density necessary to destroy the superconducting state is in the regime 10^6 - 10^7 A/cm^2. This is probably true for currents flowing in the London skin depth. However, what is measured in the experiment is the total current flowing through the Ta tip. The measurements of section 6.1 have yielded Silsbee critical currents less than the total current values quoted by the authors of reference 10 for the onset of radiative emission. Gregory[140] has recently argued that work hardening of the Ta metal tip during construction may cause the metal to develop type II superconducting behaviour, with greatly increased critical current density. The present author's experience with machined Ta wires of diameters

$\sim$ 100μm does not support this hypothesis (Table 6.1).

There was clear evidence in the present work of Joule heating at the Ta tip-oxide contact both the increase in He^4 exchange gas pressure and the strong bubbling of He^4 liquid for injection current $\gtrsim$ 0.5A. Melting of the Ta tip can be taken as an extreme result of this heating effect (Fig. 6.3). With the system in He^4 exchange gas, the main routes for heat conduction are through:

(a) The Ta tip and tip support.

(b) The anodic oxide - Al junction base.

(c) He^4 exchange gas.

The thermal conductivity of the Ta metal in the vicinity of T_c is not particularly high ($\sim$ 80 mj / mole / $^\circ$K) whereas that of Aluminium Oxide (Al_2O_3) may be much higher ($\sim$ 1j / mole / $^\circ$K). A calculation of the total thermal conductances available via the above mechanisms indicates that the Ta tip temperature must increase by at least 1°K while dissipating 1 watt of Joule heat. Thus operation in liquid He^4 is highly desirable but even in this medium strong bubbling is inevitable during current injection and the resultant gas sheath may prove fatal for stable operation.

If one studies the literature on p-n junction injection lasers[143], one finds that for injection currents below

threshold, a relatively broad band spontaneous output is observed. As the injection current is increased, the spontaneous output power also increases with the accompanying effect of line narrowing as threshold is approached. At threshold, sharp spikes appear in the frequency spectrum corresponding to increased output at normal mode frequencies of the resonant cavity. The important point here is that the threshold for lasing appears in the frequency spectrum rather than the power output. Thus with a broad band detector such as a bolometer, one should not observe a dramatic change in the output power unless there is some directional effect in the Ta cavity leading to increased output in the bolometer direction above threshold. (In the case of a cylindrical GaAs laser[144], a broad pancake of light was observed emanating from the plane of the junction which was perpendicular to the cylinder axis. An extensive description of the operation of such closed cavity lasers is contained in the book by D. Ross[145].)

The evidence which is hardest to criticise is given in reference 12 where data was obtained for the frequency output from the Ta junction versus temperature, which appears to follow a BCS energy gap curve. However this data is scanty (consisting of four check points!). Since it is relatively easy to drive the Ta metal normal using a magnetic field at $T = 4.26^{\circ}K$, one wonders why such a simple experiment was not attempted. Also, since the threshold

current varies as $(2\Delta)^3$ (equation 5.101), one expects an increase of $\sim$ 30 in the threshold current density if the He^4 bath is pumped from 4.26°K to 1.5°K, assuming the other parameters remain roughly the same. No data was reported on this effect.

A final point relates to the power threshold curve given in reference 10. Besides the analytic form suggested[10], this data has been found to closely follow the parabola

$$P = 7.8 \times 10^{-19} \ (J - 10^5)^2$$

where P is the power in watts and J the current density in A/cm^2. This would correspond to some radiative process having a sharp threshold at $J \sim 10^5$ A/cm^2, and varying in the same way as Joule heating. A square law variation of P with J is also supported by the fact that there was a ten-fold increase in the detected power at the first harmonic of the ac driving current as compared with the power detected at the fundamental frequency.

CHAPTER VII

SUMMARY AND SUGGESTIONS FOR FURTHER WORK

7.1 The M-SQUID

The main contribution to knowledge in this area has been the development of reasonably stable rugged devices using weak links of $NbSe_2$. The present technique of construction using mechanical contacts to the crystal does lead to device failure in some cases. The use of evaporated Pb contacts which may then be soldered to a suitable bulk body may solve this technical problem[151]. This latter technique may also reduce the rather large intrinsic noise estimated by Wheatley[98] for the present devices. (The $NbSe_2$ device noise was at least a factor of 20 greater than the noise in an equivalent point contact version.)

The main feature which was not understood with the present detectors was the size of the weak link critical current. From the measurements on the planar M-SQUIDS, this current appeared to be at least an order of magnitude larger than expected.

7.2 The R-SQUID

The study outlined in Chapter IV has indicated that point-contact R-SQUIDS can function as compact, highly

sensitive spectrometers in the microwave regime, at least for frequencies up to $\sim$ 70 GHz, with Q-values approaching 10^4. Despite the use of a comparatively crude radiation coupling scheme, a minimum detectable power sensitivity of $\sim 10^{-12}$ watt /$\sqrt{\text{Hz}}$ at 70 GHz was achieved. The systematic investigation of the response has indicated that the high frequency properties of the R-SQUID are only partially understood. The features which require elucidation are:

(a) The observation of a single line only in the heterodyne output at 30 MHz.

(b) The shape of this line (Fig. 4.9 (i)).

(c) The rf bias amplification effect (Fig. 4.9 (ii)).

(d) The variation of harmonic content in the output spectrum Figs. 4.7, 4.13.

(e) The response at 70 GHz for tiny contacts (Fig. 4.11).

The analysis presented in Chapter II leads one to expect a rather complex behaviour, even in the case of a weak link displaying ideal Josephson behaviour. Some or all of the above behaviour (a - e) may be due to the use of point contacts, since the coupling of radiation to such elements is not well understood.

7.3 The Superconducting Maser

The experiments and analysis presented in the first three sections of Chapter VI have raised serious doubts about the feasibility of constructing a maser using a superconductor. On the basis of the criticisms presented in section 6.4, the author feels that the data in the literature 10, 12, 13 is rather inconclusive. It is useless to speculate on the nature of the radiative output observed by Gregory et al until a much more detailed study is presented by those authors. Finally, a recent attempt by P. Wyder to duplicate the Gregory experiment using Nb tips has resulted in a radiative output which was not connected with any superconducting properties.

7.4 Suggestions for Further Studies

There is currently much activity in the field of Josephson tunneling and its applications. The present emphasis is more on the applied aspects of these effects and an interesting survey has been given recently by J. Clarke[147].

Extensions of the present work would include the use of fractional turn loops[72] in an $NbSe_2$ M-SQUID. The use of such loops would enable the weak link cross dimension to be larger. An interesting experimental sideline might also be the exploration of the proximity effect in such layer structures. The technique of anodising the $NbSe_2$ layers

has been unsuccessful but an overlayer of normal metal with a matching thermal expansion coefficient might not be as destructive as the oxide layer.

A logical step in the development of the R-SQUID would be the use of $NbSe_2$ weak links to replace the point contact. This structure would be expected to be stable and robust and would allow a detailed study to be made of the broad band response of the R-SQUID. Actually this approach was attempted several times by the author using a pressure contact system similar to that of Fig. 3.7 with a bulk body containing a resistive section sandwiched between superconducting pieces similar to Fig. 4.1. However no rf detection pattern was observed and no lines could be detected when the junction was irradiated with $\sim$ 1μ watt of 70 GHz power using the dip stick assembly of Fig. 4.3. The culprit was probably the superconducting contacts to the $NbSe_2$ crystal, since only one bulk body was constructed.

A simpler initial experiment would be to try and observe microwave induced steps in the dc I vs V characteristic. Due to their high normal state resistance R_N, such weak links should prove more sensitive to radiation than the evaporated Dayem bridges which usually have $R_N < 1\Omega$. A high value of R_N leads to a lower impedance mismatch between the junction and free space (377Ω). (Note that microwave-induced steps are not always observed with Dayem bridges even for

high incident powers e.g. in the case of NbN[93].)

The point contact R-SQUIDS were tested in two microwave regimes only (26.5 - 40) GHz, and (67 - 73) GHz. Theoretically the device should function up to frequencies $\sim 10^{12}$ Hz or even higher, and there is thus some interest in studying the device response to radiation from say an HCN maser at 891 GHz. With the high Q-values attainable $\gtrsim 10^4$ it should have possible to resolve some of the mode structure of such masers. Alternatively, the broad band response of the R-SQUID could be examined by either using the tail end of the Mercury spectrum or by using a He^4 discharge tube in a waveguide[148].

The R-SQUID sensitivity is good, but not the ultimate $\sim 10^{-14}$ watt /$\sqrt{Hz}$[147]. Higher sensitivity could be achieved with the present structure by mounting the point contact or other weak links in a tunable cavity which could be part of the R-SQUID structure. However, this will probably require some technical ingenuity.

The discussion of further studies up till now has been mainly of a technical nature concerned with improving the current state-of-the-art detectors. A more fundamental line of study would involve the examination of the superconductivity of $NbSe_2$ by tunneling. This has been attempted already by the present author in a brief but unfruitful study. Ten junctions of the form $NbSe_2$ - oxide - Al were

formed by growing an oxide in an $NbSe_2$ layer by the anodic technique (section 5.2). An Al overlayer of $\sim$ 2000Å thickness was then evaporated to complete the junction. The I vs V curves did not show the expected characteristic at $T = 4.2^{\circ}K$ ($T_c = 7^{\circ}K$), and dI/dV vs V curves tended to be rather complex, the most prominent feature being a gross zero bias anomoly whose shape changed considerably after the junction was warmed to room temperature. These results show that the anodic oxide layer presents a rather dirty barrier. Recently Frindt and Clayman[149] have measured an energy gap for $NbSe_2$ of $2\Delta(0) = 2.1$ meV using far-infrared absorption in thin samples. The BCS energy gap gave a reasonable fit to the temperature dependence. However no systematic structure was observed in the tunneling curves at $4.2^{\circ}K$ for this voltage bias. Probably more careful preparation of the oxide barriers will bring success. Once suitable junctions can be prepared, there is the possibility of observing phonon effects related to the two dimensional crystal structure. This study may also throw some light on the phenomenon of two-dimensional superconducitivity which has been raucously criticised by B. Matthias in a recent article[150].

Additional information on these phonons might be obtained by duplicating the Eisenmenger-Dayem experiment[108,152], using tunnel junctions of $NbSe_2$. Due to the fact that one can prepare $NbSe_2$ layers with almost exactly parallel surfaces, there exists the possibility of designing a cavity for these incoherent

phonons and thus producing a phonon maser. However, the theory of such a device has yet to be presented, but will probably follow the analysis of section 6.3 with modifications to cover the phonon case.

APPENDIX A

FOURIER ANALYSIS OF SQUID OUTPUT EMF

The pulse train can be initally Fourier analysed using the applied flux Φ_x as the expansion variable, where transients caused by circuit reactance are ignored. The emf is assumed to be a series of square pulses width τ, amplitude $\Phi_o \tau^{-1}$:

$$E = \frac{1}{2}a_o + \sum_n a_n \cos\left(\frac{2\pi n}{\Phi_o}\Phi_x\right) \qquad \text{A.1}$$

For convenience the a_n are converted to be functions of the time interval T between pulses and the transit time τ. Thus

$$a_o = \frac{2\Phi_o}{T} \qquad \text{A.2}$$

$$a_n = \frac{2\Phi_o}{\pi n \tau} \sin\left(\frac{\pi n \tau}{T}\right) \qquad \text{A.3}$$

In the limit $\tau << T$, the emf is independent of τ and becomes

$$E = \frac{2\Phi_o}{T} + \frac{4\Phi_o}{T} \sum \cos\left(\frac{2\pi n \Phi_x}{\Phi_o}\right) \qquad \text{A.4}$$

If $\Phi_x = \Phi_{DC} + \Phi_{rf} \sin \omega t$, then T is no longer constant but can be given approximately as

$$T = \frac{\pi}{2\omega} \cdot \frac{\Phi_o}{\Phi_{rf}} \qquad \text{A.5}$$

Finally

$$E = \frac{2\omega\Phi_{rf}}{\pi} + \frac{4\omega\Phi_{rf}}{\pi} \sum \cos \frac{2n\pi}{\Phi_o}\left(\Phi_{DC} + \Phi_{rf}\sin\omega t\right) \qquad \text{A.6}$$

where the oscillatory term may be expanded in a Bessel function series:

$$E = \frac{2\omega\Phi_{rf}}{\pi} + \frac{4\omega\Phi_{rf}}{\pi} \sum_n \sum_m \cos\left(\frac{2n\pi\Phi_{DC}}{\Phi_o}\right) J_m\left(\frac{2n\pi\Phi_{rf}}{\Phi_o}\right) \sin(m\omega t) \qquad \text{A.7}$$

APPENDIX B

NITROGEN LEVEL SENSING CIRCUIT

A schematic diagram of the nitrogen level sensing circuit is shown in Fig. B.1. The sensing element consisted of a pair of temperature sensitive diodes (type 1N191) enclosed in a 4" long probe formed by the diodes and a shield of heat shrinkable tubing to insulate the diodes from cold gas. The top diode D_1 had a high forward resistance at liquid nitrogen temperatures (16KΩ) while the diode D_2 had a low forward resistance at room temperature.

When both diodes were above the liquid nitrogen level a current of 18mA flowed through the solenoid (S_1) and closed the relay switch. This in turn actuated the solenoid valve (V) leading to a pressurisation of the LN_2 storage dewar and transfer began. As the filling proceeded, at some stage diode D_2 became covered and the solenoid current dropped to the value permitted by the 300 Ω shunt resistance, for this case ∿ 8mA. This current was still sufficient to energise the solenoid and the current did not drop below the solenoid cut-out value until diode D_1 was covered. This in turn de-energised the storage dewar pressurising solenoid value V and transfer ceased. As the LN_2 level gradually fell, D_1 became uncovered but in the cold gas there was still insufficient current to energise S_1 and the latter switch remained open

until D_2 was also uncovered. Once the initial diode current had been established this device proved to be extremely reliable and functioned perfectly over a three year period.

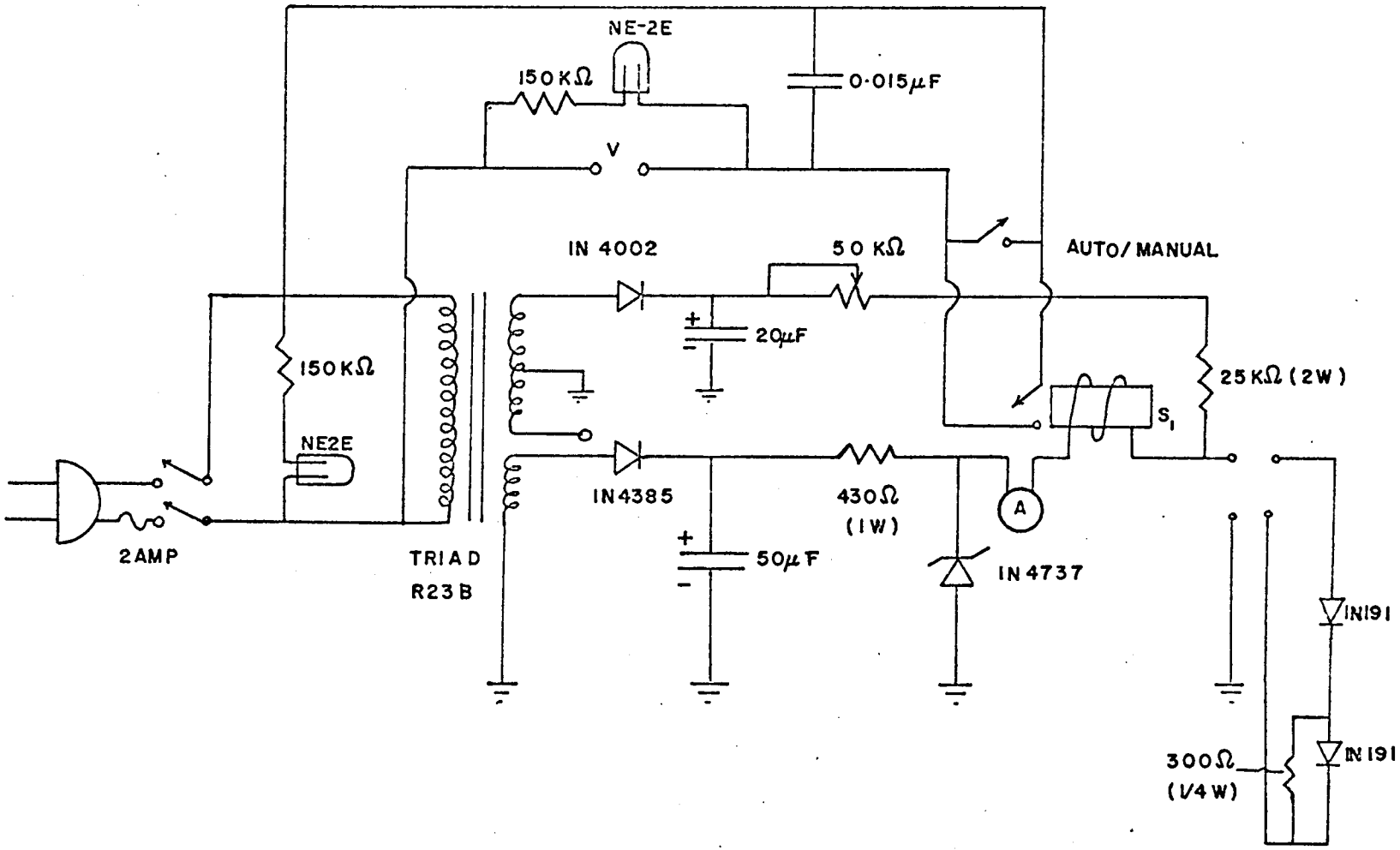

Fig. B-1 Electronic schematic of liquid nitrogen level sensing circuit.

V = General controls magnetic valve K25EW1532.

S_1 = Sigma relay 41F 200S SIL (200Ω Coil).

REFERENCES

1. F. London, Superfluids 1, (Dover 1960 2nd Ed.).

2. J. Bardeen, L. Cooper, J.R. Schrieffer, Phys. Rev. 108, 1175 (1957).

3. B. Josephson, Phys. Lett. 1, 251 (1962).

4. B. Josephson, Adv. in Physics (GB) 14, 19 (1965).

5. P. W. Anderson, in "Lectures on the Many Body Problem", Vol. II edited by E. R. Caianiello (Academic Press Inc., New York, 1964).

6. R. C. Jaklevic, J. Lambe, J. E. Mercereau, A. H. Silver, Phys. Rev. 140, A 1628 (1965).

7. A. H. Silver, J. E. Zimmerman, Phys. Rev. 157, 317 (1967).

8. J. E. Zimmerman, P. Thiene, J. T. Harding, J. Appl. Phys. 41, 1572 (1970).

9. F. Consadori, A. A. Fife, R. F. Frindt, S. Gygax, Appl. Phys. Lett. 18, 233 (1971), (Patent Pending).

10. W. D. Gregory, L. Leopold, D. Repici, Can. J. Phys. 47, 1171 (1969).

W. D. Gregory, L. Leopold, D. Repici, J. Bostock, Phys. Lett. 29A, 13 (1969).

11. A. Yariv, Quantum Electronics (J. Wiley 1967).

12. L. Leopold, W. D. Gregory, D. Repici, R. F. Averill, Phys. Lett. 30A, 507 (1969).

13. W. D. Gregory, L. Leopold, D. Repici, J. Bostock, R. F. Averill, Proceedings of the 12th International Conference on Low Temperature Physics (Kyoto, Japan 1970) p. 207.

14. B. Josephson in "Superconductivity" Vol. I, Chapter 9; Edited by R. Parks (Marcel Dekker, New York 1969).

15. P. W. Anderson, in Progress in Low Temperature Physics Vol. 5, p. 1, Edited by C. J. Gorter (North Holland, Amsterdam 1966).

16. J. Clarke, Am. J. Phys. 38, 1071 (1970).

17. J. Matisoo, IEEE Trans. on Magnetics 5, 848 (1969).

18. B. W. Petley, Contemp. Phys. 10, 139 (1969).

19. R. P. Feynmann, The Feynmann Lectures in Physics Vol. III, p. 21-1 (Addison-Wesley 1966).

20. V. L. Ginsburg, L. D. Landau, Soviet Physics JETP 20, 1064 (1950).

21. P. W. Anderson, J. M. Rowell, Phys. Rev. Lett. 10, 230 (1963).

22. V. Ambegaokar, A. Baratoff, Phys. Rev. Lett. 10, 846 (1963) ibid 11, 104(E) (1963).

23. E. Riedel, Z. Naturforsch, 19a, 1634 (1964).

24. N. R. Werthamer, Phys. Rev 147, 255 (1966)

25. C. A. Hamilton, S. Shapiro, Phys. Rev. Lett. 26, 426 (1971).

26. J. Clarke, Proc. Roy. Soc. (London) A308, 477 (1969). For theory see Ref. 38; also

L. G. Aslamasov, A. I. Larkin, Y. N. Ovchinnikov, Soviet Physics JETP 28, 171 (1969);

C. Ichii, Prog. in Theor. Phys. (Japan) 44, 1525 (1970).

27. P. W. Anderson, A. H. Dayem, Phys. Rev. Lett. 13, 195 (1964).

28. A. H. Dayem, J. Wiegand, Phys. Rev. 155, 419 (1967).

29. H. A. Notarys, J. E. Mercereau, R. Kirschmann, Phys. Lett. 34A, 209 (1970).

30. M. Nisenoff, Revue de Physique Appliquée 5, 21 (1970).

31. J. E. Zimmerman, A. H. Silver, Phys. Rev. 141, 367 (1966).

32. J. Clarke, Phil Mag. 13, 115 (1966).

33. S. A. Buchner, J. T. Chen, D. N. Langenberg, Phys. Rev. Lett. 25, 738 (1970).

34. D. E. McCumber, J. Appl. Phys. 39, 3113 (1968).

35. P. Hansma, J. N. Sweet, G. I. Rochlin, Bull. Am. Phys. Soc. 16, 399 (1971).

36. L. G. Aslamasov, A. I. Larkin, Soviet Physics, JETP Lett. 9, 150 (1969).

37. W. D. Stewart, Appl. Phys. Lett. 12, 277 (1968).

38. J. Clarke, B. Pippard, J. R. Waldram, To be published Physica (1971). Also presented at the International Conference on the Science of Superconductivity, Stanford (1969).

39. J. E. Zimmerman, D. B. Sullivan, Mechanical Analogues of Time Dependent Josephson Phenomena. Preprint 1971.

40. J. E. Zimmerman, P. Thiene, Phys. Rev. 177, 758 (1968).

41. S. Shapiro, Phys. Rev. Lett. 11, 80 (1963) and Rev. Mod. Phys. 36, 223 (1964).

42. C. C. Grimes, S. Shapiro, Phys. Rev. 169, 397 (1968).

43. I. Yanson, V. Svistonov, I. Dmitrenko, Soviet Physics JETP 21, 650 (1965).

44. J. E. Zimmerman, J. A. Cowen, A. H. Silver, Appl. Phys. Lett. 9, 353 (1966).

45. B. N. Taylor, W. H. Parker, D. N. Langenberg, Rev. Mod. Phys. 41, 375 (1969).

46. J. Clarke, Phys. Rev. Lett. 21, 1566 (1968).

47. T. Finnegan, A. Denenstein, D. N. Langenberg, J. McMenamin, D. E. Novoseller, Phys. Rev. Lett. 23, 229 (1969).

48. P. A. Lee, M.O. Scully, Phys. Rev. Lett. 22, 23 (1969).

49. M. J. Stephen, Phys. Rev. 186, 393 (1969).

50. D. E. McCumber, Phys. Rev. Lett. 23, 1228 (1969).

51. F. Bloch, Phys. Rev. Lett. 21, 1241 (1968) and Phys. Rev. B2, 109 (1970).

52. T. A. Fulton, R. C. Dynes, Phys. Rev. Lett. 25, 794 (1970).

53. A. Baratoff, J. A. Blackburn, B. B. Schwartz, Phys. Rev. Lett. 25, 1096 (1970).

54. J. Matisoo, Proc. IEEE 55, 172 (1967).

55. T. D. Clark, Phys. Lett. 27A, 585 (1968).

56. C. C. Grimes, P. L. Richards, S. Shapiro, J. Appl. Phys. 39, 3905 (1968).

57. P. L. Richards, S. A. Sterling, Appl. Phys. Lett. 14, 394 (1969).

58. J. E. Zimmerman, Quarterly Technical Reports, 1968-1969; Philco Ford, Aeronutronic Division, Newport Beach, California.

59. J. E. Zimmerman, J. Appl. Phys. 41, 1589 (1970).

60. J. E. Zimmerman, J. T. Harding, J. Appl. Phys. 41, 1581 (1970).

61. J. E. Mercereau, Revue de Physique Appliquée 5, 13 (1970).

62. J. M. Goodkind, D. L. Stolfa, Rev. Sci. Inst. 41, 799 (1970).

63. M. B. Simmonds, W. H. Parker, J. Appl. Phys. 42, 38 (1971).

64. J. E. Zimmerman, A. H. Silver, Phys. Rev. Lett. 19, 14 (1967).

65. A. H. Silver, J. E. Zimmerman, R. A. Kamper, Appl. Phys. Lett. 11, 209 (1967).

66. J. E. Zimmerman, A. H. Silver, Appl. Phys. Lett. 10, 142 (1967).

67. J. E. Zimmerman, A. H. Silver, J. Appl. Phys. 39, 2679 (1968).

68. R. A. Kamper, J. E. Zimmerman, J. Appl. Phys. 42, 132 (1971).

69. R. A. Kamper, L. O. Mullen, D. B. Sullivan, NBS Technical Note 381 (1969). Available from U.S. Superintendent of Documents, U.S. Gov't Printing Office, Washington, D. C. 20402.

70. J. E. Zimmerman, J. Appl. Phys. 42, 30 (1971).

71. D. G. McDonald, A. S. Risley, J. D. Cupp, K. M. Evenson, Appl. Phys. Lett. 18, 162 (1971).

72. J. E. Zimmerman, "Sensitivity Enhancement of Superconducting Quantum Devices Through the use of Fractional Turn Loops (To be published J. Appl. Phys. Sept. 1971).

73. J. E. Zimmerman, A. H. Silver, Phys. Rev. 167, 418 (1968).

74. J. E. Mercereau, Reference 14, Vol. 1, Chapter 8.

75. A. Longacre Jr., S. Shapiro, Bull. Am. Phys. Soc. 16, 399 (March 1971).

76. W. A. Harrison, "Solid State Theory", p. 519 (McGraw-Hill Co., New York, 1970).

77. D. B. Sullivan, R. L. Peterson, V. E. Kose, J. E. Zimmerman, J. Appl. Phys. 41, 4865 (1970).

78. A. I. Larkin, Yu. N. Ovchinnikov, Soviet Physics JETP 55, 323 (1968).

79. E. Revolinsky, G. A. Spiering, D. J. Beerntsen, J. Chem. Phys. Solids 26, 1029 (1965).

80. R. Kershaw, M. Vlasse, A. Wold, Inorganic Chemistry 6, 1599 (1967).

81. R. F. Frindt, J. Appl. Phys. 37, 1928 (1966).

82. R. F. Frindt, Private Communication.

83. W. J. McG. Tegart, Electrolytic and Chemical Polishing of Metals (Pergamon Press 1957).

84. B. Heinrich, Private Communication.

85. L. Young, Anodic Oxide Films (Academic Press, New York, 1961).

86. C. C. Grimes, A. H. Dayem, Appl. Phys. Lett. 9, 47 (1966).

87. F. S. Rusin, G. D. Bogomolov, Soviet Physics JETP Lett. 4, 236 (1966).

88. A. Contaldo, Rev. Sci. Inst. 38, 1543 (1967).

89. N. R. Werthamer, S. Shapiro, Phys. Rev. 164, 523 (1967).

90. A. Arrott, Private Communication.

91. E. D. Lamotte, Y. Huang, C. Alstetter, Trans. of Met. Soc. of AIME 239, 1625 (1967).

92. D. W. Deis, J. R. Gavaler, J. K. Hulm, C. K. Jones, J. Appl. Phys. 40, 2153 (1969).

93. M. A. Janocko, J. R. Gavaler, C. K. Jones, R. D. Blaugher, J. Appl. Phys. 42, 182 (1971).

94. H. Zimmer, Appl. Phys. Lett. 10, 193 (1967).

95. P. Russer, Archiv der Electrischen Ubertragung (Wiesbaden) 23, 417 (1969).

96. W. S. Boyle, K. F. Rodgers, J. Opt. Soc. Am. 49, 66 (1959).

97. R. Bachman, H. C. Kirsch, T. H. Geballe, Rev. Sci. Inst. 41, 547 (1970).

98. J. Wheatley, Private Communication.

99. J. E. Zimmerman, Fifth (Final) Quarterly Technical Report, Philco-Ford, Now. 1968, p. 34.

100. V. E. Kose, D. B. Sullivan, J. Appl. Phys. 41, 169 (1970).

101. L. Leopold, D. Repici, W. D. Gregory, Can. J. Phys. 47, 1167 (1969).

102. G. Lasher, IBM, J. Res. Dev. 7, 58 (1963).

103. J. R. Schrieffer, D. M. Ginsberg, Phys. Rev. Lett. 8, 207 (1962).

104. A. Rothwarf, M. Cohen, Phys. Rev. 130, 1401 (1963).

105. A. Rothwarf, B. N. Taylor, Phys. Rev. Lett. 19, 27 (1967).

106. D. M. Ginsberg, Phys. Rev. Lett. 8, 204 (1962).

107. B. I. Miller, A. H. Dayem, Phys. Rev. Lett. 18, 1000 (1967).

108. W. Eisenmenger, A. H. Dayem, Phys. Rev. Lett. 18, 125 (1967).

109. J. L. Levine, S. Y. Hsieh, Phys. Rev. Lett. 20, 994 (1968).

110. S. Y. Hsieh, J. L. Levine, Phys. Rev. Lett. 20, 1502 (1968).

111. R. C. Dynes, V. Narayanamurti, M. Chin, Phys. Rev. Lett 26, 181 (1971).

112. A. Rothwarf, Phys. Rev. Lett. 23, 468 (1969).

113. W. van Roosbroeck, W. Shockley, Phys. Rev. 94, 1558 (1954).

114. E. Burstein, D. N. Langenberg, B. N. Taylor, Phys. Rev. Lett. 6, 92 (1961).

115. P. Beckmann, "Scattering of Light by Rough Surfaces" in Progress in Optics 6 (North Holland, Amsterdam 1967).

116. L. Leopold, W. D. Gregory, J. Bostock, Internal Report, Georgetown University, Washington, (1969).

117. L. Holland, Vacuum Deposition of Thin Films, p. 344, J Wiley and Sons, New York 1961).

118. F. J. Low, J. Opt. Soc. Am. 51, 1300 (1961).

119. P. Richards, "Developments in the Detection of Far Infrared Radiation" in Proceedings of the Eighth European Congress on Molecular Spectroscopy Copenhagen, 1965 (London, Butterwaite).

120. R. C. Jones, J. Opt. Soc. Am. 43, 1 (1953).

121. J. A. Blackburn, D. Hemming, J. D. Leslie, Appl. Opt. 7, 979 (1968).

122. P. deTrey, Private Communication.

123. K. Knott, El. Lett. 1, 250 (1965).

124. P. deGennes, Superconductivity of Metals & Alloys (Benjamin 1966) p. 38.

125. C. H. Hinricks, C. A. Swenson, Phys. Rev. 123, 1109 (1961).

126. P. C. Eastman, J. Datars, Can. J. Phys. 41, 161 (1963).

127. M. G. A. Bernard, G. Duraffourg, Phys. Stat. Solidi 1, 659 (1961).

128. M. Tinkham in Low Temperature Physics, Les Houches Summer School Lectures (1961) (Edited by C. deWitt, B. Dreyfus, P. deGennes, Gordon and Breach) p. 204.

129. D. Ginsberg, L. C. Hebel, Reference 14, Vol. 1, Chapter 4.

130. D. C. Mattis, J. Bardeen, Phys. Rev. 111, 412 (1958).

131. P. B. Miller, Phys. Rev. 118, 928 (1960).

132. T. P. Sheahen, Phys. Rev. 149, 368 (1966).

133. W. F. Vinen, Reference 14, Vol. II, Chapter 20.

134. S. L. Norman, Phys. Rev. 167, 393 (1968).

135. L. F. Mattheis, Phys. Rev. B1, 373 (1970).

136. J. J. Hauser, H. C. Theurer, Rev. Mod. Phys. 36, 80 (1964).

137. W. L. MacMillan, Phys. Rev. 167, 331 (1968).

138. P. L. Richards, M. Tinkham, Phys. Rev. 119, 575 (1960).

139. M. Tinkham, in Optical Properties of Metals and Alloys, Edited by F. Abeles (North Holland Publishing Co., Amsterdam 1966) p. 431.

140. W. D. Gregory, Private Communication.

141. J. F. Cochran, Annals of Physics 19, 186 (1962).

142. R. Conte, Elements de Cryogenie (Masson et Cie, Paris, 1970).

143. G. Burns, M. Nathan, Proc. I.E.E.E. 52, 770 (1964).

144. K. Arnold, S. Mayburg, J. Appl. Phys. 34, 3136 (1963).

145. D. Röss, Lasers Light Amplifiers and Oscillators (Academic Press, New York, 1969).

146. P. Wyder, (University of Nijwegan, Netherlands) Private communication.

147. J. Clarke, Physics Today, August 1971, p. 30.

148. T. Carver, Private Communication.

149. B. P. Clayman, R. F. Frindt, To be published.

150. B. Matthias, Physics Today, August 1971, p. 23.

151. M.B. Burbank, Private Communication

152. J.P. Schulz, O. Weiss, Proceedings of the 12th Conference on Low Temperature Physics (Edited by E. Kanda 1971) p. 433.

153. D.J. Huntley, J. Kopp, R.F. Frindt. (To be published.)